

Developing hydrogen oxidation electrocatalysts using a frustrated Lewis pair approach



Elliot John Lawrence

A thesis submitted in accordance with the requirements for the degree of
Doctor of Philosophy (PhD) from the University of East Anglia.

School of Chemistry, University of East Anglia

January 2015

© This copy of the thesis has been supplied on condition that anyone who consults it is understood to recognise that its copyright rests with the author and that use of any information derived there from must be in accordance with current UK Copyright Law. In addition, any quotation or extract must include full attribution.

I Abstract

In order for hydrogen to be utilised as an energy vector, precious metals such as platinum are often employed as electrocatalysts, to enable the efficient conversion of hydrogen into electrical energy. However, the low abundance and high cost of such metals limits their economic viability.

Frustrated Lewis pairs (FLPs) are capable of heterolytically cleaving hydrogen, and have found application in hydrogenation chemistry. In this thesis, the hydrogen-activating ability of FLPs is exploited for the development of new, metal-free electrocatalysts for hydrogen oxidation. In essence, this approach combines FLP hydrogen activation with the electrochemical oxidation of the resulting borohydride.

Initially, a fundamental study into the single-electron reduction of the archetypal Lewis acid, tris(pentafluorophenyl)borane, was undertaken in low donor strength solvents. This allowed pertinent thermodynamic, kinetic and mechanistic information to be obtained.

The redox chemistry of the archetypal FLP system, tris(pentafluorophenyl)borane/tri-*t*-butylphosphine, was then studied for the first time. FLP pre-activation of hydrogen was found to decrease the required potential for non-aqueous hydrogen oxidation by 610 mV at inexpensive and abundant carbon electrodes. This system was then extended to include platinum electrode materials, where strong surface electrocatalytic effects were exhibited.

The combined electrochemical-frustrated Lewis pair approach was applied to a series of carbene-stabilised borenium cations. Their efficacy towards the electrocatalytic oxidation of hydrogen was assessed. The borenium cation derived from 9-borabicyclo[3.3.1]nonane decreased the required voltage for hydrogen oxidation by 910 mV. This system also exhibited improved catalyst recyclability compared with the original tris(pentafluorophenyl)borane system.

Finally, the cyclic voltammetry of two regioisomers of tris[bis(trifluoromethyl)phenyl]borane was explored for the first time. Solutions of tris[3,5-bis(trifluoromethyl)phenyl]borane in the donor solvent tetrahydrofuran were highly effective for facile hydrogen cleavage. Replacing the Lewis basic component of conventional FLP systems with donor solvents is a new approach to FLP chemistry, and proffers many advantages for electrochemical-FLP systems.

II Acknowledgements

First and foremost, I would like to express my utmost gratitude to Dr. Gregory Wildgoose, without whom this work would not have been possible. He has provided me with many opportunities throughout my time in his research group, including a unique project that has constantly challenged and stimulated my mind. I would like to offer my special thanks to Dr. Andrew Ashley (Imperial College London) for his ideas and advice. The main concept that embodies this thesis was jointly conceived by Dr. Wildgoose and Dr. Ashley; the results contained herein are the first product of an ongoing collaboration. I would like to offer my special thanks to my secondary supervisor, Prof. Simon Lancaster, who has always offered his support and advice.

I am particularly grateful for the advice and assistance given by Dr. Robin Blagg, including the proof-reading of this thesis, the solution and refinement of crystallographic data, and for rendering images of molecular structures for my thesis. I wish to acknowledge the support and advice provided by Dr. David Day, his positive attitude and friendship never failed to elevate my mood. My special thanks are extended to the remainder of the Wildgoose group members both past and present, particularly Dr. Thomas Dann and Mr. James Buttress.

The assistance provided by Dr. Vasily Oganessian in performing DFT calculations on my systems, was greatly appreciated. The results have provided me with a deeper understanding of this work. Digital simulation of my electrochemical data would have been more difficult without Dr. Colin MacDonald, who set up DOSY experiments on the NMR spectrometer. I would like to thank Dr. David Hughes for his time in solving and refining crystallographic data. I would also like to thank Ms. Kate Resner and Dr. Thomas Herrington for their collaborations.

Thank you to the National Crystallographic Service at Southampton for collecting crystallographic data for my compounds.^[1] I also wish to acknowledge the use of the EPSRC funded National Chemical Database Service hosted by the Royal Society of Chemistry. I wish to acknowledge the financial support received from the Engineering and Physical Sciences Research Council *via* a Doctoral Training Account studentship under the grant number EP/J500409/; the research leading to these results has also received funding from the European Research Council under the ERC Grant Agreement number 307061.

Finally I would like to acknowledge the limitless support provided by my fiancée, Natasha Ayres, and my family throughout my studies, and particularly during the preparation of this thesis.

III Table of contents

I	Abstract	i
II	Acknowledgements	iii
III	Table of contents	v
IV	List of figures	xi
V	List of schemes	xv
VI	List of tables	xvii
VII	List of equations	xix
VIII	List of abbreviations	xxi
	With respect to electrochemistry	xxii
	With respect to abbreviated words and phrases	xxiii
	Compound structures	xxiv
	Colour scheme for molecular structures	xxix
	Chapter 1 Introduction	1
	1.1 Hydrogen discovery and production	2
	1.2 The hydrogen economy	4
	1.3 Hydrogen fuel cells	5
	1.4 Pt as an electrocatalyst for H ₂ oxidation	7
	1.5 Non-precious metal electrocatalysts for H ₂ oxidation	9
	1.6 Frustrated Lewis pairs	17
	1.7 Electrochemical methods	36
	1.7.1 Electrochemical equilibria	36
	1.7.2 Electrode kinetics	37
	1.7.3 Mass transport – diffusion, convection and migration	41
	1.7.4 Supporting electrolyte	44
	1.7.5 Electrode materials	45

1.7.6	The need for a three-electrode setup	46
1.7.7	Chronoamperometry	46
1.7.8	Cyclic voltammetry	50
1.7.9	Coupled chemical reactions and adsorption	56
1.7.10	Simulation of cyclic voltammetric data	59
1.8	Aims	63

Chapter 2 Results and discussion

Exploring the redox chemistry of $B(C_6F_5)_3$ 65

2.1	Overview	66
2.2	Electrochemical experiments	68
2.3	Digital simulation	75
2.4	Computational modelling of $B(C_6F_5)_3^{*-}$	79
2.5	Exploring the fate of $B(C_6F_5)_3^{*-}$	81
2.6	Summary	84

Chapter 3 Results and discussion

The first electrochemical study of frustrated Lewis pairs ..87

3.1	Overview	88
3.2	Authentic $[HB(C_6F_5)_3]^-$	89
3.3	Initial electrochemical studies	90
3.4	Spectroscopic studies	96
3.5	Computational modelling	98
3.6	Proof of concept	100
3.7	Summary	105

Chapter 4 Results and discussion

Surface catalytic effects at Pt electrodes..... 107

4.1	Overview	108
4.2	Electrochemical studies	108
4.3	Competition experiments	113

4.4	Steric effects	115
4.5	Proof of concept	120
4.6	Summary	121
Chapter 5 Results and discussion		
Borenium cations		123
5.1	Overview	124
5.2	Synthesis and characterization of the borenium cations	125
5.3	Electrochemical study of the borenium cations	127
5.4	Study into FLP H ₂ activation	136
5.5	Electrochemical studies into the NHC-borane adduct	140
5.6	Proton-mediated generation of the borenium cation	142
5.7	Digital simulation of the NHC-borane oxidation	142
5.8	Electrocatalyst recyclability	146
5.9	Summary	147
Chapter 6 Results and discussion		
Tris[bis(trifluoromethyl)phenyl]boranes		149
6.1	Overview	150
6.2	Synthesis and characterization of the boranes	151
6.3	Electrochemical study of the boranes	153
6.4	Exploring FLP H ₂ activation using B{C ₆ H ₃ (2,4-CF ₃) ₂ } ₃	159
6.5	Ethereal solvents as the Lewis base for FLP H ₂ activation	159
6.6	Electrochemical studies of the H ₂ activation products	164
6.7	Investigating <i>in situ</i> H ₂ oxidation	168
6.8	Hydride shuttle processes between boranes	170
6.9	Summary	172
Chapter 7 Conclusions and future work		175
7.1	Conclusions	176
7.2	Future work	178

Chapter 8 Experimental methods and materials	183
8.1 General considerations	184
8.2 Materials	184
8.2.1 Solvents	184
8.2.2 Gases	184
8.2.3 Reagents	184
8.3 Instrumentation	185
8.4 DFT computational modelling	185
8.5 Electrochemical methods	186
8.5.1 General methods	186
8.5.2 Digital simulation of voltammetric data	187
8.6 Synthetic methods	187
8.6.1 Chemical reduction of 8 for NMR studies	188
8.6.2 Preparation of Na[8 -H]	188
8.6.3 Preparation of [ⁿ Bu ₄ N][8 -H]	188
8.6.4 Preparation of [TMP-D][DB(C ₆ F ₅) ₃]	189
8.6.5 Preparation of [ⁿ Bu ₄ N][8 -D]	189
8.6.6 Preparation of Na[24 -H]	190
8.6.7 Preparation of [ⁿ Bu ₄ N][24 -H]	190
8.6.8 Preparation of [25]OTf	190
8.6.9 Preparation of [26]OTf	191
8.6.10 Preparation of [27]OTf	191
8.6.11 Proton-mediated generation of 19 [B(C ₆ F ₅) ₄]	192
8.6.12 Preparation of 28	192
8.6.13 Preparation of Na[20 -H]	193
8.6.14 <i>In situ</i> formation of [H(THF) _n][(μ -H)(20) ₂]	193
8.6.15 Isolated [H(THF) ₂][(μ -H)(20) ₂]	193
8.6.16 Hydride transfer between [TMP-H][(μ -H)(20) ₂] and 8	194

References	195
Appendix of crystallographic data	211

IV List of figures

Figure 1 Renewable methods of H ₂ production.	4
Figure 2 Basic principle of H ₂ fuel cell operation.	6
Figure 3 Grove’s gaseous voltaic battery – the first H ₂ fuel cell	7
Figure 4 a) Typical structural features of the [FeFe] and [NiFe] hydrogenase enzymes; b) a simple depiction of the active site of an [FeFe] hydrogenase enzyme.	11
Figure 5 Citations per year for the term “frustrated Lewis pair”.	21
Figure 6 Proposed electron transfer mechanistic model for heterolytic H ₂ activation by a FLP.	24
Figure 7 Molecular structure of 19 ⁺	29
Figure 8 Effect of the charge transfer coefficient (α) on the symmetry of the interacting Gibbs free energy curves.	40
Figure 9 Symmetry of the diffusion field at a planar electrode surface.	41
Figure 10 Examples of weakly coordinating anions.	44
Figure 11 The structure of glassy-carbon.	46
Figure 12 Chronoamperometry at a macrodisk electrode.	47
Figure 13 Chronoamperometry at microdisk vs macrodisk electrodes.	48
Figure 14 Diffusion field symmetries at microdisk and macrodisk electrodes at long experiment times.	49
Figure 15 Potential-time profile applied in cyclic voltammetry experiments.	50
Figure 16 Cyclic voltammetry at microdisk and macrodisk electrodes.	51
Figure 17 Simulated CVs exhibiting reversible, <i>quasi</i> -reversible, and irreversible behaviour at a macrodisk electrode.	52
Figure 18 An annotated simulated CV exhibiting reversible behaviour at a macrodisk electrode.	53
Figure 19 a) Simulated CVs of varying scan rates for a reversible single-electron oxidation, and b) a Randles-Sevcik plot showing the linear relationship of peak current with square root scan rate.	55
Figure 20 Simulated CVs of varying scan rates for an oxidative <i>EC</i> process.	57
Figure 21 Simulated CV for an oxidative <i>EC</i> ’ process.	59
Figure 22 Scheme of the boundary conditions in an electrochemical system involving an <i>EC</i> mechanism.	61
Figure 23 Molecular structure of 8 -THF.	67

Figure 24 Overlaid CVs of 8 in CH ₂ Cl ₂ and DFB, recorded at varying scan rates..	69
Figure 25 Experimental chronoamperograms and Shoup-Szabo best fits for the reduction of 8 in CH ₂ Cl ₂ and DFB.	72
Figure 26 Linear sweep voltammogram for the one-electron reduction of 8 in CH ₂ Cl ₂ and DFB.	74
Figure 27 Experimental and simulated overlaid CVs for the reduction of 8 in CH ₂ Cl ₂ .	76
Figure 28 Experimental and simulated overlaid CVs for the reduction of 8 in DFB.	77
Figure 29 The SOMO of 8 ^{•-} and its corresponding spin-density.	79
Figure 30 View of the geometry optimized structures of 8 and 8 ^{•-} with the partial charges shown for each atom.	80
Figure 31 Molecular structure of [8 -H] ⁻ .	90
Figure 32 CV of a 4.9 mM solution of [ⁿ Bu ₄ N][8 -H] in CH ₂ Cl ₂ over the full potential window.	91
Figure 33 Experimental and simulated overlaid CVs for the oxidation of [ⁿ Bu ₄ N][8 -H] (2.9 mM) in CH ₂ Cl ₂ .	93
Figure 34 Experimental and simulated overlaid CVs for the oxidation of [ⁿ Bu ₄ N][8 -H] (4.9 mM) in CH ₂ Cl ₂ .	94
Figure 35 ³¹ P{ ¹ H} NMR spectra of aliquots taken before and after the oxidative bulk electrolysis of [ⁿ Bu ₄ N][8 -D] in the presence of excess 12 .	98
Figure 36 View of the geometry-optimized structure of [8 -H] ⁻ along with its corresponding HOMO, and the SOMOs of [8 -H] [•] and 8 ^{•-} .	99
Figure 37 View of the geometry optimized structure of [8 -H] ⁻ with partial charges shown for each atom.	100
Figure 38 ¹¹ B NMR spectrum showing the reaction progress of H ₂ activation by the 8/12 FLP.	101
Figure 39 a) CV of 12/8 after admission to H ₂ . b) CV of a H ₂ -saturated solution at a GCE.	102
Figure 40 Repeat oxidative bulk electrolysis cycles of the 8/12 FLP following overnight exposure to H ₂ .	104
Figure 41 Overlaid CVs of [ⁿ Bu ₄ N][8 -H] (2.3 and 4.8 mM) at a Pt electrode.	109
Figure 42 Overlaid CVs comparing [ⁿ Bu ₄ N][8 -H] recorded at Pt and glassy carbon electrodes.	110
Figure 43 Overlaid CVs showing the effect of adding increasing molar equivalents of 6-bromo-1-hexene to [ⁿ Bu ₄ N][8 -H] at a Pt macrodisk electrode.	114
Figure 44 Space-filling view of the boranes 8 and 24 .	116
Figure 45 Molecular structure of [24 -H] ⁻ .	117
Figure 46 Space-filling view of [8 -H] ⁻ and [24 -H] ⁻ .	118

Figure 47 Overlaid CVs comparing [ⁿ Bu ₄ N][8 -H] and [ⁿ Bu ₄ N][24 -H] at a Pt electrode.	120
Figure 48 Overlaid CVs demonstrating the 8 /TMP FLP system before and after a 1 h sparge with H ₂	121
Figure 49 Molecular structures of the dimesitylborenium cations 25 ⁺ and 26 ⁺	127
Figure 50 Overlaid CVs comparing the borenium compounds 25 [OTf], 26 [OTf], 27 [OTf], and 19 [B(C ₆ F ₅) ₄] at varying scan rates.	128
Figure 51 Experimental and simulated CVs for the reduction of 25 [OTf].	130
Figure 52 Experimental and simulated CVs for the reduction of 26 [OTf].	131
Figure 53 Experimental and simulated CVs for the reduction of 27 [OTf].	132
Figure 54 Experimental and simulated CVs for the reduction of 19 [B(C ₆ F ₅) ₄].	133
Figure 55 Space-filling view of the borenium cation 25 ⁺ , 26 ⁺ , 27 ⁺ , and 19 ⁺	136
Figure 56 Photograph of samples obtained after 24 hours when 26 [OTf] is treated with 12 in either CD ₂ Cl ₂ or CDCl ₃	138
Figure 57 Initially proposed abnormal carbene adduct.	138
Figure 58 a) Overlaid CVs of 19 -H recorded at varying scan rates; b) CVs comparing 19 -H, [ⁿ Bu ₄ N][8 -H], and H ₂	141
Figure 59 Experimental and simulated CVs showing the full potential window following the oxidation of 19 -H.	143
Figure 60 Randles-Sevcik and Laviron plots comparing simulated and experimental peak current/potential data against the square root of scan rate.	144
Figure 61 Repeat oxidative bulk electrolysis cycles of 19 -H, generated from the overnight exposure of 19 [B(C ₆ F ₅) ₄]/ 12 to H ₂	147
Figure 62 Molecular structures of the B{C ₆ H ₃ (CF ₃) ₂ } ₃ variants 20 , and 28	151
Figure 63 Overlaid CVs for a) 20 , and b) 28 at varying scan rates.	153
Figure 64 Experimental and simulated CVs for the reduction of authentic 20 at varying scan rates.	155
Figure 65 Experimental and simulated CVs for the reduction of authentic 28 at varying scan rates.	156
Figure 66 Space-filling views of 20 and 28	159
Figure 67 Experimental CVs of the isolated bridging hydrides [TMP-H][(μ -H)(20) ₂], and [H(THF) ₂][(μ -H)(20) ₂].	166
Figure 68 Overlaid CVs for the authentic terminal hydride Na[20 -H] at varying scan rates.	168
Figure 69 CV of the 20 /TMP FLP in THF.	170

V List of schemes

Scheme 1 Steam reforming of CH ₄ to generate syngas.....	2
Scheme 2 The water-gas shift reaction.	2
Scheme 3 The electrolysis of deionised water at PEM electrolyzers.	3
Scheme 4 Synthesis of a structural [FeFe] hydrogenase model (3) by Pickett and co-workers..	12
Scheme 5 Mechanism of electrocatalytic H ₂ oxidation by 4 -H in the presence of a Brønsted base.	14
Scheme 6 Mechanism of electrocatalytic H ₂ oxidation by 5 in the presence of a Brønsted base.	16
Scheme 7 Formation of a classical Lewis adduct (6).	17
Scheme 8 Brown's early work into steric frustration.	18
Scheme 9 Preparation and demonstration of a phosphino-borane (11) that is capable of reversible H ₂ activation.	19
Scheme 10 Activation of H ₂ by 8 /phosphine FLPs.	20
Scheme 11 H ₂ activation by the 8 /TMP FLP.....	22
Scheme 12 H ₂ activation and side-reaction of the 8 /Im ^t Bu ₂ FLP.....	22
Scheme 13 Catalytic imine hydrogenation by 8	25
Scheme 14 Attempt to hydrogenate the bulky imine (14) using a catalytic quantity of 8	26
Scheme 15 Catalytic asymmetric imine hydrogenation using FLPs comprised of chiral boranes.....	26
Scheme 16 2,6-Lutidine (lut) and 8 exhibit both classical and frustrated behaviour.....	27
Scheme 17 Hydroboration using Piers' borane to give an intramolecular phosphine-borane adduct that effects H ₂ activation.....	28
Scheme 18 Reaction of tertiary amines (NEt ₃) with 8	28
Scheme 19 Alternative resonance form of 19 ⁺	30
Scheme 20 FLP activation of H ₂ using a borenium cation (19 ⁺).....	30
Scheme 21 Examples of Lewis acids that favour the formation of bridging hydrides (μ-H).	32
Scheme 22 The formation of a classical Lewis adduct (LB· 20) between 20 and a Lewis base drives the conversion of the bridging hydride ([μ-H] 20 ₂) ⁻ into a terminal hydride ([20 -H]) ⁻	33
Scheme 23 Examples of small molecule activation by FLPs containing 8	34
Scheme 24 Activation of H ₂ by the ferrocenyl phosphine 23/8 FLP.....	35
Scheme 25 The single-electron electrochemical reduction of A results in the formation of B...36	

Scheme 26 A generic <i>EC</i> reaction. Y is electroinactive.....	57
Scheme 27 A generic <i>EC'</i> reaction. Y and B are electroinactive.....	58
Scheme 28 The electrochemical-FLP approach to the electrocatalysis of H ₂ oxidation.	64
Scheme 29 Postulated EC mechanism for the reduction of B(C ₆ F ₅) ₃ , 8	70
Scheme 30 The proposed electrochemical-FLP concept of H ₂ oxidation electrocatalysis.....	88
Scheme 31 Proposed mechanism and associated thermodynamic and kinetic parameters used to simulate the oxidation of [8-H] ⁻ at a GCE.....	92
Scheme 32 Hypothesised H ₂ evolution pathway i.....	96
Scheme 33 Hypothesised H ₂ evolution pathway ii.....	96
Scheme 34 a) The proposed redox mechanism with individual steps for the electrocatalytic oxidation of [8-H] ⁻ at a Pt electrode surface.	112
Scheme 35 Reaction of the radical scavenger, 6-bromo-1-hexene, with H [*] from electrogenerated [8-H] [*]	113
Scheme 36 Preparation of 25 [OTf], 26 [OTf], and 27 [OTf].	125
Scheme 37 The proposed mechanism and parameters used in the digital simulation of the voltammetric reduction of 25 [OTf], 26 [OTf], 27 [OTf] and 19 [B(C ₆ F ₅) ₄].....	129
Scheme 38 The proposed mechanism and associated thermodynamic and kinetic parameters used in digital simulation of the voltammetric oxidation of 19 -H.	140
Scheme 39 Preparation of 20 and 28	152
Scheme 40 The proposed mechanism and parameters used in digital simulation of the voltammetric reduction of the 20 and 28	157
Scheme 41 Postulated H ₂ activation equilibria exhibited by 20 when paired with the Lewis bases TMP and THF.	163
Scheme 42 Postulated product (30) of THF ring-opening by 20 /TMP.	169
Scheme 43 Hydride shuttle process between [TMP-H][μ-H(20) ₂] and 8	171
Scheme 44 New concept for electrocatalytic H ₂ production using a hydroxyphenylborane....	181

VI List of tables

Table 1 Comparing the cyclic voltammetric behaviour of macro- and microdisk electrodes.	56
Table 2 Simulated parameters for the voltammetric reduction of 8	78
Table 3 ^{11}B NMR data and analysis for the reduction of 8 with $\text{Co}^{\text{II}}(\text{Cp}^{\text{Me5}})_2$ in CH_2Cl_2	82
Table 4 ^{19}F NMR data and analysis for the reduction of 8 with $\text{Co}^{\text{II}}(\text{Cp}^{\text{Me5}})_2$ in CH_2Cl_2	83
Table 5 Globally optimized best-fit thermodynamic and kinetic parameters obtained from the digital simulation of voltammetric data for $[\text{nBu}_4\text{N}][\mathbf{8}\text{-H}]$ at a GCE.	95
Table 6 Globally optimized best-fit thermodynamic and kinetic parameters obtained from digital simulation of the voltammetric data for 25 [OTf], 26 [OTf], 27 [OTf] and 19 [$\text{B}(\text{C}_6\text{F}_5)_4$].	134
Table 7 Globally optimized best-fit thermodynamic and kinetic parameters obtained from digital simulation of the voltammetric data for 19 -H.	145
Table 8 Globally optimized best-fit thermodynamic and kinetic parameters obtained from digital simulation of the voltammetric data for 20 and 28	157
Table 9 Crystallographic data	213

VII List of equations

Equation 1 Electrochemical definition of an overpotential (η).....	8
Equation 2 The measured electrode potential (E) at a Pt wire electrode vs a reference electrode.	37
Equation 3 The Nernst equation.....	37
Equation 4 The measured current in terms of the reactant flux (j) and the electroactive area (A).	38
Equation 5 The net flux of reactant A at the electrode surface (undergoing reduction to B). ...	38
Equation 6 The observed electrochemical rate constant for the forward (k_f) and backward (k_b) electrochemical reactions.	38
Equation 7 The net flux of reactant A in terms of its overpotential.....	39
Equation 8 The net flux of reactant A in terms of its overpotential.....	39
Equation 9 The Butler-Volmer equation.	39
Equation 10 The charge transfer coefficient (α) in terms of Gibbs free energy change (ΔG) and the reorganisation energy (λ).	40
Equation 11 Fick's first law of diffusion.....	42
Equation 12 Stokes-Einstein equation.....	42
Equation 13 Fick's second law of diffusion for a planar electrode.....	42
Equation 14 The Cottrell equation.	47
Equation 15 The diffusion-limited steady-state current (i_{ss}) at a microdisk electrode of radius r	49
Equation 16 The current-time transient at a microdisk electrode of radius r	50
Equation 17 The Shoup-Szabo expression for $f(\tau)$	50
Equation 18 The mass transport coefficient (m_T).....	53
Equation 19 The mid-peak potential (E_{mid}) for a reversible electrode process.	54
Equation 20 The Randles-Sevcik equation.	54
Equation 21 General boundary conditions for an electrochemical experiment.	61
Equation 22 Finite difference equations for the approximation of partial derivatives.	62
Equation 23 Linear equations for the backward implicit method.....	63
Equation 24 Charge transfer coefficient (α) in terms of Gibbs free energy change (ΔG) and the solvent reorganisation energy (λ_o).....	81

VIII List of abbreviations

ATR	–	Attenuated total reflectance
B ⁺	–	Borenium cation (generic)
BDE	–	Bond dissociation energy
Cp	–	$\eta^5\text{-C}_5\text{H}_5$
Cp ^{Me5}	–	$\eta^5\text{-C}_5\text{Me}_5$
DFT	–	Density functional theory
DOSY	–	Diffusion-ordered NMR spectroscopy
EPR	–	Electron paramagnetic resonance
ESI-MS	–	Electrospray ionisation-mass spectrometry
<i>e</i>	–	Elementary unit of charge (1.602×10^{-19} C)
ee	–	Enantiomeric excess
Fc	–	Ferrocenyl ($\eta^5\text{-C}_5\text{H}_5$)Fe($\eta^5\text{-C}_5\text{H}_4$)
FLP	–	Frustrated Lewis pair
$\sigma_{para}(X)$	–	Hammett parameter for substituent X in the <i>para</i> -aryl position
HOMO	–	Highest occupied molecular orbital
h	–	Hour/s
HAT	–	Hydrogen atom transfer
Im	–	Imidazol-2-ylidene (free <i>N</i> -heterocyclic carbene)
IR	–	Infrared
IUPAC	–	International Union of Pure and Applied Chemistry
L	–	Ligand (datively bound and neutral)
LA	–	Lewis acid
LB	–	Lewis base
LUMO	–	Lowest unoccupied molecular orbital
pK _a	–	Logarithmic acid dissociation constant
Mes	–	Mesitylene group (C ₆ H ₂ Me ₃)
NHC	–	<i>N</i> -Heterocyclic carbene
NMR	–	Nuclear magnetic resonance
[NiFe] _{S77}	–	An O ₂ stable [NiFe] hydrogenase from <i>Citrobacter</i> sp. S-77
χ_E	–	Pauling electronegativity value for element E
PCET	–	Proton-coupled electron transfer
SOMO	–	Singly occupied molecular orbital

ΔH^0	–	Standard enthalpy change (kJ mol^{-1})
R	–	Substituent (σ -bound)
$E_s(X)$	–	Taft steric substituent constant for substituent X
fmes	–	2,4,6-Tris(trifluoromethyl)phenyl group
UV-Vis	–	UV-Visible
λ_{max}	–	Wavelength of maximum absorption in UV-visible spectroscopy

With respect to electrochemistry

T	–	Absolute temperature (K)
γ_X	–	Activity coefficient for species X
k_B	–	Boltzmann's constant ($1.38 \times 10^{-23} \text{ J K}^{-1}$)
C_{dl}	–	Capacitive charging (background) current
$\frac{\partial c}{\partial t}$	–	Change in concentration with time
α and β	–	Charge transfer coefficients
c_j^l	–	Concentration described in terms of point space (j) and time (l)
$[X]_0$	–	Concentration of species X at the electrode surface (mol L^{-1})
CV	–	Cyclic voltammogram
k	–	Chemical rate constant ($\text{M}^{1-n} \text{ s}^{-1}$; n is the overall rate order)
D	–	Diffusion coefficient ($\text{cm}^2 \text{ s}^{-1}$)
j	–	Diffusive flux ($\text{mol cm}^2 \text{ s}^{-1}$)
d	–	Diffusion layer on ordinate x
φ	–	Electrical potential (V)
A	–	Electroactive area (cm^2)
r	–	Electroactive radius (cm)
F	–	Faraday constant ($96485.3 \text{ C mol}^{-1}$)
k_f	–	Forward electrochemical rate constant (m s^{-1})
R	–	Gas constant ($8.314 \text{ V C K}^{-1} \text{ mol}^{-1}$)
G	–	Gibbs free energy (J mol^{-1})
ΔG	–	Gibbs free energy change (J mol^{-1})
GCE	–	Glassy carbon macrodisk working electrode
E	–	Heterogeneous electron transfer (Testa and Reinmuth notation)
C	–	Homogeneous chemical reaction (Testa and Reinmuth notation)
$c_{t=0}$	–	Initial concentration of the electroactive species (mol L^{-1})
λ_i	–	Inner-sphere reorganisation energy (J mol^{-1})

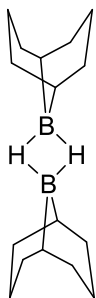
$\frac{\partial c}{\partial x}$	–	Local concentration gradient at point x ($\text{mol L}^{-1} \text{m}^{-1}$)
m_T	–	Mass transport coefficient
E_{mid}	–	Mid-peak potential (V)
n	–	Number of electrons involved in electrode process
E	–	Experimentally observed reduction potential (V)
k	–	Observed electrochemical rate constant (cm s^{-1} for a 1 st order process)
OCP	–	Open circuit potential
η	–	Overpotential (V)
λ_o	–	Outer-sphere reorganisation energy (J mol^{-1})
PEM	–	Proton exchange membrane
i_p	–	Peak current (A)
E_p	–	Peak potential (V)
ΔE_{pp}	–	Peak-to-peak separation (V)
$[\varphi_M - \varphi_S]$	–	Potential difference at a single electrode-solution interface (V)
$\frac{\partial^2 c}{\partial x^2}$	–	Rate of change in the local concentration gradient
λ	–	Reorganisation energy (J mol^{-1})
k_b	–	Reverse (oxidative) electrochemical rate constant (m s^{-1})
ν	–	Scan rate (V s^{-1})
λ_0	–	Solvent reorganisation energy (J mol^{-1})
x	–	Spatial ordinate for theoretical models of diffusion
k^0	–	Standard electrochemical rate constant (cm s^{-1})
SHE	–	Standard hydrogen electrode (for $\text{Cp}_2\text{Fe}^{0/+}$, $E^0 = +0.64$ vs SHE)
E^0	–	Standard reduction potential (V)
i_{ss}	–	Steady-state current at a microdisk electrode
t	–	Time (s)
Q	–	Total charge passed (C)
η_V	–	Viscosity (Pa s)

With respect to abbreviated words and phrases

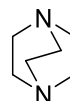
<i>ca</i>	–	Circa
<i>cf.</i>	–	Confer
<i>e.g.</i>	–	Exempli gratia
<i>et al.</i>	–	Et alii

etc.	–	Etcetera
<i>i.e.</i>	–	Id est
<i>vs</i>	–	Versus

Compound structures



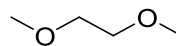
9-BBN = 9-Borabicyclo[3.3.1]nonane



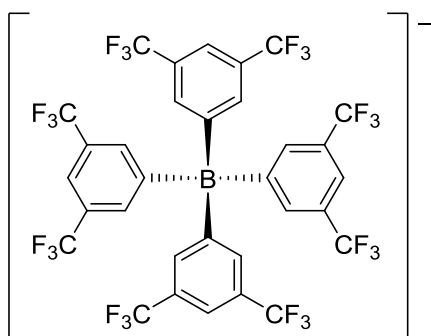
DABCO = 1,4-Diazabicyclo[2.2.2]octane



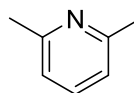
DFB = 1,2-Difluorobenzene



DME = Dimethoxyethane



[BArF₂₄]⁻ = Kobayashi's anion, tetrakis[3,5-bis(trifluoromethyl)phenyl]borate



lut = 2,6-Lutidine



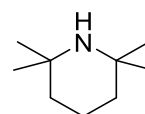
py = Pyridine



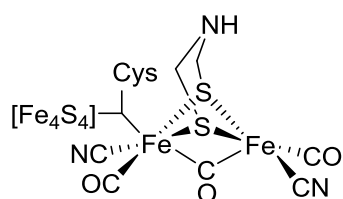
THF = Tetrahydrofuran



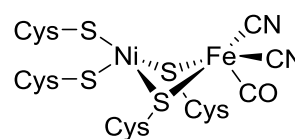
THT = Tetrahydrothiophene



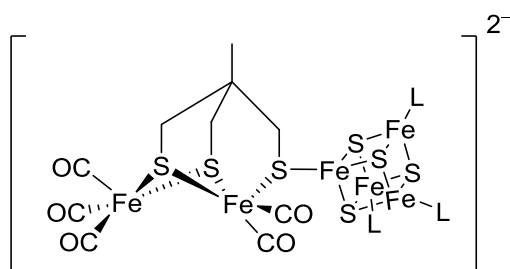
TMP = 2,2,6,6-Tetramethylpiperidine



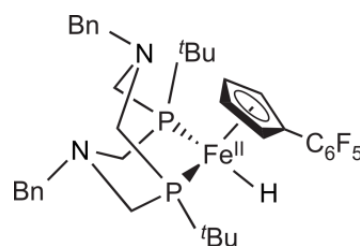
1



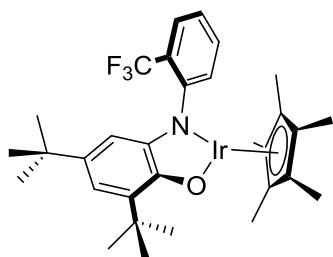
2



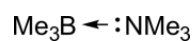
3



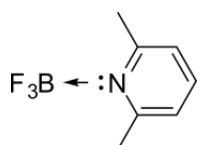
4-H



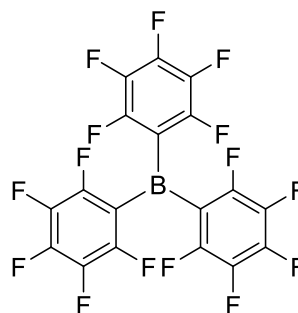
5



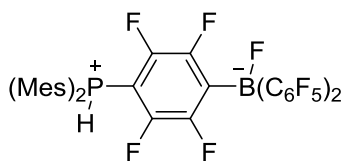
6



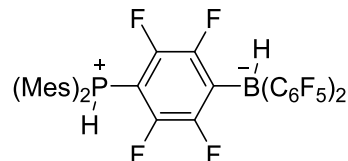
7



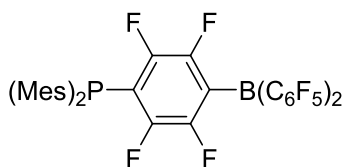
8



9



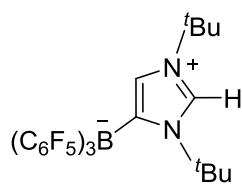
10



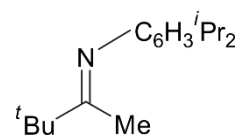
11



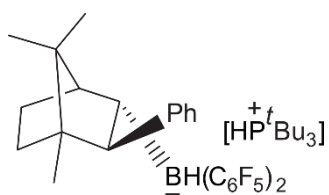
12



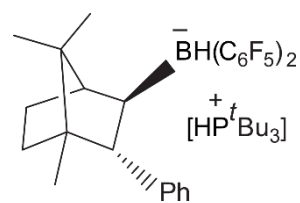
13



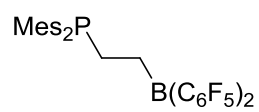
14



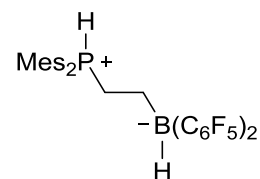
15



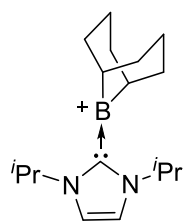
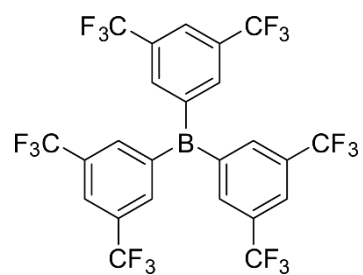
16



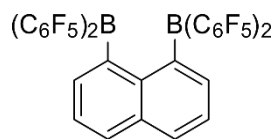
17



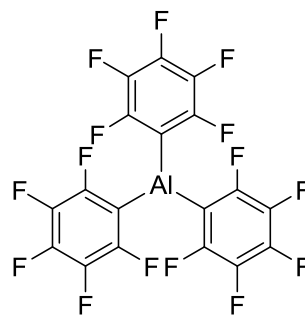
18

19⁺

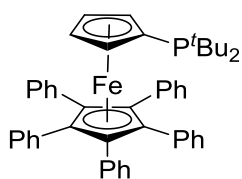
20



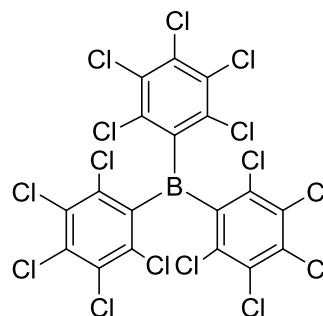
21



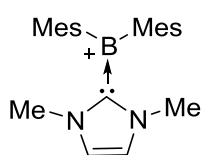
22



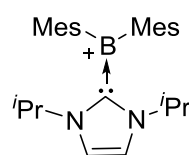
23



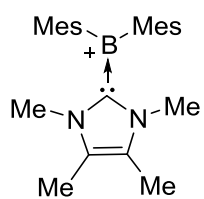
24



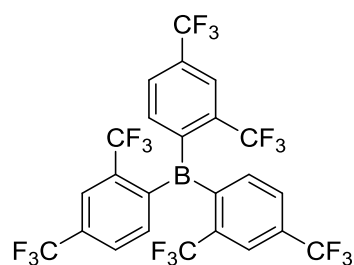
25⁺



26⁺



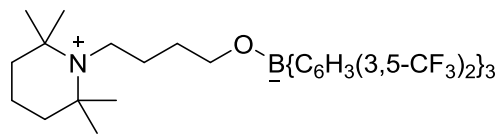
27⁺



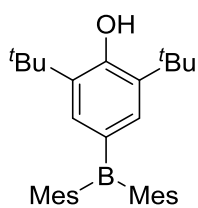
28



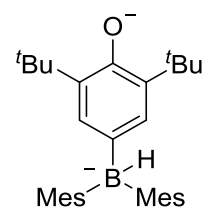
29



30



31



32

Colour scheme for molecular structures



Al



B



C



Cl



F



H



N



O

Chapter 1

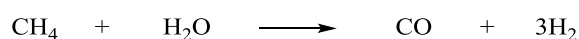
Introduction

1.1 Hydrogen discovery and production

Hydrogen is the most abundant element in the universe.^[2] In its molecular form, H₂ is a highly reactive yet non-polluting gas. Whilst, H₂ is the main constituent of stars and can be found as interstellar gas, on planet Earth it is relatively low in abundance. Despite elemental hydrogen accounting for *ca* 15% of the atoms in the Earth's crust and oceans,^[2,3] the majority of this is locked up in molecules such as water, CH₄ and other organic materials.

H₂ is believed to have first been produced towards the end of the 15th century by early researchers who dissolved metals in acids.^[4] Despite this, it wasn't until the 18th century that H₂ was finally isolated and identified by the English nobleman, H. Cavendish.^[5] Cavendish found that a common gas (described as "inflammable air" and known today to be H₂) could be produced from the combination of different metals and different acids.

Today, H₂ is mainly produced on an industrial scale from natural gas (where CH₄ is the main component) or oil-refinery feedstocks using steam reforming.^[6] A mixture of the hydrocarbon feedstock (*e.g.* CH₄) and steam is subjected to high temperatures and pressure (typically 850°C at 25 atm) in the presence of a metal catalyst (such as nickel) to generate a mixture of CO and H₂, known as synthesis gas or "syngas" (**Scheme 1**). This process is highly endothermic ($\Delta H^0 = +206.2 \text{ kJ mol}^{-1}$). Syngas is often utilised for the industrial-scale production of methanol and other useful hydrocarbons in the Fischer-Tropsch process.^[7]



Scheme 1 Steam reforming of CH₄ to generate syngas ($\Delta H^0 = +206.2 \text{ kJ mol}^{-1}$).

An additional equivalent of H₂ can be recovered from the exothermic water-gas shift reaction shown in **Scheme 2**.



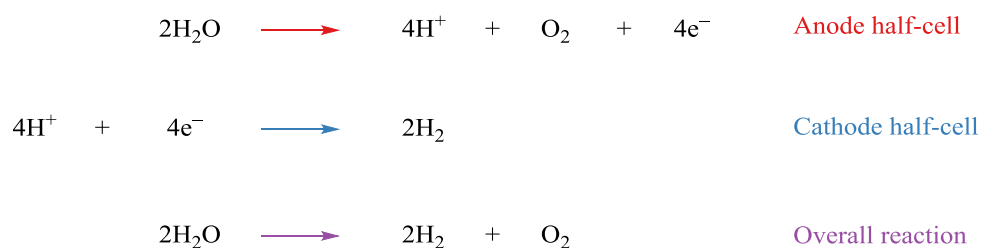
Scheme 2 The water-gas shift reaction ($\Delta H^0 = -41.1 \text{ kJ mol}^{-1}$).

Steam reforming is a highly energy intensive process that uses a non-renewable feedstock, requires metal catalysts, and generates a greenhouse gas (CO₂). In addition to this, the overall efficiency of the process on an industrial scale is rarely above 80%.^[6] As far as this process is concerned, there are no economic or environmental advantages to using H₂ as a fuel for energy. The main source of H₂ is neither sustainable nor environmentally clean.

Thankfully, huge efforts have been invested into the development of new, renewable technologies that allow the sustainable and carbon-neutral production of H₂. Sustainable methods of H₂ production employ either water or biomass as feedstocks.^[8]

A significant energetic driving force is required in order to split water due to the intrinsic strength of the H-O bonds (bond dissociation energy, BDE = 497.1 kJ mol⁻¹)^[3], however, a number of technologies exist.^[8,9] These include electrolysis,^[10] photocatalysis (artificial photosynthesis),^[11,12] and thermochemical reactions that are driven using concentrated solar energy.^[13]

Whilst the electrolysis of water is capable of generating ultra-pure H₂ and has been proven on an industrial scale, its widespread adoption has been limited by the cost of electricity vs hydrocarbon feedstocks.^[4] The half-cell equations shown in **Scheme 3** describe the splitting of deionised water at the anode and cathode of proton exchange membrane (PEM) electrolyzers.^[8,10]



Scheme 3 The electrolysis of deionised water at PEM electrolyzers ($E^0_{\text{cell}} = -1.23 \text{ V}$).^[14]

H₂ can be produced from biomass using a variety of thermochemical (pyrolysis and gasification) and biological (biophotolysis, fermentation and the biological water-gas shift reaction) processes.^[15,16]

Ultimately, the energy that is required to drive all of these aforementioned (water splitting or biomass conversion) processes can be harnessed from the solar energy of the Sun (see **Figure 1**).^[17] However, for electrochemical processes the required electricity may be generated from other renewable resources including wind, waves, tidal currents and geothermal energy.

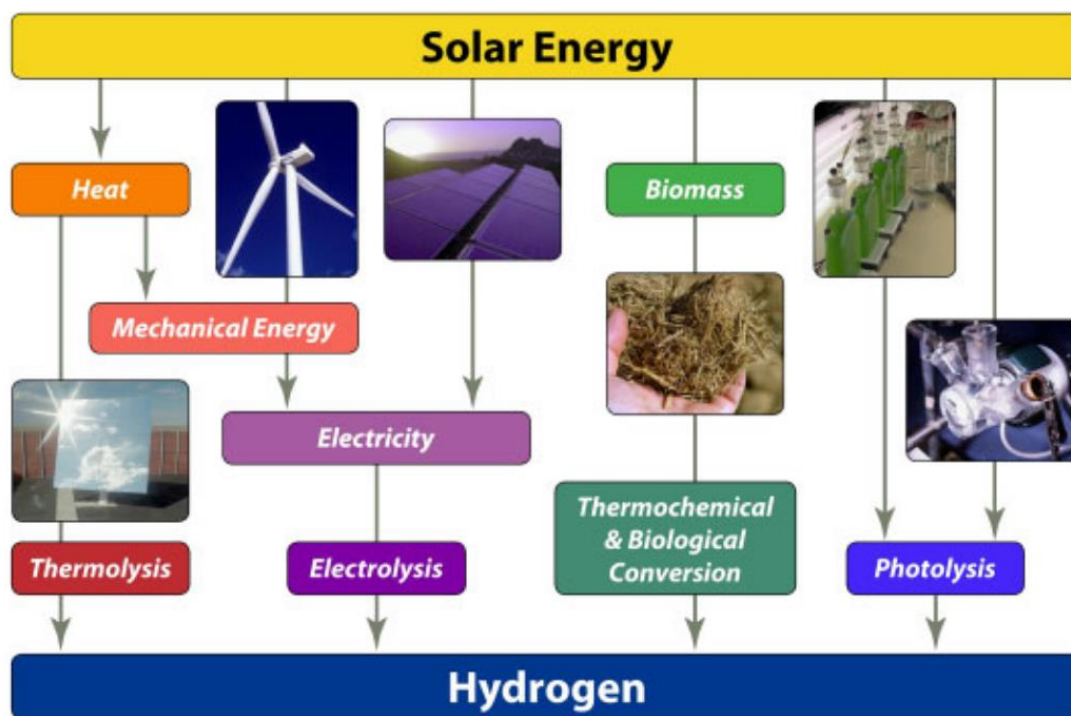


Figure 1 Renewable methods of H₂ production (reproduced from reference [8]).

1.2 The hydrogen economy

As the demand for sustainable and carbon-neutral sources of electricity increases, there is a need for new technologies that allow the efficient storage and utilization of energy.^[18] H₂ is attractive as an energy vector. Energy from renewable sources may be stored in its chemical bond (BDE = 435.8 kJ mol⁻¹),^[3] and when there is a high energy demand, this chemical energy may be converted back into electricity. This simple concept is the basis of a “hydrogen economy”.^[4,9]

Contrary to popular belief, one must emphasise the fact that H₂ is not a true energy source. In contrast to natural gas or crude oil, H₂ does not freely exist in abundance (on Earth at least). Much like electricity, H₂ must be manufactured by man; it is therefore not a primary energy source.

The foundation for a successful hydrogen economy is a readily available, cheap, carbon-neutral and renewable primary energy source *i.e.* H₂O or biomass, from which H₂ would be sustainably produced. As a storage medium for energy, H₂ would be stored as a pressurised gas, or more safely in H₂-absorbing materials, and other fuels such as MeOH. Safety issues aside for now, H₂ could be transported in pipelines or tankers over large distances.

In this hydrogen economy, H₂ could be used to fuel internal-combustion engines for transportation. As opposed to conventional gasoline and diesel engines (which also emit carbonaceous and inorganic particulates, CO, CO₂, and nitrogen oxides) the exhaust gases from the combustion of H₂ would mainly constitute H₂O, although a small quantity of nitrogen oxides would be inevitably generated due to the high operating temperatures. Better still, electricity (for transportation and backup/portable power) can be generated from H₂ in a safer, cleaner, and more efficient approach using fuel cell technology.^[4,19]

1.3 Hydrogen fuel cells

H₂ fuel cells are electrochemical engines that effectively perform the combustion process (reaction with O₂) in a controlled and flameless manner. This produces electricity along with pure H₂O and some heat.^[4] As opposed to internal-combustion engines, fuel cells do not emit nitrogen oxides, have no moving parts and have the potential for greater efficiency. To generate electricity from the combustion of H₂ ($\Delta H = -286 \text{ kJ mol}^{-1}$) the heat produced is used to produce steam and turn a turbine (converting heat to mechanical energy) which would drive a generator (converting mechanical energy to electricity). Owing to the difficulty in transferring heat efficiently, this is an extremely inefficient process. In contrast, fuel cells directly convert chemical energy into electrical energy with a maximum efficiency of 83%.^[19]

Batteries (galvanic/voltaic cells) and fuel cells convert chemical energy into electrical energy *via* redox reactions at the anode and cathode.^[18] They are the opposite to electrolyzers, which convert electrical energy into chemical energy (fuel) *e.g.* the production of H₂ from the electrolysis of H₂O, as described by the reaction in **Scheme 3**. Batteries differ from fuel cells in that the electrodes participate in the spontaneous redox reactions, and that the system is closed from the environment. In fuel cells, the electrodes simply function as charge-transfer media and the device is driven by a continuous supply of fuel for the redox reaction, which is delivered from outside the cell.

The processes involved in the operation of a H₂ fuel cell are shown in **Figure 2**.^[19] The basic setup involves two Pt electrodes that are separated by a permeable membrane electrolyte *i.e.* an electrochemically inactive polymer that is conductive and neutralizes separated charge. H₂ and O₂ are supplied at opposite sides of the cell. At the anode, H₂ undergoes oxidation to generate 2 H⁺ and 2 e⁻. The electrons are transferred to the Pt electrode, making it negatively charged. At the cathode, O₂ removes 4 e⁻ from the Pt electrode, making it positively charged, where it is combined with 4 H⁺ to give 2 H₂O molecules. For reasons that are not yet fully understood, this O₂ reduction reaction is the rate-limiting step in aqueous fuel cell systems.^[19]

The local depletion of protons establishes an electrochemical gradient, causing the migration of H^+ across the electrolyte membrane (from the anode to the cathode compartment) to maintain electroneutrality. The interaction of these two half-cell processes establishes a potential drop (an open circuit potential) between the anode and the cathode, which can be utilised for useful work in an external circuit. The spatial separation of these two half-cell reactions essentially allows H_2 to be “electrochemically combusted” with limited heat generation. It is worth noting that this approach is not limited to H_2 – the combustion of any fuel can be separated into two half-cell reactions, and therefore any fuel can be utilised in a fuel cell for electricity generation (borohydride, $[BH_4]^-$, is another well-developed example)^[20–22].

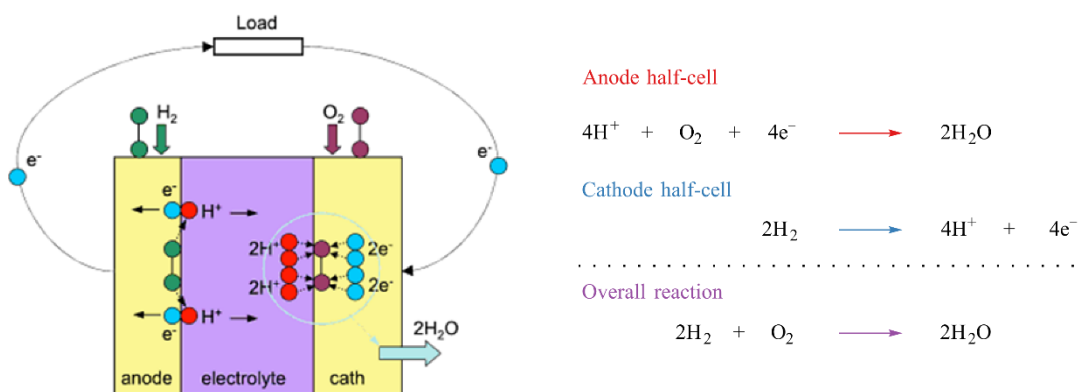


Figure 2 Basic principle of H_2 fuel cell operation (adapted from reference [19]).

The first known example of a H_2 fuel cell was fabricated by Grove in 1839.^[23] Two tubes, one containing H_2 and the other containing O_2 , were each inverted over Pt electrodes, which were submerged into a beaker of aqueous H_2SO_4 . After connecting 26 of these cells in series, Grove was able to use the current generated from this dubbed “gaseous voltaic battery” to drive the electrolysis of H_2O (**Figure 3**).^[24]

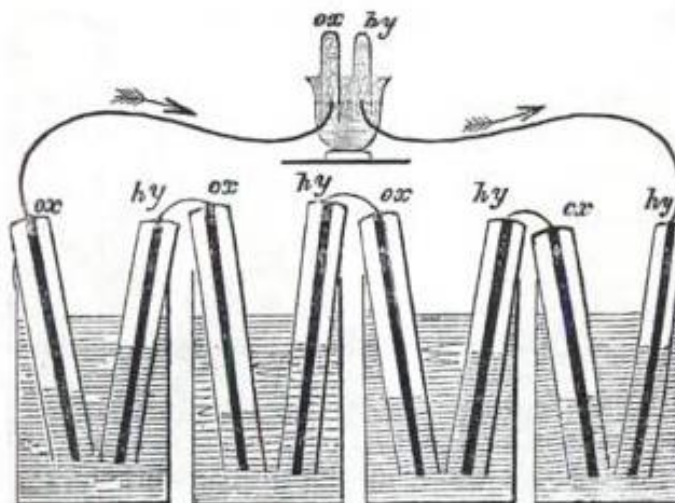


Figure 3 Grove's gaseous voltaic battery – the first H₂ fuel cell (reproduced from reference [23]).

Arguably, today's conventional fuel cells differ very little to the early example that was demonstrated by Grove nearly 200 years ago. Today, Pt is still the most widely used electrode material,^[19–22,25–28] and is often used for both half-cell reactions of a fuel cell (H₂/fuel oxidation and O₂ reduction). The high cost and relative scarcity of such electrode materials (50.5 US\$/g for Pt,^[29] yearly average at the time of writing) presents a significant economic barrier to the widespread adoption of fuel cell technology. Of course, this is also true for a multitude of processes, and as a result, huge efforts have been made to find inexpensive and abundant alternatives to the precious metals.^[30]

1.4 Pt as an electrocatalyst for H₂ oxidation

Pt electrodes are electrocatalytic towards the H₂ oxidation reaction. By definition, an electrocatalyst is a species that increases the rate of electron transfer *i.e.* the standard electrochemical rate constant (k^0), which results in an increase of the Faradaic current (the current that passes at an electrode surface during an electrochemical reaction).^[31] Since this current increase is sometimes masked by other non-electrochemical rate-limiting steps, the greatest indication of an electrocatalytic effect is the shift of the electrode reaction to a lower overpotential. An overpotential (η) is the deviation between the experimentally observed reduction potential (E) and its standard potential (E^0), and is required for a given current to flow at an electrode (**Equation 1**).^[31] Essentially, η is the additional energetic “driving force” required to overcome the kinetics of an electrochemical reaction.

$$\eta = E - E^0$$

Equation 1 Electrochemical definition of an overpotential (η) in terms of the experimentally observed reduction potential and its value under standard conditions (E^0).

Analogous to chemical catalysis, electrocatalysis can be either homogeneous or heterogeneous in character. In homogeneous electrocatalysis, both the electrocatalyst and the substrate are in the same phase. In heterogeneous electrocatalysis, the catalyst is either immobilised on the electrode surface or the electrode itself performs as the catalyst. In the case of the H₂ oxidation reaction at Pt electrodes, the electrode material itself is the heterogeneous electrocatalyst.

The uncatalyzed conversion of the energy stored in the H-H chemical bond to electricity comes at a considerable energetic cost. Pt (and other precious metal) surfaces are capable of the dissociative adsorption (chemisorption) of H₂, in which the H-H bonds break in favour of Pt-H bond formation on the electrode surface.^[32] This adsorption mechanism gives rise to much increased electrode kinetics, which provides an electrocatalytic effect.^[28,33] In the absence of a suitable electrocatalyst, the oxidation of H₂ to generate two protons and two electrons requires a large overpotential. Indeed the H₂ oxidation electrode reaction is observed at much lower potentials at Pt (fast k^0 , small η) compared to carbon-based electrodes (slow k^0 , large η). Typically, in aqueous solutions at carbon electrodes this overpotential is several hundred millivolts in excess of the thermodynamic potential of the H₂/H⁺ couple. In non-aqueous electrolytes the problem is exacerbated – at bare glassy carbon electrodes (GCEs, see 1.7.5), the overpotential for H₂ oxidation is large and broad, ill-defined oxidation waves are observed in the cyclic voltammetry.

In a bid to find a compromise between Pt cost and a low overpotential at the anode, attempts have been made to fabricate composite electrode materials that have low Pt loadings whilst maintaining a large electroactive Pt surface area. Conventional fuel cells tend to employ nanostructured Pt-group metals that are loaded onto a carbon support material (Pt/C) and then embedded into a polymer matrix.^[19] Again, this technology deviates very little from work of Grove, who found that the use of platinized platinum (Pt particles deposited on a bulk Pt electrode) produced greater currents, due to a significant increase in the electroactive area (which he described as the “surface of action”) compared to the geometric area of the electrode.^[23] Electron conductive polymers such as polyaniline, polypyrrole, polyacetylene or polythiophene can be applied to immobilize and disperse Pt nanoparticles.^[34–36] The conductivity,

porous structure and high surface area of such materials allow efficient shuttling of electrons between the electrode surface and the metal particles, which can be easily dispersed throughout the matrix. Lamy and co-workers prepared Pt-modified polyaniline composite electrode material through the oxidative electropolymerisation of aniline onto a GCE surface followed by the electrodeposition of Pt particles *via* the reduction of K_2PtCl_6 .^[26] They explored H_2 oxidation at various different Pt loadings, and found that they could achieve electrocatalytic activities similar to the bulk material at a Pt loading of *ca* $150 \mu g cm^{-3}$. Polypyrrole-based materials are highly desirable for electrode applications due to being environmentally stable, easy to prepare, yet highly conductive. By virtue of its high oxidation potential, polypyrrole was found to be more electrochemically stable than conventional carbon support materials.^[37] More recently, this concept has been extended to Pt-encapsulated graphene nanosheets.^[38,39] An unusually high electrocatalytic activity towards methanol oxidation was achieved through the formation of sub-nano Pt clusters (<0.5 nm in diameter) using this approach. Whilst composite electrode materials can provide a significant decrease in the extent of Pt loading compared to bulk Pt, this is unfortunately not sufficient. The United States Department of Energy estimate that the Pt content of current PEM fuel cells would need to be cut by a quarter (to 30 US\$/kW) for fuel cell technology to become a viable alternative to the internal combustion engine.^[40]

Another issue relating to the use of Pt-containing nanocomposite materials is that they are inherently unstable.^[41,42] Investigations into the degradation mechanism of these electrocatalysts have indicated that the leaching or aggregation of particles results in the loss of catalytic activity.^[43–45] The current state-of-the-art strategies used in the stabilisation of Pt-based fuel cell electrocatalysts have recently been reviewed by Cao and co-workers.^[41]

The cost and stability of Pt-based electrocatalysts presents a significant barrier to the commercialisation and wide-spread adoption of current fuel cell technology. Thus, there is clear demand for new H_2 oxidation electrocatalysts that are free from precious metals.

1.5 Non-precious metal electrocatalysts for H_2 oxidation

Great efforts have been made to find inexpensive and abundant alternatives to the platinum group metals for the anodic H_2 oxidation reaction. In the late 1960s and early 1970s the tungsten oxides (WO_n and M_nWO_3 , where $M = Na, K, Ba, Pb, Tl, U$ or Cd) were explored as potential heterogeneous electrocatalytic anode and cathode materials for H_2 fuel cell applications.^[46,47] The electrocatalytic activity of these materials was found to be insufficient for their application as electrode materials, especially with respect to the H_2 oxidation reaction.

The use of tungsten carbide (WC) as an electrocatalytic anode material was explored by Böhm in 1968, who found that WC possessed a good electrical conductivity (WC has the lowest reported electrical resistivity of any of the interstitial carbides)^[48] whilst exhibiting catalytic activity towards H₂ oxidation.^[49,50] Shortly after, the apparent Pt-like catalytic behaviour of WC was reported for H₂ oxidation and hydrogenolysis reactions by Levy and Boudart.^[51] This pioneering body of work has since provided the impetus for the study of WC-based materials as a viable alternative to Pt electrodes for H₂ oxidation.^[52–56] WC electrodes have been employed successfully for the H₂ oxidation half-cell in PEM fuel cells, achieving high current densities.^[54] However, the electrochemical activity of WC for the oxidation of pure H₂ is still 4 orders of magnitude lower than that of Pt (at 25°C).^[57]

This thesis concerns the development of molecular electrocatalysts. The advantage of molecular electrocatalysts is that they allow the use of cheap and ubiquitous electrode materials, such as plain graphitic carbon electrodes. Another advantage, from a developmental perspective, is that more mechanistic information can be extracted from the study of homogeneous catalysts.

The majority of molecular electrocatalysts for H₂ oxidation (or production) have taken inspiration from the hydrogenase enzymes that are found in nature.^[30,58–65] These enzymes are responsible for H₂ production in microbial organisms such as green algae.^[16] [FeFe] hydrogenase and [NiFe] hydrogenase are the most-studied class of hydrogenase enzyme, and feature coordinatively unsaturated metal centres that are bound to ligands such as CO and CN.^[58,63,64] Various structural, theoretical, and spectroscopic investigations have provided strong evidence to suggest that a pendent amine is present on the dithiolate ligand in [FeFe] hydrogenase.^[66–69] These enzymes are capable of catalysing the interconversion of H⁺ and H₂, demonstrating that this property is not unique to Pt metal. The transfer of electrons, to or from the active site, occurs through a series of neighbouring [Fe₄S₄] cubane clusters (ferredoxins) that form an electron transport chain (essentially a molecular wire). The respective supply/removal of H₂ and H⁺ occurs through hydrophobic channels and a H⁺ transport chain. Typical structural features of [FeFe] and [NiFe] hydrogenase enzymes, along with a simple depiction of an [FeFe] hydrogenase enzyme active site, are illustrated in **Figure 4**.

a)



b)

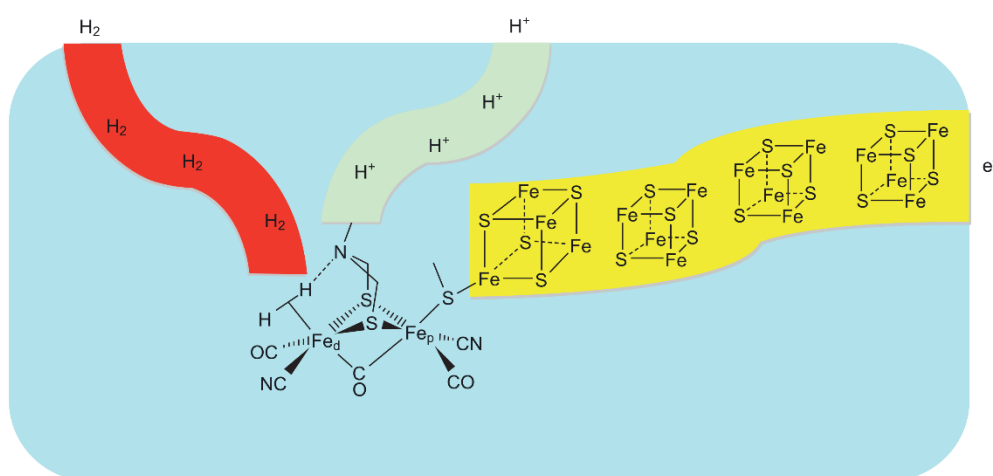
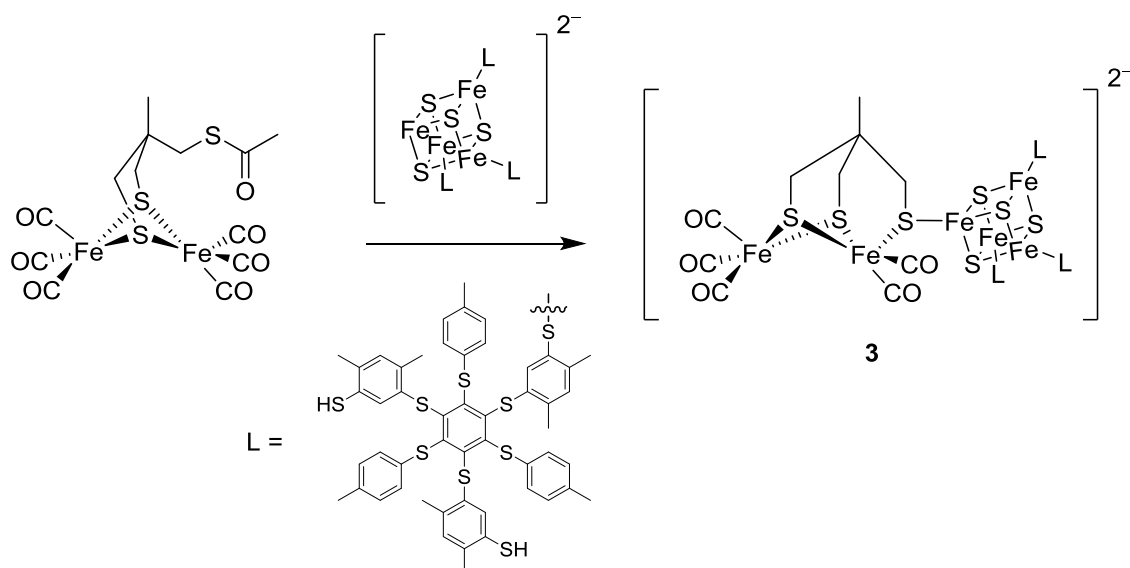


Figure 4 a) Typical structural features of the [FeFe] (**1**) and [NiFe] (**2**) hydrogenase enzymes; b) a simple depiction of the active site of an [FeFe] hydrogenase enzyme, the channels that exist for H₂, H⁺ and e⁻ transport have been emphasised (reproduced from reference [30]).

The first crystal structures of the [NiFe] and [FeFe] hydrogenases were first reported by Fontecilla-Camps *et al.*^[70] and Peters *et al.*,^[71] respectively. Since then, several groups have made efforts to synthesise structural models of hydrogenase active sites.^[59,63,72,73] These models perform some of the same reactions as the natural hydrogenase enzymes. A good example of this is the pioneering work of Pickett and co-workers in 2005, who reported the first synthesis of a metallosulfur cluster core (**3**) that structurally resembles the active site of an [FeFe] hydrogenase.^[74] Complex **3** was prepared by reacting a thioacetyl di-iron complex with an [Fe₄S₄] cubane cluster, where three of the Fe atoms were sterically blocked by a large chelating ligand (**Scheme 4**). The electrocatalytic reduction of H⁺, to produce H₂, was demonstrated using **3** as a functioning structural model of an [FeFe] hydrogenase.



Scheme 4 Synthesis of a structural [FeFe] hydrogenase model (**3**) by Pickett and co-workers.

In 2009, Tard and Pickett published a comprehensive review into the development of structural and functional analogues of the active sites of [Fe], [NiFe], and [FeFe] hydrogenases.^[59] The most up-to-date review that details advances made in elucidating the structure and function of these enzymes was published by Lubitz *et al.* in early 2014.^[65]

Many prominent research groups (most notably the groups of DuBois, Bullock, and Rakowski DuBois) have been active in the development of “bio-inspired” molecular electrocatalysts *i.e.* functional models of hydrogenase enzymes.^[30,60,75] Rather than attempting to build elegant structural models that mimic the precise structural features of [FeFe] hydrogenases (*cf.* the work of Pickett and co-workers)^[74], this approach simply and effectively focuses on retaining two main features:

- i) The use of abundant and inexpensive metals.
- ii) The incorporation of pendent base groups in close proximity to the metal centre. This takes inspiration from the proposed amine moiety on the dithiolate ligand of [FeFe] hydrogenase.

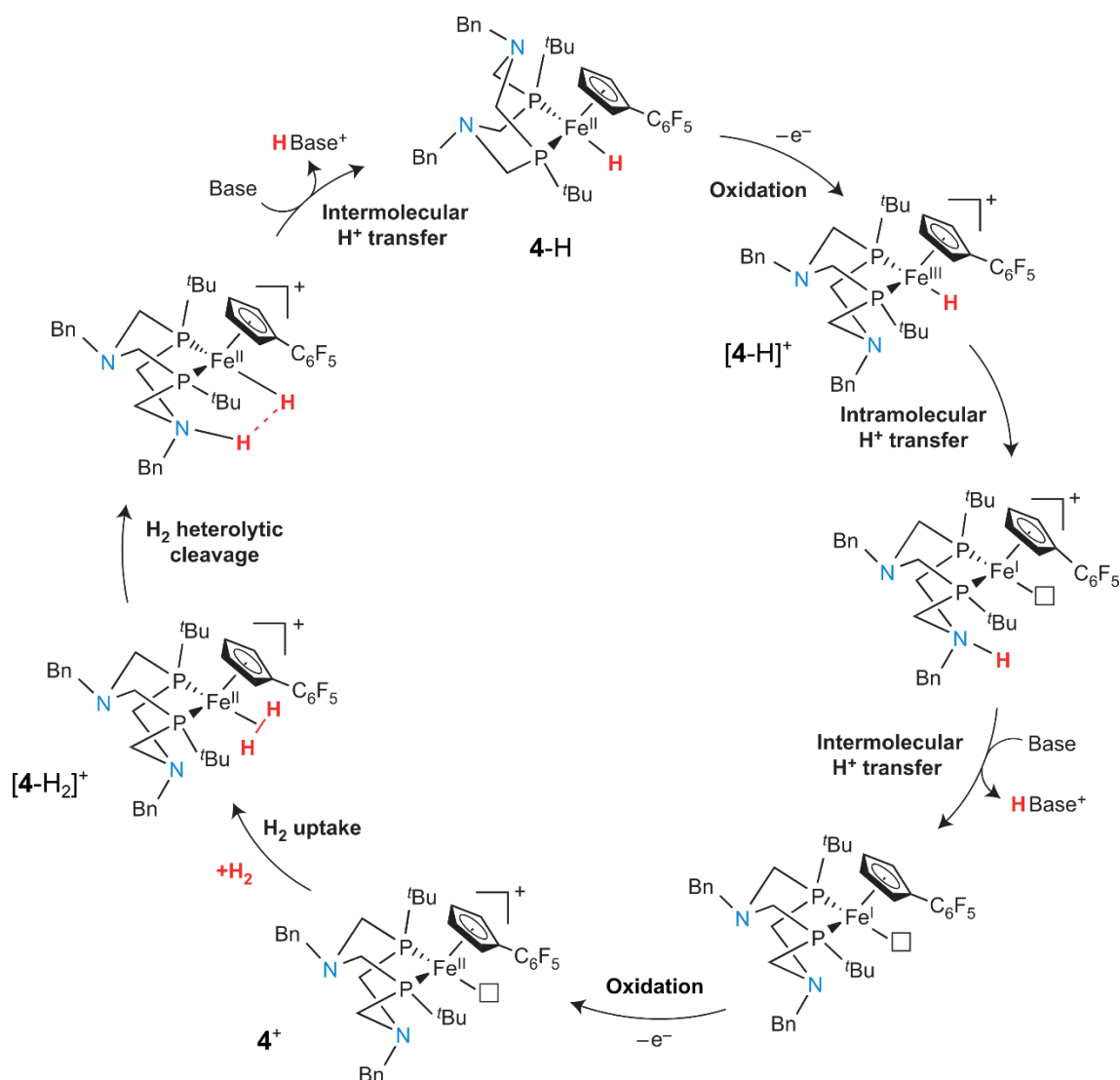
These enzyme mimics are able to overcome the high energy cost that is required to heterolytically cleave H₂ (318.0 kJ mol⁻¹ in MeCN)^[76,77] by virtue of the strong hydride acceptor ability of the metal centre and the strong proton acceptor ability of the pendent base groups. Fe is generally attractive for catalysis due to its high earth-abundance (it is the second most

abundant metallic element in the Earth's crust after Al and much easier/cheaper to extract)^[2] along with being inexpensive and of low toxicity; indeed, in this respect, Bolm recently suggested that a “new iron age” may be upon us.^[78] A multitude of complexes containing Ni,^[79–84] Fe,^[85–89] Co^[90–93], and Mo^[94–96] metals have been reported to be effective electrocatalysts for H₂ production, and a number of complexes containing Ni^[79,97,98] and Fe^[85,99,100] metal centres have been demonstrated to be effective H₂ oxidation electrocatalysts. The development of molecular electrocatalysts using this approach was most recently reviewed by DuBois and Bullock in 2011.^[60]

A molecular H₂ oxidation electrocatalyst of notable interest is the Fe-H complex (**4-H**) shown in **Scheme 5**.^[100] This complex was synthesised by Bullock and co-workers in 2013, and was designed to mimic the active site of [FeFe] hydrogenase. The active form (**4**⁺) features a vacant coordination site on a single Fe^{II} centre (for H₂ binding) with pendent amine groups in close proximity (on a bidentate cyclic phosphine ligand).

Cyclic voltammetry of a 1 mM solution of **4-H** in fluorobenzene was recorded under H₂ (1.0 atm) in the presence of increasing quantities (0–52 mM) of the Brønsted base, *N*-methylpyrrolidine. The current of the oxidation wave was observed to increase with added base; this behaviour is highly indicative of an underlying electrocatalytic mechanism – where the starting material is catalytically regenerated by a follow-up chemical reaction after electrooxidation (see 1.7 below for further information on electrochemical techniques). Furthermore, **4-H** provided the highest turnover frequencies reported for H₂ oxidation using an Fe complex (0.66–2.0 s⁻¹), at low overpotentials and room temperature.

The proposed mechanism for the electrocatalytic oxidation of H₂, in the presence of **4-H**, is illustrated in **Scheme 5**. Initially, the Fe^{II} centre of **4-H** undergoes single-electron oxidation to give Fe^{III}, [**4-H**]⁺. This increases the acidity of the Fe-H bond, facilitating the intramolecular transfer of H⁺ to the pendent amine group, which is then deprotonated intermolecularly by the added base. Single-electron oxidation of the resulting Fe^I centre to Fe^{II} (**4**⁺) facilitates the binding of H₂ to give the dihydrogen adduct, [**4-H₂**]⁺. The heterolytic cleavage of H₂ (mediated by the pendent amine) is followed by another intermolecular H⁺ transfer process, regenerating the initial complex (**4-H**) and closing the electrocatalytic cycle.



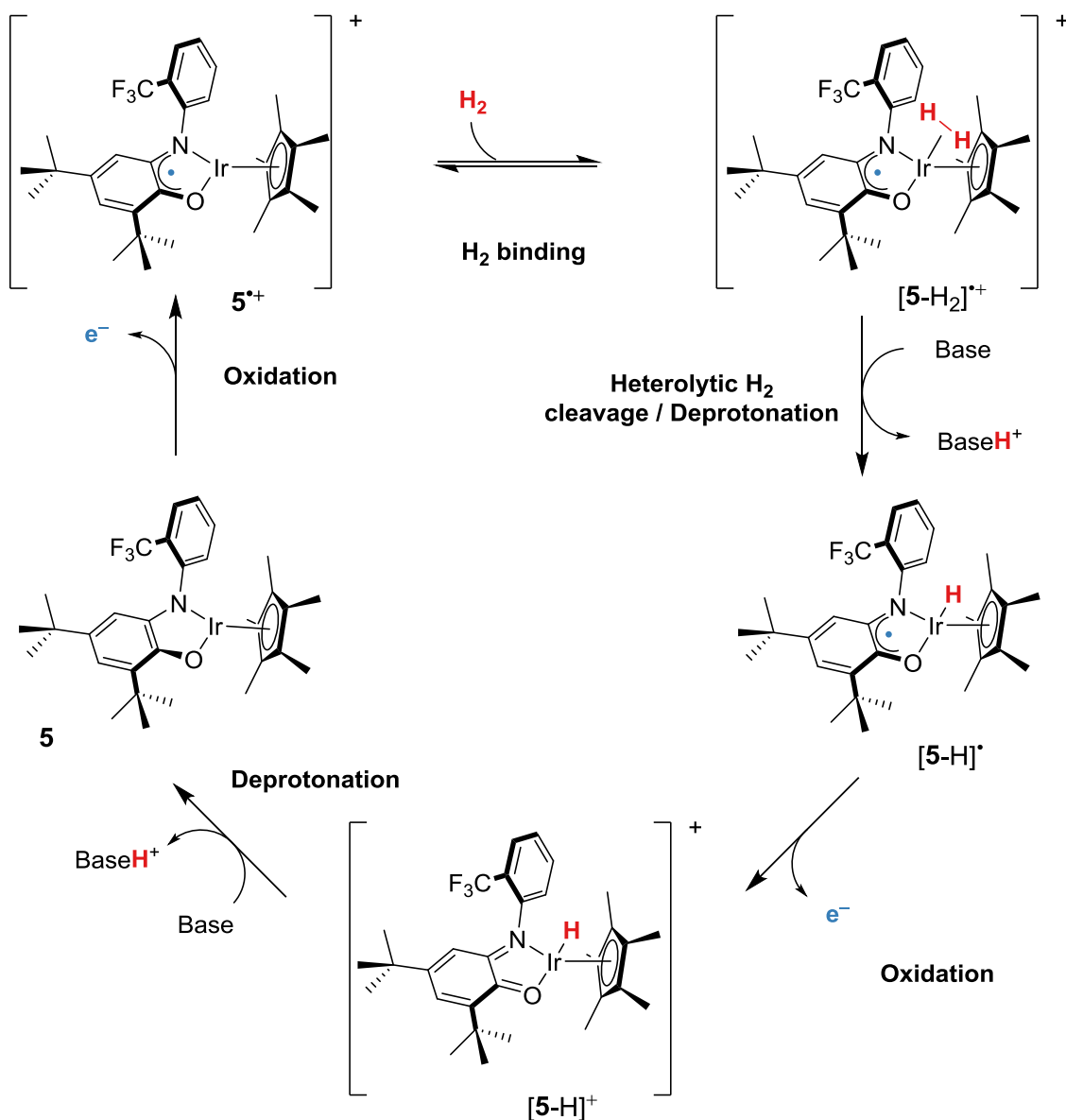
Scheme 5 Mechanism of electrocatalytic H₂ oxidation by Bullock's pendent amine-containing Fe^{II} complex (4-H) in the presence of a Brønsted base (reproduced from reference [100]).

A significant barrier to the adoption of hydrogenase-derived technology is that the enzymes (and their mimics) are often highly sensitive to O₂, losing their electrocatalytic activity on exposure to air. Ogo and co-workers have recently isolated a new bacterium strain (*Citrobacter* sp. S-77) containing an O₂-stable membrane-bound [NiFe] hydrogenase, [NiFe]_{S77}.^[101] They purified and biochemically characterized [NiFe]_{S77}, which was found to be potent towards H₂ oxidation, yet remarkably stability towards O₂ (retaining 95% of its original H₂ oxidation activity following exposure to air for 30 h). The group very recently constructed a fuel cell comprising a [NiFe]_{S77} electrode as the anode and a conventional Pt/C cathode.^[102] The [NiFe]_{S77} electrode was prepared by physisorbing [NiFe]_{S77} onto carbon black, which was then physisorbed onto a hydrophobic carbon cloth. The mass activity of the [NiFe]_{S77} electrode

(functioning as an anode) was found to be 637 times higher than Pt for 1 mg of either electrode material. When considering the mass activity for 1 mg of Fe and Ni metal atoms vs Pt atoms, the result was a staggering 506 000 fold improvement in activity. The electrode is also stable to air and can be recovered quantitatively after exposure to CO, unlike Pt surfaces which are “poisoned” and become inactive.

Rauchfuss and co-workers took an alternative approach to H₂ oxidation electrocatalysis. They prepared an unsaturated Ir^{III} complex containing bulky redox non-innocent amidophenolate ligands (**5**) – shown in **Scheme 6** along with the proposed H₂ oxidation mechanism.^[103,104] The amidophenolate ligands are strong π -donors and capable of stabilising the electronically unsaturated 16-electron complex. However, these ligand π -donor orbitals are also the HOMO (highest occupied molecular orbital) and are redox-active. Single-electron oxidation of the amidophenolate ligand, to give a cationic complex (**5**^{•+}), causes a weakening of the metal-ligand bond and decreases the electron density on the metal centre. This induces Lewis acidity in the metal centre, allowing the formation of a H₂ adduct, [**5**-H₂]^{•+}, that is susceptible to deprotonation on addition of a weakly-coordinating base (2,6-di-*tert*-butylpyridine), forming the hydride, [**5**-H][•]. Further, ligand-centered, single-electron oxidation of [**5**-H][•] generates [**5**-H]⁺, which undergoes another deprotonation step to regenerate **5** and close the electrocatalytic cycle. The oxidation state of the Ir^{III} complex formally remains constant throughout the cycle. Subtle changes in the electron-donor properties of the redox-active ligand are induced by its oxidation; this modifies the Lewis and Brønsted acidity of the intermediates and drives the overall oxidation of H₂. They found that the relative rate of H₂ oxidation was strongly dependent on the ion-pairing ability of the counterion; indeed, the reduction of [**5**[•]][B(C₆F₅)₄] by H₂ is about 30 times faster than that of analogous [**5**[•]][PF₆].

The tutorial overview of Lyaskovskyy and de Bruin provides further examples that illustrate the power of redox non-innocent ligands for general catalytic applications.^[105]

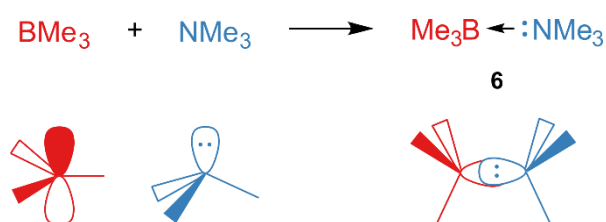


Scheme 6 Mechanism of electrocatalytic H₂ oxidation by Rauchfuss' Ir^{III} amidophenolate complex (5) in the presence of a weakly-coordinating base.

All of the aforementioned approaches still use metal-containing catalysts, and there are a greater number of literature reports that focus on biomimetic electrocatalysts for the reverse process – H₂ production *via* H⁺ reduction – than for H₂ oxidation.^[60] To the best of my knowledge, there are currently no metal-free electrocatalysts for the H₂ oxidation reaction. The greatest challenges in developing H₂ energy technologies still remain – to find systems that are catalytic in terms of H₂ bond cleavage, that operate at low overpotentials (*i.e.* that are “electrocatalytic”), that are metal-free and/or employ inexpensive, readily-available electrode materials such as carbon, and that are simple and economically viable to produce.

1.6 Frustrated Lewis pairs

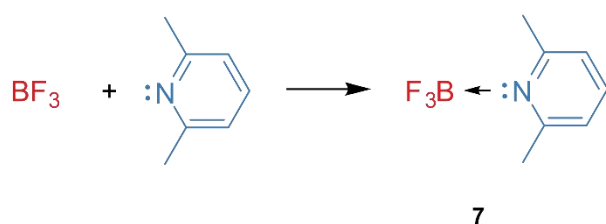
Lewis introduced his theory of acids and bases in 1923;^[106] this was in the same year that Brønsted and Lowry had independently published their own definitions.^[107–109] As opposed to the Brønsted-Lowry model, where an acid is defined as a H⁺ donor, a Lewis acid is a species that is capable of accepting a pair of electrons from a Lewis base (electron pair donor). The combination of a simple Lewis acid and base, for example BMe₃ and NMe₃ respectively, results in the formation of a classical Lewis adduct, Me₃BNMe₃ (**6**), as shown in **Scheme 7**.^[110] In this reaction, the Lewis acidity of BMe₃ is effectively quenched through a (dative) bonding interaction between its lowest unoccupied molecular orbital (LUMO) and the HOMO of NMe₃, and both central atoms (B and N) achieve an octet of electrons in their valence shell.



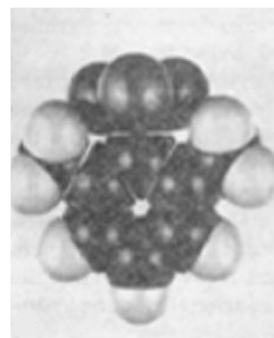
Scheme 7 Formation of a classical Lewis adduct (**6**).

The influence of steric effects on the formation of classical Lewis adducts was first uncovered by Brown and co-workers in 1942.^[111] They were investigating the reaction of different pyridines with simple boranes when they failed to form a classical Lewis adduct from the combination of 2,6-lutidine (lut) and BMe₃. This was in stark contrast to the corresponding combination of lut and BF₃, which reacted to give adduct **7**, as expected from Lewis acid-base theory (**Scheme 8**). The inability of BMe₃ to form an adduct with lut was rationalized in terms of the steric hindrance of the Me groups on the approaching Lewis acid and base. This argument was supported by the construction of molecular models (**Scheme 8b** and **d**).

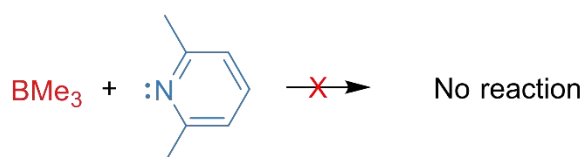
a)



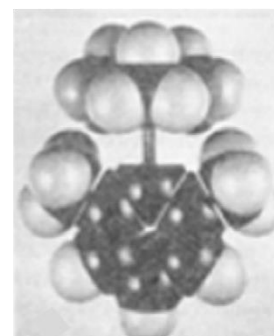
b)



c)



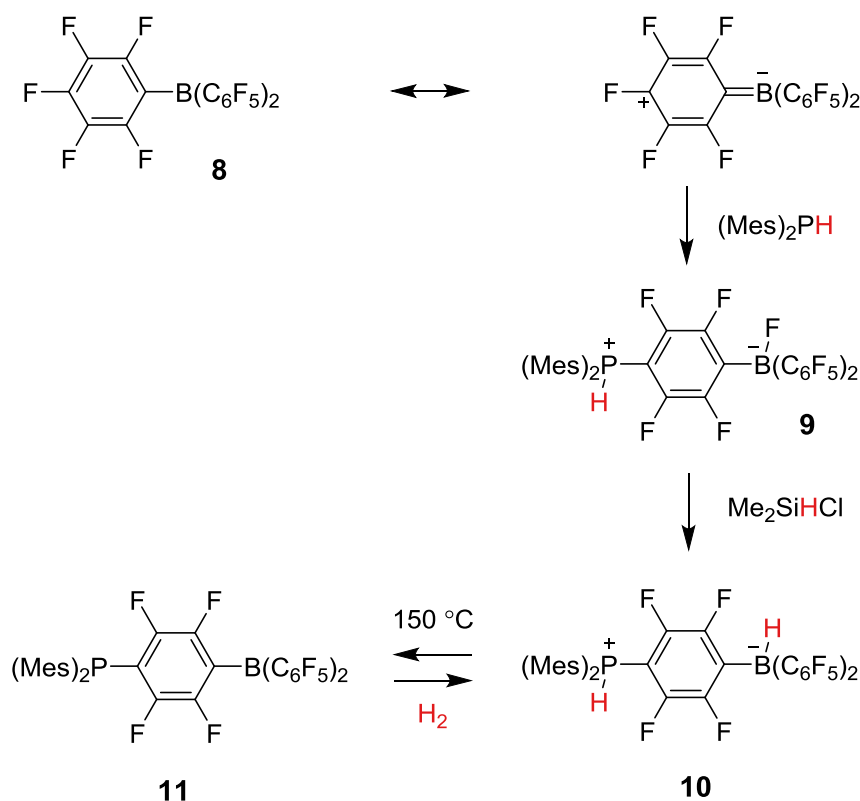
d)



Scheme 8 Brown's early work into steric frustration: a) The formation of the classical Lewis adduct, **7**, and b) Brown's original molecular model of **7**; c) no reaction was observed between BMe_3 and 2,6-lutidine (lut), d) Brown's original molecular model rationalises the lack of reactivity in terms of steric effects (photos are reproduced from reference [111]).

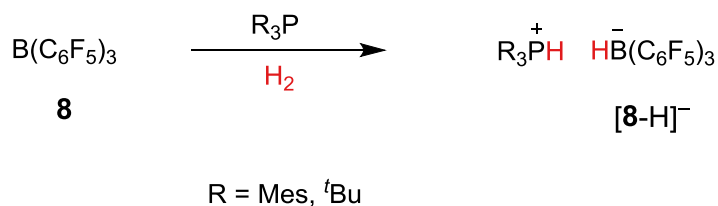
In 2006, Stephan and co-workers were investigating the interaction of phosphines with $\text{B}(\text{C}_6\text{F}_5)_3$ (**8**).^[112] This strong-yet-bulky Lewis acid, **8**, was known to behave as a traditional Lewis acid, forming classical Lewis adducts when combined with various Lewis bases.^[113,114] However, they found that **8** undergoes *para*-nucleophilic aromatic substitution with the sterically bulky secondary phosphine, Mes_2PH ($\text{Mes} = \text{C}_6\text{H}_2\text{Me}_3$), to afford the zwitterionic phosphonium borate, **9** (**Scheme 9**). The treatment of **9** with Me_2SiHCl effected H^-/F^- exchange to give the zwitterionic product, **10**. Considering that **10** contains both hydridic and protic fragments, it was found to be remarkably stable towards H_2 evolution. On heating to 150°C , the elimination of H_2 was achieved and the deep orange-red phosphino-borane (**11**) was generated. According to classical Lewis theory, one would expect the intermolecular formation of classical Lewis adducts. Manners and co-workers had previously reported a number of cyclic and polymeric structures that were formed from the thermal, or catalytically-induced, elimination of H_2 from simple phosphino-boranes of the form $\text{R}_2\text{PH}(\text{BH}_3)$.^[115,116] However, **11** was surprisingly found to be monomeric in

solution; this exception was rationalized in terms of the steric encumbrance of the P and B centres by the surrounding groups. Most remarkably, when **11** was admitted to H₂ (1 atm) at room temperature, the orange-red colour discharged and **10** was regenerated. Until this pioneering work, the facile heterolytic cleavage of H₂ by a metal-free system was unprecedented. The ability of **10** to activate H₂ was attributed to the “unquenched” Lewis acidity and basicity of the borane and phosphine components, resulting from the steric preclusion of adduct formation.



Scheme 9 Preparation and demonstration of a phosphino-borane (**11**) that is capable of reversible H₂ activation.

To examine the generality of this H₂ activation chemistry, Welch and Stephan extended their approach to separate Lewis acid and base components.^[117] When the bulky phosphines, PMes₃ and P^tBu₃ (**12**), were combined with B(C₆F₅)₃ (**8**), they found no evidence of classical Lewis adduct formation; only the individual component resonances were observed by NMR spectroscopy, even when the reaction mixture was cooled to -50°C. On exposure to H₂ (at 1 atm and room temperature), phosphonium salts of the form [R₃PH][**8**-H] were rapidly generated through the facile heterolytic cleavage of H₂. Unlike **10**, these salts were thermally stable to the liberation of H₂, even when heated to 150°C.



Scheme 10 Activation of H₂ by **8**/phosphine FLPs.

The range of Lewis acidity and basicity that is required for H₂ activation to occur was explored by employing BPh₃ as a weaker Lewis acid. The rate of H₂ activation was found to be much slower when **12** was combined with BPh₃, and the product, [**12**-H][HBPh₃], was only isolated in 33% yield (compared to the 90% yield reported for analogous [**12**-H][**8**-H]). When the basicity of the phosphine was also decreased through substituting **12** for PMes₃ (whilst still employing BPh₃), no reaction was observed. The same was true when a strong Lewis base (**12**) was used in combination with the much weaker Lewis acid, BMes₃. Whilst these Lewis acid and base combinations did not form adducts, this observation suggested that a sufficiently strong combined Lewis acidity/basicity is required to effect the activation of H₂. Pápai and co-workers later related the thermodynamic feasibility of H₂ activation to the acid-base strengths of experimentally-studied systems, through quantum chemical calculations.^[118]

Stephan later coined the term “frustrated Lewis pairs” (FLPs) to describe the behaviour of these three-component systems.^[119] Since their advent, FLPs have emerged as an intense and rapidly growing area of research (**Figure 5**). The application of FLPs for the activation of H₂ and other small molecules has been reviewed extensively.^[30,120–122] The latest and most comprehensive review was written by Stephan and published in *Comprehensive Inorganic Chemistry II* in 2013.^[120]

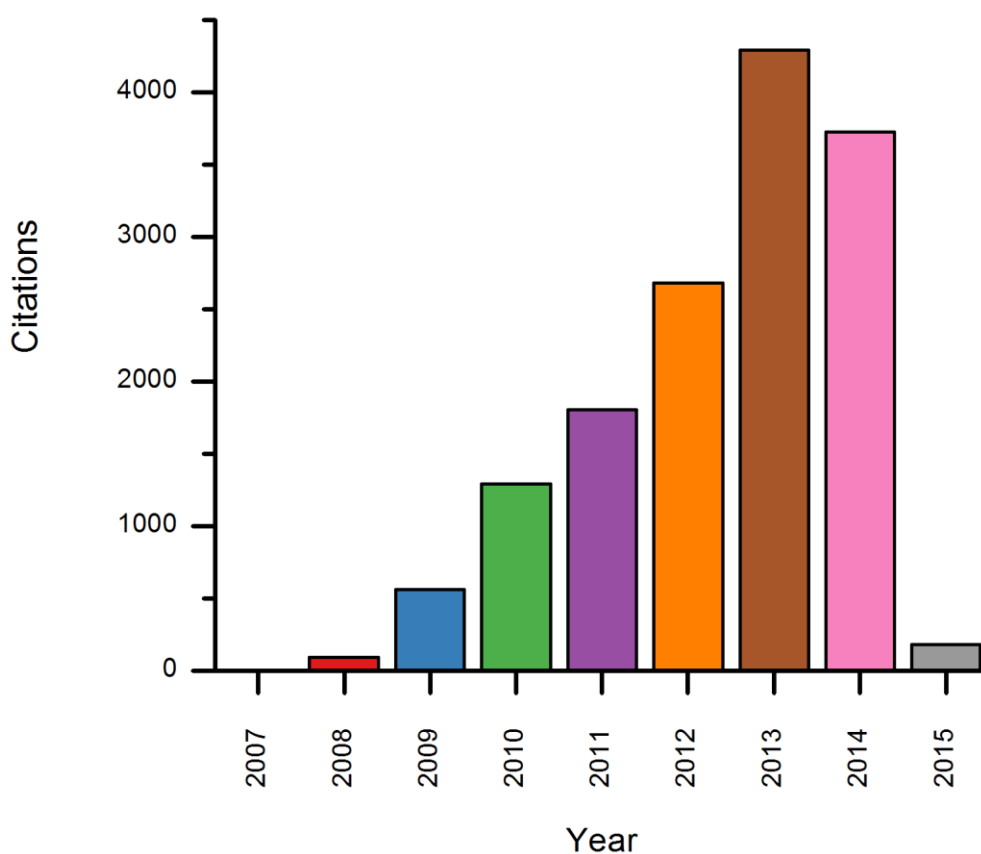
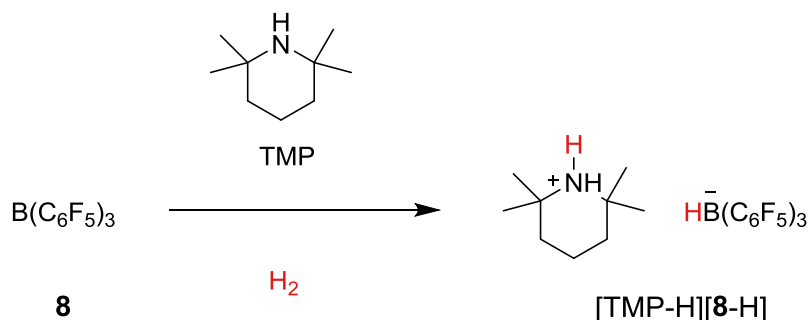


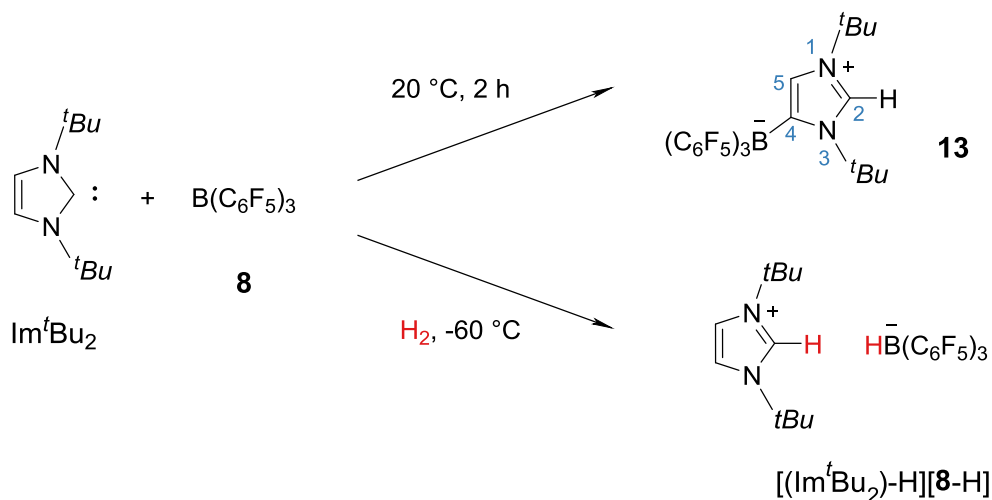
Figure 5 Citations per year for the term “frustrated Lewis pair” (supplied by Web of Science™ on 20/01/2015).^[123]

FLPs are not limited to the use of phosphines as the Lewis base. In a later study, Rieger and co-workers studied the application of bulky amines as the Lewis base. They found that 2,2,6,6-tetramethylpiperidine (TMP) and **8** did not combine to form a classical Lewis adduct, yet on exposure to H₂ yielded the corresponding ammonium borohydride, [TMP-H][**8**-H] (**Scheme 12**).^[124] From a NMR spectroscopic study, they speculated that on exposure to H₂ (at 1 atm and room temperature) an intermediate complex forms where the cation and the anion are strongly associated (N-H⋯H-B). The reaction can be driven towards the product, [TMP-H][**8**-H], through evaporation of the solvent, leaving the solution for 1 day, or by heating.



Scheme 11 H₂ activation by the **8**/TMP FLP.

The groups of Tamm and Stephan simultaneously published (in the same issue of *Angew. Chem. Int. Ed.*) their independent work into the application of sterically bulky *N*-heterocyclic carbenes (NHCs) as the Lewis base component of FLPs for H₂ activation.^[125,126] When combined with **8**, the NHC (tBuN)₂C₃H₂ (Im^tBu₂) was discovered to be an effective FLP for H₂ activation. However, Tamm and co-workers found that when left to stand at room temperature for 2 hours, a reaction occurs to give an abnormal carbene (**13**) *via* substitution of the H substituent at the C-4 position on the NHC for **8**. This could be avoided by keeping the reaction mixture cold (−60 °C) prior to H₂ exposure, on which immediate H₂ cleavage occurs to afford [(Im^tBu₂)-H][**8**-H].



Scheme 12 H₂ activation and side-reaction of the **8**/Im^tBu₂ FLP.

The unusual, metal-like ability of FLPs to heterolytically activate H₂ has prompted a number of detailed computational mechanistic studies. Pápai and co-workers initiated a computational study into the **12**/**8** system.^[118,127] They determined that an energy minimum for the approach of **12** and **8** is obtained when the B-P separation is 4.2 Å. This encounter complex was reported

to be stabilised by intermolecular H...F interactions, a claim that has been supported by similar reports from other research groups.^[125,128,129] It was proposed that H₂ reacted by traversing into the “pocket” of the encounter complex and then undergoing synergistic electron transfer steps between:

- i) The lone pair (HOMO) of the Lewis base and the anti-bonding (σ^*) molecular orbital of H₂.
- ii) The bonding (σ) orbital of H₂ and the vacant p orbital (LUMO) on the Lewis acid.

It was proposed that this results in the weakening and subsequent heterolytic cleavage of the H-H bond. In the transition state structure, the H₂ molecule was found to be slightly elongated, and almost aligned with the B-P axis.

Grimme and co-workers were unhappy with the notion that H₂ bond cleavage occurs *via* an almost linear P-H-H-B arrangement in the transition state. They suggested that this result was obtained from the insufficient treatment of intramolecular London dispersion forces between the large substituents. Using a dispersion-corrected density functional theory (DFT) method, they obtained a non-linear P-H-H-B transition state.^[130,131] They then suggested a simpler mechanistic picture where heterolytic bond cleavage results from the polarisation of H₂, which is induced by the strong electric field within the FLP cavity. In this electric field model, the entry of H₂ into the FLP cavity provided the barrier and the subsequent heterolysis process was completely barrierless.

Pápai and co-workers have since re-evaluated the ability of the electron transfer and electric field models to explain the mechanism of H₂ cleavage by FLPs.^[132] They admitted that in their previous study, the insufficient treatment of dispersion effects had indeed resulted in an underestimated P-H-H-B bend. Using an improved DFT model, they performed computational studies on 6 different FLP systems that had previously been explored experimentally, and contrasted the predictions from both models. They found that FLPs with similar reactivity show remarkably different electric field characteristics, and that the electric field generated is too small to provide a qualitative interpretation for any change in electronic structure. They also found that donor/acceptor interactions of the FLP with H₂ were present in the transition states of all systems studied. Using this model, the characteristic non-linear arrangement of the transition state can be rationalized by considering the optimum orbital overlaps for electron transfer to occur, whereas the electric field model provides no explanation for this required geometry. Indeed, the parallel orientation of H₂ to the electric field should suffice for this model. The results of this work suggest that the earlier electron transfer model still provides the best

description for the mechanism of heterolytic H₂ cleavage by FLPs. An illustration of this mechanistic model is depicted in **Figure 6**.

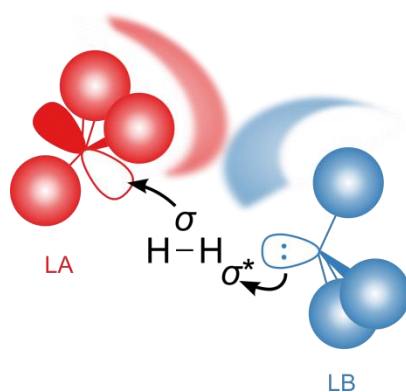
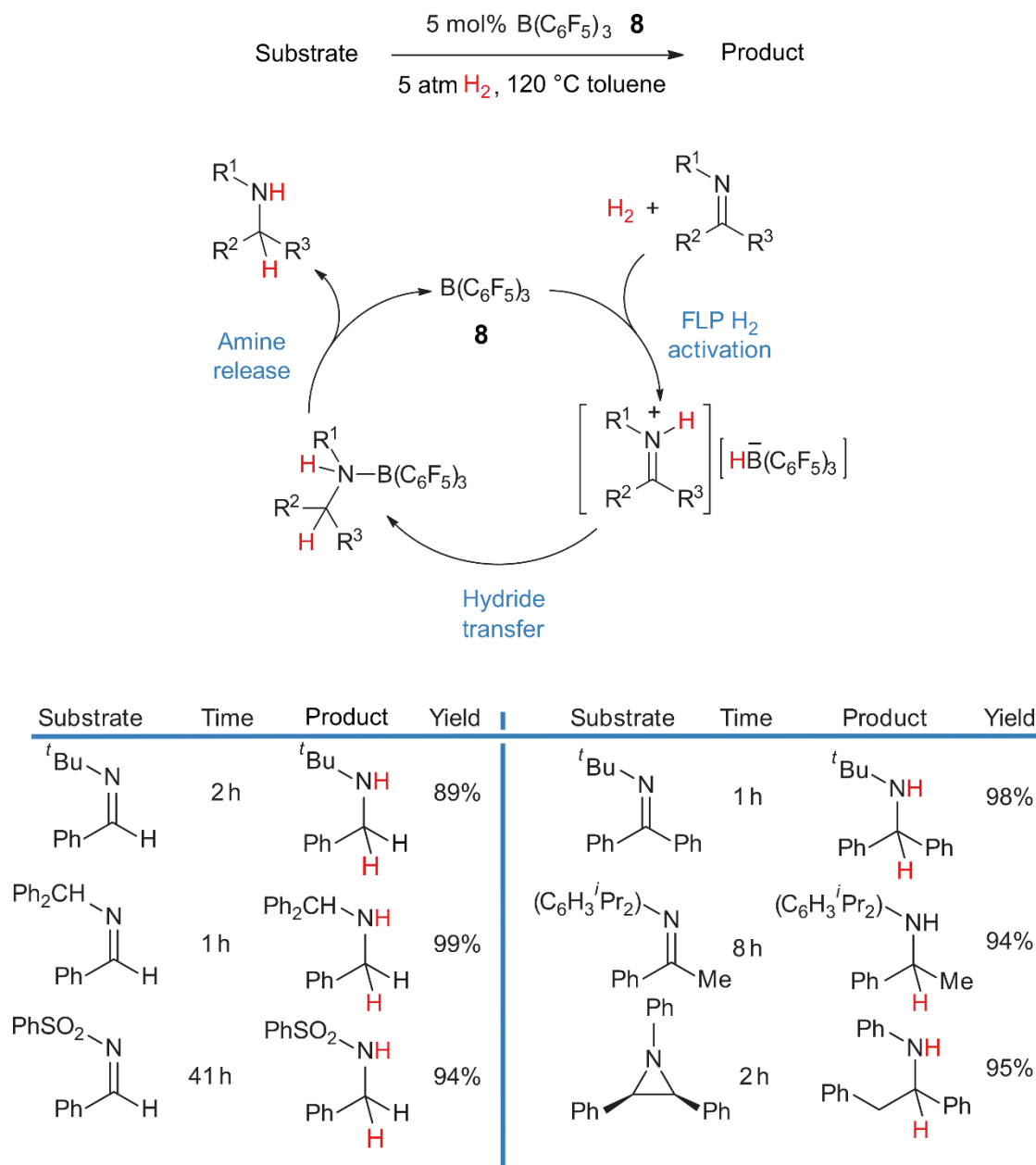


Figure 6 Proposed electron transfer mechanistic model for heterolytic H₂ activation by a FLP, a non-linear transition state is shown (LA = Lewis acid, LB = Lewis base).

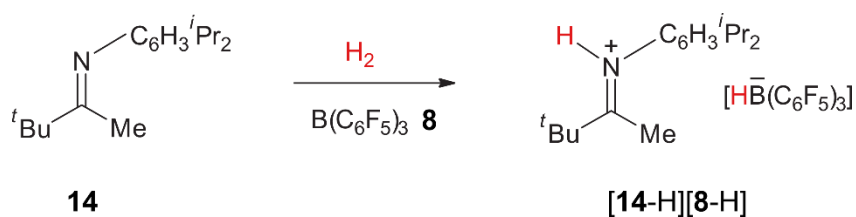
The application of FLPs towards the hydrogenation of organic substrates has been reported extensively. A wide range of functional groups including imines, enamines, nitriles;^[133–136] aldehydes,^[124] and ketones^[137] have been reduced by delivery of the H⁻ fragment following FLP H₂ activation.

Stephan and co-workers were able to hydrogenate sterically encumbered imines using a catalytic quantity of **8** (5 mol%), generating the corresponding amines in high isolated yields.^[133] The presence of additional Lewis base is not required since the imines are themselves Lewis basic and sufficiently sterically bulky. Activation of H₂ by the imine and **8** initially generates the iminium borohydride intermediate (**Scheme 13**). Hydride transfer from [**8**-H]⁻ affords the amine and releases **8**, which is then available for another hydrogenation cycle.



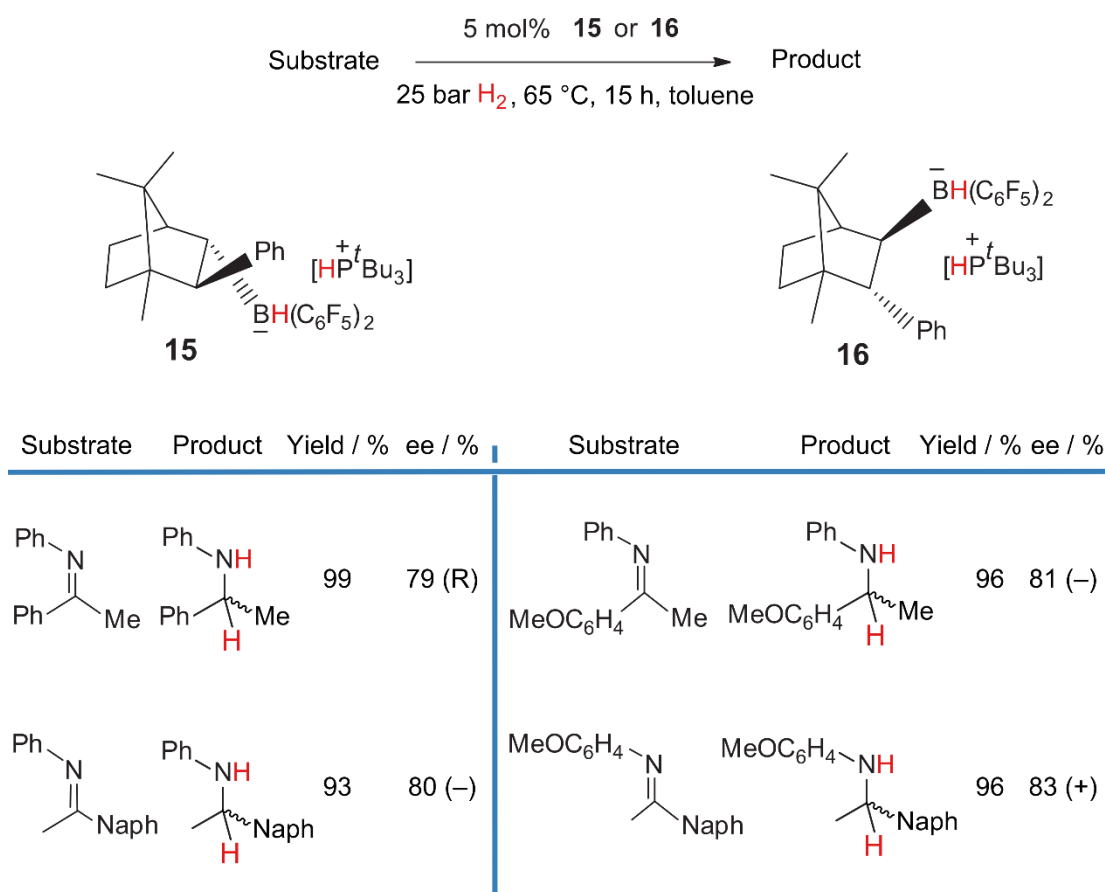
Scheme 13 Catalytic imine hydrogenation by **8**.

While this approach is limited to imines that are sufficiently basic and sterically congested, it is worth noting the bulky ketamine (**14**) was too bulky and precluded the final hydride transfer to the iminium salt. After a 48 hour reflux, only the salt [**14-H**][**8-H**] was obtained (**Scheme 14**).



Scheme 14 Attempt to hydrogenate the bulky imine (**14**) using catalytic quantity of **8**.

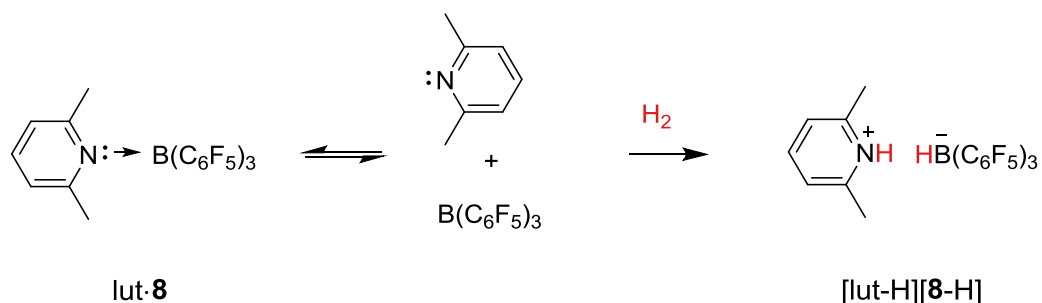
Catalytic asymmetric hydrogenation has been achieved by employing chiral boranes as one of the FLP components.^[138–140] Klankermayer and co-workers were able to achieve high enantiomeric excesses (ee) of up to 83% for imine hydrogenation using boranes derived from camphor (**15** and **16**, see **Scheme 15**).^[139]



Scheme 15 Catalytic asymmetric imine hydrogenation using FLPs comprised of chiral boranes (**15** and **16**).

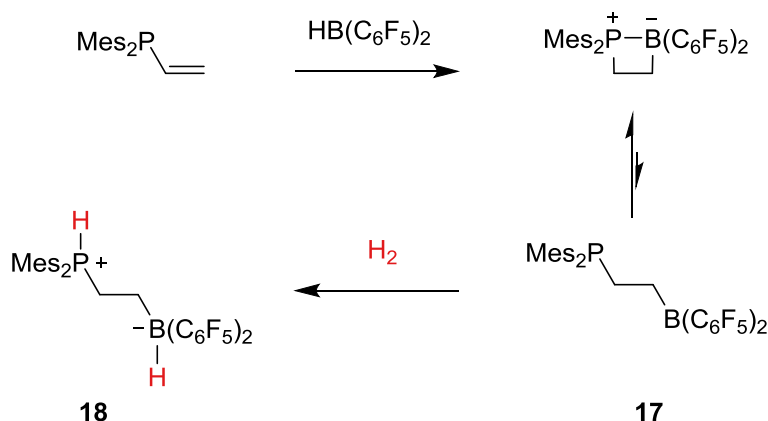
For a Lewis acid-base combination to be suitable for FLP H_2 activation it was often assumed that the pair must be sterically precluded to the extent that negligible classical Lewis adduct formation is apparent. Early reports suggested that Lewis acid-base combinations

behaved either classically (*i.e.* they reacted to give classical Lewis adducts) or as FLPs. Inspired by the early work of Brown,^[111] Geier and Stephan explored the use of FLPs containing lut further.^[141,142] The combination of lut and **8** afforded an equilibrium mixture of the free components and the classical Lewis adduct, lut·**8**, (**Scheme 16**). The equilibrium could be driven towards the formation of lut·**8** by cooling the sample to -40°C . When H_2 (1 atm) was admitted to this mixture at room temperature, the H_2 activation product, [lut-H][**8**-H], was obtained. This system effectively rebuts the previous assumption that Lewis acid-base combinations are mutually exclusive towards either classical or FLP behaviour. Instead, this study suggests that the exhibition of classical vs FLP reactivity is a continuous function of steric preclusion *i.e.* is based on the relative strength of the dative bond in the adduct (provided that the Lewis acid and base are still sufficiently strong to effect H_2 cleavage).



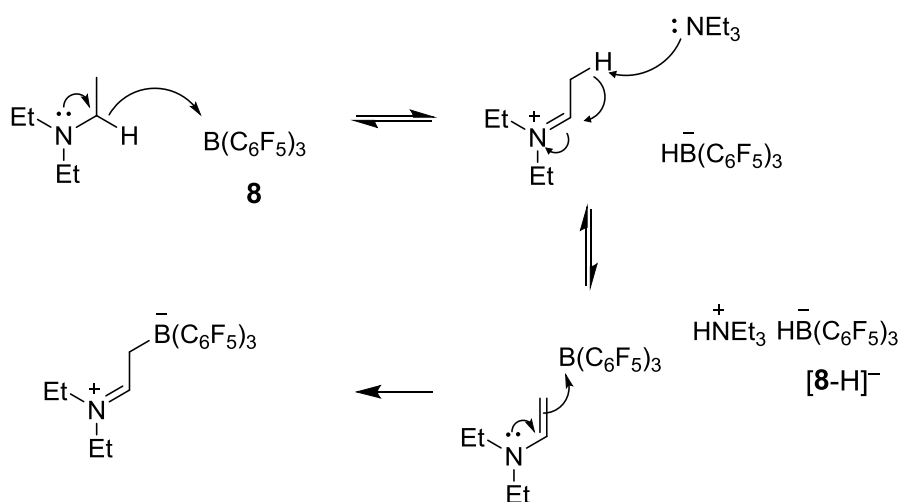
Scheme 16 2,6-Lutidine (lut) and **8** exhibit both classical and frustrated behaviour.

It is worth noting that a similar phenomenon was observed by Erker and co-workers in their early work on intramolecular phosphine-borane FLPs,^[143] shortly after the advent of Stephan's initial FLP system (**11**).^[112] They were utilising the hydroboration of various alkenylphosphines with "Piers' borane", $\text{HB}(\text{C}_6\text{F}_5)_2$, as a route to the preparation of new intramolecular FLPs. The resulting hydroboration product (**17**) of $(\text{Mes})_2\text{PCHCH}_2$ was found to exist in equilibrium between the open-chain and four-membered ring forms, the latter arising from the formation of an intramolecular P-B bonding interaction. Computational studies suggested that this interaction was weakened through ring strain. On admission of **17** to H_2 , the corresponding zwitterionic H_2 activation product, **18**, was formed (**Scheme 17**). **17** was found to be a much more active catalyst than **8** for the metal-free hydrogenation of imines and operated under milder conditions (25°C , 1.5 atm), although much greater catalyst loadings (> 20 mol%) were sometimes required.^[136]



Scheme 17 Hydroboration using Piers' borane to give an intramolecular phosphine-borane adduct that effects H₂ activation.

In addition to the adequate frustration that is required for H₂ activation, the Lewis acid-base combination must also be free from any other deactivation pathways. For example, **8** is incompatible with tertiary amines that possess H substituents on the C positions that are α and β to the N atom.^[113] When NEt₃ is treated with **8**, α -hydride abstraction initially affords the borohydride, [8-H]⁻, and an iminium intermediate. A second equivalent of NEt₃ then abstracts a β -proton from this intermediate to generate [Et₃NH]⁺ and an enamine, which undergoes further reaction with a second equivalent of **8** to give a zwitterion (**Scheme 18**).^[144] This reaction proceeds cleanly and in quantitative yield.



Scheme 18 Reaction of tertiary amines (NEt₃) with **8**.

The Lewis acid component of a FLP is most often a strongly electrophilic borane, typically **8** or a derivative thereof.^[112,117,124,125,145] For this reason, **8** is often considered to be the mainstay

Lewis acid for FLP applications. However, FLP H₂ activation has also been achieved using boron-based Lewis acids that do not contain C₆F₅ groups.^[146–151] An interesting example is the NHC-stabilised borenium cation, [(Im'Pr₂)(BC₈H₁₄)]⁺ {**19**⁺; Im'Pr₂ = C₃H₂(N'Pr)₂}, that is derived from the ubiquitous borane reagent 9-borabicyclo[3.3.1]nonane (9-BBN) (**Figure 7**).

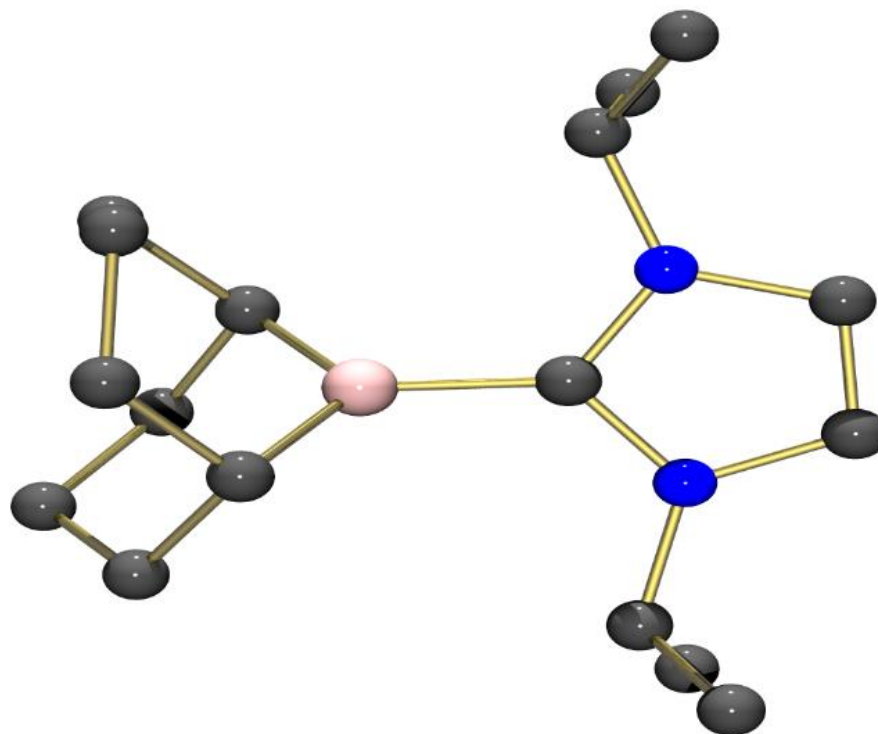
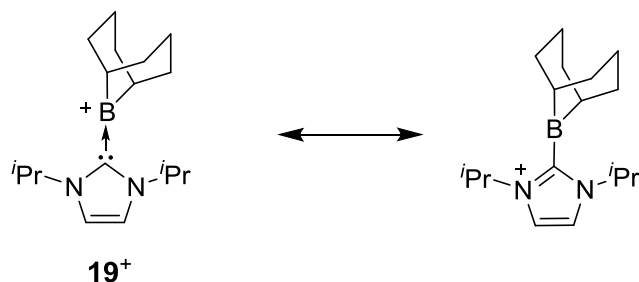


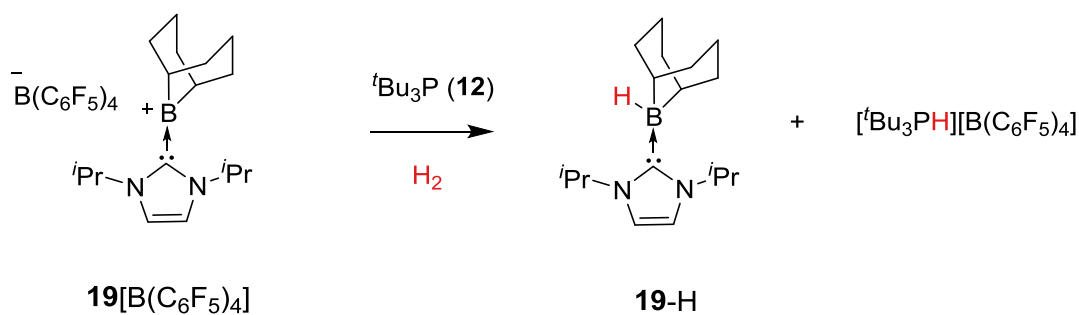
Figure 7 Molecular structure of **19**⁺.

Borenium cations are three-coordinate borocations, [LBR₂]⁺, that possess two σ -bound substituents (R) and a datively bound neutral ligand (L). The ligand stabilises the borocation by occupying the third coordination site and reducing the electrophilicity of the boron centre.^[152–154] The notion of formally representing the positive charge on the B atom, rather than the N atom of the NHC, (see **Scheme 19**) is supported by the following arguments:

- i) B is more electropositive, *i.e.* less electronegative, than N (Pauling electronegativity, $\chi_{\text{B}} = 2.04$ vs $\chi_{\text{N}} = 3.04$).
- ii) Previous computational studies have suggested that there is significant positive charge localised on the boron centre.^[153,155]
- iii) Such compounds behave as though they are boron cations; the boron centre is highly electrophilic and the site of Lewis acidity.

Scheme 19 Alternative resonance form of **19⁺**.

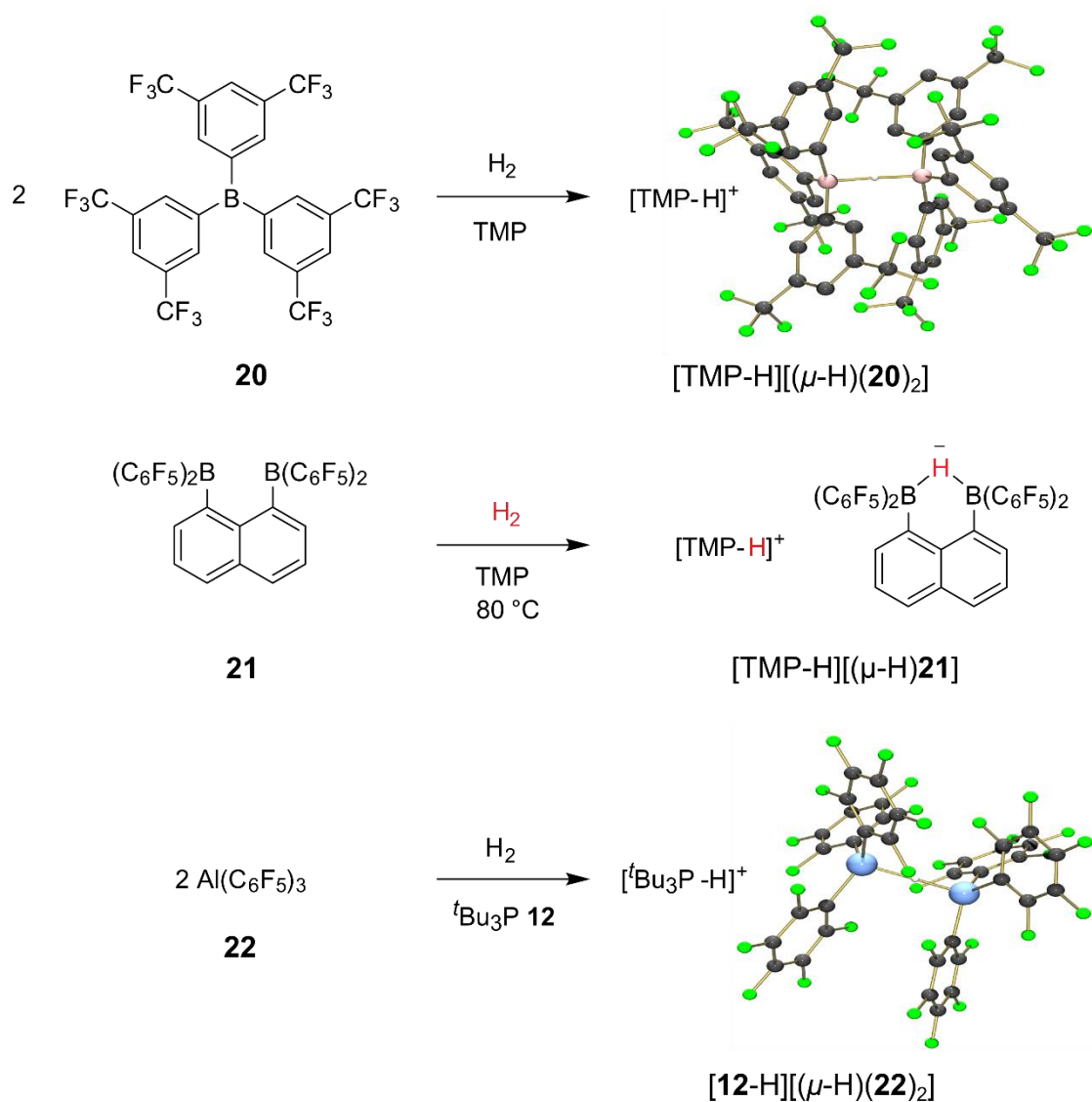
Stephan's group found that when **19**[B(C₆F₅)₄] is combined with the bulky phosphine (**12**), it forms a FLP that is capable of H₂ activation, affording the neutral NHC-borane adduct (**19-H**) and the phosphonium salt, [**12-H**][B(C₆F₅)₄] (Scheme 20).

Scheme 20 FLP activation of H₂ using a borenium cation (**19⁺**).

The lack of electron-withdrawing groups in **19⁺** imparts considerable hydridic character to the neutral NHC-borane adduct, even in comparison with anionic borohydrides such as [**8-H**]⁻.^[150,156] Indeed, it was reported that **8** is capable of abstracting H⁻ from **19-H**, to generate the salt **19**[HB(C₆F₅)₃].^[150] The hydride donor properties of NHC-borane adducts have previously been exploited for the reduction of various substrates,^[157,158] and Stephan and co-workers have found **19-H** to be a potent and highly selective catalyst for the hydrogenation of imines and enamines at room temperature. Also, **19⁺** was found to be much more tolerant of different functional groups when compared to archetypal **8**.

Another Lewis acid that does not contain C₆F₅ groups, yet has been successfully applied for FLP H₂ activation, is tris[3,5-bis(trifluoromethyl)phenyl]borane (**20**). FLP H₂ activation of **20** was reported in 2012 by our collaborators (the research group of Dr. A. Ashley)^[146] and another independent group,^[147] who were simultaneously working on the same Lewis acid. In stark contrast to the majority of previous FLP systems, H₂ activation by **20** was found to be dominated by the formation of a bridging hydride, [(μ-H)(**20**)₂]⁻ (Scheme 21). Bridging hydrides are rare in

FLP chemistry, the only previous borane example being 1,8-bis(dipentafluorophenylboryl)naphthalene (**21**).^[159] **21** contains two Lewis acidic centres that are pre-organised for the formation of a bridging hydride, when combined with a molar equivalent of TMP and admitted to H₂. The tendency of **20** to form a bridging hydride most likely results from the low steric demand of the surrounding groups, combined with a strong Lewis acidity, when compared to **8** (which is dominated by terminal hydride formation, as illustrated by the many examples in this chapter). Indeed, the corresponding aluminium analogue of **8**, Al(C₆F₅)₃ (**22**), is far less bulky^[160] albeit less Lewis acidic,^[161] and also favours the formation of a bridging hydride, [12-H][(μ -H)(**22**)₂], when H₂ is admitted to the **22/12** FLP system.^[162] The reduced steric bulk of **22** results from Al having a much larger covalent radius than B (121(4) vs 84(3) pm).



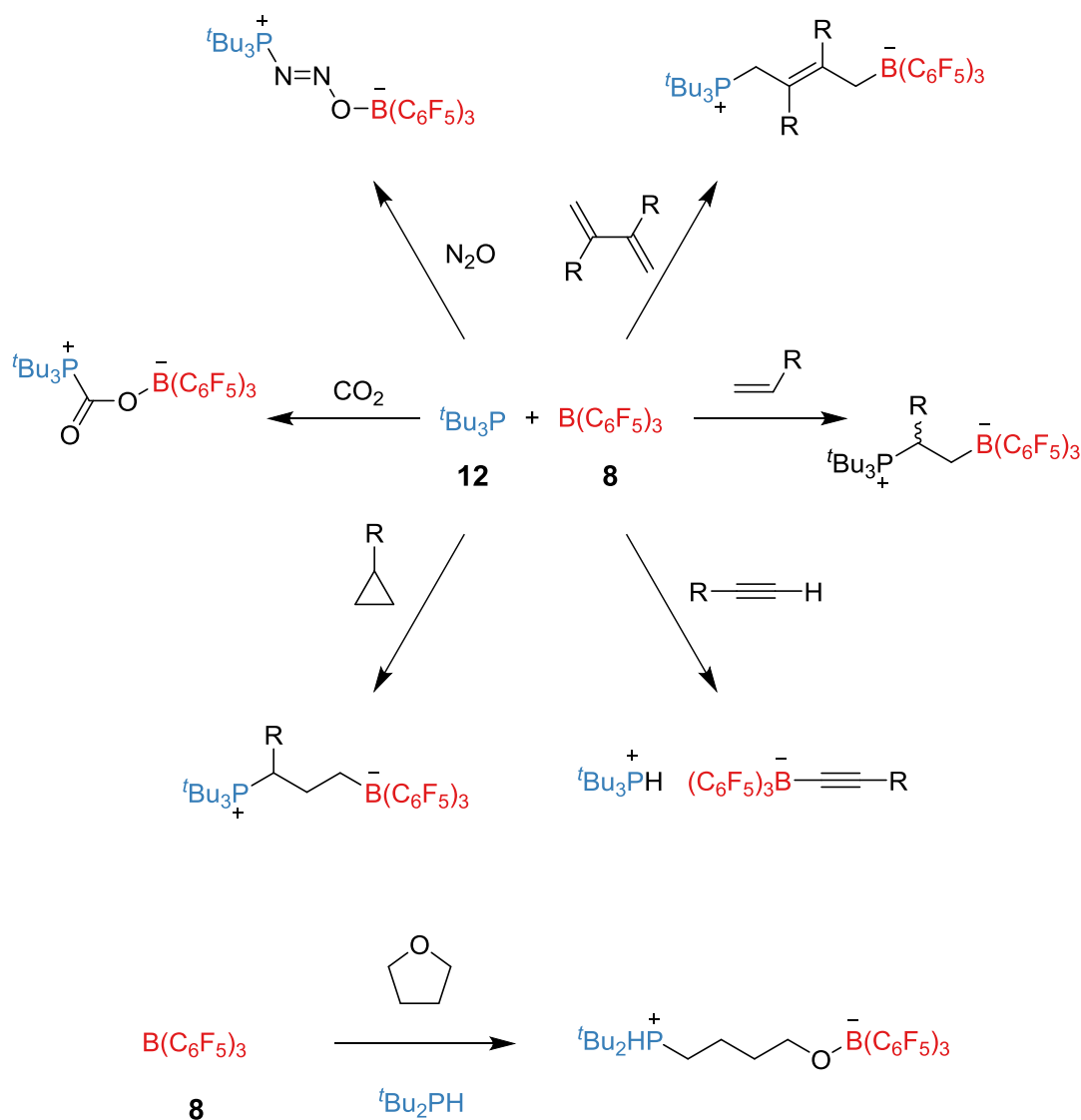
Scheme 21 Examples of Lewis acids that favour the formation of bridging hydrides ($\mu\text{-H}$).

Ashley and Tamm both found that the addition of a Lewis base/donor solvent (LB = pyridine (py), tetrahydrofuran (THF), CH₃CN) to $[(\mu\text{-H})(\mathbf{20})_2]^-$ resulted in the formation of the terminal hydride, $[\mathbf{20}\text{-H}]^-$, and a classical Lewis adduct, LB·**20** (**Scheme 22**). The Lewis base is able to effectively sequester any excess Lewis acid, **20**, that is bound to the $[\mathbf{20}\text{-H}]^-$ unit as $[(\mu\text{-H})(\mathbf{20})_2]^-$.



Scheme 22 The formation of a classical Lewis adduct (LB·**20**) between **20** and Lewis base (LB = py, THF, CH₃CN) drives the conversion of the bridging hydride ($[(\mu\text{-H})\mathbf{20}_2]^-$) into a terminal hydride ($[\mathbf{20}\text{-H}]^-$).

FLP chemistry is not limited to the heterolytic cleavage of H₂; the activation of C-F bonds^[163] and small molecules including alkenes,^[119,164] dienes,^[165] alkynes,^[166–168] cyclopropanes,^[169] tetrahydrofuran (THF),^[125,170–172] isocyanates,^[173] NO₂,^[174,175] CO₂,^[176–178] and O₂^[179] has also been demonstrated. The reactivity of FLPs (comprised of **8**) towards a variety of different small molecules is demonstrated by the examples shown in **Scheme 23**.

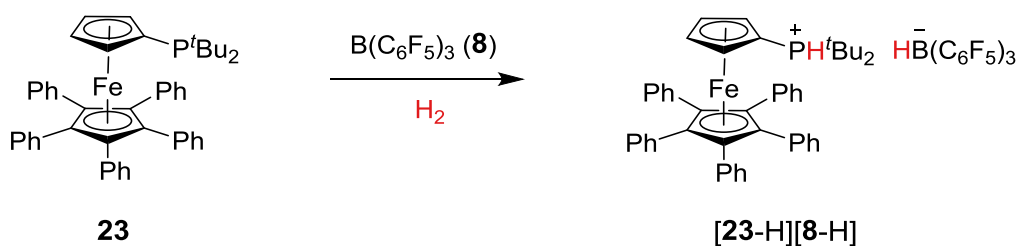


Scheme 23 Examples of small molecule activation by FLPs containing **8**.

It is worth noting that FLPs are not limited to the main group;^[180–182] Wass and co-workers previously demonstrated the ability of zirconocene-phosphinoaryloxide complexes to mimic the reactivity of FLPs whilst offering additional, unprecedented reactivity towards C-Cl and C-O bond cleavage as well as CO_x (x = 1-2) reduction.^[181]

I am only aware of two prior reports that combine electrochemistry with FLP systems. Stephan and co-workers explored the combination of various mono- and bis-

ferrocenylphosphines with **8** for the generation of new FLPs.^[183] The ferrocenyl groups were incorporated as a method of increasing the steric encumbrance of the Lewis base. In most cases, the *para*-substitution products were obtained, analogous to the reaction illustrated in **Scheme 9** (where **9** is generated). However, the bulky phosphine (**23**) did not react with **8** and was found to be effective for the irreversible heterolysis of H₂, forming [**23-H**][**8-H**]. Cyclic voltammetry was performed on [**23-H**][**8-H**], where the *quasi*-reversible oxidation of the ferrocenyl redox label was observed along with the reduction of [**23-H**]⁺.



Scheme 24 Activation of H₂ by the ferrocenyl phosphine (**23**)/**8** FLP.

Aldridge and co-workers have provided a more inspiring example of a combined electrochemical-FLP study.^[184] Inspired by Stephan's application of FLPs for the trapping of N₂O (see **Scheme 23**),^[175] they successfully employed an FLP system comprising ^tBu₃P (**12**) and the ferrocenyl borane, FcB(C₆F₅)₂, for the detection of N₂O. The reaction of N₂O with this FLP generates the product, ^tBu₃P·N₂O·BFc(C₆F₅)₂, which can be detected by a cathodic shift of 300 mV in the Fc^{0/+} {Fc = CpFe(η⁵-C₅H₄), where Cp = (η⁵-C₅H₅)} *quasi*-reversible oxidation wave. More importantly, this characteristic shift was demonstrated to allow for the detection of small quantities of the N₂O-trapped product (<100 μM), and was not observed in the presence of O₂.

As highlighted in this section, the application of FLP H₂ activation chemistry is currently mainly limited to synthetic transformations – where the resulting H⁻ and H⁺ fragments are delivered to appropriate substrates. Returning to fuel cell technology (discussed in 1.3-1.5), aqueous-phase [BH₄]⁻ electrochemistry has been reviewed extensively because of its potential for fuel cell applications.^[20–22] The advantage of using [BH₄]⁻ (rather than H₂) as a fuel is that a Pt electrocatalyst is not required – cheap and ubiquitous carbon electrodes can be employed. However, the commercialisation of direct borohydride fuel cells (systems that oxidise [BH₄]⁻ directly) has been hampered by the fact that these systems cannot be recharged. It is extremely difficult to regenerate [BH₄]⁻ from metaborate, [BO₂]⁻ (the product of alkaline [BH₄]⁻ oxidation).^[21,185] In the previous section I stated that, to the best of my knowledge, there are currently no metal-free electrocatalysts for the H₂ oxidation reaction. In light of the relatively

recent developments in FLP chemistry: the ability of such systems to activate H₂ and generate borohydrides without the need for metals, I believe that a full investigation of the electrochemical properties of FLPs is warranted. FLPs may offer a new electrocatalytic approach to H₂ oxidation.

1.7 Electrochemical methods

This section aims to provide the reader with the basic principles of the electrochemical methods that will feature in this thesis. Throughout this section, the reversible single-electron reduction process shown in **Scheme 25** will be considered.



Scheme 25 The single-electron electrochemical reduction of A results in the formation of B.

1.7.1 Electrochemical equilibria

Analogous to chemical reactions, the direction of an electrochemical process is governed by thermodynamics. When a system is at equilibrium, its Gibbs free energy (*G*) is minimised. Considering the hypothetical electrochemical reaction shown in **Scheme 25**, if an inert electrode (such as a Pt wire) is inserted into a solution containing a mixture of the oxidised (A) and reduced (B) species, then an electrochemical equilibrium becomes established between the two species and the electrons in the electrode. The initial net movement of electrons is infinitesimally small, such that the change in concentration of A and B at the electrode surface is negligible. When the equilibrium is reached, the transfer of electrons to and from the electrode is balanced and no further net change in the solution composition occurs. The onset of this equilibrium gives rise to charge separation between the electrode and the solution; indeed, an “electrode potential”, $[\varphi_M - \varphi_S]_{Pt}$, now exists at this interface. It is impossible to measure an absolute value for the potential difference across a single electrode-solution interface, and therefore an additional electrode must be introduced. This second (and necessary) “reference” electrode-solution interface is assigned an arbitrary potential of $[\varphi_M - \varphi_S]_{Reference} = 0$ V. Thus, the electrode potential (*E*) at the Pt wire-solution interface can now be measured relative to that at the reference electrode (**Equation 2**).

$$E = [\varphi_M - \varphi_S]_{\text{Pt}} - [\varphi_M - \varphi_S]_{\text{Reference}}$$

Equation 2 The measured electrode potential (E) at a Pt wire electrode vs a reference electrode.

In non-aqueous electrochemistry (which features throughout this thesis) a Ag wire is often used as a *pseudo*-reference electrode. The potential difference across the Ag wire-solution interface is not fixed, since changes in the electrode surface chemistry *i.e.* passivation due to adsorption, corrosion, *etc.* leads to a continuous drift in the electrode potential. The recorded potential must therefore be referenced externally; the current IUPAC convention is to correct the recorded potentials to the $\text{Cp}_2\text{Fe}^{0/+}$ redox couple.^[186]

The Nernst equation relates the observed reduction potential (E) of an electrochemical reaction to its standard reduction potential (E^0) in terms of the activities of the species involved – denoted as $\gamma_X[X]_0$ for species X of concentration $[X]_0$ at the electrode surface. The activity coefficient, γ_X , accounts for solution non-ideality resulting from ion-ion and solvent-ion interactions in the electrolyte; for ideal solutions, γ_X approaches unity. The Nernst equation is shown below (**Equation 2**) for the electrochemical reduction of A to B (according to **Scheme 25**).^[33,187]

$$E = E^0 - \frac{RT}{nF} \ln \frac{\gamma_B [B]_0}{\gamma_A [A]_0}$$

Equation 3 The Nernst equation describing the observed reduction potential (E) for an n electron process ($n = 1$ in this case). R = gas constant ($8.314 \text{ V C K}^{-1} \text{ mol}^{-1}$); T = temperature (K); F = Faraday constant ($96485.3 \text{ C mol}^{-1}$).

When considering complex electrochemical systems that involve multiple reversible electrochemical reactions, it is important to remember that multiple Nernstian equilibria are under operation. Therefore, the experimentally observed reduction potentials (E) may deviate significantly from the standard value (E^0).

1.7.2 Electrode kinetics

The current passed at an electrode surface during electrolysis is directly proportional to the electroactive area of the electrode (A) and the flux of reactant to the electrode surface (j) (**Equation 4**).

$$i = nFAj$$

Equation 4 The measured current is related to the flux of reactant (j) and the electroactive area (A) at the electrode.

The net flux of reactant undergoing electrolysis at the electrode (j) can be expressed in terms of the relative rates of the forward (k_f) and reverse (k_b) electrochemical reactions. In the case of the electrochemical reaction shown in **Scheme 25**, **Equation 5** describes the net flux of reactant A undergoing reduction to form product B.

$$j = k_f [A]_0 - k_b [B]_0$$

Equation 5 The net flux of reactant A at the electrode surface (undergoing reduction to B).

The kinetics of an electrochemical reaction are dependent on the potential that is applied. In the case of the reduction of A, k_f would be expected to be dominant at relatively negative potentials, since the electrode is providing a large driving force for the forward reaction. The potential-dependence of the rate constants k_f and k_b can be expressed in terms of the overpotential ($\eta = E - E^0$, refer back to **Equation 1** in 1.4) by the electrochemical representation of the Arrhenius equation (**Equation 6**).

$$\begin{aligned} \text{a)} \quad k_f &= k_f^0 e^{\frac{-\alpha\eta nF}{RT}} \\ \text{b)} \quad k_b &= k_b^0 e^{\frac{(1-\alpha)\eta nF}{RT}} \end{aligned}$$

Equation 6 The observed electrochemical rate constant for a) the forward (k_f), and b) the backward (k_b) electrochemical reactions in terms of the overpotential, constants, k_f^0 and k_b^0 , and the charge transfer coefficient, α .

The combination of **Equations 5-6** provides an expression for the net flux of reactant in terms of the overpotential (**Equation 7**).

$$j = [A]_0 k_f^0 e^{\frac{-\alpha \eta n F}{RT}} - [B]_0 k_b^0 e^{\frac{(1-\alpha) \eta n F}{RT}}$$

Equation 7 The net flux of reactant A in terms of its overpotential.

When the forward and backward electrochemical rate constants are equal, an equilibrium has become established and there is no net flux of reactant ($j = 0$). Under these conditions, **Equation 7** is found to reduce to the Nernst equation (**Equation 3**) when the constants k_f^0 and k_b^0 are equal ($k_f^0 = k_b^0$). Based on this observation, **Equation 7** can therefore be simplified by replacing k_f^0 and k_b^0 by the standard electrochemical rate constant (k^0) – as shown in **Equation 8**.

$$j = k^0 \left[[A]_0 e^{\frac{-\alpha \eta n F}{RT}} - [B]_0 e^{\frac{(1-\alpha) \eta n F}{RT}} \right]$$

Equation 8 The net flux of reactant A in terms of its overpotential.

The combination of **Equation 4** and **Equation 8** yields the Butler-Volmer equation (**Equation 9**), which relates the observed current to the applied potential (through the overpotential) and the electrode surface concentrations of the electroactive species. The Butler-Volmer model of electrode kinetics forms the basis to the solution of all electrochemical problems. The Butler-Volmer equation shows that a small perturbation in the applied potential (E) gives rise to a significant increase in the rate of an electrochemical reaction *e.g.* a 1 Volt change in E will provide a *ca* 10^9 fold increase in the observed electrochemical rate constant (k).

$$i = nFAk^0 \left[[A]_0 e^{\frac{-\alpha \eta n F}{RT}} - [B]_0 e^{\frac{(1-\alpha) \eta n F}{RT}} \right]$$

Equation 9 The Butler-Volmer equation describing the observed current (i) in terms of the standard electrochemical rate constant, k^0 , and the charge transfer coefficient, α .

For a reductive (cathodic) electrode process, the observed rate of electron transfer *i.e.* the observed electrochemical rate constant (k), increases as the electrode potential becomes more negative. The standard electrochemical rate constant (k^0) is simply a measure of the relative rate of electron transfer for a redox couple. If k^0 is large then an electrochemical

equilibrium is rapidly attained; if k^0 is small then the converse is true, and Nernstian behaviour will not be observed (the electrode process is described as irreversible). Values of k^0 may span many orders of magnitude, indeed values have been reported to range from 10^{-9} to 10 cm s^{-1} .^[33] The electrochemical parameter α is known as the charge transfer coefficient and can range from a value of 0 to 1; it describes whether the transition state lies closest to the reactants ($\alpha = 0$) or the products ($\alpha = 1$) in terms of reaction coordinate. In most systems, α is often found to lie in the range 0.3 and 0.7, and can usually be approximated to 0.5 (which suggests a symmetrical interaction between the free energy curves of the electroactive species – see **Figure 8**) in the absence of any measurements.

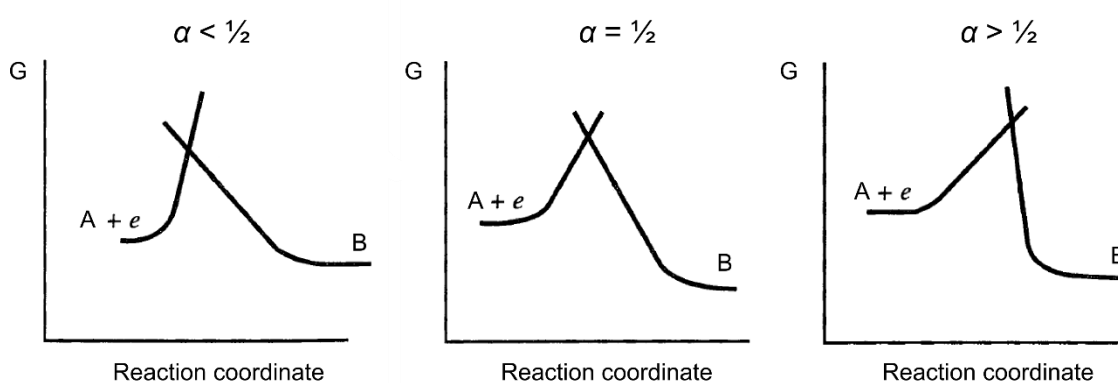


Figure 8 The effect of the charge transfer coefficient (α) on the symmetry of the interacting Gibbs free energy curves for the reduction of A to B (adapted from reference [33]).

The charge transfer coefficient α also describes the relationship between the Marcus theory of electron transfer and Butler-Volmer kinetics (**Equation 10**).

$$\alpha = \frac{1}{2} \left[1 + \frac{\Delta G}{\lambda} \right]$$

Equation 10 Charge transfer coefficient in terms of Gibbs free energy change (ΔG) and the reorganisation energy (λ).

Marcus theory describes the rate of adiabatic electron transfer in terms of the reorganisation energy (λ). This is comprised of contributions from inner (λ_i) and outer (λ_o) sphere reorganisation energies. The term λ_i describes changes in bond strength and angles during electron transfer, and λ_o depends on contributions from dipole reorientation and electric polarization of the surrounding solvent molecules.^[187]

The Gibbs free energy term (ΔG) in **Equation 10** is not fixed; indeed, ΔG changes with the applied electrode potential, and as a result of this, α is a potential-dependent quantity. However, since kinetic data is often collected over a very narrow potential range, α is often treated as a constant value. At applied potentials close to E^0 (where $\Delta G = 0$) *i.e.* a redox couple under equilibrium conditions, α is approximately 0.5. In the limit $\Delta G \gg 0$, the electrode reaction is not spontaneous and since $\Delta G \approx \lambda$, α tends towards 1. Conversely, in the limit $\Delta G \ll 0$, the electrode reaction is spontaneous and driven by the electrode potential; at this limit, $\Delta G \approx -\lambda$ and α tends towards 0.

1.7.3 Mass transport – diffusion, convection and migration

Electrons transfer between the electrode surface and the electroactive species *e.g.* A, by quantum mechanical tunnelling over a distance of *ca* 10-20 Å.^[187] This results in a depletion zone, whereby additional “unreacted” electroactive species must first diffuse (down the concentration gradient) from the bulk solution to within this distance before further electron transfer may occur. The diffusion process can be adequately described by Fick’s laws.^[188,189] The symmetry of the diffusion field is dependent on the geometry of the electroactive surface area of the electrode. Planar electrodes present a simple case where linear diffusion occurs in one direction along the ordinate x (**Figure 9**).

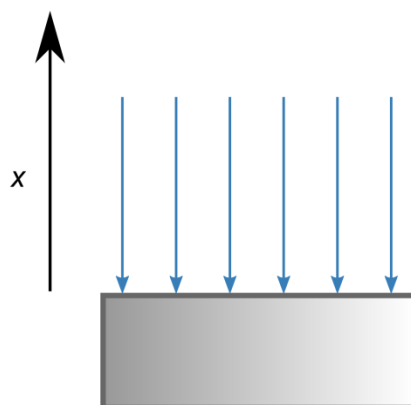


Figure 9 Symmetry of the diffusion field at a planar electrode surface.

At any point from the electrode, x , there will be diffusive flux (j). This is quantified by Fick’s first law (**Equation 11**) and is proportional to the local concentration gradient, $\frac{\partial c}{\partial x}$. The negative sign indicates that the flux is down the concentration gradient, and the proportionality constant D is known as the diffusion constant.^[190,191]

$$j = -D \frac{\partial c}{\partial x}$$

Equation 11 Fick's first law of diffusion.

The magnitude of D increases with increasing temperature, and decreases with increasing solvent viscosity; values are typically in the range of 10^{-6} to 10^{-5} $\text{cm}^2 \text{s}^{-1}$ for common non-aqueous electrochemical solvents (CH_2Cl_2 , THF, CH_3CN etc.) at room temperature. Larger molecules create more viscous drag, and therefore diffuse more slowly than smaller molecules. If a molecule is assumed to be spherical, then the value of D is related to temperature (T), solvent viscosity (η_v), and particle radius (r) by the Stokes-Einstein equation (**Equation 12**).^[192]

$$D = \frac{k_B T}{6\pi\eta_v r}$$

Equation 12 Stokes-Einstein equation – k_B = Boltzmann's constant (1.38×10^{-23} J K^{-1}).

The change in concentration with time, $\frac{\partial c}{\partial t}$, at point x is described by Fick's second law (**Equation 13**) and is proportional to the rate of change in the local concentration gradient, $\frac{\partial^2 c}{\partial x^2}$.

$$\frac{\partial c}{\partial t} = D \frac{\partial^2 c}{\partial x^2}$$

Equation 13 Fick's second law of diffusion for a planar electrode.

Natural convection involves the movement of molecules from more to less dense regions *i.e.* density gradients. This phenomenon maintains the concentration of the bulk solution at a constant value. During electrolysis, the reactant becomes depleted and the new product builds up at the electrode surface. This causes a change in local densities and establishes a density gradient, making natural convection inevitable. However, close to the electrode surface, additional frictional forces limit this effect. Considering that the timescale of most electrochemical measurements is relatively short (10-20 s), it is assumed that the vicinity of the electrode surface is free of any convection processes. This zone is therefore described as the diffusion layer. Whilst slight temperature variations in the bulk solution may also induce natural convection, it is assumed that electrochemical experiments are perfectly thermostatted. Indeed, experiments may be successfully interpreted using diffusion-only models – the unpredictable

and irreproducible nature of natural convection effects would be very difficult to model (although significant progress has been made in the last decade).^[193]

Forced convection is the deliberate agitation of the solution by a mechanical means *i.e.* stirring or swirling. For electrochemical techniques that operate under diffusion control (all the analytical techniques that will be discussed in this section and feature throughout this thesis), it is necessary to mechanically agitate the solution between experimental runs, since diffusion is a relatively slow process over large distances. This effectively refreshes the electrode-solution interface. For electrochemical techniques that operate over a longer timescale, forced convection is deliberately used to dominate the other migration effects (such as diffusion and natural convection), since its hydrodynamic behaviour is well-defined. For example, stirring is employed throughout bulk electrolysis experiments – where the electrochemical conversion of reactant to product is driven to completion.

Migration effects concern the movement of ions due to their electrostatic interaction with an external electric field *i.e.* the applied electrical potential at the electrode. Faradaic current is the electron current that flows during electrolysis.^[33] In the absence of electrolysis, there is a build-up of surface charge at the working electrode surface. Supporting electrolyte, an inert salt, is deliberately added in concentrations *ca* two orders of magnitude greater than the electroactive species of study. This balances the buildup of electrode surface charge through the formation of an adsorption layer of solvated and unsolvated electrolyte ions.^[192] Supporting electrolyte also ensures that the potential drop ($\varphi_M - \varphi_S$) between the electrode and solution is compressed to within 10-20 Å – the distance where quantum mechanical tunneling occurs. In doing so, the electric field outside of this range is zero. Diffusion is therefore the only means of mass transport from the bulk solution to this region *i.e.* migration effects are eliminated. If the potential drop was to occur over a distance greater than this, then the full potential would not be available to drive the electrochemical reaction forwards.

The density of the electrical double-layer (formed by the electrolyte) is highly ordered at the electrode surface, but becomes more diffuse as the distance from the electrode is increased. This results from Brownian motion and is adequately described by the Grahame model.^[194] As the applied electrode potential changes, capacitive charging currents arise from the continuous movement of electrolyte, since the composition of the electrolyte double-layer is highly dynamic. This capacitive charging current, often referred to as the double-layer capacitance (C_{dl}), is observed as a background signal and is directly proportional to the electroactive surface area of the working electrode (and the voltage scan rate in cyclic voltammetry, see 1.7.8 below).

1.7.4 Supporting electrolyte

Non-aqueous electrochemical experiments are predominantly conducted in CH_3CN , THF, or CH_2Cl_2 containing supporting electrolyte comprising $[\text{}^n\text{Bu}_4\text{N}]^+$ salts of either $[\text{BF}_4]^-$, $[\text{PF}_6]^-$, $[\text{ClO}_4]^-$, or $[\text{CF}_3\text{SO}_3]^-$. Such supporting electrolytes suffer from poor conductivities due to incomplete dissociation of the ion pairs.^[195] Another issue relates to the nucleophilicity of the anion component. Whilst $[\text{BF}_4]^-$ was long believed to be a “non-coordinating anion”, it is now widely accepted that such a notion is in fact incorrect.^[196] The non-innocence of $[\text{BF}_4]^-$ as a non-coordinating anion has previously been demonstrated through its coordination to cationic main group metals, and its vulnerability to undergo decomposition *via* fluoride abstraction reactions.^[197] The observation of such behaviour in synthetic organometallic chemistry has driven the development of a new family of weakly coordinating anions that are of a very low nucleophilicity.^[198]

Weakly coordinating anions feature a low overall charge that is delocalised as fully as possible over the whole anion; no atom or group bears a high level of charge. Effective candidates are kinetically and thermodynamically stable and contain only weakly basic sites on their periphery. Two excellent examples are Kobayashi’s anion, tetrakis[3,5-bis(trifluoromethyl)phenyl]borate, $[\text{BArF}_{24}]^-$,^[199] and $[\text{B}(\text{C}_6\text{F}_5)_4]^-$ (Figure 10).^[200]

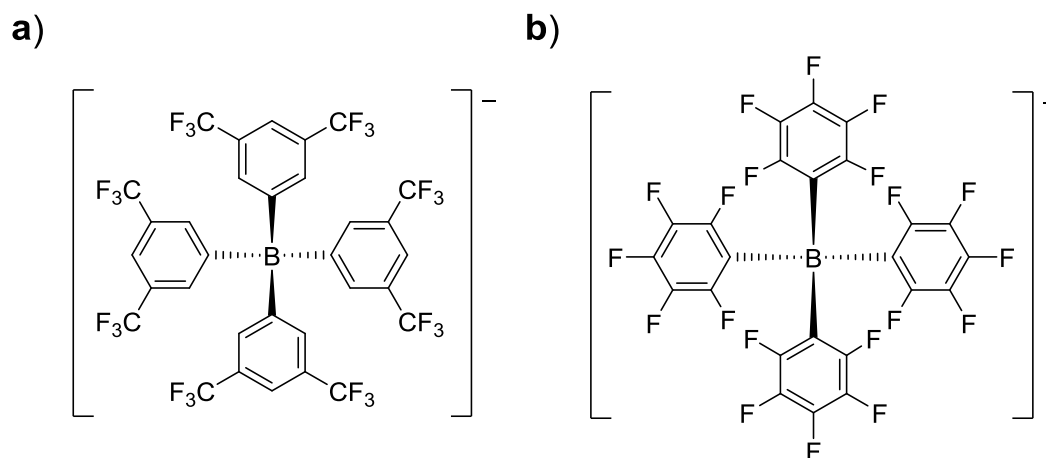


Figure 10 Examples of weakly coordinating anions: a) Kobayashi’s anion, $[\text{BArF}_{24}]^-$; and b) $[\text{B}(\text{C}_6\text{F}_5)_4]^-$.

An electrolyte solution of $[\text{}^n\text{Bu}_4\text{N}][\text{BArF}_{24}]$ in CH_2Cl_2 was first investigated by Mann and co-workers in 1991, using cyclic voltammetry.^[201] They were able to obtain *quasi*-reversible cyclic voltammetry for the single-electron oxidations of Cp_2Ru and Cp_2Os . This result was in stark contrast to the behaviour observed when traditional electrolytes were used. In the case of traditional electrolyte such as LiClO_4 , irreversible two-electron processes are observed,

suggesting that the electrogenerated cations are susceptible to interaction and reaction with the non-innocent electrolyte anions.

The electrochemical application of the weakly coordinating electrolyte, [n Bu₄N][B(C₆F₅)₄], was first explored by LeSuer and Geiger almost a decade later in 2000.^[202] They were interested in finding a system that provided a more positive potential window than that of [n Bu₄N][BArF₂₄]. The potential window is defined as the potential range where the electrolyte/solvent mixture remains electroinactive, beyond which large currents are observed as a result of solvent or electrolyte decomposition. Indeed, the anodic limit for [n Bu₄N][B(C₆F₅)₄] was found to occur at +1.84 V vs Cp₂Fe^{0/+} compared with +1.55 V vs Cp₂Fe^{0/+} for [n Bu₄N][BArF₂₄] in CH₂Cl₂. The relative advantages and disadvantages of [n Bu₄N][B(C₆F₅)₄] vs [n Bu₄N][BArF₂₄] have since been revisited by Geiger and co-workers.^[195,203]

For the electrochemical study of strong Lewis acids such as boranes, it is advisable to limit the electrolyte system to non-donor solvents such as CH₂Cl₂. As highlighted in 1.6, the tendency of boranes to form classical Lewis adducts with strong and sterically unencumbered donor solvents, such as THF or CH₃CN, is high. 1,2-Difluorobenzene (DFB) has been reported to provide significant advantages for electrochemical studies over CH₂Cl₂.^[204] It has a high dielectric constant (13.8 vs 8.9 for CH₂Cl₂) that permits the dissolution of electrolyte salts and highly polar/ionic electroactive species. DFB is also weakly-coordinating and relatively chemically inert with a wide potential window. However, its expense presents a significant disadvantage that limits its widespread use.

The use of a weakly coordinating electrolyte for the electrochemical study of Lewis acidic (and oxophilic) boranes will preclude the occurrence of any side-reactions that involve either halide abstraction or classical Lewis adduct formation. Such reactions would be highly likely if traditional electrolytes containing [BF₄]⁻, [PF₆]⁻, or [ClO₄]⁻ were employed.^[197]

1.7.5 Electrode materials

Glassy carbon is defined as an aggranular, non-graphitizable carbon material with a very high isotropy of its structural and physical properties and with a very low permeability for liquids and gases. The original surfaces and the fracture surfaces are described to have a glass-like appearance.^[205] The surface structure of glassy carbon is composed of interwoven graphitic ribbons. The edges of the graphitic ribbons (where the graphite layers terminate) are decorated with a large density of oxygen-containing surface functionalities containing carbonyl and hydroxyl moieties.^[206] Compared to Pt electrodes, GCEs are cheap and ubiquitous but, in general, do not perform electrocatalysis.

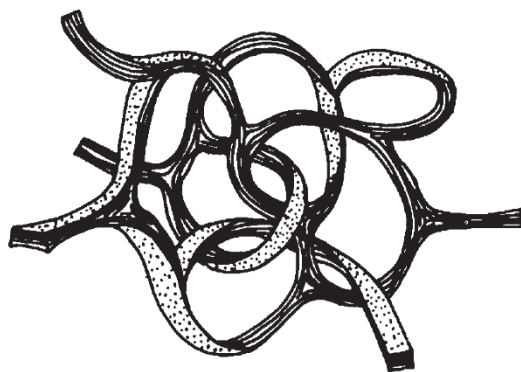


Figure 11 The structure of glassy-carbon (adapted from reference [207]).

1.7.6 The need for a three-electrode setup

In 1.7.1, the requirement for a reference electrode was discussed. All the electrochemical techniques that feature in this thesis use a three-electrode setup:

- i) The working electrode (glassy carbon or Pt) is the site of interest. It is the flow of current/potential across the working electrode-solution interface that is being measured.
- ii) The reference electrode (Ag wire) provides a means of measuring the applied potential at the working electrode (see 1.7.1). Whenever possible, it is corrected to the $\text{Cp}_2\text{Fe}^{0/+}$ redox couple (according to IUPAC recommendations).^[186]
- iii) The counter electrode (Pt wire or gauze) simply functions as an electron source or sink, in order to maintain the potential at the working electrode surface. This prevents large currents from passing through the reference electrode, and causing fluctuations and drift in its potential, $[\varphi_M - \varphi_S]_{\text{Reference}}$.

1.7.7 Chronoamperometry

In single step chronoamperometry, the potential is stepped from a value where no electrolysis occurs (E_1) to a value where the electroactive species undergoes complete electrolysis at the electrode surface (E_2). In double-step experiments, the potential is then stepped to another potential. For experiments that feature reversible electrochemical reactions, this value is usually set to the initial potential (E_1) so that the products are converted back to the reactants. The current response for this process is measured as a function of time. An example of such an experiment at a macrodisk electrode (where the electroactive radius r is of the order

of millimetres and, predominantly, planar diffusion is exhibited)^[208] is shown in **Figure 12** for a reversible oxidation (e.g. the oxidation of B to A in **Scheme 25**).

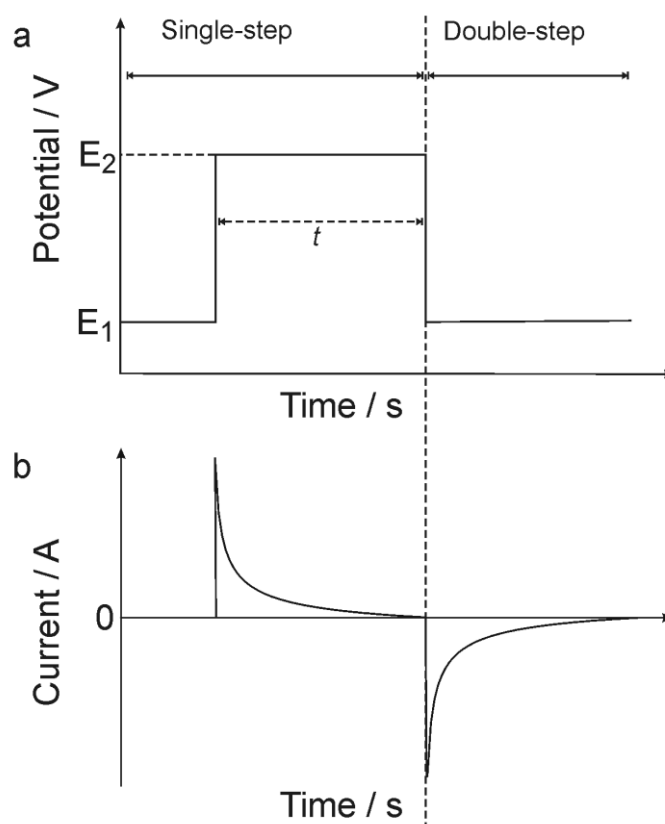


Figure 12 Chronoamperometry at a macrodisk electrode: a) the potential-time profile applied at the working electrode and b) the current-time response measured.

As described previously in 1.7.2, the current passed is directly proportional to the electroactive area of the electrode (A) and the flux of reactant to the electrode surface (j) (**Equation 4**). The solution of Fick's second law (**Equation 13**), to give the diffusive flux (change in concentration) of the electroactive species at the electrode surface as a function of time, results in the Cottrell equation (**Equation 14**).^[209]

$$j = \frac{nFA\sqrt{D}c_{t=0}}{\sqrt{\pi t}}$$

Equation 14 The Cottrell equation (current-time transient) at a macrodisk electrode of electroactive area A . $c_{t=0}$ is the initial concentration of the electroactive species.

The Cottrell equation (**Equation 14**) shows that the current passed at a macrodisk electrode is inversely proportional to the square-root of time ($t^{1/2}$). In practical terms, a

chronoamperogram that is recorded at a macrodisk electrode will show a current-time response that decays towards zero current (as illustrated in **Figure 12b**). As time progresses, the product builds up at the electrode surface and, conversely, the reactant becomes depleted. The diffusion layer (of thickness d) expands, and the reactant must diffuse over an ever-increasing distance before it can undergo electron transfer with the electrode surface. Since the electrode radius (r) is considerably larger than the diffusion layer thickness (d), the current that passes is limited by the diffusive flux. If the electrode area (A) and the number of electrons (n) involved in the electrochemical process are known, then the current-time response can be fitted using the Cottrell equation, to determine the diffusion coefficient (D) of the reactant.

It is interesting to compare the current-time response at a macrodisk electrode to that at a microdisk electrode (where the electrode radius r is of the order of micrometres) for the same oxidation process (**Figure 13**). In stark contrast to the current-time response at a macrodisk electrode where the current converges to zero current, at a microdisk electrode the current instead converges towards a steady-state current (i_{ss}).

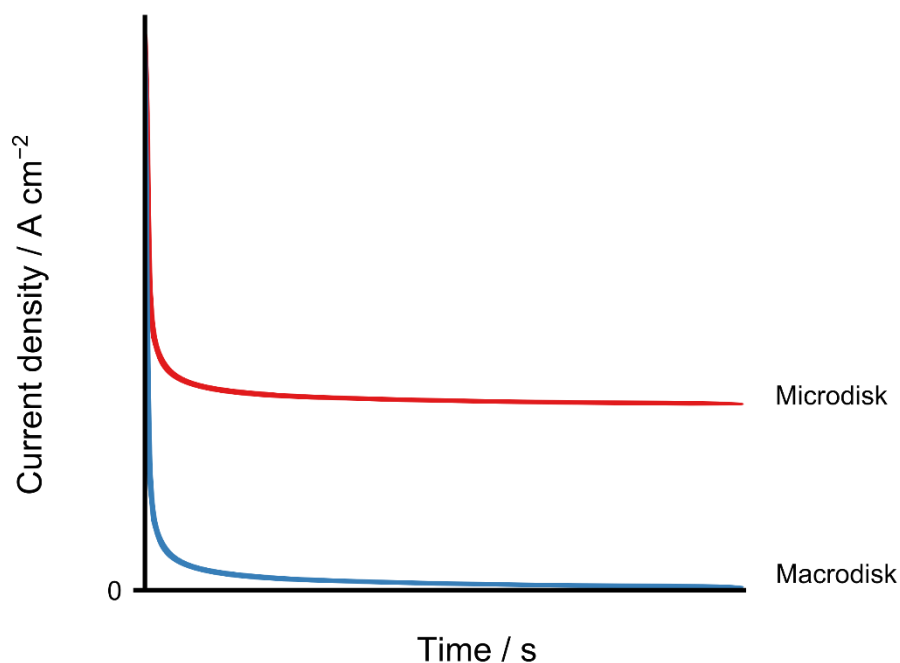


Figure 13 Chronoamperometry at microdisk (red line) vs macrodisk (blue line) electrodes.

This phenomenon results from the diffusional field symmetry at a microdisk electrode being dissimilar to that at a macrodisk electrode at long experiment times, which is a consequence of edge-effects. As discussed previously, the diffusion symmetry at a macrodisk electrode can be approximated to being planar. Realistically, planar diffusion accounts for more than 95% of mass transport at macrodisk electrodes, with the remaining contribution (<5%)

resulting from convergent diffusion on the edge of the electrode. As the electrode size decreases, there is an enhancement in the edge-effects, since the circumference to area ratio increases. At microdisk electrode geometries, edge-effects dominate to the extent that more than 95% of mass transport occurs by convergent diffusion (**Figure 14**).

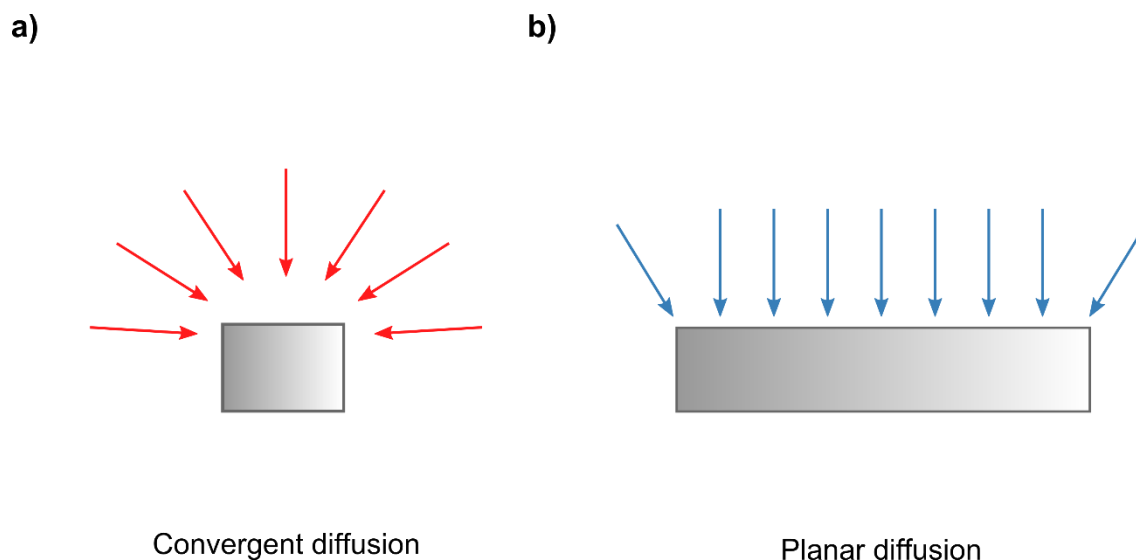


Figure 14 Diffusion field symmetries at a) microdisk and b) macrodisk electrodes at long experiment times (predominantly convergent and planar, respectively).

During a chronoamperometry experiment at a microdisk electrode, the initial perturbation in applied potential results in a Cottrellian current response that is predominantly planar, since the diffusion layer thickness (d) is relatively small compared to the electrode radius (r). However, as the diffusion layer expands, the convergence of the flux lines to a common point has the consequence of almost infinite diffusional flux, and the electrode is fed by a constant concentration gradient. The steady-state current (i_{ss}) that eventually flows is given by **Equation 15**. Provided that the number of electrons involved in an electrode reaction is known, the diffusion coefficient can be estimated from the measured steady-state current.

$$i_{ss} = 4nFc_{t=0}Dr$$

Equation 15 The diffusion-limited steady-state current (i_{ss}) at a microdisk electrode of radius r .

The full current-time transient at a microdisk electrode is expressed by **Equation 16**, where $f(\tau)$ is a function of dimensionless time, $\tau = \frac{4Dt}{r^2}$.

$$i = 4nFc_{t=0}Drf(\tau)$$

Equation 16 The current-time transient at a microdisk electrode of radius r .

A numerical expression for $f(\tau)$ was obtained by Shoup and Szabo (**Equation 17**),^[210] and provides an accurate approximation (with a maximum error of less than 0.6%) for the current-time transient at both the short and long experimental time limits.

$$f(\tau) = 0.7854 + 0.8863\tau^{-1/2} + 0.2146e^{-0.7823\tau^{-1/2}}$$

Equation 17 The Shoup-Szabo expression for $f(\tau)$.

The significance of this result is that for a sample of known initial concentration ($c_{t=0}$), both the diffusion coefficient (D) and the number of electrons (n) involved in the electrode process can be simultaneously determined through data fitting. This is provided that the electroactive radius (r) is accurately known.

1.7.8 Cyclic voltammetry

In cyclic voltammetry experiments, the applied potential at the working electrode is swept from a start potential (E_1) to an upper vertex potential (E_2) and back again to the stop potential ($E_3 = E_1$) at a constant voltage scan rate, ν (**Figure 15**). Note that it is not necessary for the start and stop potentials to have the same values.

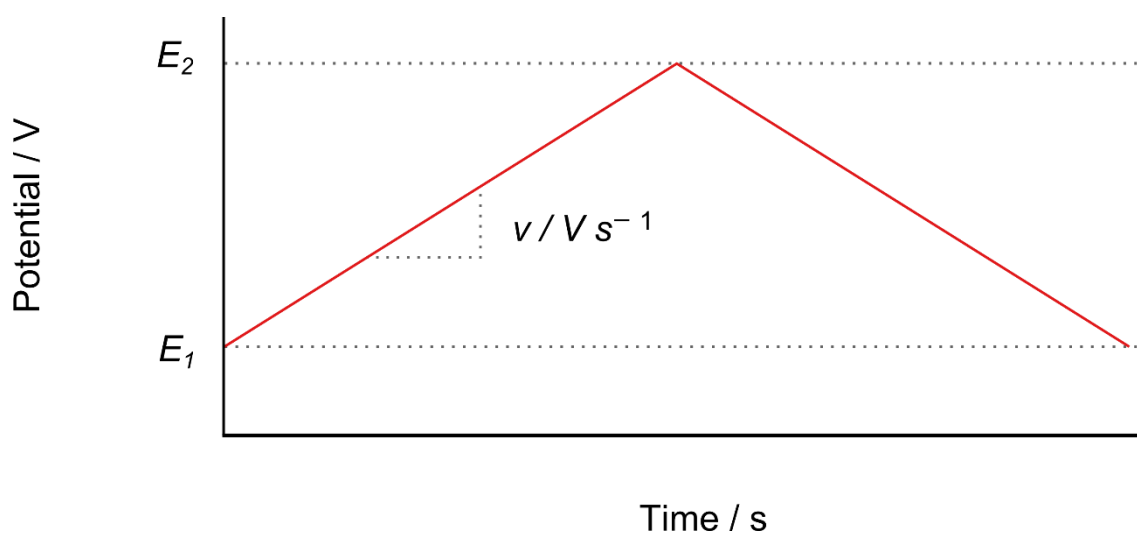


Figure 15 Potential-time profile applied in cyclic voltammetry experiments.

The current that flows is measured and plotted against the applied potential to produce the resulting cyclic voltammogram (CV). An example of a CV recorded at a microdisk and macrodisk electrode is shown in **Figure 16** for a reversible oxidation (e.g. the oxidation of B to A, shown in **Scheme 25**).

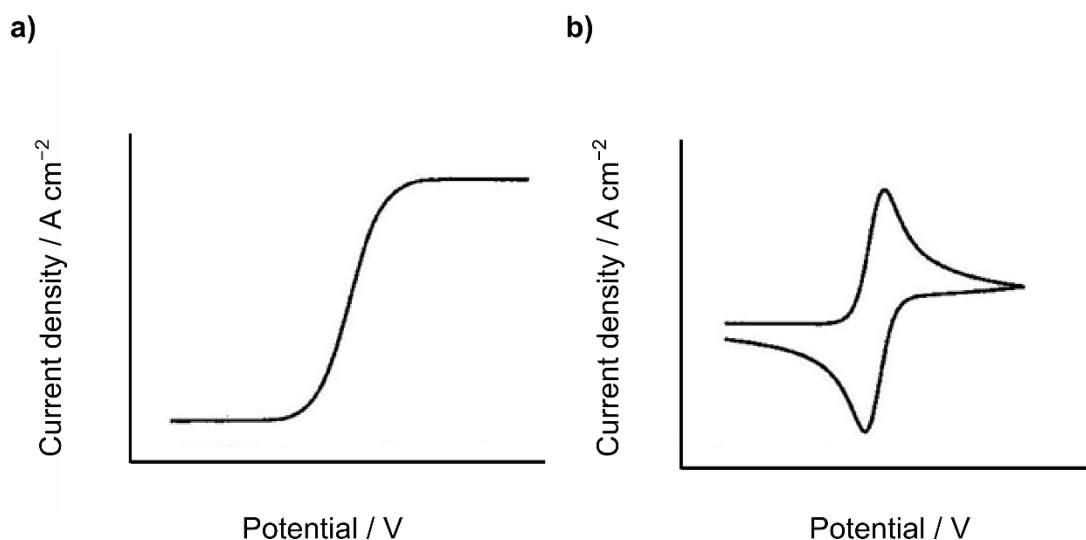


Figure 16 Cyclic voltammetry at a) microdisk, and b) macrodisk electrodes (adapted from reference [187]).

At the microdisk electrode, a sigmoidal current response is observed, whereby the steady-state current (i_{ss} , discussed in the previous sub-section) is rapidly established. On the reverse scan, the current response is often almost overlaid. For this reason, linear sweep voltammetry (where the reverse scan from E_2 to E_1 is absent) is often performed at microdisk electrodes, since the reverse scan does not provide any further information. All further discussion on cyclic voltammetry will assume that the working electrode is a macrodisk.

In stark contrast, at the macrodisk electrode the CV exhibits a well-defined peak for both the forward and the reverse scans. This corresponds to the oxidation of B to A, and the reduction of A back to B. The appearance of a peak results from the depletion of material at the electrode surface, as the current becomes diffusion-limited and decays towards zero (Cottrellian behaviour).

Note that throughout this thesis, a positive current is indicative of an oxidative (anodic) electrode process and a negative current is indicative of a reductive (cathodic) electrode process. The E axis starts are more negative potentials on the left and increasingly positive potentials are found further to the right. This is the current IUPAC recommendation for sign conventions and the plotting of electrochemical data.^[211]

In 1.7.2, electrode kinetics were discussed in terms of the standard electrochemical rate constant (k^0). It was stated that the relative magnitude of k^0 characterises whether an electrochemical process is deemed as electrochemically reversible or irreversible, depending on whether fast or slow electrode kinetics are respectively apparent. Cyclic voltammetry is an excellent tool for determining whether an electrochemical process is reversible or irreversible. **Figure 17** demonstrates how the appearance of a CV changes with different k^0 values (whilst maintaining the other electrochemical parameters constant) for a single-electron oxidation process.

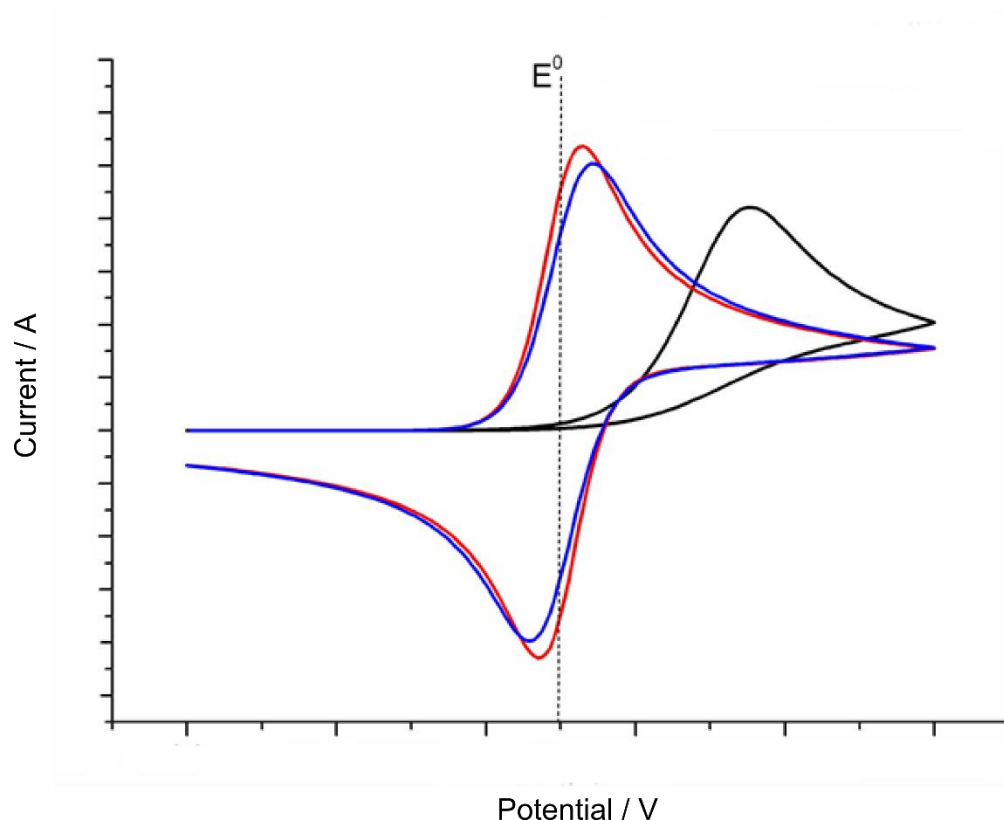


Figure 17 Simulated CVs exhibiting reversible (red line, $k^0 = 1 \text{ cm s}^{-1}$), *quasi*-reversible (blue line, $k^0 = 10^{-2} \text{ cm s}^{-1}$), and irreversible (black line, $k^0 = 10^{-5} \text{ cm s}^{-1}$) behaviour at a macrodisk electrode.

As the relative magnitude of k^0 decreases, the peak-to-peak separation increases until it reaches the irreversible limit. At this limit the peak-to-peak separation is large, and in extreme cases the back-peak is not always observed on the reverse scan. It is important to consider that the majority of systems are *quasi*-reversible; they exhibit reversible-like wave shapes with the back-peak present, but do not conform to the ideal behaviour exhibited at the reversible limit.

When considering the reversibility of an electrochemical process, it is important to consider that the relative magnitude of k^0 is measured against the rate of mass transport. The

rate of mass transport is described by the mass transport coefficient (m_T) which is defined as the ratio of the diffusion coefficient (D) to the diffusion layer thickness (d) (**Equation 18**).

$$m_T = \frac{D}{d}$$

Equation 18 The mass transport coefficient, m_T .

In the reversible limit the rate of the electrode process is much faster than that of diffusion ($k^0 \gg m_T$) whereas in the irreversible limit, the converse is true ($k^0 \ll m_T$). In the irreversible limit, the rate of the electrode process is so slow that the oxidised product diffuses away from the electrode surface before it can undergo reduction back to the reactant.

In the reversible limit, the peak-to-peak separation (ΔE_{pp}) given by the difference between the oxidative and reductive peak potentials ($E_{p,ox}$ and $E_{p,red}$ respectively, shown in **Figure 18**) is 57 mV at 293 K. This is irrespective of the voltage scan rate (v) employed (**Figure 19**); however, for *quasi*-reversible and irreversible processes, ΔE_{pp} is variable and increases with increasing scan rate, v .

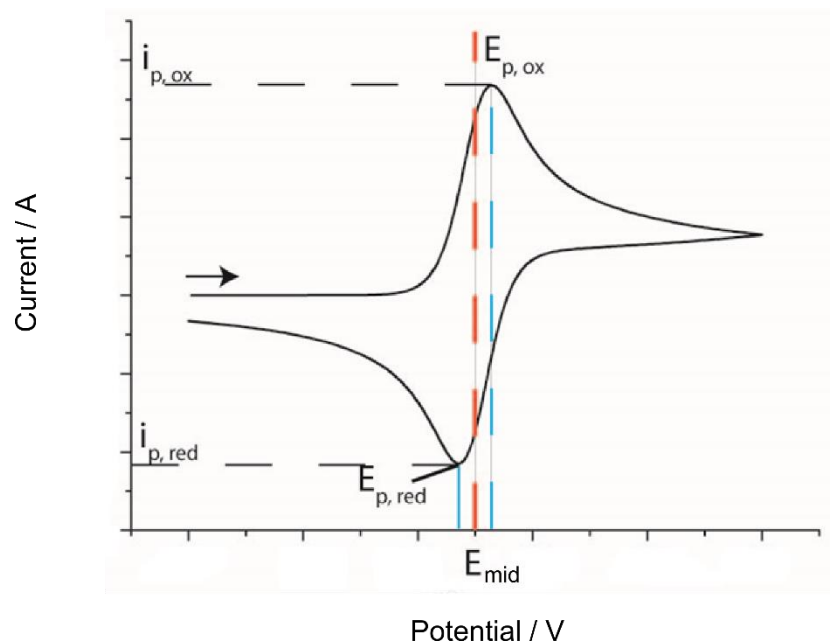


Figure 18 An annotated simulated CV exhibiting reversible behaviour at a macrodisk electrode.

For reversible systems under standard conditions, the average value of the peak potentials (**Equation 19**) is equal to the standard reduction potential (E^0), provided that the charge transfer coefficient $\alpha = 0.5$. However, under non-standard conditions and for *quasi*-

reversible systems, it is cautious to define this value as the mid-peak potential, E_{mid} .^[212] It is a highly important thermodynamic parameter that gauges how readily an electroactive species undergoes oxidation or reduction.

$$E_{\text{mid}} = \frac{E_{p,\text{ox}} + E_{p,\text{red}}}{2}$$

Equation 19 The mid-peak potential (E_{mid}) for a reversible electrode process.

Under reversible conditions, the ratio of the oxidative and reductive peak currents ($i_{p,\text{ox}}$ and $i_{p,\text{red}}$, respectively) are equal ($\frac{i_{p,\text{ox}}}{i_{p,\text{red}}} = 1$). In both the reversible and irreversible limits, the peak current (i_p) is observed to be directly proportional to the square root of scan rate ($\nu^{1/2}$), albeit with a different proportionality constant, if the electroactive species is dissolved in solution and under diffusion control. This effect is demonstrated for a reversible system in **Figure 19**, and the scan rate dependence of peak current is described by the Randles-Sevcik equation (**Equation 20**).

$$i_p = 2.69 \times 10^5 n^{\frac{3}{2}} A D^{\frac{1}{2}} c_{\text{bulk}} \nu^{\frac{1}{2}}$$

Equation 20 The Randles-Sevcik equation describing the dependence of voltage scan rate, ν , on peak current, i_p , for a reversible process operating under diffusion control at 25°C.

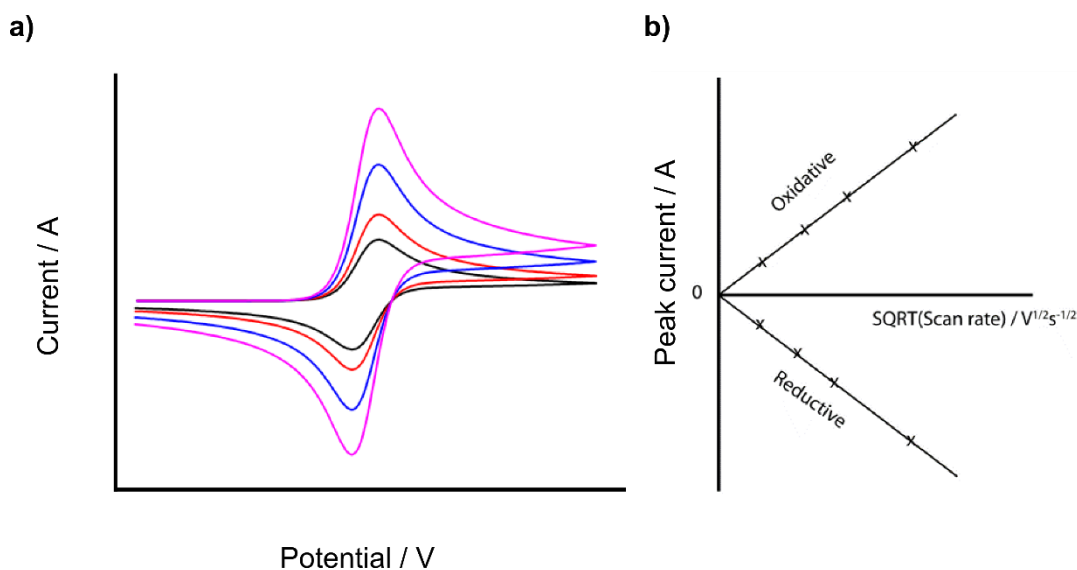


Figure 19 a) Simulated CVs of varying scan rates (v) for a reversible single-electron oxidation, and b) a Randles-Sevcik plot showing the linear relationship of peak current (i_p) with square root scan rate ($v^{1/2}$).

One must note that while peak current increases with voltage scan rate, the total charge passed (Q) remains constant (since $i = \frac{dQ}{dt}$). Since the thickness of the diffusion layer (d) increases with time, it is much thinner at the faster scan rates and the flux of the reactant undergoing electrolysis (at the electrode surface) is much greater. It is also important to note that the $v^{1/2}$ dependence on current is not necessarily linear under *quasi*-reversible conditions.

Finally, it is helpful to summarise this and preceding sub-sections by comparing the voltammetric behaviour of a macrodisk electrode with that of a microdisk electrode (**Table 1**).

Table 1 Comparing the cyclic voltammetric behaviour (mass transport effects) of macro- and microdisk electrodes (adapted from reference [187]).

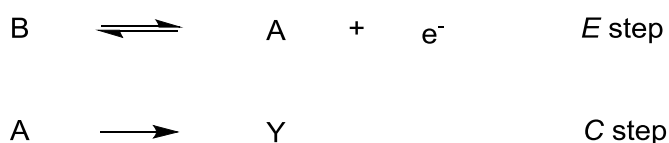
	Electrode geometry	
	Macrodisk	Microdisk ^[a]
<i>d vs r</i>	$d \ll r$	$d \gg r$
Observed response	Defined peak, i_p	Steady-state current, i_{ss}
<i>v</i> dependence?	Yes	No
<i>i</i> dependence	$i_p \propto v^{1/2} D^{1/2} A$	$i_{ss} \propto r D$

[a] Note that this behaviour is applicable at slow to modest scan rates; at very high scan rates, a microdisk electrode may exhibit macrodisk-like behaviour *i.e.* the observation of defined peaks with a scan rate dependence.

1.7.9 Coupled chemical reactions and adsorption

All the previously described systems feature the simple A/B redox couple shown in **Scheme 25**, where A and B are both chemically stable on the timescale of the electrochemical experiment. In reality, this simplistic model does not hold true and homogeneous chemical follow-up steps can be in operation. This is particularly true for the development of electrocatalytic systems, where the electrogenerated species perform an important role rather than sitting stable and dormant in solution. Testa and Reinmuth notation is used to describe the exact mechanism involved in an electrochemical system where multiple electrode processes may be coupled to multiple chemical reactions.^[213] This notation uses the italicised letters *E* and *C* to denote a heterogeneous electron transfer and a homogeneous chemical reaction, respectively. The ordering of the letters describes the specific order of these steps. Using this convention, the simple system involving the A/B redox couple (**Scheme 25**) can be described as an *E* reaction.

The *EC* reaction presents the simplest case of an electrochemical process coupled to a chemical reaction. It denotes that single-electron transfer is followed by chemical reaction of the electrogenerated product to give an electroinactive product. An example of an *EC* reaction is given in **Scheme 26** for the oxidation of B to A, where A undergoes conversion in solution to form electroinactive Y.



Scheme 26 A generic EC reaction. Y is electroinactive.

The cyclic voltammetric behaviour exhibited by such a system is shown in **Figure 20**. The variation of voltage scan rate (ν) provides kinetic information on the rate of the coupled C step. At low scan rates (orange line) one may erroneously assume, at first glance, that the absence of a back-peak suggests that the redox couple is simply electrochemically irreversible (E_{irr}). As the voltage scan rate increases however, the kinetics of the C step are surpassed by the rate at which the potential switches from a value where oxidative current flows to one where reductive current begins to flow. At fast scan rates, species A can be reduced back to B before it undergoes further reaction in solution to form electroinactive Y.

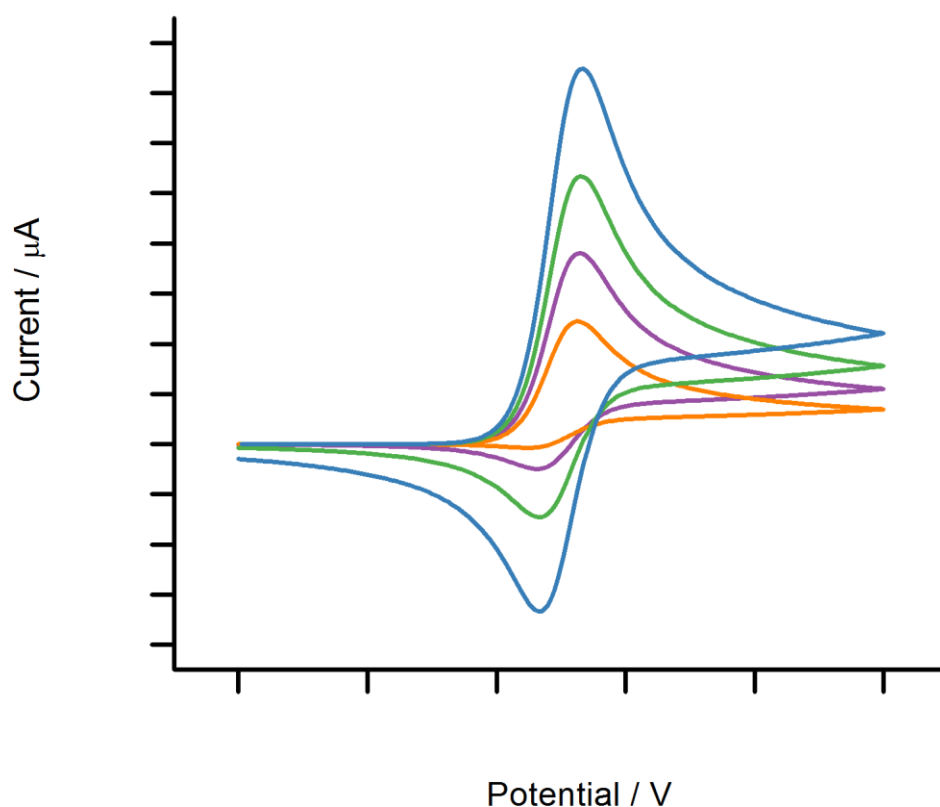
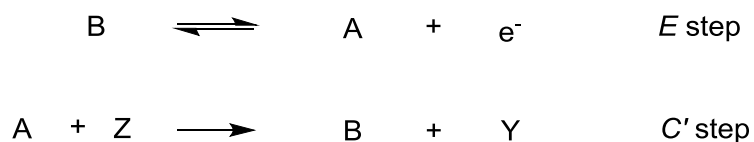


Figure 20 Simulated CVs of varying scan rates (ν) for an oxidative EC process.

An EC' reaction denotes an electrochemical system where the follow-up chemical reaction rapidly regenerates the starting material, rendering the process electrocatalytic. In the example shown in **Scheme 27**, the single-electron electrochemical oxidation of B results in the formation of A, which undergoes a catalytic homogeneous follow-up reaction with electroinactive Z to regenerate B and electroinactive Y.



Scheme 27 A generic EC' reaction. Y and B are electroinactive.

When an underlying EC' mechanism is apparent, the resulting CV may become sigmoidal in appearance (see **Figure 21**) if the rate constant of the C' step is sufficiently large. This is because the rapid and constant regeneration of the electroactive species (B) results in the perceived “infinite flux” of B at the electrode surface. The steady-state current that passes is limited by the kinetics of the electrode reaction and the rate of the catalytic chemical reaction (turnover frequency), which in this case is dependent on the concentration of Z. For many EC' processes with modest catalytic rates, peak shaped voltammetry is still observed, except that either the oxidation or reduction process being catalysed exhibits an enhanced peak current compared to the simple E case in the absence of electrocatalysis, and a correspondingly diminished reverse peak current.

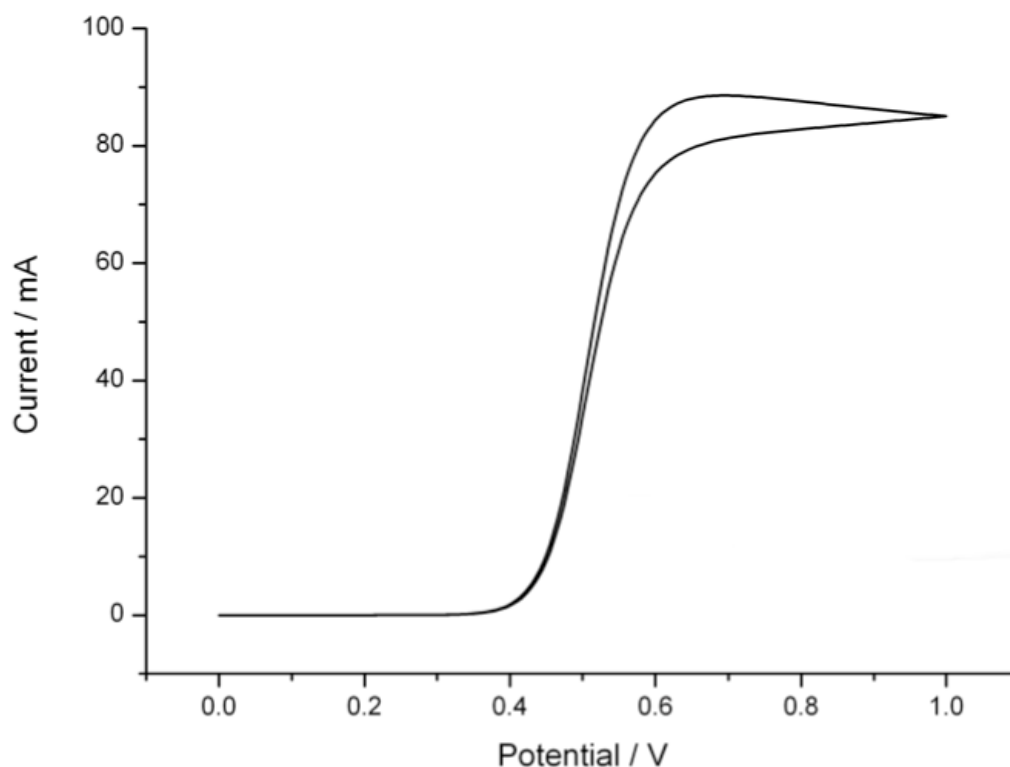


Figure 21 Simulated CV for an oxidative EC' process.

Such an electrocatalytic effect was observed in the cyclic voltammetry of the Fe-based molecular H_2 oxidation electrocatalyst (**4-H**), discussed in 1.5. In the presence of H_2 and added base (*N*-methylpyrrolidine), **4-H** exhibited a catalytic oxidation wave. In this case, the current was limited by the concentration of the added base, and was observed to increase until 44 equivalents of base were added in total. Above this concentration, no significant increase in current was observed with further additions of base; instead, the current was limited by the kinetics of the electrode reaction and the turnover rate.

1.7.10 Simulation of cyclic voltammetric data

The simulation of cyclic voltammetric data allows pertinent kinetic and thermodynamic parameters (E^0 , α , k^0 , k_1 etc.) to be extracted for the heterogeneous electrode reactions and any coupled homogeneous chemical reactions. This information allows the experimental behaviour of an electrochemical system to become well-understood and predictable, aiding in the further development and optimisation of such systems. The accurate simulation of voltammetric data requires the appropriate theoretical models; such models are well-established and have been discussed in the preceding sub-sections.

The simulation of cyclic voltammograms relies on the resolution of the multiple partial differential equations that define mass transport.^[214] This allows the concentration profiles of all the electroactive species present to be modelled as a function of both distance, x , and time, t . From this, the current-potential-time response of the system may then be calculated for a given perturbation in applied potential at the electrode surface. The solution of this mathematical problem may be accomplished using analytical, semi-analytical or numerical methods. Analytical methods are attractive, since they provide exact solutions to mathematical problems. However, the complexity of the electrochemical systems (for example, the presence of multiple electroactive species and follow-up chemical reactions) limits their feasibility. Numerical methods are the best option, and offer very accurate approximations to the true solution through the iterative optimisation of simulated data.

Since Fick's second law (**Equation 13**) is a second order differential equation, its solution is only possible through the introduction of the boundary conditions – conditions that the solutions must meet within specified regions. The first boundary condition concerns the concentration profiles at the beginning of the electrochemical experiment, $t = 0$. If the system is at equilibrium then the concentration of any species is uniform across the solution; the initial condition is expressed by **Equation 21a**. For a planar electrode, the limiting condition is sometimes defined for the furthest point away from the electrode surface. Here, it is assumed that the concentrations of the species are unperturbed and inexhaustible by the electrode reaction, regardless of the experimental time. For the semi-infinite diffusion model, it is assumed that any point on x beyond the diffusion layer (at $x = d$) tends towards the infinite limit expressed by **Equation 21b**. Within the diffusion layer or infinite limit, the concentration and diffusive flux of the electroactive species at the electrode surface is dependent on the applied potential. For a reversible process this can be expressed in terms of the relative rates of the forward (k_f) and reverse (k_b) electrochemical reactions (reduction and oxidation, respectively), as indicated by **Equation 21c**. The potential dependence of the rate constants is described by Butler-Volmer kinetics (discussed in 1.7.2). Mass is conserved applying the condition set out by **Equation 21d**; the flux of product, B, from the surface must be balanced by the flux of reactant, A, to the surface. Where an electroinactive product is generated through homogeneous chemical reactions, *e.g.* as in an *EC* process, the product is assumed to have zero flux at the electrode surface (**Equation 21e**). A simple depiction of the various boundary conditions for an *EC* mechanism is shown in **Figure 22**.

- a) $c(x, t = 0) = c_{\text{bulk}}$
- b) $c(d \rightarrow \infty, t) = c_{\text{bulk}}$
- c) $D_A \left(\frac{\partial c_A}{\partial x} \right)_{x=0} = k_f c_A(x=0) - k_b c_B(x=0)$
- d) $D_A \left(\frac{\partial c_A}{\partial x} \right)_{x=0} = -D_B \left(\frac{\partial c_B}{\partial x} \right)_{x=0}$
- e) $D_{\text{Electroinactive}} \left(\frac{\partial c_{\text{Electroinactive}}}{\partial x} \right)_{x=0} = 0$

Equation 21 General boundary conditions for an electrochemical experiment.

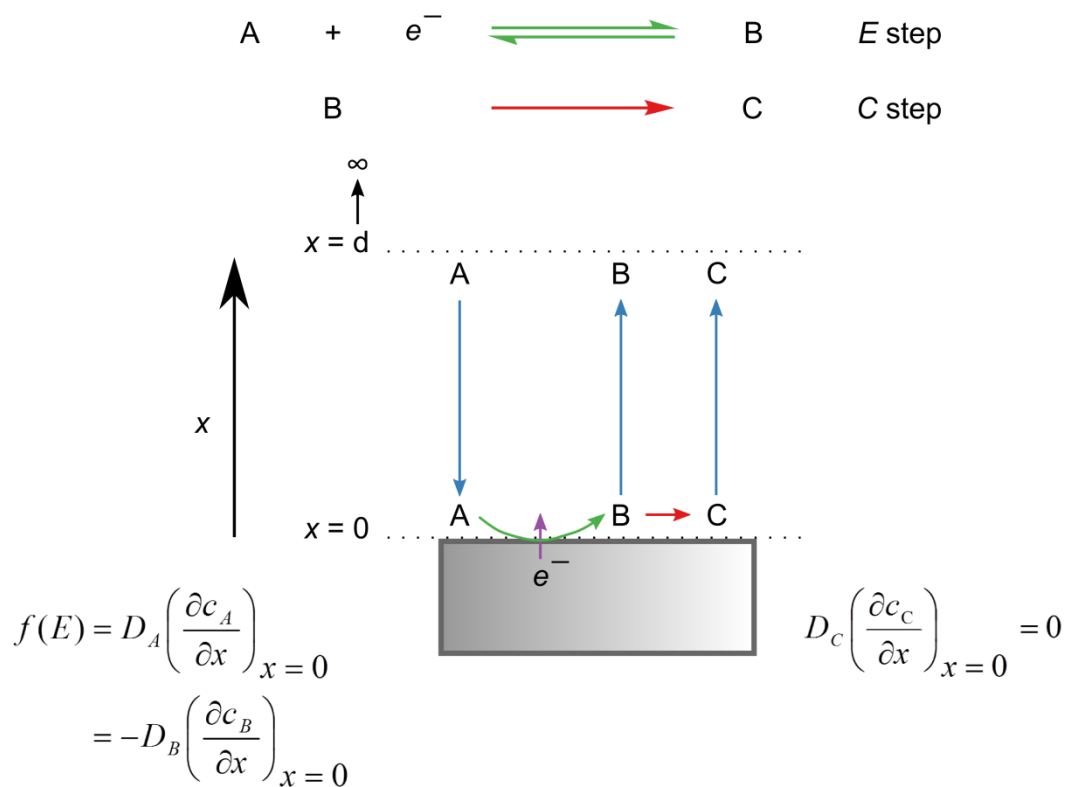


Figure 22 Scheme of the boundary conditions in an electrochemical system involving an EC mechanism.

As well as defining boundary conditions, the number and order of the heterogeneous electron transfer (E) and homogeneous chemical reaction (C) processes must also be defined *e.g.* E , EC , ECE etc. In addition to this, the appropriate electrical perturbation applied must be considered. For example, when attempting to simulate cyclic voltammetric data, the potential of the working electrode and its scan rate (ν) must be taken into account.

Finite difference equations are used as approximations of partial derivatives to model the concentration profiles. Concentration is approximated to be a function of discrete points in time (t) and one-dimensional space (x). Points in the x -direction are assigned as natural numbers $j = 0, 1, 2, 3\dots$ that are spaced Δx apart, whereas points in time are analogously assigned as natural numbers $l = 0, 1, 2, 3\dots$ that are spaced Δt apart. Any point concentration may therefore be described by its j and l values as c_j^l . Thus, finite difference equations for the concentration gradients, $\frac{\partial c}{\partial x}$, between points (*e.g.* $j \pm \frac{1}{2}$) and at a point (*e.g.* j) may be defined by **Equation 22a**, **b**, and **c** respectively. The combination of **Equation 22a** and **b** provides an approximation for the second derivative, $\frac{\partial^2 c}{\partial x^2}$ (**Equation 22d**). An approximation for the change in concentration with time, $\frac{\partial c}{\partial t}$, may also be defined by **Equation 22e**.

$$\begin{aligned}
 \text{a)} \quad & \frac{\partial c}{\partial x} = \frac{c_{j+1}^l - c_j^l}{\Delta x} \\
 \text{b)} \quad & \frac{\partial c}{\partial x} = \frac{c_j^l - c_{j-1}^l}{\Delta x} \\
 \text{c)} \quad & \frac{\partial c}{\partial x} = \frac{c_{j+1}^l - c_{j-1}^l}{2\Delta x} \\
 \text{d)} \quad & \frac{\partial^2 c}{\partial x^2} = \frac{\left(\frac{\partial c}{\partial x}\right)_{j+\frac{1}{2}} - \left(\frac{\partial c}{\partial x}\right)_{j-\frac{1}{2}}}{\Delta x} = \frac{c_{j+1}^l - 2c_j^l + c_{j-1}^l}{(\Delta x)^2} \\
 \text{e)} \quad & \frac{\partial c}{\partial t} = \frac{c_j^l - c_j^{l-1}}{\Delta t}
 \end{aligned}$$

Equation 22 Finite difference equations for the approximation of partial derivatives.

The backward implicit method is frequently used as a numerical method for approximating a set of concentrations in one- and two-dimensional spatial systems. This method applies the described finite difference equations to discretise mass transport. Fick's second law

(Equation 13) can be described by combining Equation 22d and e to give Equation 23a, which can be rearranged to give a set of linear equations (Equation 23b).

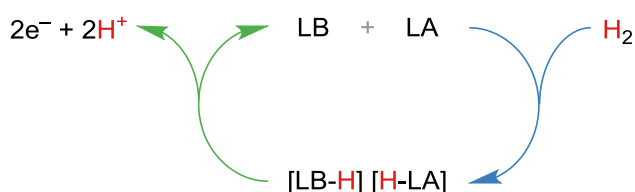
$$\begin{aligned} \text{a)} \quad & \frac{c_j^l - c_j^{l-1}}{\Delta t} = D \frac{c_{j+1}^l - 2c_j^l + c_{j-1}^l}{(\Delta x)^2} \\ \text{b)} \quad & c_j^{l-1} = -\lambda c_{j-1}^l + (2\lambda + 1)c_j^l - \lambda c_{j+1}^l \\ \text{Where:} \quad & \lambda = \frac{D\Delta t}{(\Delta x)^2} \end{aligned}$$

Equation 23 Conversion of Fick's second law into a set of linear equations for the backward implicit method

Any boundary conditions that are applicable for the simulation are then applied and the linear equation is arranged into a matrix equation, which is solved sequentially after inserting the initial bulk concentration values. Multiple iterations will eventually give a steady-state system, where the concentration profile no longer changes with further iterations. This process is repeated for the timescale of the experiment, to build up a description of how the concentration-distance profiles change with time. The diffusional flux of reactant to the electrode surface can be used directly to calculate the current that passes at the working electrode (from the Butler-Volmer equation, Equation 9). From this, a simulated CV can be produced. Owing to the complexity of electrochemical systems, simulation is performed using computational software such as DigiElch,^[215] which can be run on a modern standard desktop computer.

1.8 Aims

My primary aim is to combine the ability of FLPs to “pre-activate” H₂ with the non-aqueous electrochemical oxidation of the resulting borohydride (Scheme 28). It is envisaged that two-electron oxidation of the borohydride will be more energetically favourable than that of H₂ at cheap and ubiquitous carbon electrodes, effectively lowering the potential (driving force) that is required *i.e.* performing electrocatalysis. Assuming that electrooxidation of the borohydride regenerates the Lewis acid (LA), the system should be catalytic *i.e.* fully recyclable, unlike conventional direct borohydride fuel cell technology.^[21,185]



Scheme 28 The electrochemical-FLP approach to the electrocatalysis of H₂ oxidation.

To realize this concept, a thorough electrochemical study of FLPs and electron deficient boron-based Lewis acids is required. An ideal and logical starting point is to study systems based on the archetypal Lewis acid, B(C₆F₅)₃ (**8**).

I aspire to pioneer a new and unique approach to the development of electrocatalysts for H₂ oxidation. Combined electrochemical-FLPs may ultimately find application in the anodic half-cell of a H₂ fuel cell. However, please note that I am not concerned with the fabrication of fuel cell prototypes, nor am I concerned with coupling the H₂ oxidation reaction to the O₂ reduction reaction. Indeed, such attempts would be well beyond the scope of this project and should be reserved for a time when suitable and stable electrochemical-FLP systems have been identified and optimised.

Chapter 2

Results and discussion

Exploring the redox chemistry of $\text{B}(\text{C}_6\text{F}_5)_3$

2.1 Overview

When Massey and co-workers first reported $B(C_6F_5)_3$ (**8**) in 1963,^[216–218] they noted that it had a tendency to form strong adducts with a number of different Lewis bases. The Lewis acidity of **8** was later measured and determined to be intermediate between BF_3 and BCl_3 .^[218–220] Unlike the boron trihalides, however, **8** is a relatively thermally stable solid that exhibits a good resistance to hydrolysis.^[221,222] **8** therefore offers an unprecedented ease of handling, combined with strong Lewis acidity and adequate steric bulk. It is for this reason that Piers and Chivers described **8** as “the ideal boron-based Lewis acid”.^[222]

Aside from its application as an archetypal Lewis acid for FLP applications (as discussed in 1.4), **8** has found numerous applications in synthetic organic transformations,^[223–227] the preparation of weakly coordinating anions,^[228–230] and the activation of olefin polymerization catalysts.^[231–235]

In addition to its interesting Lewis acidic properties, the ability of **8** to act as a one-electron oxidant was accidentally discovered by Norton’s group in 1999.^[236] Erker and co-workers had previously demonstrated that **8** could be used to open zirconocycles to generate effective olefin polymerization catalysts.^[237] When Norton and co-workers attempted to extend this concept to heteroatom-substituted zirconocycles, they noted the partial oxidation of their catalyst. Soon afterwards, Green *et al.* also observed the one-electron oxidation of a η^2 -vinyl molybdenum complex in the presence of **8**.^[238] Norton’s group further investigated the redox properties of **8**; they chemically reduced **8** using the strong reluctant decamethylcobaltocene, $Co^{II}(Cp^{Me_5})_2$ ($Cp^{Me_5} = \eta^5-C_5Me_5$), and studied the resulting $\mathbf{8}^{\bullet-}$ intermediate *via* EPR and UV-vis spectroscopic methods.^[239] The rate of decomposition of $\mathbf{8}^{\bullet-}$ was determined to be *ca* $5.7 \times 10^{-3} s^{-1}$ at 23°C using UV-vis spectrophotometry ($\lambda_{max} = 603 \text{ nm}$).^[239] However, this value should be treated with some caution, given that the experiments were performed in the donor solvent THF and the formation of the **8**·THF adduct is well known (**Figure 23**).^[240–242]

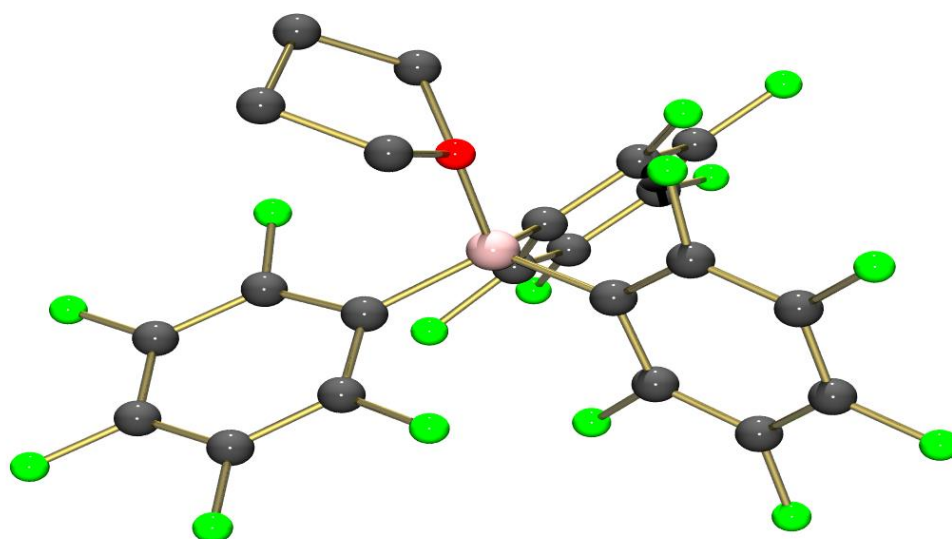


Figure 23 Molecular structure of **8**·THF.^[241]

Despite there being an interest in the redox properties of **8**, its direct electrochemical reduction initially proved to be difficult. Early attempts to record the cyclic voltammetry of **8** were made using either coordinating (donor) solvents, *e.g.* THF, and/or common supporting electrolyte salts of ClO_4^- , PF_6^- or BF_4^- – which can react with electrophilic species such as **8**. These experimental conditions resulted in ill-defined cyclic voltammograms at best, and only enabled predictions of the reduction potential of **8**.^[236,243] In 2011, O'Hare and collaborators (including my supervisor, G. Wildgoose) demonstrated, for the first time, the direct reduction of **8** using cyclic voltammetry.^[244] This was achieved by employing a carefully selected weakly-coordinating electrolyte and solvent system that was composed of Kobayashi's anion, $[^nBu_4N][B\{3,5-(CF_3)_2C_6H_3\}_4]$, and CH_2Cl_2 .^[203] However, no further mechanistic or kinetic studies were undertaken at that time.

This classical Lewis acid is the foundation of my initial work into the development of H_2 oxidation electrocatalysts using a FLP approach. Therefore, it is important that any gap in understanding is addressed before progressing to more complex systems. In this chapter, I report a kinetic and mechanistic study into the one-electron reduction of **8** in two low donor solvents: CH_2Cl_2 and DFB. Electrochemical experiments, combined with digital simulation of voltammetric data, DFT computational studies and multinuclear NMR analysis allow thermodynamic, kinetic and mechanistic information on the redox activity of **8** to be obtained,

whilst also alluding to the fate of the electro-/chemically-generated radical anion, $\mathbf{8}^{\bullet-}$ *i.e.* its decomposition products.

The results contained herein have been published in the journal Dalton Transactions.^[245]

2.2 Electrochemical experiments

The direct voltammetric reduction of $\mathbf{8}$ was explored at a Pt macrodisk electrode using cyclic voltammetry (**Figure 1**). A weakly coordinating electrolyte system composed of a solution of $[^nBu_4N][B(C_6F_5)_4]$ in either CH_2Cl_2 or DFB solvents was selected to avoid any reaction of $\mathbf{8}$ with coordinating solvent or anions of the supporting electrolyte. Similar voltammetric behaviour was observed for both solvents. Upon first scanning (at 100 mV s^{-1}) from the open circuit potential (OCP) towards more negative potentials a reduction wave was observed at -1.82 and $-1.67\text{ V vs }Cp_2Fe^{0/+}$ for CH_2Cl_2 and DFB respectively. There was an absence of the corresponding oxidative back-peak when the scan direction was reversed at slow scan rates ($<500\text{ mV s}^{-1}$). However, at faster scan rates ($500\text{-}5000\text{ mV s}^{-1}$) a small oxidation wave was observable, becoming more pronounced as the scan rate was increased.

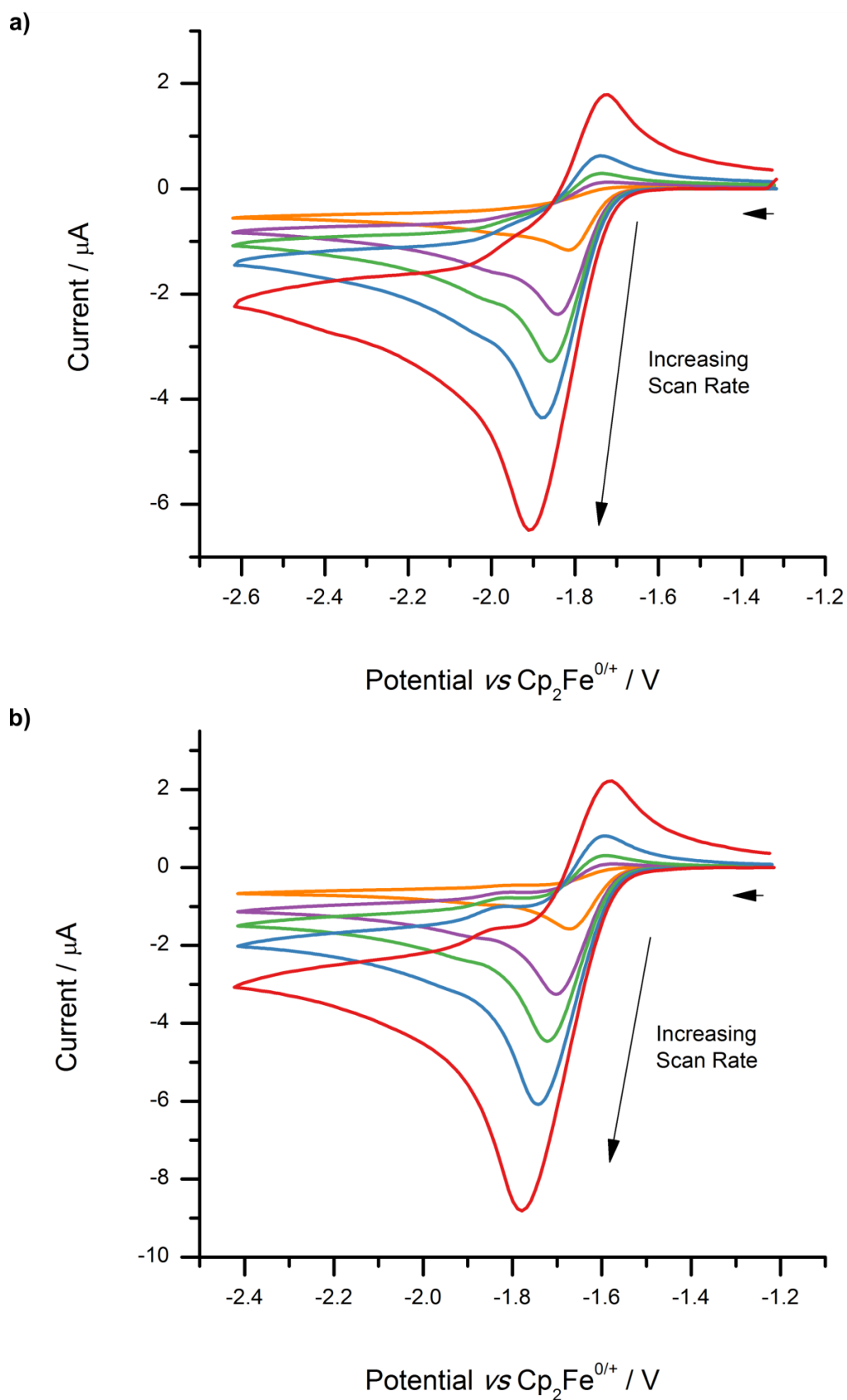
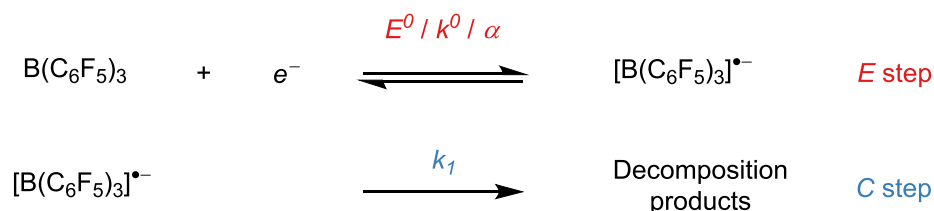


Figure 24 Overlaid CVs of **8** in a) CH_2Cl_2 (5.0 mM) and b) DFB (5.1 mM), recorded at scan rates (v) of 100, 500, 1000, 2000 and 5000 mV s^{-1} at a Pt macrodisk working electrode.

The observed voltammetric behaviour is highly indicative of an underlying *EC* mechanism, when described using Testa-Reinmuth notation.^[213] Initially, **8** undergoes a heterogeneous, electrochemically *quasi-reversible* reduction (*E*-step) at the electrode surface. This is rapidly followed by an irreversible, homogeneous chemical step in the solution (*C*-step) to form electroinactive decomposition products – as evidenced by the absence of any other significant features in the CV. Indeed, it is well-known that radical-chain mechanisms usually gives rise to complex product mixtures, and so it safe to assume that the same is true of $\mathbf{8}^{\bullet-}$. As the scan rate is increased, the kinetics of the chemical follow-up step begin to be outrun on the voltammetric timescale, and the re-oxidation of intermediate $\mathbf{8}^{\bullet-}$ back to the neutral parent compound, **8**, is observed (**Scheme 1**).



Scheme 29 Postulated EC mechanism for the reduction of $B(C_6F_5)_3$, **8**.

On closer inspection, additional small reduction and corresponding oxidation waves are also observed at more cathodic (negative) potentials – ca 200 mV – than the main $B(C_6F_5)_3$ (**8**) reduction peak. Their broad, symmetric wave shape is very characteristic of surface-adsorbed species. In light of the NMR analysis of the reaction products (*vide infra*) this is tentatively attributed to the formation of radical species on the electrode surface during the decomposition process of $\mathbf{8}^{\bullet-}$.

To fully understand the mechanism of **8** reduction, the voltammetric process needs to be digitally simulated. But first, in order to perform this, the number of electrons (n) involved in the reduction process must be determined analytically. The diffusion coefficient (D) of **8** is also required for simulation purposes. Values of n and D were determined simultaneously by performing single potential-step chronoamperometry at a Pt microdisk electrode and numerically fitting the experimental data using the Shoup-Szabo approximation (see 1.7 for further details).^[210] This function accurately predicts the current response at a microdisk electrode over the entire time domain to a maximum error of less than 0.6%.^[210] This is provided that both the concentration of the redox active species and the radius of the microelectrode are accurately known. Chronoamperomograms were recorded for the reduction of **8** in both CH_2Cl_2 and DFB, and are shown in **Figure 25** along with the Shoup-Szabo best fits (which were

determined using Origin™ software^[246]). The fitted data confirm that **8** undergoes single-electron ($n = 1$) reduction in both solvent systems, with diffusion coefficients of $(8.5 \pm 0.1) \times 10^{-6}$ and $(3.9 \pm 0.1) \times 10^{-6} \text{ cm}^2 \text{ s}^{-1}$ for CH_2Cl_2 and DFB respectively. The difference in the value of the diffusion coefficient between CH_2Cl_2 and DFB likely reflects the greater viscosity of DFB compared to CH_2Cl_2 .

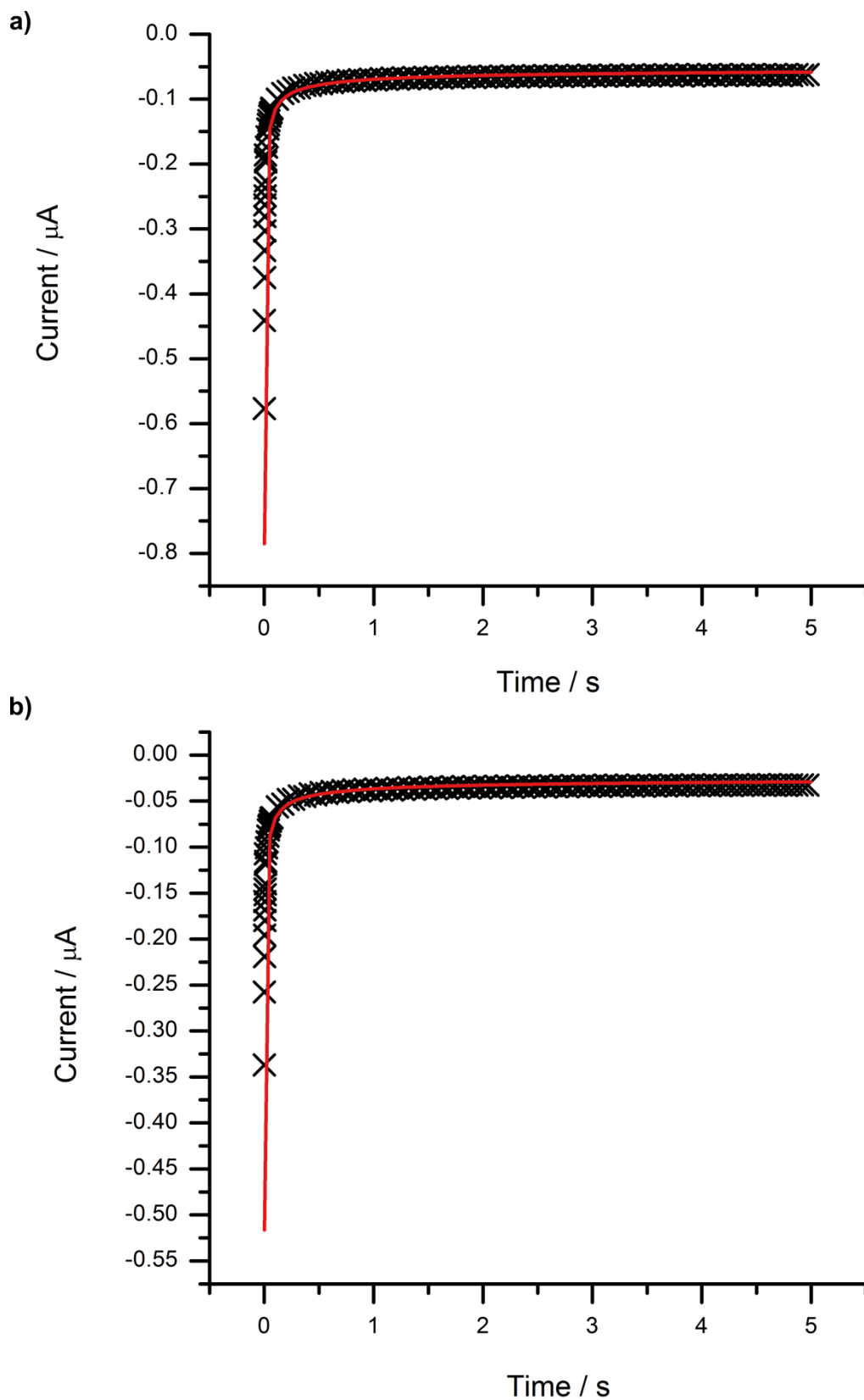


Figure 25 Experimental chronoamperograms (crosses) and Shoup-Szabo best fits (line) for the reduction of **8** in a) CH_2Cl_2 (4.8 mM, 31 μm electroactive radius) and b) DFB (5.0 mM, 30 μm electroactive radius) at a Pt microdisk working electrode.

To further confirm the diffusion coefficients of **8**, steady-state linear sweep voltammetry was performed at Pt microdisk electrodes in both solvent systems (**Figure 26**). Assuming a single-electron reduction process, the diffusion coefficients of **8** can be determined from the measured steady-state current, which is diffusion-limited at microdisk electrode geometries (see 1.6 for further details).^[187] The diffusion coefficient, D , was found to be $(8.4 \pm 0.1) \times 10^{-6}$ and $(4.7 \pm 0.1) \times 10^{-6} \text{ cm}^2 \text{ s}^{-1}$ for CH_2Cl_2 and DFB respectively. Considering the experimental error encountered in accurately measuring a steady-state current, these D values are in excellent agreement with those obtained using chronoamperometry.

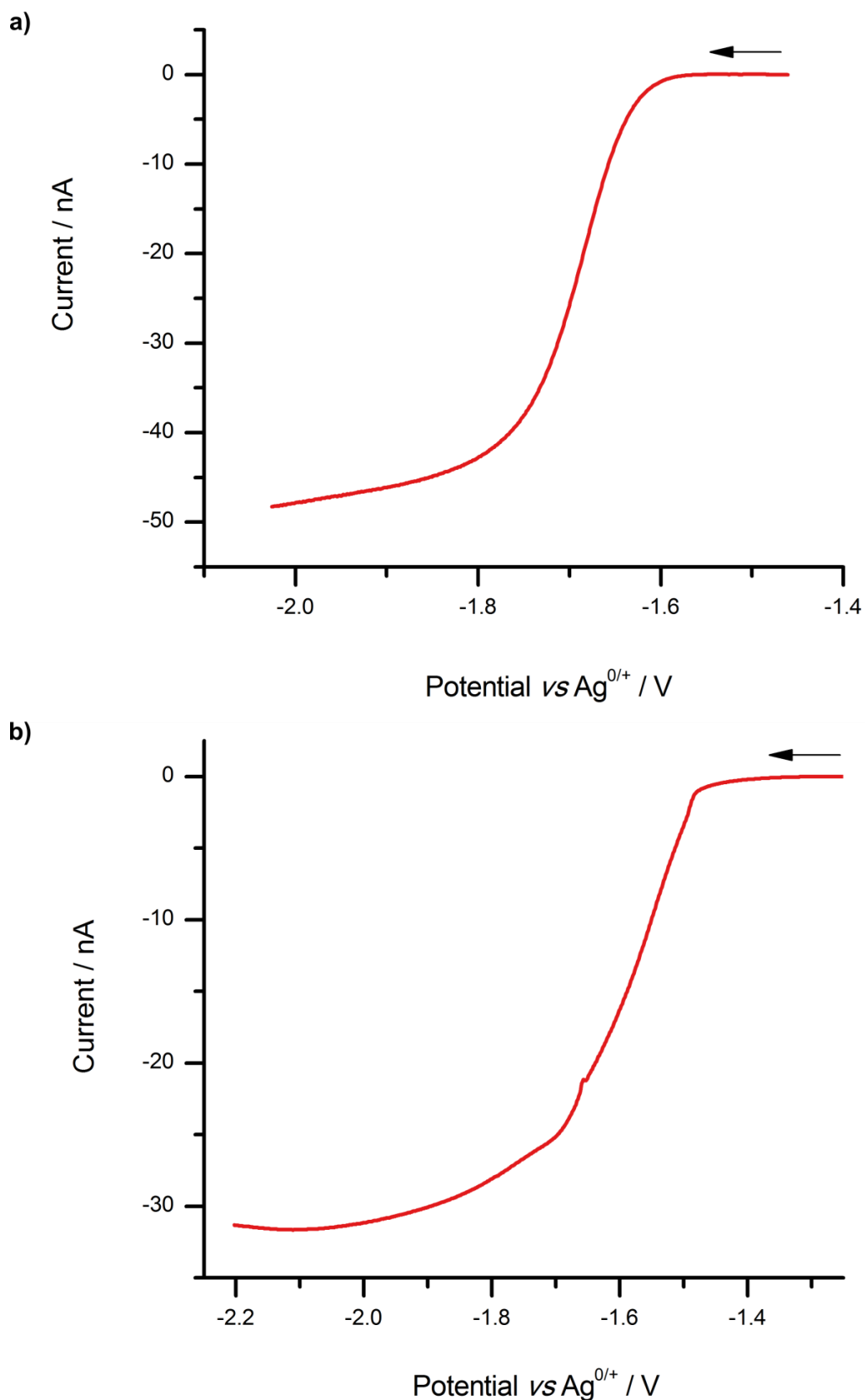


Figure 26 Linear sweep voltammogram for the one-electron reduction of **8** in a) CH_2Cl_2 (4.8 mM, 31 μm electroactive radius) and b) DFB (5.0 mM, 30 μm electroactive radius), recorded at a scan rate of 5 mV s^{-1} at a Pt microdisk working electrode.

2.3 Digital simulation

Having ascertained that **8** undergoes single-electron reduction, along with quantifying its D values in the solvents studied, the next step was to perform digital simulation of the experimentally-observed cyclic voltammetric data in order to extract kinetic and thermodynamic parameters. The voltammetric reduction of **8** produced very good fits between simulation and experiment, as shown in **Figure 27** and **Figure 28**, when modelled as a simple EC process (**Scheme 1**). A variety of other plausible, yet more complex, mechanisms for the decay of $\mathbf{8}^{\bullet-}$ were also simulated. These included its decomposition to form further redox-active products (ECE), disproportionation ($DISP$), and bimolecular radical recombination (EC_2 or EC_2E) mechanisms. However, none of these mechanisms were found to fit the observed voltammetry. The globally optimized parameters for the electrochemical reduction (E^0 , α , and k^0) and the *pseudo*-first order rate constant (k_1) for the homogeneous chemical decomposition step are given in **Table 2** for the best fit obtained (using the EC reaction model).

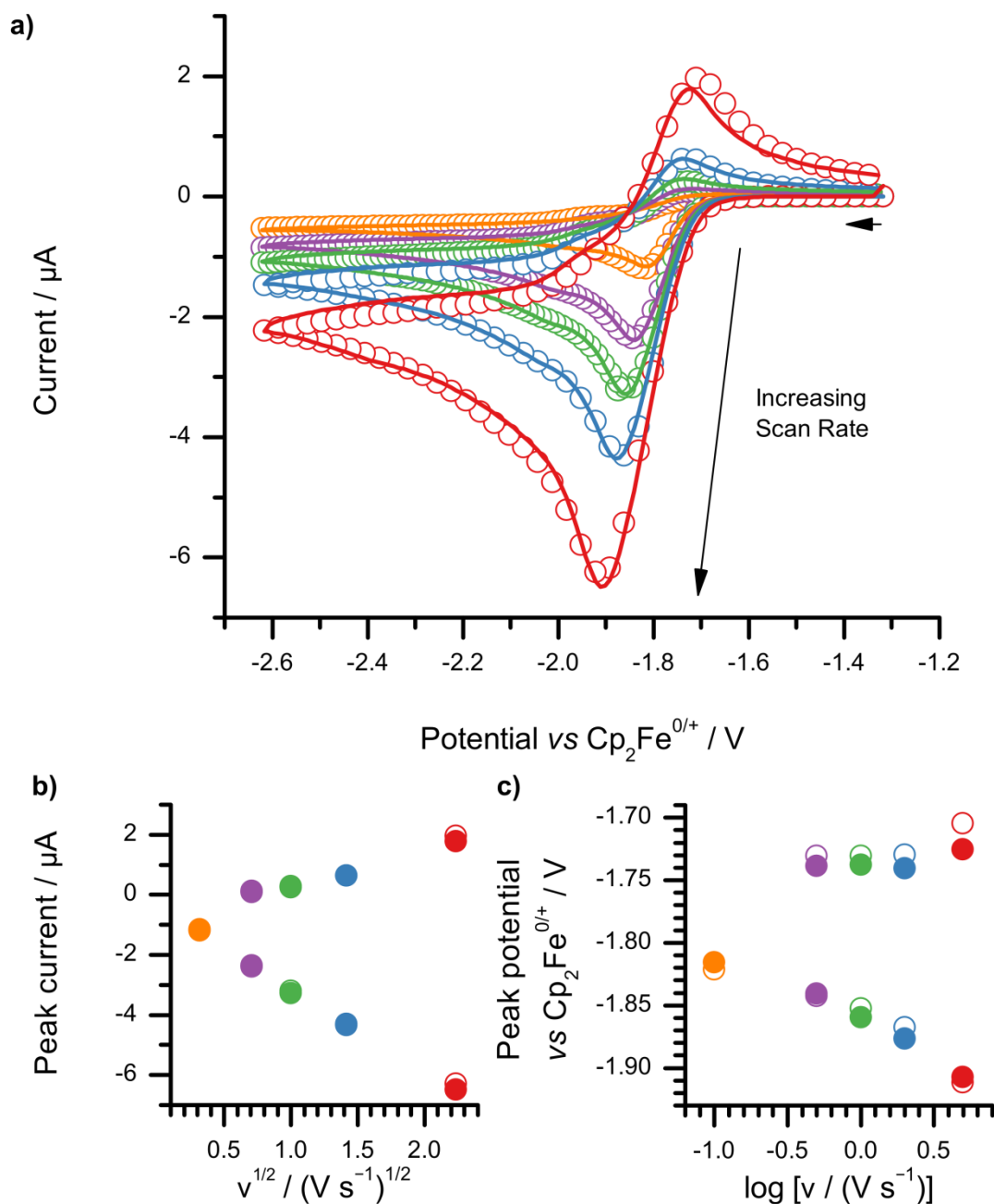


Figure 27 a) Experimental (line) and simulated (open circles) overlaid CVs for the reduction of **8** (5.0 mM) in CH_2Cl_2 at a Pt macrodisk working electrode; b) corresponding Randles-Sevcik plot comparing simulated (open circles) and experimental (closed circles) peak currents against the square root of scan rate (v); c) corresponding Laviron plot comparing simulated (open circles) and experimental (closed circles) peak potentials against the logarithm of scan rate (v). $v = 100, 500, 1000, 2000$ and 5000 mV s^{-1} .

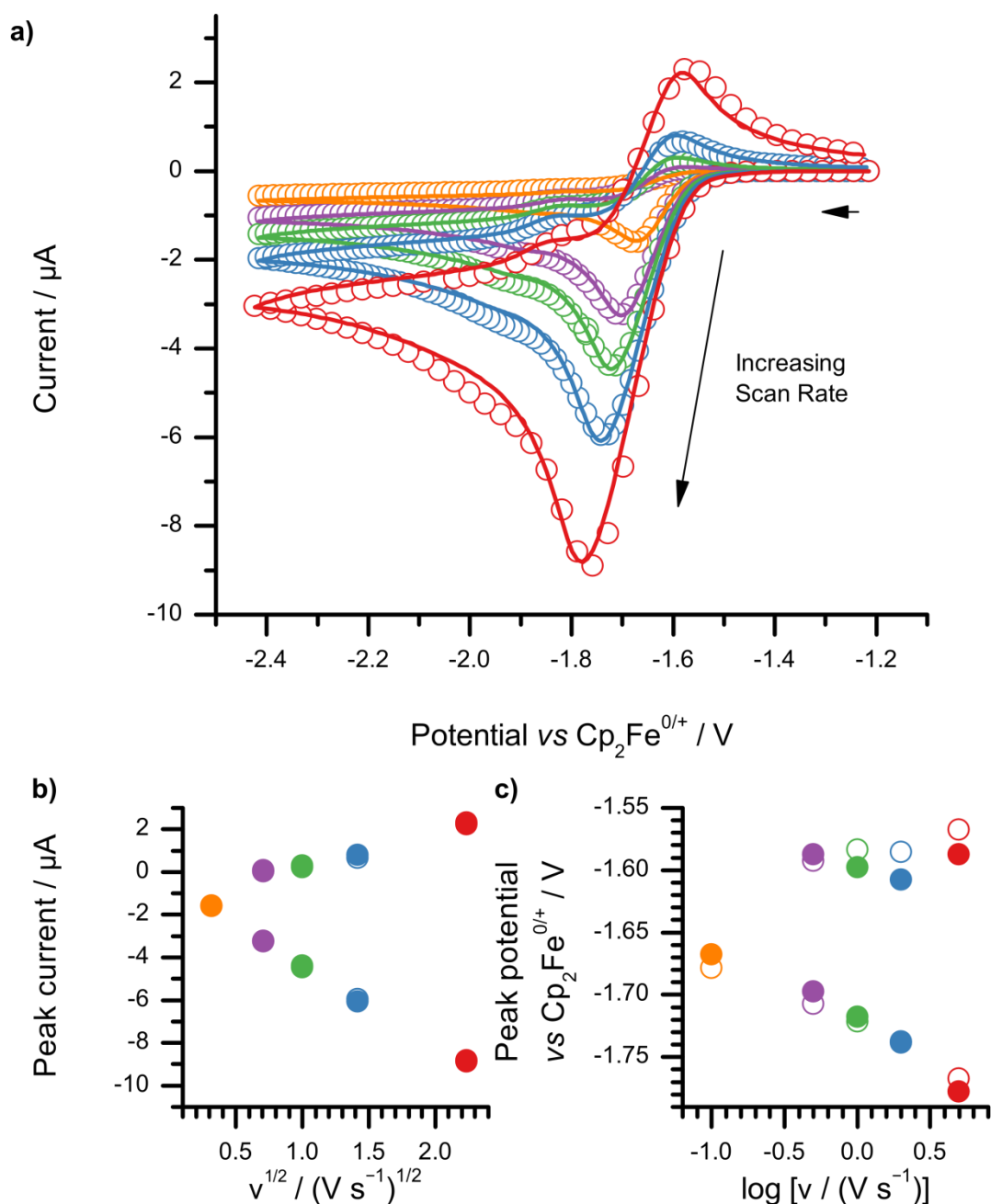


Figure 28 a) Experimental (line) and simulated (open circles) overlaid CVs for the reduction of **8** (5.1 mM) in DFB at a Pt macrodisk working electrode; b) corresponding Randles-Sevcik plot comparing simulated (open circles) and experimental (closed circles) peak currents against the square root of scan rate (v); c) corresponding Laviron plot comparing simulated (open circles) and experimental (closed circles) peak potentials against the logarithm of scan rate (v). $v = 100, 500, 1000, 2000$ and 5000 mV s^{-1} .

Table 2 Simulated parameters for the voltammetric reduction of **8**.

Parameter	CH ₂ Cl ₂	DFB
E^0 vs Cp ₂ Fe ^{0/+} / V	-1.79 ± 0.05	-1.65 ± 0.05
α	0.5 ± 0.05	0.5 ± 0.05
k^0 / 10 ⁻² cm ² s ⁻¹	1.3 ± 0.2	1.1 ± 0.2
$D_{\mathbf{8}}$ / 10 ⁻⁶ cm ² s ⁻¹	8.5 ± 0.1	3.9 ± 0.1
$D_{\mathbf{8}^{\bullet-}}$ / 10 ⁻⁶ cm ² s ⁻¹	8.5 ± 0.1	3.9 ± 0.1
k_1 / s ⁻¹	6.1 ± 0.1	7.7 ± 0.2

The E^0 values for the reduction of **8** were found to be 0.5-0.6 V more negative than the value predicted by Cummings *et al.* during their electrochemical study of the series B(Mes)_{*n*}(C₆F₅)_{3-*n*} (*n* = 1-3).^[243] Their measurements were made in the coordinating electrolyte system, THF/[NBu₄][PF₆], and required the equilibrium constants for THF adduct formation (**8**·THF) to be accounted for. Since these values were crudely estimated by measuring chemical shifts of ¹¹B NMR spectra with varying amounts of THF, and assuming that the chemical shift change between free borane and the THF-bound Lewis adduct is the same for all compounds in their series, it is likely that their predicted E^0 values are inaccurate. Also, the potential for abstraction of F⁻ from the supporting electrolyte was not considered.

The modest value of the standard electrochemical rate constant (k^0) suggests that the reduction of **8** is an electrochemically *quasi*-reversible process. However, the chemical reactivity of **8**^{•-} limits the observation of the corresponding (oxidative) back-peak, except at relatively fast scan rates. **8**^{•-} undergoes a rapid follow-up chemical reaction with *pseudo*-first order rate constants (k_1) of 6.1 ± 0.1 and 7.7 ± 0.1 s⁻¹ in CH₂Cl₂ and DFB respectively. These values obtained in weakly coordinating solvents are approximately three orders of magnitude larger than the decomposition rate constant reported by Norton and co-workers using EPR measurements in the donor solvent, THF.^[239] Indeed the follow-up reaction in CH₂Cl₂ or DFB occurs so rapidly as to preclude any kinetic measurements using EPR techniques. When **8** was reduced using the strong single-electron chemical reductant, Co^{II}(Cp^{Me5})₂ (E^0 = -1.94 V vs Cp₂Fe^{0/+} in CH₂Cl₂)^[247], it was found that the decomposition of **8**^{•-} occurred too rapidly (<5 s) to be able to measure the EPR signal. This was despite my best efforts, including freezing one or both solutions to -196 °C

prior to mixing and then allowing to thaw to -50°C in the spectrometer. Visually, this corresponded to a rapid (almost immediate) colour change from a blue solution to a yellow solution on mixing. This indicated the complete formation of $[\text{Co}^{\text{III}}(\text{Cp}^{\text{Me5}})_2]^+$, even at -78°C .

2.4 Computational modelling of $B(C_6F_5)_3^{\bullet-}$

Given the strong Lewis acidity of **8**, it is somewhat curious to find that k^0 is only of the order of $10^{-2} \text{ cm s}^{-1}$ *i.e.* it exhibits *quasi-reversible* electrode kinetics. To help understand this, DFT computational modelling of the **8** and **8** $^{\bullet-}$ species was performed by V. Oganeyan to ascertain the optimised (gas phase) geometry, singly occupied molecular orbital (SOMO), and comparative charge and spin density distributions. For spin-unrestricted types of calculations, the unpaired molecular orbital of **8** $^{\bullet-}$ is best represented by the SOMO shown in **Figure 29a**. The resulting spin density distribution of **8** $^{\bullet-}$ is shown in **Figure 29b**, and the charge distributions (based on Mulliken electron population analysis) of **8** and **8** $^{\bullet-}$, respectively, are shown in **Figure 30**.

The optimised geometries of **8** and **8** $^{\bullet-}$ reveal little deviation from planarity around the trigonal planar boron centre, although the torsion angle between the aryl rings and the central plane containing the B atom is reduced from 37° , in the case of **8**, to 34° in the **8** $^{\bullet-}$ species. This is due to delocalisation of some spin density onto the C_6F_5 rings, within the SOMO.

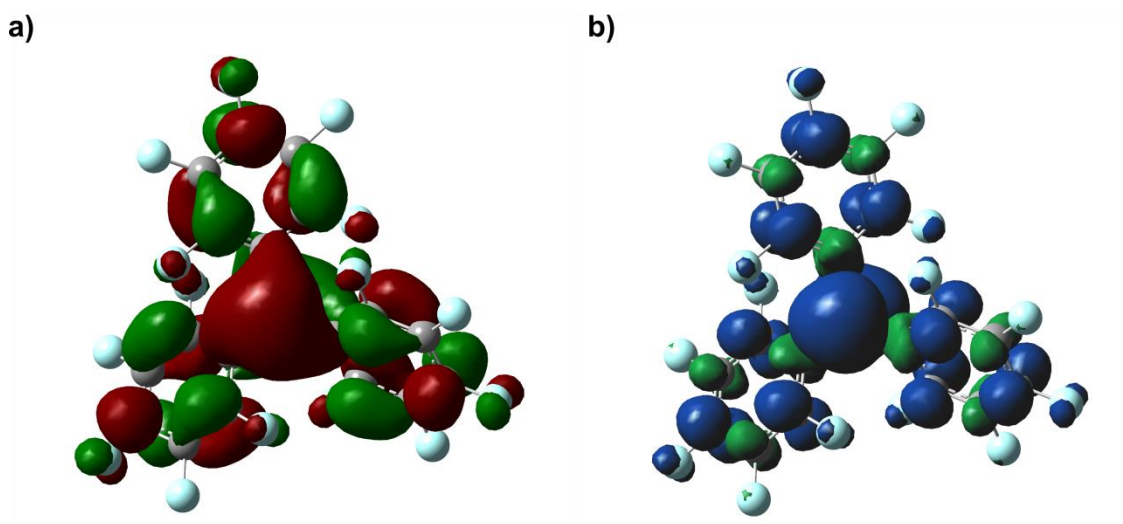
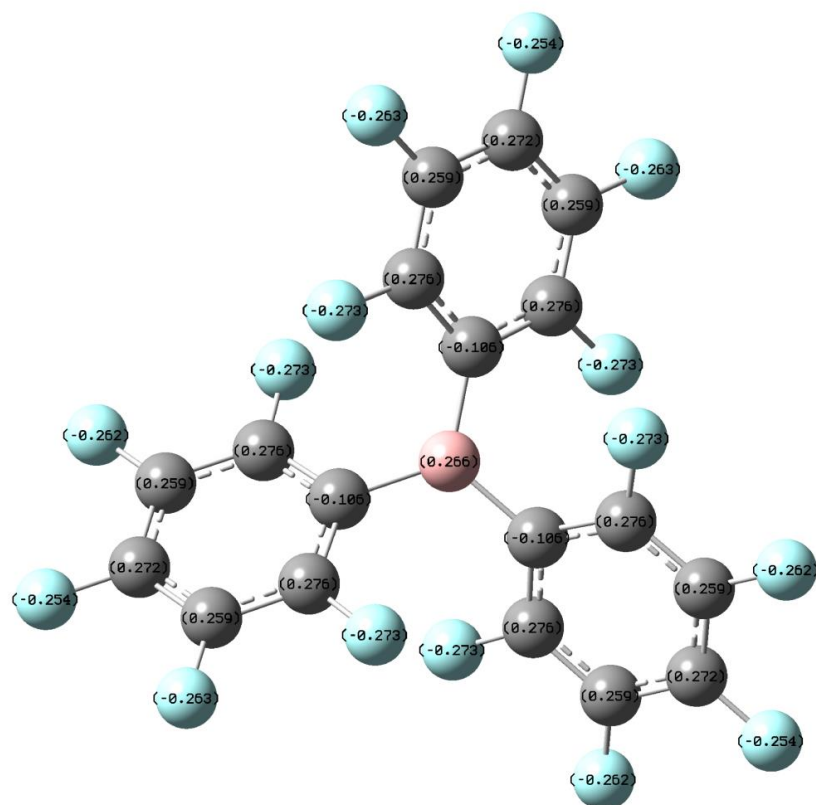


Figure 29 DFT calculated a) SOMO of **8** $^{\bullet-}$ and b) its corresponding spin-density.

a)



b)

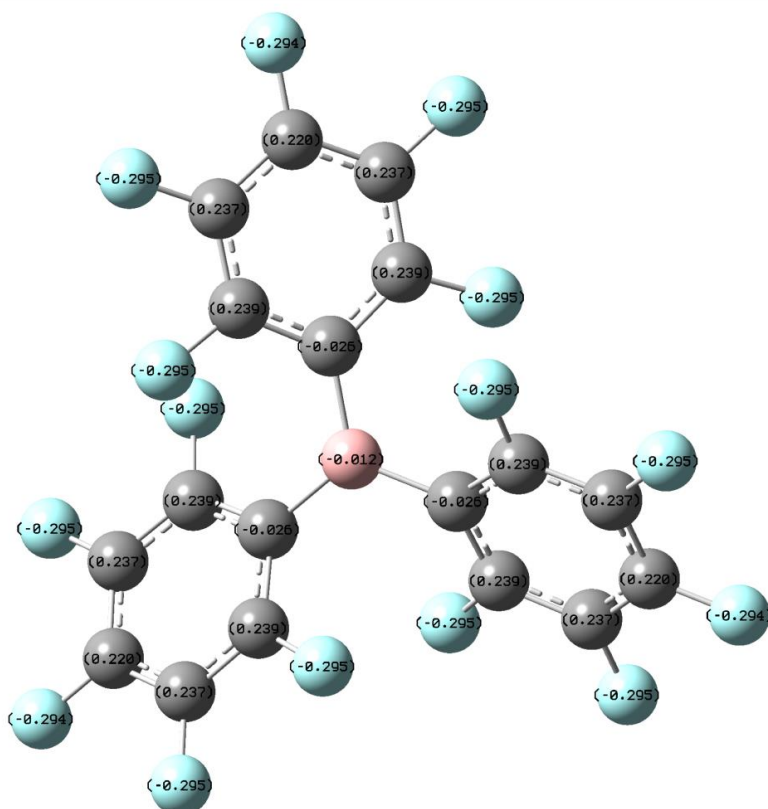


Figure 30 View of the geometry optimized structures of a) **8** and b) **8⁻**. Partial charges are shown for each atom (units are e), based on Mulliken electron population analysis.

The relationship between Marcus theory and Butler-Volmer kinetics was described in 1.7 by **Equation 10**. To reiterate, λ_i describes changes in bond strength and angles during electron transfer, and λ_o depends on contributions from the (dipole) reorientation and electronic polarization of the surrounding solvent molecules.^[187] Given that DFT calculations indicate that there is no significant change between the structures of **8** and **8^{•-}**, one can infer that the solvent reorganisation energy (λ_o) is the rate-limiting factor during electron transfer (**Equation 24**).

$$\alpha = \frac{1}{2} \left(1 + \frac{\Delta G}{\lambda_o} \right)$$

Equation 24 Charge transfer coefficient (α) in terms of Gibbs free energy change (ΔG) and the solvent reorganisation energy (λ_o).

Since the obtained values of α are close to 0.5 in either solvent system (**Table 2**), it is suggested that the reorganisation energy (λ_o) is very much larger than the Gibbs free energy change (ΔG) for this electrochemical process.

DFT modelling shows that when **8** is reduced, both spin and charge density are predominantly localized on the boron-centre of **8^{•-}**. Together with the indication that solvent reorganisation is strongly coupled to the electron transfer, these findings may indicate that the decomposition of **8^{•-}** predominantly proceeds *via* reaction with solvent at the boron centre to form four-coordinate species (*vide infra*).

2.5 Exploring the fate of $B(C_6F_5)_3^{\bullet-}$

Finally, I attempted to elucidate the reaction products that result from the decay of **8^{•-}**, using ^{11}B and ^{19}F NMR spectroscopy. When a colourless solution of **8** (in either CH_2Cl_2 or DFB) was treated with an aliquot of $\text{Co}^{\text{II}}(\text{Cp}^{\text{Me5}})_2$, a deep blue coloured solution was formed, indicative of the generation of **8^{•-}**. The intense blue colour rapidly discharged to give a dark yellow/brown solution upon standing. ^{11}B and ^{19}F NMR spectroscopy was performed directly on the reaction mixture using a C_6D_6 insert. Then, the sample was taken to dryness under vacuum to yield a brown residue, which was taken up in either CDCl_3 or CD_3CN (0.8 mL) for further NMR analysis (and to allow ^{19}F NMR spectra to be obtained for the DFB samples).

The ^{11}B NMR spectrum obtained after the chemical reduction of **8** in CH_2Cl_2 revealed a mixture of five radical decomposition products formed *via* reaction with the solvent. These are listed in **Table 3**. The identity of each product has also been tentatively assigned, where possible, by comparison with known literature compounds.^[117,200,248,249] The doublet observed at $\delta -0.52$

ppm has a coupling constant of 77 Hz, hence I assign this to an as yet unidentified four-coordinate borate species containing one B-H bond (*vide infra*).

Table 3 ^{11}B NMR data and analysis for the reduction of **8** with $Co^{II}(Cp^{Me_5})_2$ in CH_2Cl_2 .

δ / ppm	Multiplicity	Assignment
-0.52	d; $^1J_{B-H} = 77$ Hz	$[HCIB(C_6F_5)_2]^-$ [a]
-3.82	s	$[Cl_2B(C_6F_5)_2]^-$ [248]
-7.04	br. s	$[ClB(C_6F_5)_3]^-$ [249]
-13.40	s	$[B(C_6F_5)_4]^-$ [200]
-25.40	d; $^1J_{B-H} = 92$ Hz	$[HB(C_6F_5)_3]^-$ [117]

[a] Speculative – see text.

The corresponding ^{19}F NMR spectrum of this same sample is complex. Five signals were observed as doublets of multiplets (arising from second-order spin-spin coupling) between δ -132.0 and -135.9 ppm, corresponding to *ortho*-F nuclei on the C_6F_5 rings. A further series of broad overlapping multiplets were observed from δ -162.0 to -165.5 ppm and from δ -165.7 to -168.4 ppm, corresponding to aryl fluorine nuclei in the *para*- and *meta*- positions respectively. Whilst these latter overlapping signals could not be assigned, the *ortho*-F signals are listed in **Table 4** together with their relative product distribution, as determined by integration of the peaks. A tentative assignment has been made by comparison to literature values.^[117,200,248,249]

Table 4 ^{19}F NMR data and analysis for the reduction of **8** with $Co^{II}(Cp^{Me5})_2$ in CH_2Cl_2 .

δ / ppm	Multiplicity	Relative product distribution /%	Assignment
-132.4	dm	39 ± 1	$[ClB(C_6F_5)_3]^-$ [249]
-133.7	dm	14 ± 2	$[HB(C_6F_5)_3]^-$ [117]
-134.4	dm	21 ± 2	$[Cl_2B(C_6F_5)_2]^-$ [248]
-135.4	m	6 ± 1	$[B(C_6F_5)_4]^-$ [200]
-135.8	dm	20 ± 3	$[HCIB(C_6F_5)_2]^-$ [a]

[a] Speculative – see text.

The ^{19}F peak at δ -135.8 ppm is as yet unassigned, but it is likely to correspond to the unidentified product giving rise to the doublet at δ -0.52 ppm in the ^{11}B NMR spectrum. Based on chemical intuition, if one speculates that this signal corresponds to $[HCIB(C_6F_5)_2]^-$ (for which no previous literature characterization data exists) then it forms approximately 20% of the product distribution (based on integration of the ^{19}F NMR signals).

When the reduction of **8** was performed in DFB, three signals were observed in the ^{11}B NMR spectrum at: δ -3.88 (s, unassigned), -13.28 (s, $[B(C_6F_5)_4]^-$) [200], and -0.28 to 1.16 (br. m, unassigned) ppm. The broad multiplet between -0.28 and 1.16 ppm most likely corresponds to several structurally-related products that give rise to overlapping signals. Indeed, a complex series of overlapping multiplets were observed in the ^{19}F NMR spectrum in the range δ -131.7 to -135.4 (*ortho*-F), -161.4 to -164.7 (*para*-F), and -166.0 to -166.6 (*meta*-F) ppm, indicative of multiple products containing fluorinated aryl rings. No significant change in any of the NMR spectra was observed upon exchanging the solvent to $CDCl_3$ or CD_3CN ; this suggests that the decomposition products of $\mathbf{8}^{\bullet-}$ are exclusively four-coordinate boron compounds.

The lack of NMR data in the literature for boron compounds containing $C_6H_4F/C_6H_3F_2$ groups hindered full assignment of the products. Only $[B(C_6F_5)_4]^-$ can be assigned with any certainty. However, given that the rate of decomposition of $\mathbf{8}^{\bullet-}$ is *pseudo*-first order and similar in either solvent system, it is likely that DFB reacts with $\mathbf{8}^{\bullet-}$ in an analogous manner to CH_2Cl_2 – the solvent being in vast excess in both cases. Comparison of the ^{11}B and ^{19}F NMR spectra of authentic samples of $[^nBu_4N][BF_4]$ and $[^nBu_4N][FB(C_6F_5)_3]$ revealed no evidence for the formation of reaction products containing B–F bonds in either the dichloromethane or DFB solvent systems.

Hence, one can speculate that the unidentified (major) products of the decomposition of $\mathbf{8}^{\bullet-}$ in DFB are likely to be borate species of the form $[(C_6F_5)_{3-x}B(C_6H_4F)_x]^-$ ($x = 1-2$). Furthermore, 1H NMR ($CDCl_3$) analysis of the products from either solvent system revealed no evidence for the decomposition of $[Co^{III}(Cp^{Me_5})_2]^+$.

Whilst the decomposition of the $\mathbf{8}^{\bullet-}$ radical anion *via* reaction with solvent may not be surprising, the key point to note is that, in contradiction to Norton's earlier suggestion,^[239] $[Co^{III}(Cp^{Me_5})_2][B(C_6F_5)_4]$ is only a minor product of this reaction (approximately 5%). Further, whilst CH_2Cl_2 is known to be prone to radical attack, DFB is usually considered to be less susceptible.^[204] Yet, the $\mathbf{8}^{\bullet-}$ radical anion intermediate must be sufficiently reactive enough to decompose at a similar rate in either weakly-coordinating solvent.

Interestingly mass spectrometry of the reaction products from either DFB or CH_2Cl_2 only detected one product with molecular ion peaks at m/z values at 678.90 (100%, M^-), 677.80 (24.98%) and 679.90 (25.75%) Da. This is highly indicative of $[B(C_6F_5)_4]^-$; however, given the likelihood of fragmentation and recombination reactions in the mass spectrometer this observation must be interpreted with some caution.

2.6 Summary

The direct voltammetric reduction of $\mathbf{8}$ was studied in two weakly coordinating solvents, CH_2Cl_2 and DFB. In either case, cyclic voltammetry combined with digital simulation indicated that the electrochemical process follows an *EC* mechanism. Electrogenerated $\mathbf{8}^{\bullet-}$ undergoes a rapid chemical decomposition step in solution to form redox inactive products. Multinuclear NMR analysis of these products was obtained through the chemical reduction of $\mathbf{8}$ with $Co^{II}(Cp^{Me_5})_2$. The NMR data is indicative of the formation of several four-coordinate borate species, arising from radical reaction pathways. Hence, the reaction of solvent with $\mathbf{8}^{\bullet-}$ predominantly occurs at the boron centre; this observation is further supported by spin density and charge distribution calculations on the SOMO of $\mathbf{8}^{\bullet-}$.

Chronoamperometry at a microdisc electrode confirmed that the reduction of $\mathbf{8}$ is indeed a one-electron process. Diffusion coefficients were quantified for $\mathbf{8}$ in each of the solvents used.

Digital simulation of the voltammetric data enabled the *pseudo*-first order rate constants for the chemical decomposition of the $\mathbf{8}^{\bullet-}$ radical anion to be determined. The standard reduction potentials, E° , for $\mathbf{8}$ were determined to be -1.79 ± 0.1 V and -1.65 ± 0.1 V vs $Cp_2Fe^{0/+}$ in CH_2Cl_2 and DFB respectively.

The rate of decomposition of the radical anion is sufficiently fast in solvents of low donor strength that I was unable to measure a signal from $\mathbf{8}^{\bullet-}$ using EPR spectroscopy, even at low temperatures – in stark contrast to previous reports using strong donor solvents.^[239]

Thus, after more than fifty years since the discovery of $\mathbf{8}$, pertinent thermodynamic and kinetic parameters relating to its redox properties in selected weakly-coordinating electrolyte systems have been reported for the first time. Once again, one must emphasise the importance of carefully considering the choice of solvent when attempting to study the redox chemistry of highly electrophilic and Lewis acidic species.

This results chapter establishes the foundation for my initial work into the development of H_2 oxidation electrocatalysts using a FLP approach. Now that the fundamental electrochemical properties of $\mathbf{8}$ have been established, one can begin to explore the electrochemistry of (relatively) more complex FLP systems that feature $\mathbf{8}$ as the key component.

Chapter 3

Results and discussion

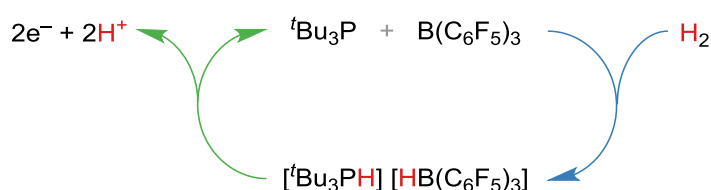
The first electrochemical study
of frustrated Lewis pairs

3.1 Overview

In Chapter 2, a kinetic and mechanistic study into the one-electron reduction of **8** in the low donor solvents, CH₂Cl₂ and DFB, was discussed. This included the extraction of thermodynamic and kinetic parameters relating to the observed electrochemical behaviour of **8**; the fate of the radical anion, **8**^{•-}, was also explored.

This chapter builds upon the fundamental work of Chapter 2, by beginning to explore the electrochemistry of FLPs. Following on from his initial success of discovering the first FLP system,^[112] Stephan's group soon incorporated **8** into an intermolecular FLP system.^[117] Through the combination of **8** with a suitably strong, yet sterically bulky Lewis base (^tBu₃P, **12**) they were able to heterolytically cleave H₂ to give a salt, [**8**-H][H-**12**], containing both hydridic and protic components. When one considers the extensive application of **8** in FLP chemistry,^[121,122,250,251] it makes perfect sense to start with systems based on **8** when beginning to explore the electrochemical properties of FLPs.

Here, I introduce a new approach that combines classical FLP chemistry with non-aqueous electrochemical oxidation of the resulting borohydride. The overall aim for the project (see 1.8) is to develop a system that uses a FLP to pre-activate H₂ and form hydridic and protic components. The hydridic component is then electrochemically oxidized to give H⁺ and 2e⁻, whilst regenerating the Lewis acidic component of the FLP. The system will ideally effect the net electrocatalytic conversion of H₂ into 2H⁺ and 2e⁻ (at much reduced potentials than that of H₂).



Scheme 30 The proposed electrochemical-FLP concept: electrooxidation of the H₂-activated **8/12** FLP results in the net generation of two protons and two electrons.

This chapter initially focusses on the electrochemical study of [**8**-H]⁻ using an authentic sample, before progressing towards *in situ* H₂ activation using the paradigm **8/12** FLP system. Here, I demonstrate that this approach allows for a significant reduction in the potential (the required energetic driving force) for non-aqueous H₂ oxidation at inexpensive and ubiquitous glassy carbon electrodes (GCEs). To the best of my knowledge, this is the first time that FLPs have been directly used for the electrochemical activation of small molecules. The results

contained in this chapter have been published in the Journal of the American Chemical Society.^[252]

3.2 Authentic $[\text{HB}(\text{C}_6\text{F}_5)_3]^-$

For initial electrochemical studies, an authentic sample of $[\text{}^n\text{Bu}_4\text{N}][\text{HB}(\text{C}_6\text{F}_5)_3]$ ($[\text{}^n\text{Bu}_4\text{N}][\mathbf{8}\text{-H}]$) was prepared by treatment of **8** with the strong hydride donor, $\text{Na}[\text{HBEt}_3]$, to generate $\text{Na}[\mathbf{8}\text{-H}]$; the resulting hydride was then metathesised with $[\text{}^n\text{Bu}_4\text{N}]\text{Cl}$ to give the product containing the hydridic component ($[\mathbf{8}\text{-H}]^-$) of the H_2 -activated FLP, **8/12**. The reason for substituting $[\mathbf{12}]^+$ for $[\text{}^n\text{Bu}_4\text{N}]^+$ is two-fold. Firstly, the electrochemical reduction of a phosphonium moiety has previously been reported by Stephan and co-workers.^[183] Since I was only concerned with the electrochemical properties of $[\mathbf{8}\text{-H}]^-$, I wanted to select an redox-innocent cation. $[\text{}^n\text{Bu}_4\text{N}]^+$ seemed to be an excellent choice, given that it is commonly used as an electrolyte and has a large potential window.^[195] Secondly, $[\text{}^n\text{Bu}_4\text{N}]^+$ imparts considerable solubility to $[\mathbf{8}\text{-H}]^-$ in the weakly-coordinating electrolyte systems, and assuming that there is no considerable ion-pairing (for the purpose of the experiment), $[\text{}^n\text{Bu}_4\text{N}]^+$ simply becomes a component of the electrolyte system.

$[\text{}^n\text{Bu}_4\text{N}][\mathbf{8}\text{-H}]$ was characterized by spectroscopic methods and X-ray crystallography. The spectral data for $[\mathbf{8}\text{-H}]^-$ is consistent with that reported by Welch and Stephan for $[\mathbf{8}\text{-H}][\mathbf{H}\text{-12}]$ – the product of FLP H_2 activation by **8/12**. The crystal structure of $[\text{}^n\text{Bu}_4\text{N}][\mathbf{8}\text{-H}]$ is shown in **Figure 31**. Colourless plates, suitable for X-ray crystallography, were grown by dissolving $[\text{}^n\text{Bu}_4\text{N}][\mathbf{8}\text{-H}]$ in a minimum quantity of CH_2Cl_2 , warming to 35°C , adding an equal quantity of light petroleum ether and then allowing the solution to cool slowly to room temperature. X-ray diffraction data were collected by the EPSRC National Crystallography Service and data solution and refinement was performed by Dr. D. Hughes. Crystallographically, two components were observed for the anion in a 92:8 ratio, with negligible structural differences; all further discussions are based on the major component. In $[\mathbf{8}\text{-H}]^-$, the geometry about the boron centre is tetrahedral, deviating from the idealised bond angle of 120° , expected for the trigonal planar geometry of **8**, to bond angles ($^\circ$) of 109.9(2), 112.18(19) and 115.47(19) for C11-B1-C21, C11-B1-C31, and C21-B1-C31 respectively. The hydride itself was clearly explicitly observed. The three C_6F_5 aryl rings have a propeller-like conformation about the B-H axis as illustrated by the torsion angles ($^\circ$) of the aryl rings about the B-H plane, which were found to be 45.4, 21.7 and 40.0. The average value for the torsion angles (approximately 36°) is close to the calculated value for the DFT-optimized geometry of **8** in 2.2. For **8**, the torsion angle between the aryl rings and

the central plane containing the B atom was found to be 37°, whereas in the radical anion, $\mathbf{8}^{\bullet-}$, the torsion angle was found to be 34°.

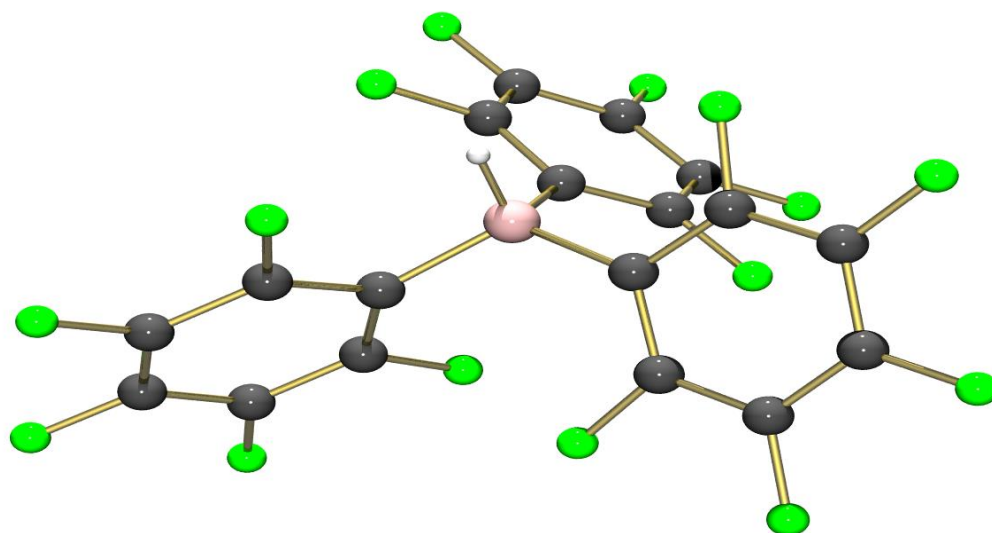


Figure 31 Molecular structure of $[\mathbf{8-H}]^-$ (only the anion and its major conformation are shown).

3.3 Initial electrochemical studies

The preparation of $[\text{}^n\text{Bu}_4\text{N}][\mathbf{8-H}]$ allowed a detailed electrochemical study into the redox behaviour of $[\mathbf{8-H}]^-$ to be undertaken. Much the same as my previous electrochemical study of $\mathbf{8}$ (Chapter 2), a weakly coordinating electrolyte system comprising $[\text{}^n\text{Bu}_4\text{N}][\text{B}(\text{C}_6\text{F}_5)_4]$ in CH_2Cl_2 was selected for all electrochemical studies to minimize the decomposition of any electrogenerated Lewis acids (such as $\mathbf{8}$).^[203,244]

The direct voltammetric oxidation of $[\text{}^n\text{Bu}_4\text{N}][\mathbf{8-H}]$, at varying concentrations, was performed at a macrodisk GCE using cyclic voltammetry (**Figures 32-34**). On sweeping the potential anodically (to more positive potentials) from the OCP at a scan rate of 100 mV s^{-1} , an oxidative wave was initially observed at $+0.88 \pm 0.01 \text{ V vs Cp}_2\text{Fe}^{0/+}$. On reversing the scan direction, no corresponding back-peak was observed. However, a small reduction wave (again, with no observable back-peak) was sometimes observed at $-1.59 \text{ V vs Cp}_2\text{Fe}^{0/+}$ (**Figure 32**). Both the oxidation wave and the reduction wave are characteristic of two related *EC* processes. The large oxidation current of the oxidation wave can be initially assigned to the two-electron oxidation of $[\mathbf{8-H}]^-$ to form H^+ and regenerate the parent Lewis acid, $\mathbf{8}$. The reduction wave is thereby assigned to the single-electron reduction of $\mathbf{8}$ (see Chapter 2).^[243] The unpredictable nature of this small and very ill-defined reduction wave is likely to result from the susceptibility

of **8** to undergo decomposition in the presence of any electrogenerated protons. Of course, it is also known that the any generation of transient $\mathbf{8}^{\bullet-}$ will lead to some loss of **8** through reaction with the solvent (see Chapter 2).

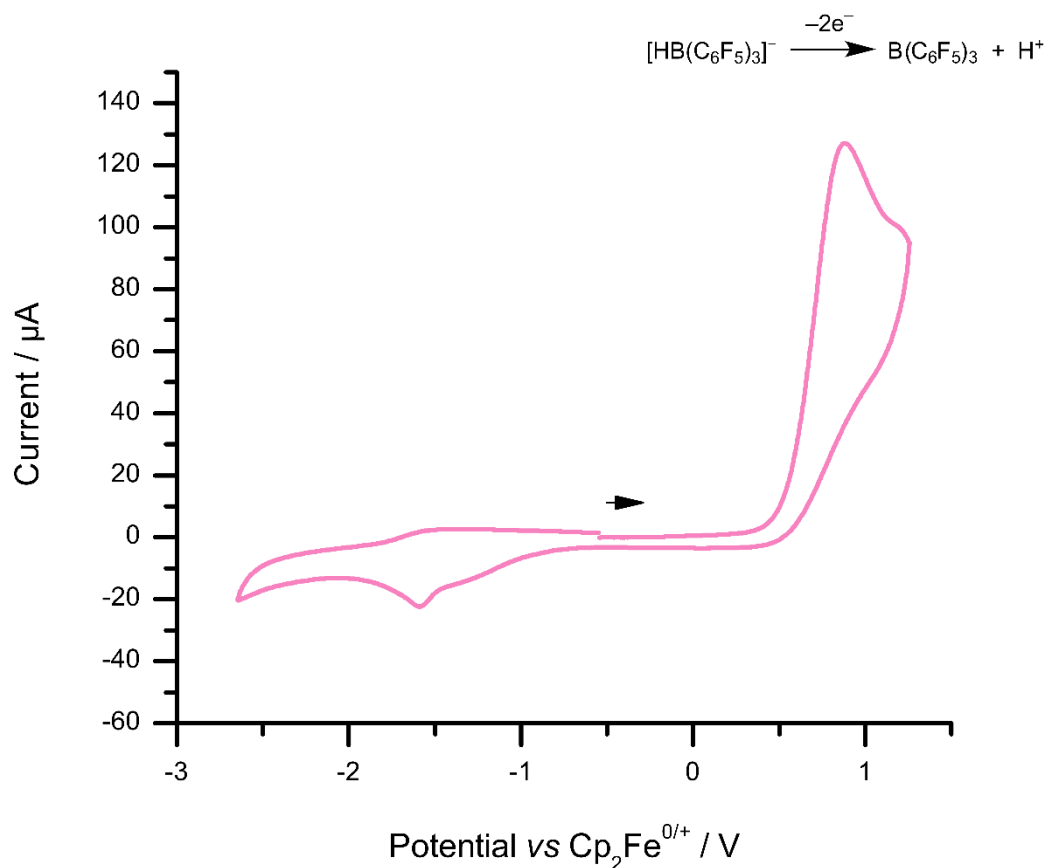
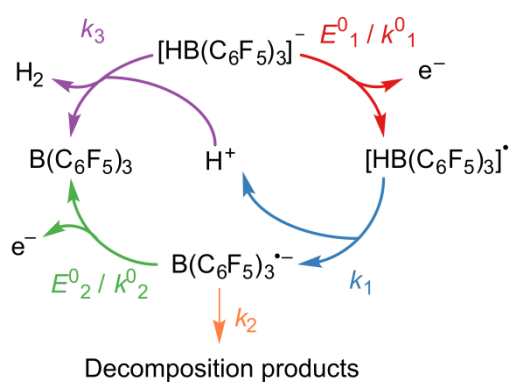


Figure 32 CV of a 4.9 mM solution of $[\text{nBu}_4\text{N}][\mathbf{8}\text{-H}]$ in CH_2Cl_2 recorded at voltage scan rate of 1000 mVs^{-1} over the full potential window on a GCE.

The observed voltammetry can be explained by the mechanism proposed in **Scheme 31**, which is supported by excellent fit between simulation and experiment at two different concentrations of $[\text{nBu}_4\text{N}][\mathbf{8}\text{-H}]$ (**Figures 33-34**), and detailed chemical and density functional theory (DFT) studies (see 3.4 and 3.5, *vide infra*). The globally optimized parameters describing the oxidation of $[\mathbf{8}\text{-H}]^-$ (**Table 5**) were obtained from digital simulation of the experimental CVs, whilst the parameters describing the reduction of **8** are taken directly from Chapter 2.

Initially, $[\mathbf{8}\text{-H}]^-$ undergoes *quasi*-reversible single-electron oxidation at the electrode surface to form $[\text{HB}(\text{C}_6\text{F}_5)_3]^\bullet$ ($[\mathbf{8}\text{-H}]^\bullet$). This electrogenerated species is transient and rapidly dissociates to give H^+ and $\mathbf{8}^{\bullet-}$. As explored in Chapter 2, $\mathbf{8}^{\bullet-}$ exhibits its own redox chemistry and therefore undergoes single-electron oxidation to generate the parent Lewis acid, **8**. Of course, $\mathbf{8}^{\bullet-}$ is susceptible to reaction with the solvent; however, since the reduction potential of the $\mathbf{8}/\mathbf{8}^{\bullet-}$

is much lower than that of $[\mathbf{8}\text{-H}]^-$, the electrooxidation of $[\mathbf{8}\text{-H}]^-$ can be almost considered as a two-electron process (leading to oxidative currents being observed). A competing side-reaction between electrogenerated H^+ and incoming $[\mathbf{8}\text{-H}]^-$ regenerates H_2 and $\mathbf{8}$. This, along with small contributions from the decay of $\mathbf{8}^{\bullet-}$, reduces the observed current to slightly less than that expected for a simple two-electron process.



Scheme 31 Proposed mechanism and associated thermodynamic and kinetic parameters used to simulate the oxidation of $[\mathbf{8}\text{-H}]^-$ at a GCE.

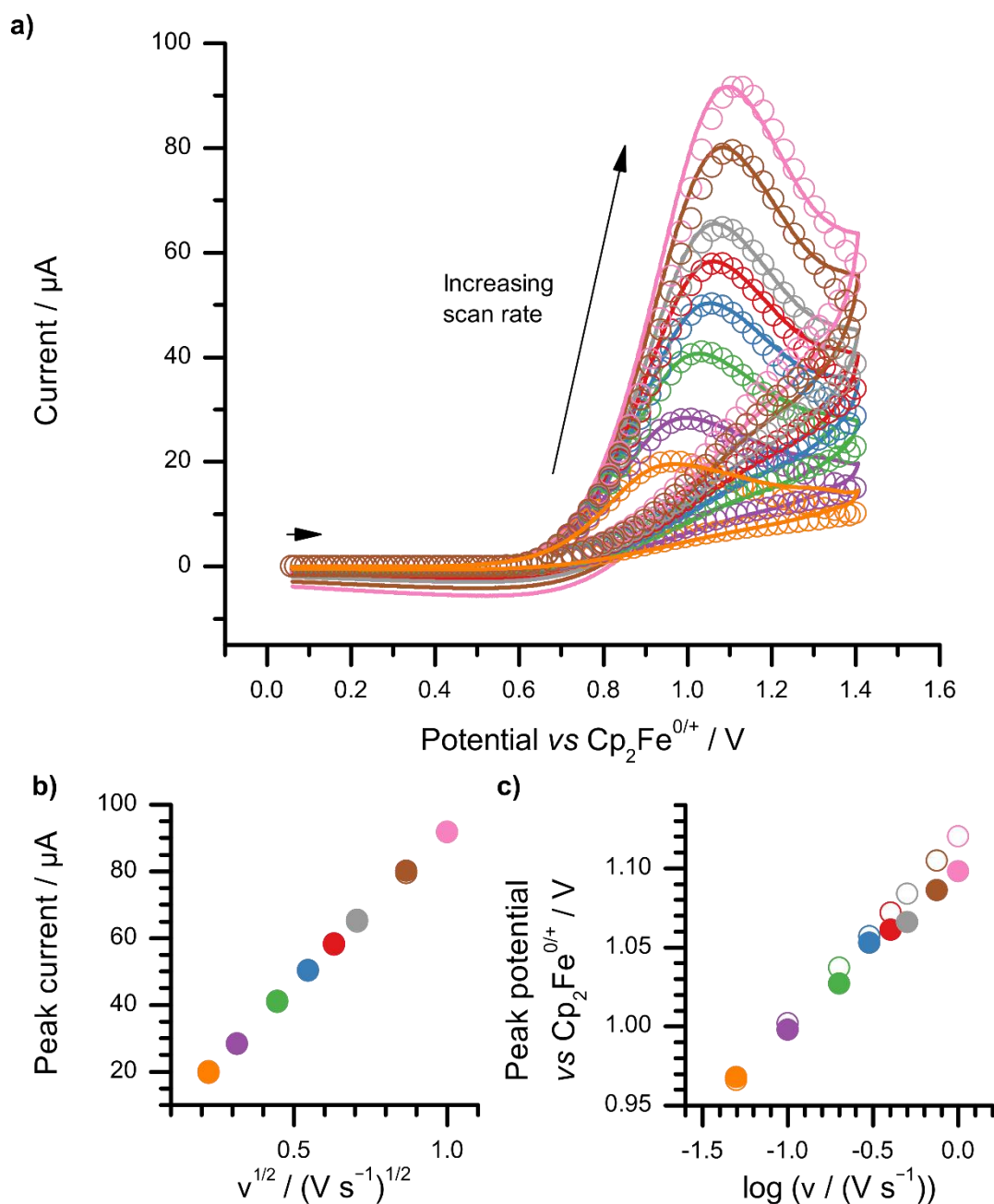


Figure 33 a) Experimental (line) and simulated (open circles) overlaid CVs for the oxidation of $[\text{tBu}_4\text{N}][\mathbf{8-H}]$ (2.9 mM) in CH_2Cl_2 at a GCE; b) corresponding Randles-Sevcik plot comparing simulated (open circles) and experimental (closed circles) peak currents against the square root of scan rate (v); c) corresponding Laviron plot comparing simulated (open circles) and experimental (closed circles) peak potentials against the logarithm of scan rate (v). $v = 50, 100, 200, 300, 400, 500, 750$ and 1000 mV s^{-1} .

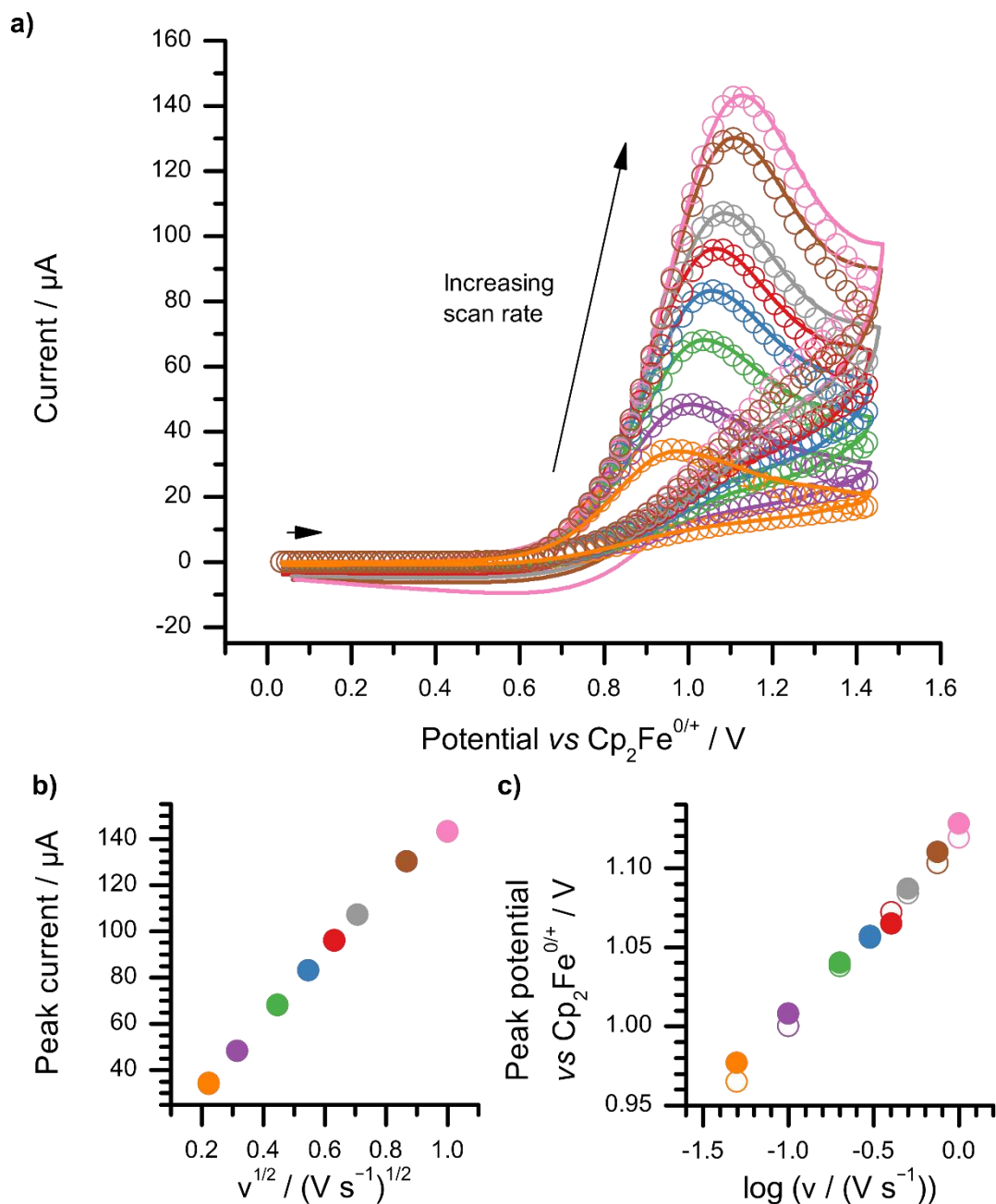


Figure 34 a) Experimental (line) and simulated (open circles) overlaid CVs for the oxidation of $[\text{nBu}_4\text{N}][\mathbf{8-H}]$ (4.9 mM) in CH_2Cl_2 at a GCE; b) corresponding Randles-Sevcik plot comparing simulated (open circles) and experimental (closed circles) peak currents against the square root of scan rate (v); c) corresponding Laviron plot comparing simulated (open circles) and experimental (closed circles) peak potentials against the logarithm of scan rate (v). $v = 50, 100, 200, 300, 400, 500, 750$ and 1000 mV s^{-1} .

Table 5 Globally optimized best-fit thermodynamic and kinetic parameters obtained from the digital simulation of voltammetric data for [ⁿBu₄N][**8**-H] at a GCE, following the mechanism proposed in **Scheme 31**.

Redox process		Redox parameters		
		$E^0 / \text{V vs Cp}_2\text{Fe}^{0/+}$	$k^0 / 10^{-2} \text{ cm s}^{-1}$	α
[8 -H] ⁻	\rightleftharpoons [8 -H] [•] + e ⁻	+1.13±0.05	1.3±0.2	0.7±0.1
8 ⁻	\rightleftharpoons 8 + e ⁻	-1.79±0.05 ^[a]	1.3±0.2 ^[a]	0.5±0.05 ^[a]

Chemical step		k / s^{-1}
[8 -H] [•]	\rightarrow 8 ⁻ + H ⁺	$k_1 > 1 \times 10^{13}$
8 ⁻	\rightarrow Decomposition products	$k_2 > 6.1^{[a]}$
[8 -H] ⁻ + H ⁺	\rightarrow 8 + H ₂	$k_3 = (1.50 \pm 0.25) \times 10^7 \text{ M}^{-1}$

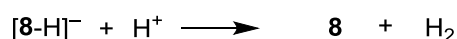
[a] Parameters are taken from my electrochemical study of **8** in Chapter 2

3.4 Spectroscopic studies

When $[\text{}^n\text{Bu}_4\text{N}][\mathbf{8}\text{-H}]$ was treated with a stoichiometric quantity of the single-electron chemical oxidant $[\text{NO}][\text{PF}_6]$ in CH_2Cl_2 , effervescence was observed. Analysis of the reaction mixture headspace using gas chromatography with a thermal conductivity detector (GC-TCD) revealed that H_2 gas was evolved.

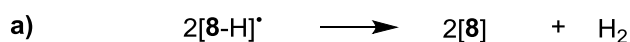
The observed production of H_2 gas can be rationalized by two plausible reaction mechanisms:

- i) The reaction of H^+ , generated by the chemical oxidation of $[\mathbf{8}\text{-H}]^-$, with $[\mathbf{8}\text{-H}]^-$ (as was proposed in **Scheme 31**).



Scheme 32 Hypothesised H_2 evolution pathway i.

- ii) Through a radical reaction pathway, which is likely to occur through a combination of the following two mechanisms:
- a) Radical disproportionation of two transient intermediate $[\mathbf{8}\text{-H}]^\bullet$ molecules, functioning as H^\bullet donors, to give $\mathbf{8}$ and H_2 .
- b) H^\bullet atom abstraction from $[\mathbf{8}\text{-H}]^-$ by intermediate $[\mathbf{8}\text{-H}]^\bullet$ to give $\mathbf{8}$, $\mathbf{8}^{\bullet-}$ and H_2 .



Scheme 33 Hypothesised H_2 evolution pathway ii.

In order to exclude the possibility of such radical pathways (ii), a control experiment was conducted using a common source of H^\bullet atoms. ${}^n\text{Bu}_3\text{SnH}$ was mixed with 4-bromobenzophenone (a hydrogen atom scavenger) in equimolar quantities, sealed in an NMR tube and then allowed to react under UV light. ${}^1\text{H}$ NMR characterization of the products revealed the formation of benzophenone *via* radical dehalogenation of 4-bromobenzophenone by H^\bullet . However, when $[\text{}^n\text{Bu}_4\text{N}][\mathbf{8}\text{-H}]$ was stoichiometrically oxidized in the presence of $[\text{NO}][\text{PF}_6]$ and an equimolar quantity of 4-bromobenzophenone, the latter was recovered in quantitative yield by NMR. No benzophenone was detected in the reaction mixture. This result is surprising, since the ability of borohydrides to participate in hydrogen atom (H^\bullet) transfer (HAT) reactions is well-known.^[253–257] This includes the radical dehalogenation of 4-bromobenzophenone, which is favoured by more

sterically bulky borohydrides such as $[\text{Li}(\text{DME})_2][\text{H}_2\text{BMe}_2]$, where DME = dimethoxyethane.^[253] This observation suggests that reactions involving $[\mathbf{8}\text{-H}]^\bullet$ are not a major contributor to the observed evolution of H_2 as a side-product.

Furthermore, effervescence is observed when $[\text{}^n\text{Bu}_4\text{N}][\mathbf{8}\text{-H}]$ and a stoichiometric amount of Jutzi's strong Brønsted acid, $[\text{H}(\text{OEt}_2)_2][\text{B}(\text{C}_6\text{F}_5)_4]$,^[258] are combined in CH_2Cl_2 . H_2 gas is once again detected in the reaction headspace, supporting the proposed proton-mediated H_2 evolution mechanism. Note that in either case, ^{11}B NMR characterization of the product mixture reveals a number of peaks in the range -0.5 to -7.0 ppm. The products of chemical oxidation of $[\mathbf{8}\text{-H}]^-$ are likely to give a complex mixture of products, including F^- abstraction products from the $[\text{PF}_6]^-$ anion present, as well as products resulting from the solvent-specific decomposition of intermediate, $\mathbf{8}^{\bullet-}$ (such as $[\text{ClB}(\text{C}_6\text{F}_5)_3]^-$, $[\text{Cl}_2\text{B}(\text{C}_6\text{F}_5)_2]^-$ and $[\text{HClB}(\text{C}_6\text{F}_5)_2]^-$ – see Chapter 2). In the case of the reaction of $[\text{}^n\text{Bu}_4\text{N}][\mathbf{8}\text{-H}]$ with $[\text{H}(\text{OEt}_2)_2][\text{B}(\text{C}_6\text{F}_5)_4]$, there is no evidence to suggest the formation of the classical Lewis adduct, $\mathbf{8}\cdot\text{Et}_2\text{O}$, or the protonation of the labile C_6F_5 groups of $\mathbf{8}$ to give HC_6F_5 .

When a deuterated sample of authentic hydride, $[\text{}^n\text{Bu}_4\text{N}][\text{DB}(\text{C}_6\text{F}_5)_3]$ ($[\text{}^n\text{Bu}_4\text{N}][\mathbf{8}\text{-D}]$), was fully oxidized in the presence of **12** at a carbon felt electrode using controlled potential bulk electrolysis, a triplet resonance was observed in the $^{31}\text{P}\{^1\text{H}\}$ NMR spectrum at δ 59.6 ppm ($J = 65.8$ Hz) (**Figure 35**), corresponding to $[\text{}^t\text{Bu}_3\text{PD}]^+$. Since the only possible source of D^+ must originate from the B-D bond (*via* the oxidation of $[\mathbf{8}\text{-D}]^-$), this result provides conclusive evidence for the proposed mechanism in **Scheme 31**, wherein B-D/B-H bond cleavage in $[\mathbf{8}\text{-D/H}]^\bullet$ results in the formation of D^+/H^+ and $\mathbf{8}^{\bullet-}$. A large quantity of the oxide, $\mathbf{12}=\text{O}$, was also generated in the process, and was observed at δ 60.7 ppm as an intense singlet.^[259] This is unsurprising, given that the oxidation potential of **12** is close to that of $[\mathbf{8}\text{-D/H}]^-$. **12** is extremely air and moisture sensitive and may have become exposed to air during its transfer to the NMR tube (despite using the appropriate inert techniques).

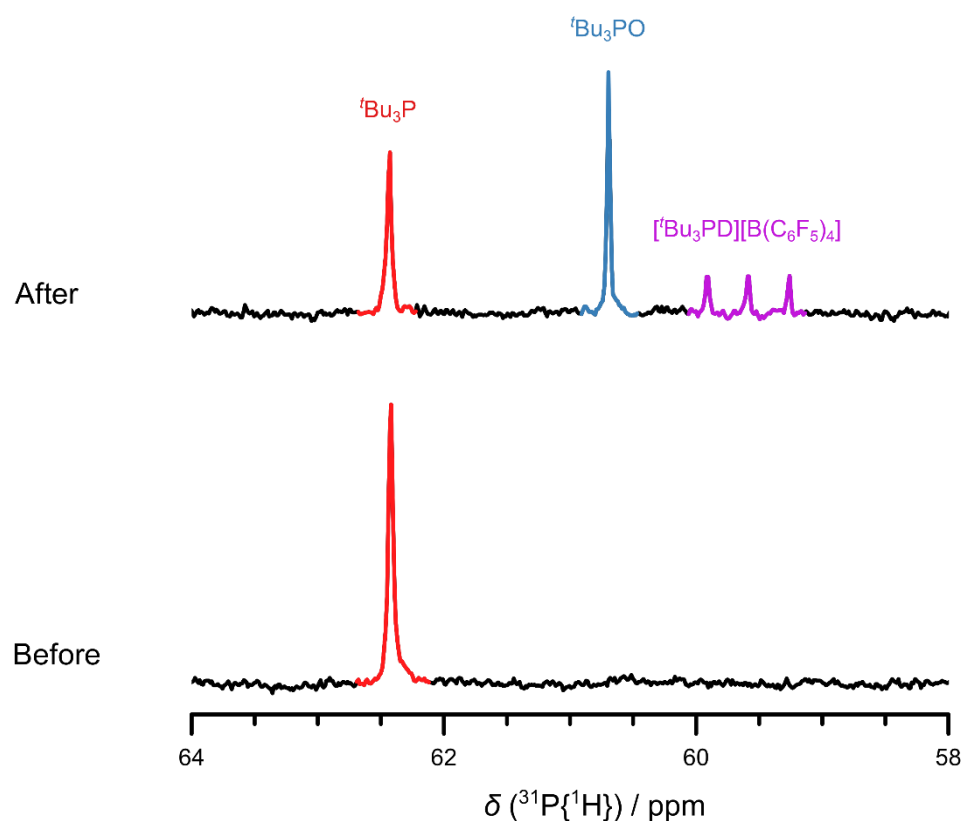


Figure 35 $^{31}\text{P}\{^1\text{H}\}$ NMR spectra of aliquots taken before and after the oxidative bulk electrolysis (+1.7 V vs $\text{Ag}^{0/+}$, 15 minutes) of $[\text{tBu}_4\text{N}][\mathbf{8}\text{-D}]$ (4.2 mM, CH_2Cl_2) at a carbon felt working electrode when in the presence of excess **12** (6 mM).

3.5 Computational modelling

DFT computational calculations were performed (by Dr. V. Oganessian) on the HOMO and the LUMO of the geometry-optimized $[\mathbf{8}\text{-H}]^-$ species, and the SOMO of $[\mathbf{8}\text{-H}]^*$, the proposed intermediate of oxidation. Interestingly, partial atomic charge calculations for $[\mathbf{8}\text{-H}]^-$ revealed that the B-H bond is not particularly polar (**Figure 37**). Contributions from the H and B atoms amount to $-0.099e$ and $+0.078e$ respectively, indicating that $[\mathbf{8}\text{-H}]^-$ is a weak hydride donor. This is consistent with the suggestion that small molecule hydrogenation (using FLPs) proceeds stepwise, with protonation preceding hydride transfer.^[118,260] The B-C and B-H BDEs for $[\mathbf{8}\text{-H}]^-$ were calculated to be $\Delta H_{\text{B-C}} = 408.1 \text{ kJ mol}^{-1}$ and $\Delta H_{\text{B-H}} = 312.2 \text{ kJ mol}^{-1}$ respectively, whilst for $[\mathbf{8}\text{-H}]^*$ the values were found to be $\Delta H_{\text{B-C}} = 71.7 \text{ kJ mol}^{-1}$ and $\Delta H_{\text{B-H}} = 34.0 \text{ kJ mol}^{-1}$ respectively. The strength of the B-H bond in $[\mathbf{8}\text{-H}]^*$ is almost comparable to a moderate hydrogen bonding interaction between $\mathbf{8}^{\bullet-}$ and H^+ .^[261] This suggests that the electrochemical oxidation of $[\mathbf{8}\text{-H}]^-$

significantly reduces the BDE of the B-H bond, facilitating its bond cleavage and lending further support to the mechanism that was proposed in **Scheme 31**.

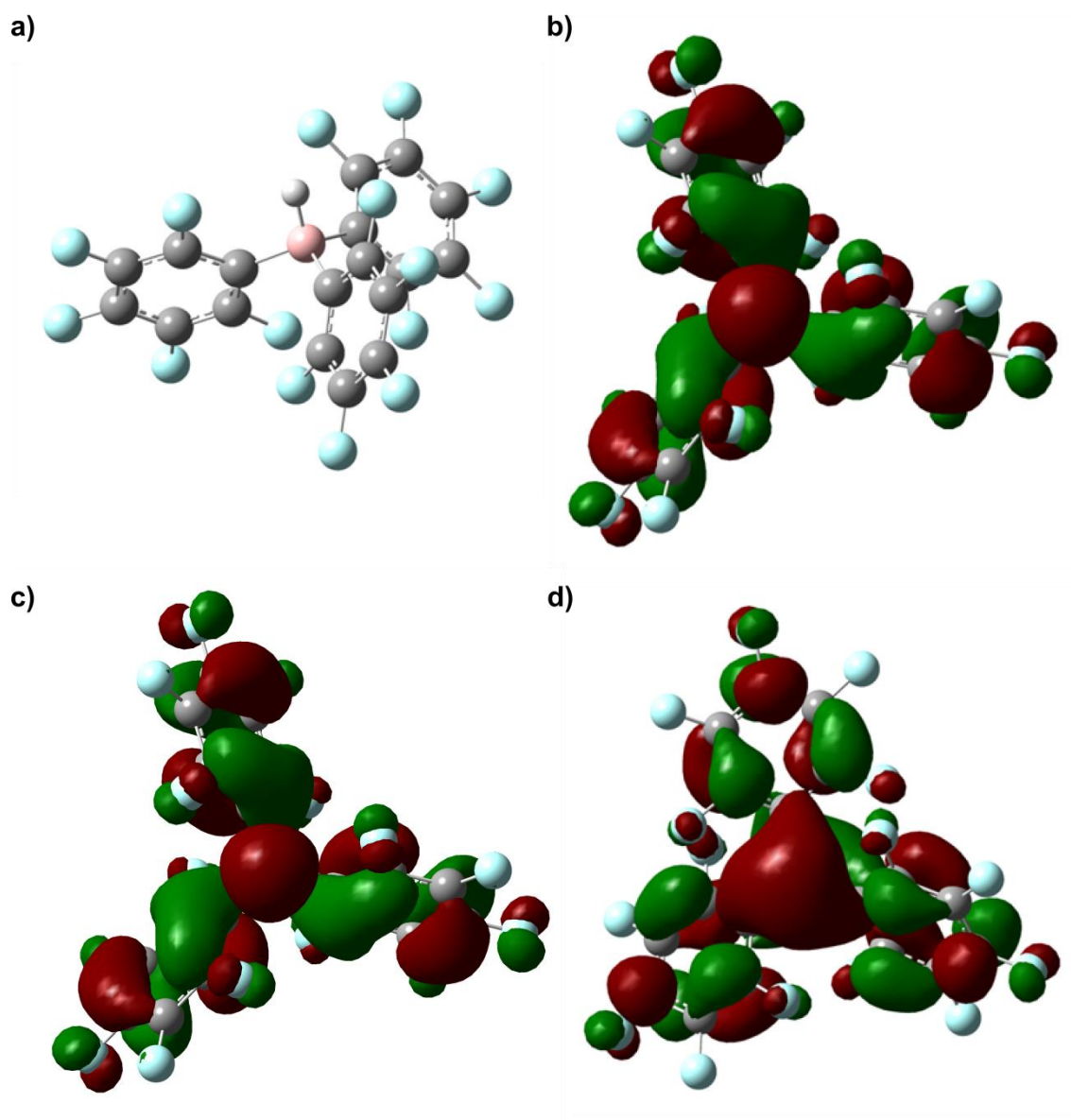


Figure 36 View of the a) geometry-optimized structure of $[8-H]^-$, b) HOMO of $[8-H]^-$, c) SOMO of $[8-H]^-$, d) SOMO of $8^{*\cdot-}$.

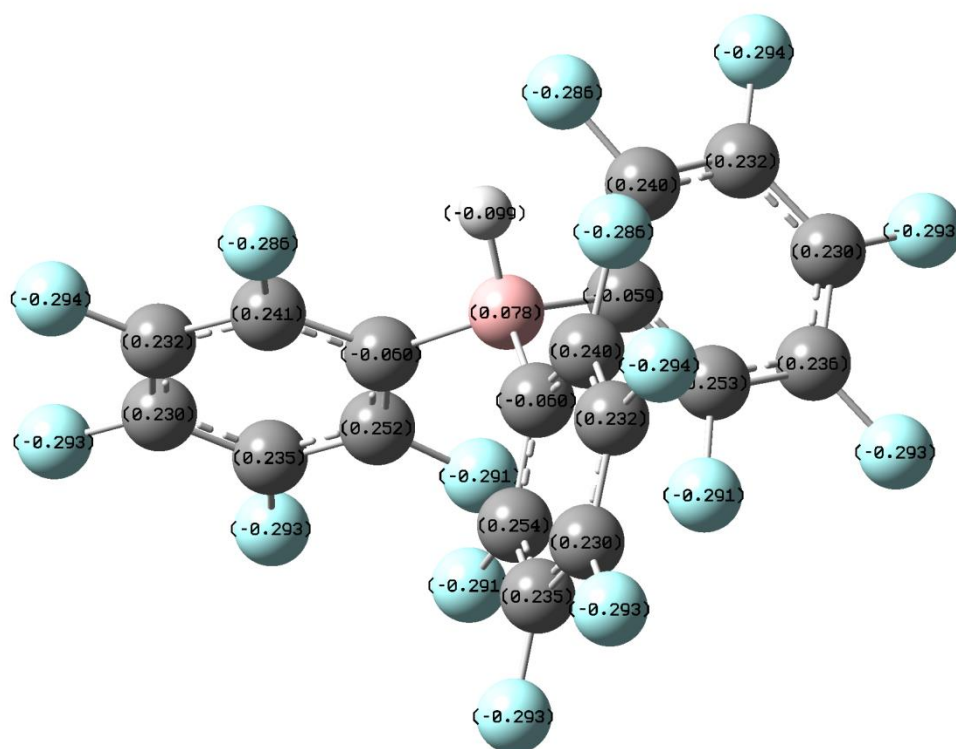


Figure 37 View of the geometry optimized structure of $[8-H]^-$ with partial charges shown for each atom (units are e), based on Mulliken electron population analysis.

3.6 Proof of concept

The redox chemistry of $[8-H]^-$ has now been studied, and its electrochemical mechanism has been elucidated. The next step was to proceed towards *in situ* electrochemical studies of the archetypal **8/12** system in the presence of H_2 . The relative rate of H_2 cleavage by this system is much slower than that of electron transfer at an electrode surface. Although Stephan describes H_2 cleavage by the **8/12** FLP as being immediate,^[120] when I monitored the reaction using ^{11}B , ^{19}F and $^{31}P\{^1H\}$ NMR spectroscopy (see **Figure 38** for ^{11}B NMR spectra), the reaction was complete after approximately 12 hours. However, some evidence of H_2 cleavage, *i.e.* the loss of the signal corresponding to **8** (*ca* δ 60 ppm) and some $[8-H][H-12]$ formation (*ca* δ -25 ppm), could be observed in the NMR spectra after 1 hour.

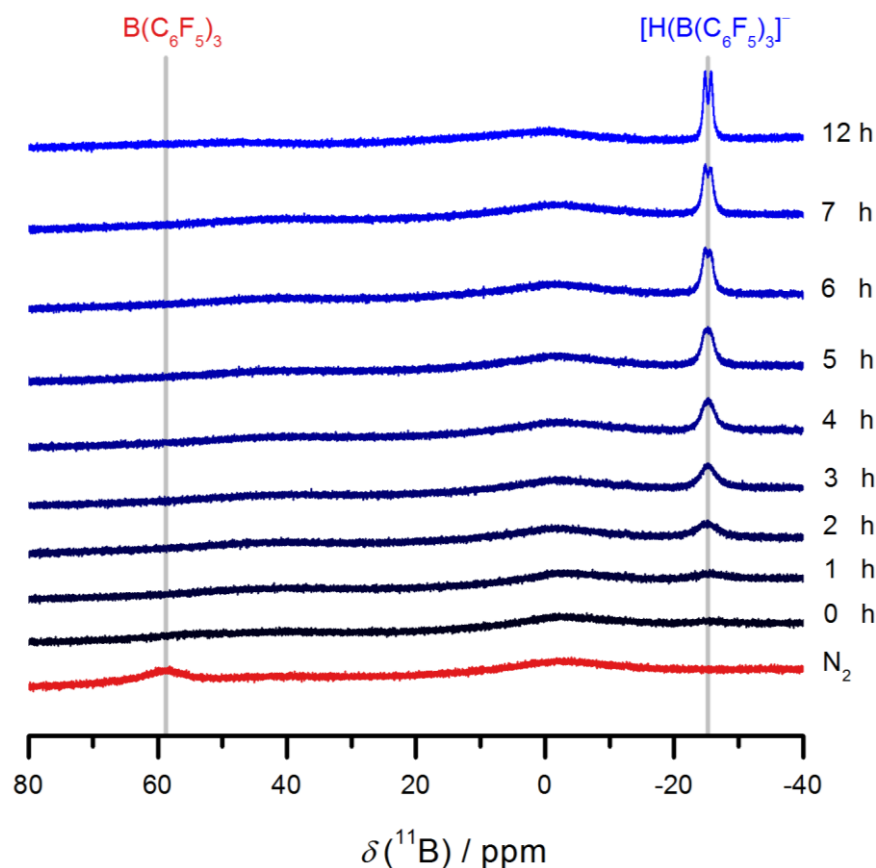


Figure 38 ^{11}B NMR spectrum showing the reaction progress of H_2 activation by the **8/12** FLP under ambient conditions.

For proof of concept, an equimolar solution of **8/12** (containing Cp_2Fe as an internal reference and $[\text{nBu}_4\text{N}][\text{B}(\text{C}_6\text{F}_5)_4]$ as supporting electrolyte) in CH_2Cl_2 was admitted to H_2 gas overnight and a CV was recorded (**Figure 39a**). The characteristic oxidation wave of $[\mathbf{8}\text{-H}]^-$ was observed, and was reassuringly identical to that of $[\text{nBu}_4\text{N}][\mathbf{8}\text{-H}]$. This was confirmed by observing a proportional increase in the oxidation current at +0.88 V vs $\text{Cp}_2\text{Fe}^{0/+}$ when the solution was spiked with a known quantity of authentic $[\text{nBu}_4\text{N}][\mathbf{8}\text{-H}]$ (**Figure 39a**). The electrode kinetics of uncatalysed H_2 oxidation at a GCE are very slow, leading to the observation of a broad and ill-defined wave at +1.49 V vs $\text{Cp}_2\text{Fe}^{0/+}$ in CH_2Cl_2 (**Figure 39b**). In this respect, a combined electrochemical-FLP approach effectively reduces the H_2 oxidation potential by 610 mV (117.7 kJ mol^{-1}). Note that whilst $[\mathbf{12}\text{-H}]^+$ was not found to be redox active at the potentials studied, the oxidation of a small quantity of unreacted **12** was apparent as a small (EC-like) oxidation wave at +0.44 V vs $\text{Cp}_2\text{Fe}^{0/+}$.

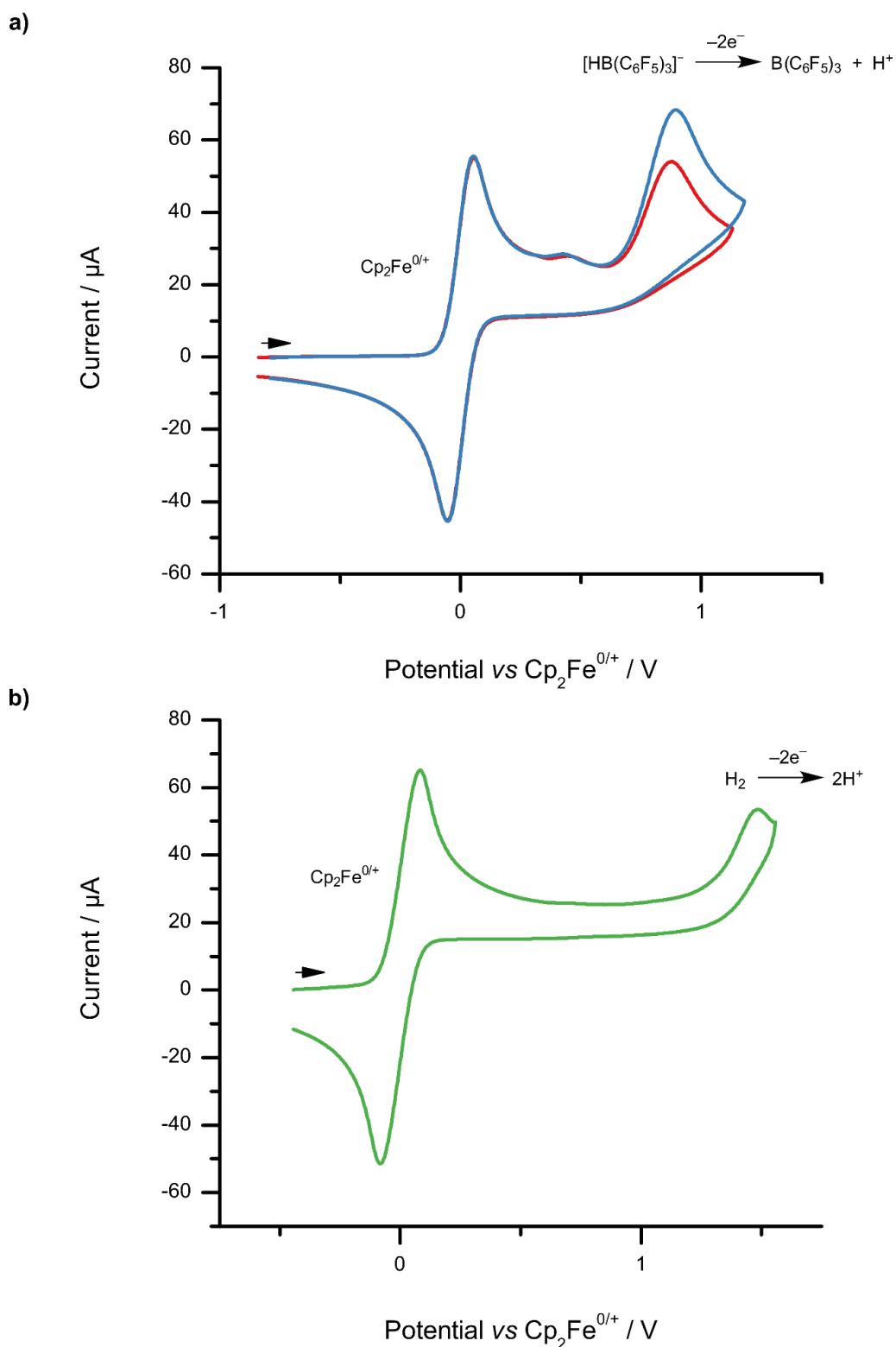


Figure 39 a) CV of a 5 mM solution of **12** and **8** in CH_2Cl_2 at a GCE after admission to H_2 (red line, $\nu = 100 \text{ mVs}^{-1}$). The addition of authentic $[\text{nBu}_4\text{N}][\mathbf{8}\text{-H}]$ to the sample confirms the observed wave as the product of H_2 activation (blue line, $\nu = 100 \text{ mVs}^{-1}$). b) CV of a H_2 -saturated CH_2Cl_2 solution (1 atm) at a GCE ($\nu = 100 \text{ mVs}^{-1}$). All samples contained Cp_2Fe as an internal standard.

To investigate whether or not this electrochemical-FLP system can be recycled, *i.e.* is catalytic in **8**, repeat oxidation cycles were performed. A 5 mM equimolar solution of **8/12** and 0.1 M [ⁿBu₄N][B(C₆F₅)₄]⁻ electrolyte in CH₂Cl₂ was sealed under an atmosphere of H₂ (1 atm) for 12 hours at room temperature. This ensured that the FLP heterolytic cleavage of H₂ had gone to completion. An initial CV was obtained, which showed the characteristic [**8-H**]⁻ oxidation wave. The reaction mixture was then subjected to controlled potential bulk electrolysis at a carbon felt electrode until all [**8-H**]⁻ had been oxidized; the oxidation wave was no longer apparent when a second CV was recorded after the bulk electrolysis step. For proof of concept, another equivalent of **12** was then added to the solution, which was again sealed under H₂ for a further 12 hours. A second bulk electrolysis cycle was undertaken, and this was then repeated once more (**Figure 40**). Disappointingly but unsurprisingly, upon a second and third electrolytic cycle, there was no evidence for the regeneration of **8**, since the re-formation of [**8-H**]⁻ could not be observed voltammetrically. This is consistent with previous NMR characterization of the products of chemical oxidation of [**8-H**]⁻. In addition to this, only a small and ill-defined reduction wave is sometimes observed for **8** following the voltammetric oxidation of [ⁿBu₄N][**8-H**]⁻ (**Figure 32, vide supra**). Clearly, any **8**^{•+} that is produced as an intermediate (following the oxidation of [**8-H**]⁻) is susceptible to side-reactions with the solvent during the (very short) timescale before successive oxidation steps. The decomposition of **8** through reaction with electrogenerated (unsolvated) H⁺ is likely to play a major role in limiting the recyclability of this system. Note that “buffering” the electrolyte using excess Lewis base (**12**) to disfavour undesirable protonolysis of **8** is not possible for this system, since **12** is redox active at similar potentials to [**8-H**]⁻.

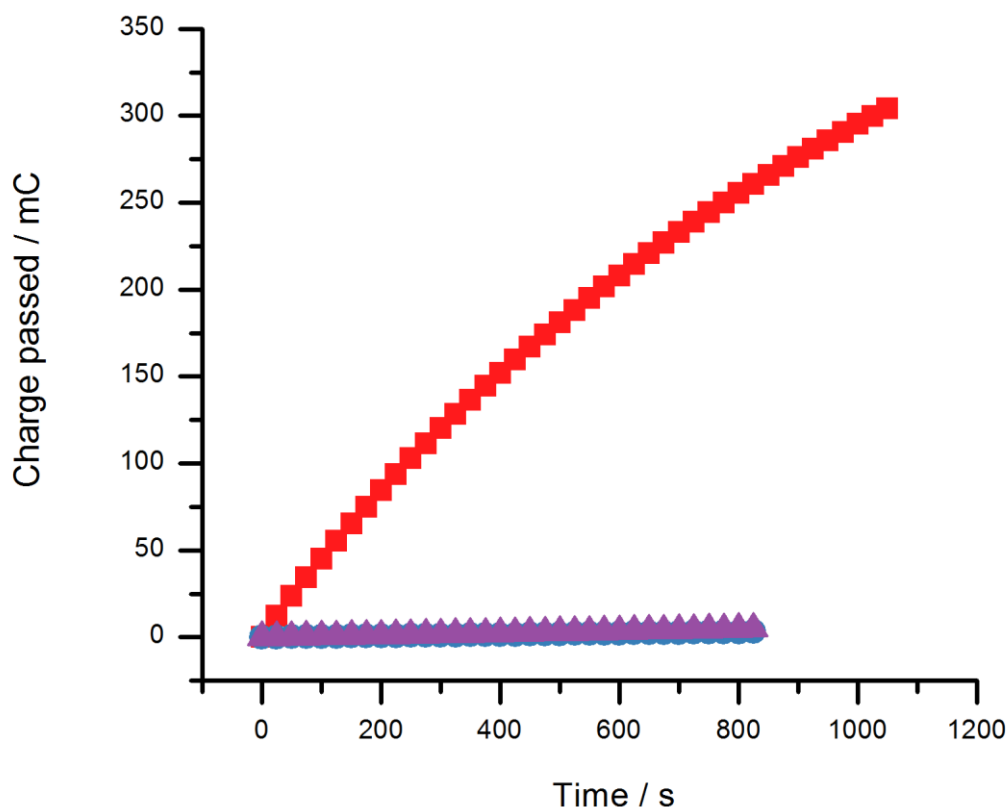


Figure 40 Repeat oxidative bulk electrolysis cycles of a 5.6 mM **8/12** solution following overnight exposure to H₂ (1 atm) demonstrates that the system cannot be recycled (■, cycle 1; ●, cycle 2; ▲, cycle 3).

This is the first study of the electrochemistry of FLPs towards H₂ activation. Whilst the classical **8/12** system appeared to be a logical starting point for these investigations, it is perhaps not surprising that this system is not optimal. However, these findings are important as they demonstrate that metal-free electrocatalysis of H₂ oxidation may be conceivable, using an electrochemical-FLP. However, one can immediately identify areas for future improvement:

- i) The competing reaction of [**8-H**]⁻ with redox-generated H⁺ results in H₂ evolution and reduces the overall efficiency of the process (although H₂ may be subsequently recycled in future systems).
- ii) Protonolysis leads to the unwanted decomposition of **8**. Either alternative Lewis acids that are resistant to protonolysis are required, or a solution that decreases the reactivity of these protons needs to be implemented.
- iii) Electrogenerated **8**⁺ (from oxidation of [**8-H**]⁻) is susceptible to reaction with the solvent, again preventing the system from being recycled. Steric and/or

electronic protection of any radical anion intermediates is required to limit this side-reaction.

- iv) The kinetics of FLP-mediated heterolytic H₂-cleavage are the rate determining step (compared to very rapid electron transfer) for this classical FLP system. FLPs with faster H₂-cleaving kinetics are required.

3.7 Summary

The complex non-aqueous redox chemistry of [8-H]⁻ has been explored for the first time, by studying an authentic borohydride sample ([ⁿBu₄N][8-H]). The pre-activation of H₂ using the 8/12 FLP system, when combined with electrochemical oxidation of the resultant borohydride, decreases the required potential for non-aqueous H₂ oxidation by 610 mV (117.7 kJ mol⁻¹) at readily available carbon electrodes. This represents a significant energy reduction whilst being metal-free, and opens up the possibility of a hitherto unexplored route to the development of economically viable energy technologies. The oxidation of *in situ* generated [8-H][H-12] by the classical 8/12 FLP system was also explored in the presence of H₂.

Whilst 8 has previously been described as “the ideal boron-based Lewis acid”,^[222] this work has identified specific areas that require development in order to advance the combined electrochemical-FLP system. It is clear from this work that 8 is not the ideal Lewis acid for such systems. Fortunately, the steric and electronic effects of Lewis acids and bases are highly tunable, providing plenty of scope to optimise such systems.

This chapter has been a preliminary investigation into the electrochemical properties of FLP. This groundwork suggests that a combined electrochemical-FLP approach may be viable for H₂ energy applications. Later chapters will focus on steric/electronic modifications to this system, in an attempt to improve recyclability, further reduce oxidation potentials, and increase the rate of H₂ cleavage.

Chapter 4

Results and discussion

Surface catalytic effects at Pt electrodes

4.1 Overview

In Chapter 3, the non-aqueous redox chemistry of the FLP borohydride component, $[\mathbf{8-H}]^-$, was explored using an authentic sample, $[{}^n\text{Bu}_4\text{N}][\mathbf{8-H}]$. The **8/12** FLP system was then utilized to activate H_2 ; this was combined with electrochemical oxidation of the resultant borohydride. Using this approach, the required potential for non-aqueous H_2 oxidation was effectively reduced by 610 mV ($117.7 \text{ kJ mol}^{-1}$) at carbon electrodes.

During the preliminary studies into the redox chemistry of $[{}^n\text{Bu}_4\text{N}][\mathbf{8-H}]$, both carbon and Pt electrodes were explored. The voltammetric response of $[\mathbf{8-H}]^-$ was found to exhibit a strong electrocatalytic effect at Pt electrode surfaces. This was in stark contrast to the response obtained using a GCE.

This chapter reports the results obtained when the combined electrochemical-FLP approach was extended to Pt electrode surfaces. Efforts were made to elucidate the underlying electrochemical mechanisms that give rise to the observed voltammetric behaviour. This included performing electrochemical studies in the presence of a radical scavenger, and sterically shielding the B-H bond through modification of the surrounding aryl groups on the Lewis acid. The electrooxidation of $[\mathbf{8-H}]^-$ was found to be dominated by HAT reactions between Pt, Pt-H adatoms, and intermediate $[\mathbf{8-H}]^\bullet$.

The results contained in this chapter have been published in *Chemistry – A European Journal*.^[262]

4.2 Electrochemical studies

The redox properties of $[{}^n\text{Bu}_4\text{N}][\mathbf{8-H}]$ was explored at a Pt macrodisk electrode using cyclic voltammetry (**Figure 41**) at varying concentration in CH_2Cl_2 containing the weakly-coordinating supporting electrolyte, $[{}^n\text{Bu}_4\text{N}][\text{B}(\text{C}_6\text{F}_5)_4]$ in a similar fashion as described in the previous chapters. As the potential was swept from the OCP to more anodic (positive) potentials at a scan rate of 100 mV s^{-1} , a large and well-defined oxidation wave was observed at $+0.49 \text{ V vs Cp}_2\text{Fe}^{0/+}$. The scan direction was reversed just before the limit of the potential window for the electrolyte system.^[203] On the return scan, the current was observed to cross-over the trace for the oxidation wave of the forward scan, indicating that an oxidation process was still in progress. The current then gradually decreased, whilst remaining positive at potentials more negative than the observed oxidation potential of $[\mathbf{8-H}]^-$. The current was observed to re-cross the forward scan trace over the potential range -0.30 to $-0.25 \text{ V vs Cp}_2\text{Fe}^{0/+}$. At more cathodic (negative) potentials, a series of small and ill-defined reduction waves were also observed.

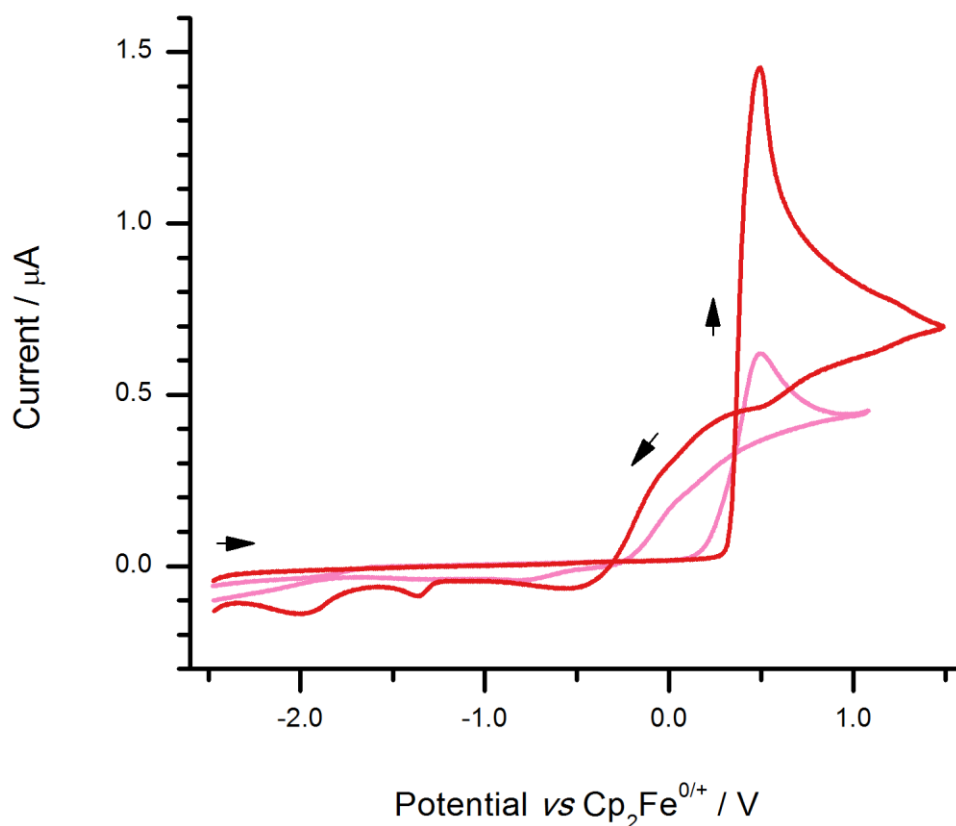


Figure 41 Overlaid CVs of [ⁿBu₄N][**8-H**] [2.3 mM (pink line) and 4.8 mM (red line)] at a Pt macrodisk electrode in CH₂Cl₂ at a scan rate (ν) of 100 mV s⁻¹.

The observed voltammetric response of [**8-H**]⁻ at a Pt macrodisk electrode contrasts significantly to what was previously observed at a GCE in Chapter 3 (**Figure 42**). As a reminder, at a GCE, [**8-H**]⁻ is observed to exhibit *EC*-like voltammetric behaviour. The oxidation wave of [**8-H**]⁻ is electrochemically reversible, however the absence of a corresponding reduction wave indicated the presence of chemical follow-up steps. No current-crossing was observed, and a small reduction wave at a more negative potential was tentatively assigned to the reduction of regenerated **8**.

Crossing-currents in cyclic voltammetry are an unusual phenomenon, and are only observed in one of the following situations:

- i) Special cases of an *ECE* reaction mechanism.^[187]
- ii) When a change in the electrode surface structure occurs, usually during an electrocatalytic process. For example, significant current-crossover is observed when methanol is oxidized at Pt electrodes, owing to the formation of various

adsorbed intermediate species that are electroactive at lower oxidation potentials.^[263]

In the case observed here, the height at which the reverse current crosses the forward-going current strongly suggests that the latter scenario, a structural change on the electrode surface, is likely to be responsible for this effect.

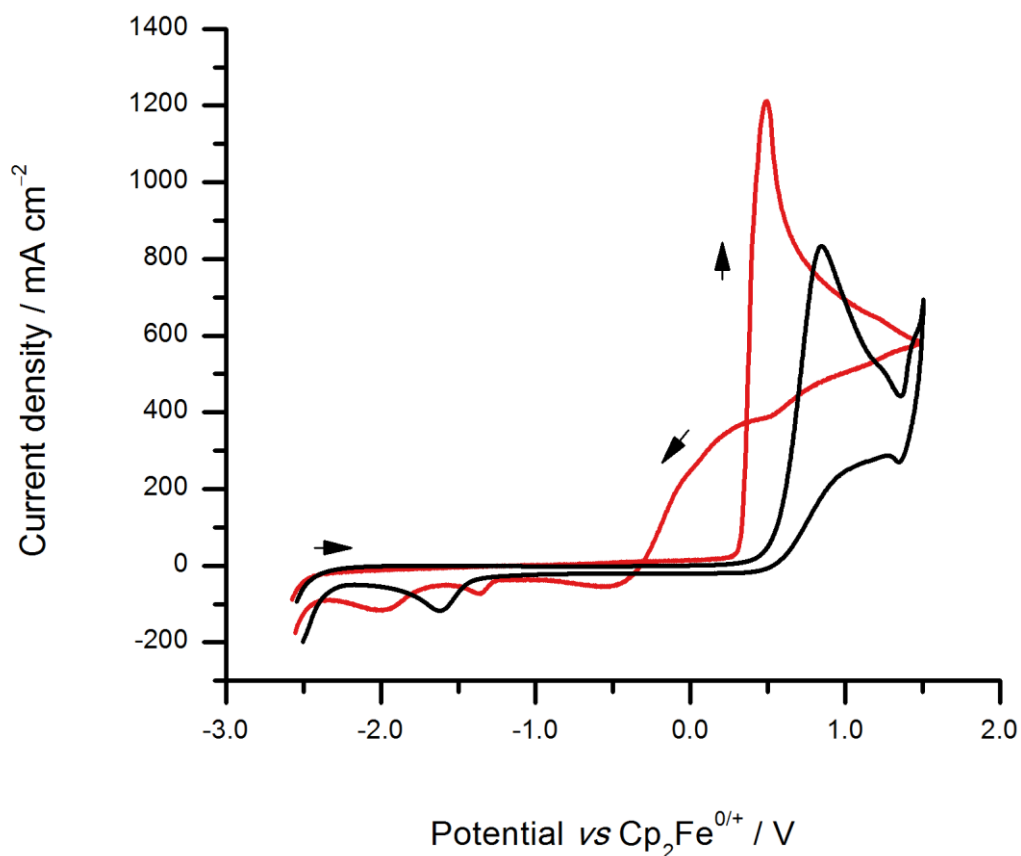


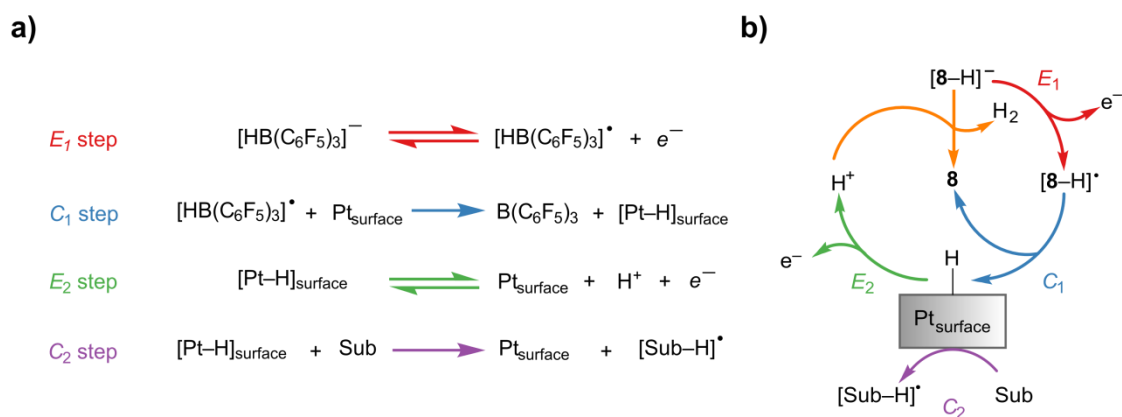
Figure 42 Overlaid CVs comparing 5 mM solutions of [ⁿBu₄N][**8-H**] recorded at Pt (red line) and glassy carbon (black line) macrodisk electrodes in CH₂Cl₂ ($\nu = 100 \text{ mV s}^{-1}$). Current density allows electrodes of different geometric areas to be directly compared.

It is clear, from the comparison of Pt and GCE voltammetric behaviour, that the Pt electrode is non-innocent and exhibits strong electrocatalytic properties (**Figure 42**). The rate of electron transfer during the oxidation of [**8-H**]⁻ is very much faster at the Pt electrode than at the GCE. This corresponds to a steeper gradient being observed at Pt (compared to the GCE) in the initial, rising part of the oxidation wave, where the observed current density is limited by electrode kinetics, along with a greater peak current density. Furthermore, strong evidence in

support of electrocatalysis at the Pt surface is exhibited by a 390 mV decrease in the oxidative peak potential, compared to glassy carbon.

To explain these observations at Pt electrodes, a modification to the original mechanism (that was given in Chapter 3) for $[\mathbf{8}\text{-H}]^-$ oxidation is proposed (**Scheme 34**). This adaptation takes into account the well-documented ability of Pt surfaces to adsorb H^\bullet atoms, as is observed for the direct, electrocatalytic oxidation of H_2 at Pt electrodes in aqueous electrolyte systems.^[26,27]

At both Pt and glassy carbon electrodes, $[\mathbf{8}\text{-H}]^-$ first undergoes a single-electron oxidation to give the transient intermediate, $[\mathbf{8}\text{-H}]^\bullet$. Previous DFT calculations (see 3.5) on the SOMO of $[\mathbf{8}\text{-H}]^\bullet$ have shown that the B-H bond becomes significantly weakened (calculated BDE is 34.0 kJ mol^{-1}) following the electrooxidation of $[\mathbf{8}\text{-H}]^-$. At carbon electrodes, $[\mathbf{8}\text{-H}]^\bullet$ very rapidly dissociates to generate a proton and $\mathbf{8}^{\bullet-}$, which undergoes further oxidation in competition with its decomposition in solution (see Chapters 2-3 for further details). However, at Pt electrodes, the surface is able to compete with the dissociation step by abstracting H^\bullet from $[\mathbf{8}\text{-H}]^\bullet$. This HAT process liberates the parent borane, $\mathbf{8}$, whilst effecting a change on the surface of the electrode by forming a H-atom (surface hydride, Pt-H). Since, the oxidation potential of Pt-H is much lower than the applied potential at this time in the cyclic voltammetric experiment (close to the main oxidation wave), it rapidly undergoes a second single-electron oxidation. This forms H^+ and electrocatalytically regenerates the Pt electrode surface. Since this process occurs throughout the beginning of the reverse sweep, the surface concentration of Pt-H builds up until the current crosses back over the forward-going scan. Owing to the presence of significant quantities of Pt-H, oxidation continues to occur throughout the reverse sweep, giving rise to an oxidative current at potentials more negative than that of the main $[\mathbf{8}\text{-H}]^-$ oxidation wave. This process ceases to occur when the applied potential approaches the reduction potential of the Pt-H system at approximately $-0.3 \text{ V vs Cp}_2\text{Fe}^{0/+}$.



Scheme 34 a) The proposed redox mechanism with individual steps for the electrocatalytic oxidation of $[\mathbf{8-H}]^-$ at a Pt electrode surface; b) the schematic representation of the entire mechanistic cycle. The decomposition pathways of $\mathbf{8}$ and $\mathbf{8}^{\bullet}$ are omitted for clarity (see Chapters 2-3 for details). Also shown is the competing HAT reaction (C_2) between a substrate (Sub) and the H-atoms on the Pt surface (Pt-H).

Note that all electron transfer steps are *quasi-reversible*, and are therefore subject to Nernstian equilibria.^[187] The rapid formation of Pt-H at the electrode effectively depletes the surface concentration of $[\mathbf{8-H}]^{\bullet}$, and causes a perturbation in the Nernstian equilibria. This phenomenon is responsible for the observed electrocatalytic effect on Pt, whereby the onset of $[\mathbf{8-H}]^-$ oxidation occurs at lower potentials than that at a GCE. Considering that the presence of follow-up chemical reactions could cause a shift in the observed redox potentials, the small reduction wave at approximately -2.0 V vs $\text{Cp}_2\text{Fe}^{0/+}$ may result from the reduction of free $\mathbf{8}$. In Chapter 3 it was shown that significant quantities of $\mathbf{8}$ are generated through the reaction of incoming $[\mathbf{8-H}]^-$ with electrogenerated H^{\bullet} . It was also noted that the majority of electro-/chemically-generated $\mathbf{8}$ undergoes decomposition through protonolysis. This explains why the reduction peak is small in comparison to the oxidation peak. Proton reduction on the polycrystalline Pt surface may also be responsible for the small and broad reduction waves that were observed between -0.3 and -1.0 V. This assignment is supported by the observation of similar voltammetric features when an electrolyte solution in CH_2Cl_2 is spiked with the strong Brønsted acid, $[\text{H}(\text{OEt}_2)_2][\text{B}(\text{C}_6\text{F}_5)_4]$.^[258]

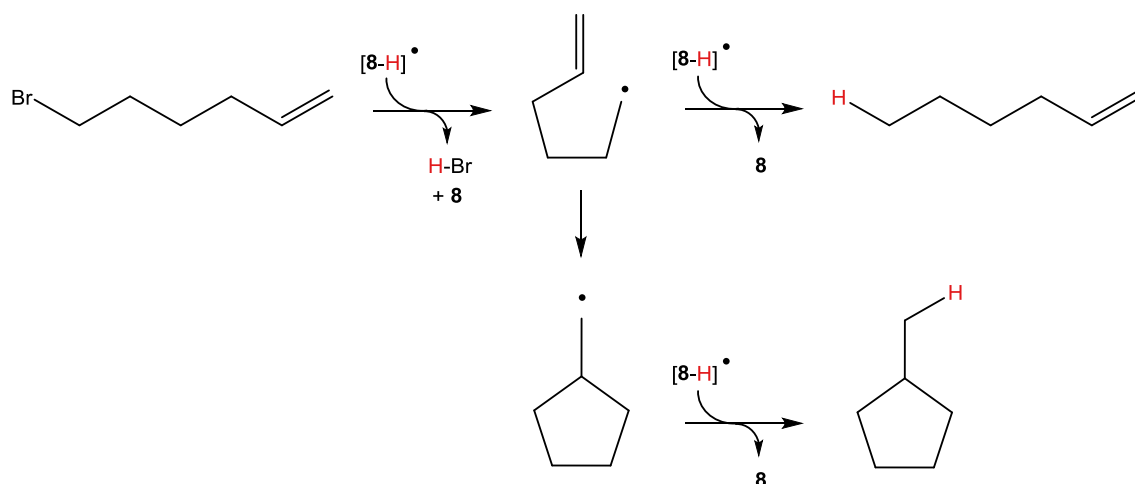
Since Pt-H formation on the surface of the electrode cannot be modelled using our diffusion-only simulation software, digital simulation of the voltammetric data is prohibited. This prevents the proposed mechanism from being confirmed through fitting of the experimental

data. It also means that relevant kinetic and thermodynamic parameters cannot be extracted. Nonetheless, evidence to support the proposed mechanism in **Scheme 34** was obtained by:

- i) Competition experiments in the presence of a radical scavenger.
- ii) Increasing the steric bulk surrounding the B-H bond.

4.3 Competition experiments

The cyclic voltammetry of $[\text{nBu}_4\text{N}][\mathbf{8-H}]$ was conducted in the presence of increasing molar equivalents of the radical scavenger, 6-bromo-1-hexene. This commonly known radical clock reagent functions as a H^\bullet atom scavenger, forming 5-hexenyl radical intermediates that cyclize at a known rate.^[264–270]



Scheme 35 Reaction of the radical scavenger, 6-bromo-1-hexene, with H^\bullet from electrogenerated $[\mathbf{8-H}]^\bullet$.

6-bromo-1-hexene was selected because neither it nor any of its intermediate radicals or cyclized products exhibit any redox chemistry in the potential window of interest. The effect of adding up to 10 molar equivalents of the radical clock on the voltammetric oxidation of $[\mathbf{8-H}]^-$ is shown in **Figure 43**.

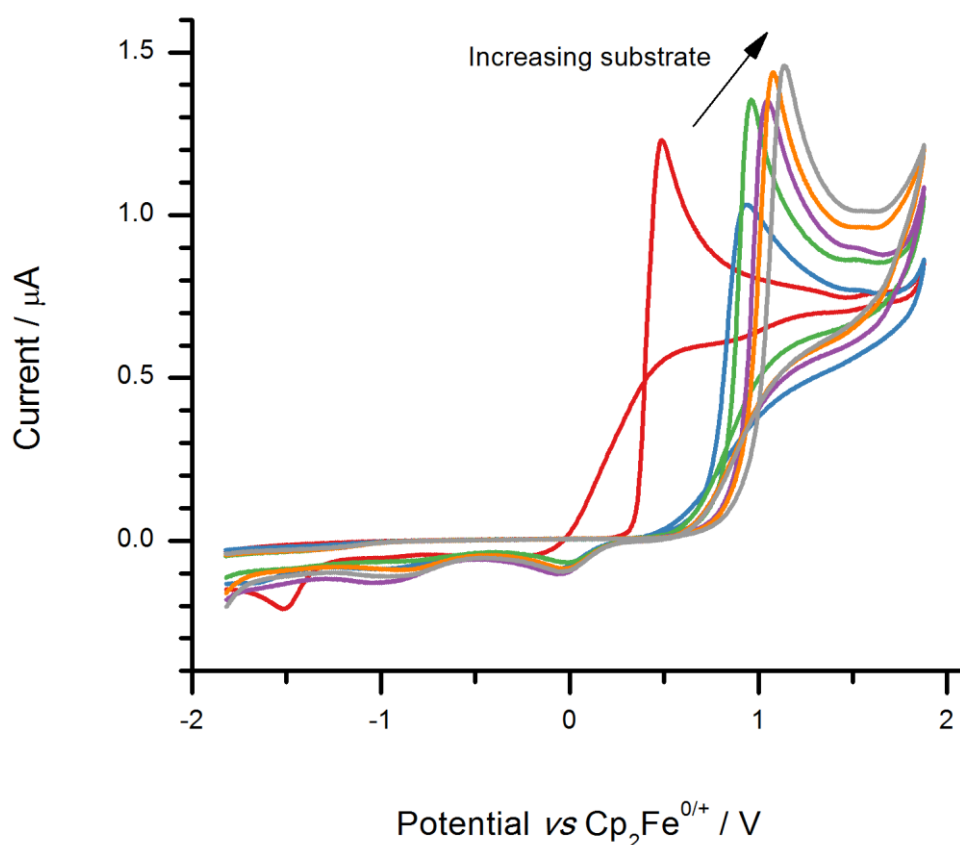


Figure 43 Overlaid CVs show the effect of adding increasing molar equivalents of 6-bromo-1-hexene (0, red; 1, blue; 2, green; 4, purple; 8, orange; and 10, grey molar equivalents) to a 4.8 mM solution of [ⁿBu₄N][8-H] (red line) in CH₂Cl₂ at a Pt macrodisk electrode ($\nu = 100 \text{ mV s}^{-1}$).

Upon the addition of the first molar equivalent of radical clock, the oxidation wave of [8-H]⁻ was observed to shift to significantly more positive potentials and decrease in height. The extent of current cross-over is significantly reduced (and almost negligible) in comparison to the CV obtained in absence of the radical clock. Indeed, the observed oxidation wave-shape and peak potential is remarkably similar to that observed at a GCE. This can be rationalized by considering why the process that gives rise to a crossing-current may have become inoperative. In this case, the radical clock competes with the Pt surface to abstract H[•] from the electrogenerated [8-H][•] intermediate. This competing pathway prevents the formation of Pt-H on the surface, and therefore the previously observed oxidation of the Pt-H surface species (as a crossing-current) at lower potentials (**Scheme 34**) is effectively inhibited. The oxidation of [8-H]⁻ at a Pt electrode now exhibits similar voltammetric behaviour to a GCE (see Chapter 3). Thus the radical atom scavenger 6-bromo-1-hexene functions as a competitive inhibitor for any

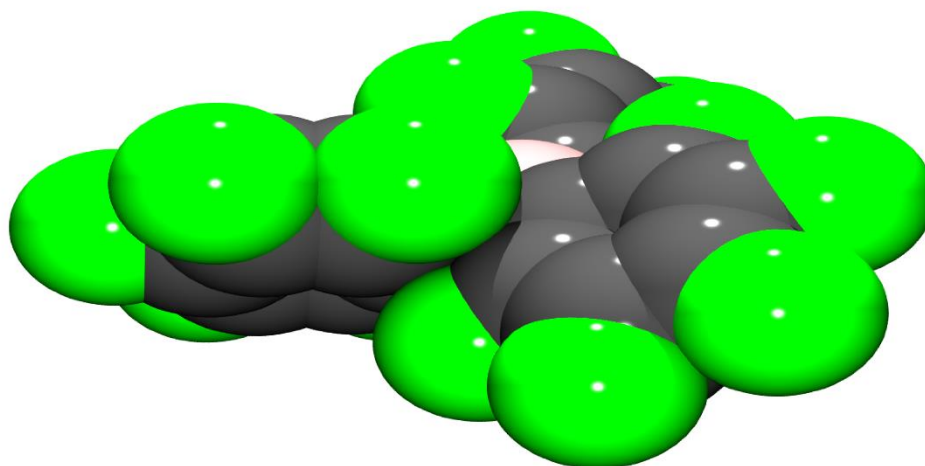
surface HAT step at the Pt electrode. As the concentration of radical clock is increased, the peak potential and current is also observed to gradually increase. The increase in peak potential is a direct effect of the reaction between 6-bromo-1-hexene and $[\mathbf{8-H}]^*$, since this reaction perturbs the Nernstian equilibria that govern the initial oxidation of $[\mathbf{8-H}]^-$. The increase in peak current can be understood in similar terms. The abstraction of H^\bullet from $[\mathbf{8-H}]^*$, by the radical scavenger, prevents its dissociation into H^+ and $\mathbf{8}^{\bullet-}$. This inhibits the reaction of H^+ with a second incoming $[\mathbf{8-H}]^-$ molecule (see **Scheme 34b**), a process that would otherwise deplete the concentration of $[\mathbf{8-H}]^-$ at the electrode surface and cause the observed oxidation current to be effectively reduced.

4.4 Steric effects

Another method to inhibit the formation of Pt-H is to increase the steric bulk around the B-H bond, and thus effectively shield the hydride from any interaction with the Pt electrode surface. My approach was to substitute the C_6F_5 groups for bulkier C_6Cl_5 groups, by synthesising the hitherto unknown borohydride, $[^nBu_4N][HB(C_6Cl_5)_3]$, $[^nBu_4N][\mathbf{24-H}]$.

$[^nBu_4N][\mathbf{24-H}]$ was prepared using a similar method to that used in the preparation of $[^nBu_4N][\mathbf{8-H}]$ in Chapter 3. Treatment of the parent perchlorinated analogue of **8**, $B(C_6Cl_5)_3$ (**24**), with $Na[HB(Et)_3]$ in toluene at $80^\circ C$ yielded $Na[\mathbf{24-H}]$. This was followed by metathesis with $[^nBu_4N]Cl$ to give $[^nBu_4N][\mathbf{24-H}]$. Note that the borane, **24**, was selected because its synthesis and redox properties have already been studied and reported by the Wildgoose research group.^[244] **24** is much more electron deficient than **8**, despite Cl being less electronegative than F (Pauling electronegativity, $\chi_{Cl} = 3.16$ vs $\chi_F = 3.98$). The π -overlap between the Cl 3p and the C 2p orbitals on the aromatic ring is weaker than that of the F 2p and C 2p orbitals; as a result, the Hammett parameter for a Cl substituent at the *para* position is greater than that for a F substituent ($\sigma_{para}(Cl) = 0.227$, $\sigma_{para}(F) = 0.062$).^[271] Where steric factors are concerned, the C_6Cl_5 groups are much bulkier than the C_6F_5 groups, with a Cl substituent occupying a similar volume as a methyl group (Taft steric substituent constant $E_s(F) = -0.46$, $E_s(Cl) = -0.97$, $E_s(Me) = -1.24$), and therefore provide greater shielding of the B centre (as illustrated by the space-filling models shown in **Figure 44**).

a)



b)

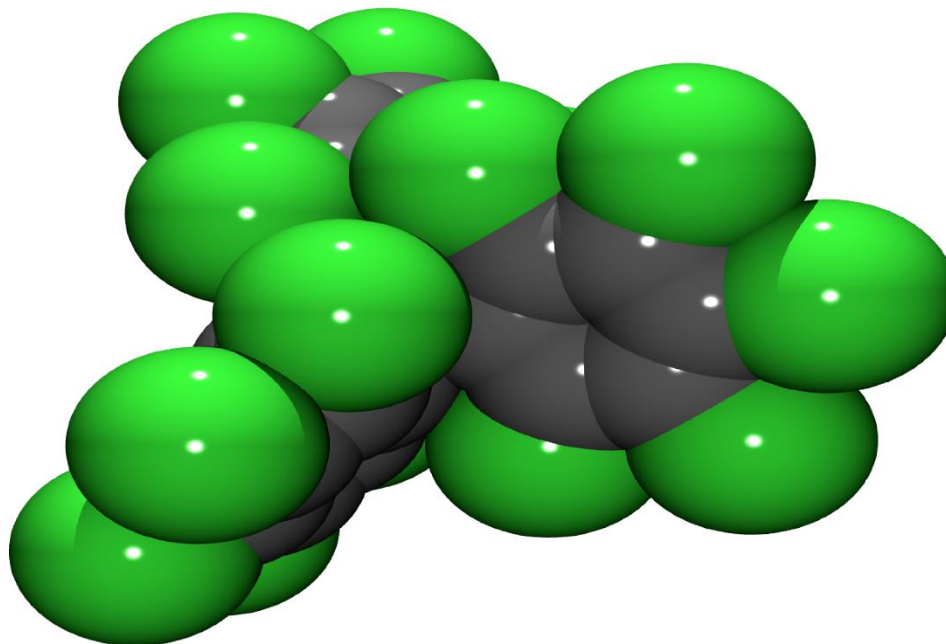


Figure 44 Space-filling view of the boranes a) **8** and b) **24**, showing the extent of steric shielding of the B centre by the surrounding C₆F₅ and C₆Cl₅ groups, respectively.

Colourless needles of [ⁿBu₄N][**24-H**], suitable for X-ray crystallography, were grown by dissolving the sample in a minimum quantity of CH₂Cl₂, warming to approximately 40°C, adding an equal quantity of light petroleum ether followed by slow-cooling to room temperature. X-ray diffraction data was collected by the EPSRC National Crystallography Service and data solution and refinement was performed by D. Hughes (see **Figure 45**). Crystallographically, two components were observed for the anion in a 69:31 ratio, with negligible structural differences.

The separation of the carbon atoms in each aryl ring was not resolved and each ipso-C site therefore accommodates both the major and minor atom sites. All further discussions are based on the major component. In $[\mathbf{24-H}]^-$, the geometry about the boron centre deviates from the trigonal planar geometry of $\mathbf{24}$ (as indicated by the sum of the bond angles, which equal 360°),^[244] towards the idealised tetrahedral bond angle of 109.5° [selected bond angles ($^\circ$) for $[\mathbf{24-H}]^-$ are 112.0(5), 111.0(6) and 112.2(6) for C11-B1-C21, C11-B1-C31, and C21-B1-C31 respectively]. The hydride itself was clearly explicitly observed. The three C_6Cl_5 aryl rings have a propeller-like conformation about the B-H axis; the torsion angles ($^\circ$) of the aryl rings about the B-H plane were found to be 38.7, 38.6 and 37.9. The average value for the torsion angles (approximately 38°) is smaller than that of the parent Lewis acid, $\mathbf{24}$, where the average torsion angles are 56° .^[244] The torsion angles in $\mathbf{24}$ are much larger than those of geometry-optimised $\mathbf{8}$ (37° ; see 2.4); this reflects the increased steric profile of the C_6Cl_5 aryl rings compared to the C_6F_5 groups. The space-filling view of the B-H bond, shown in **Figure 46b**, shows the extent to which the B-H bond is sterically shielded (effectively buried) by the surrounding C_6Cl_5 aryl rings, compared to the B-H bond in $[\mathbf{8-H}]^-$ (**Figure 46a**).

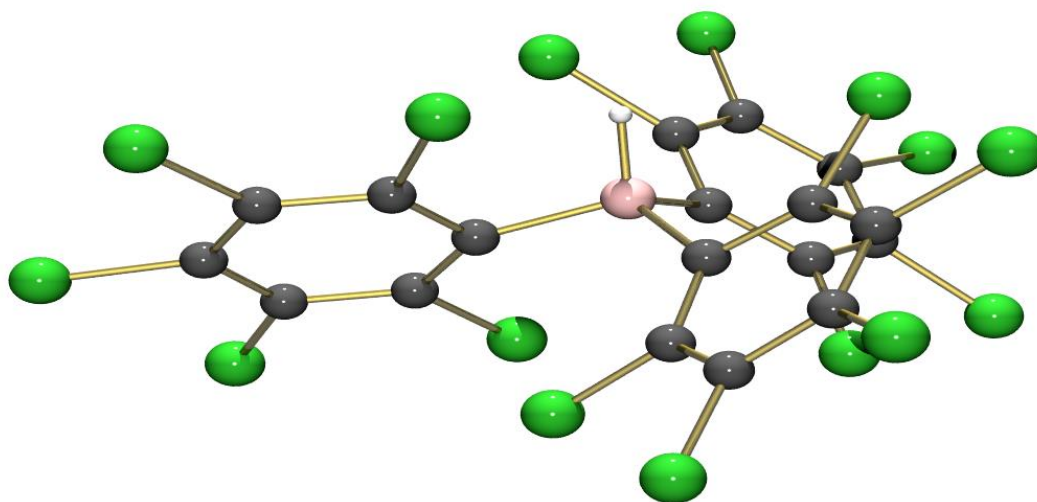
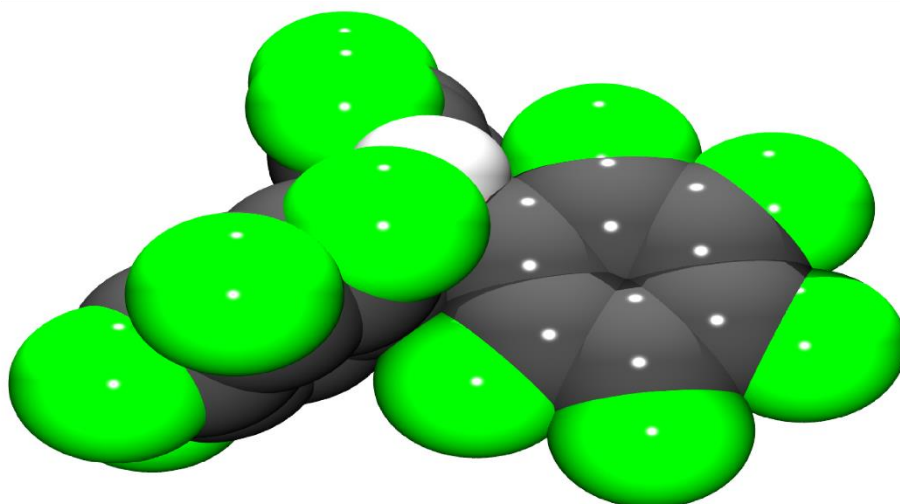


Figure 45 Molecular structure of $[\mathbf{24-H}]^-$ (only the anion and its major conformation are shown).

a)



b)

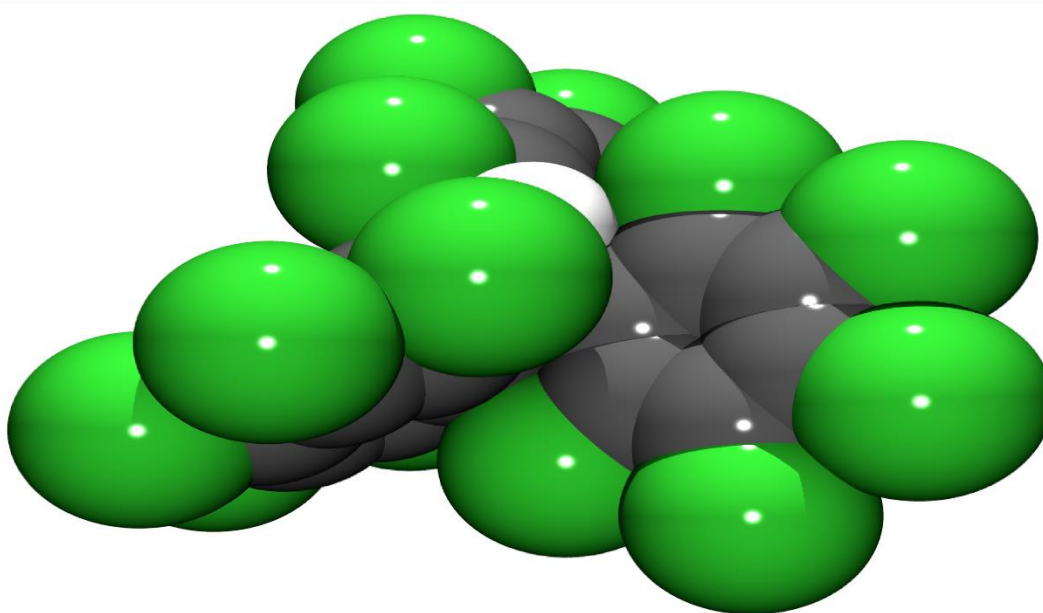


Figure 46 Space-filling view of the anions a) $[8-H]^-$, and b) $[24-H]^-$, showing the extent of steric shielding of the B-H bond by the surrounding C_6F_5 and C_6Cl_5 groups, respectively.

When cyclic voltammetry was performed on $[^nBu_4N][24-H]$ (**Figure 47**) at a Pt electrode, it was found to undergo oxidation at a slightly higher potential (*ca* 100 mV) than $[^nBu_4N][8-H]$. This suggests that $[24-H]^-$ is less hydridic than $[8-H]^-$, and is consistent with the parent borane, **24**, being more electrophilic than **8**.^[244] However, in the case of $[^nBu_4N][24-H]$, no current cross-over is observed at any scan rate. This suggests that the steric bulk around the B-H bond in $[24-H]^-$ is sufficient (see **Figure 46b**) to preclude the formation of any Pt-H surface species *via* a HAT process – electrocatalysis is not observed at a Pt electrode. This observation further supports

the proposed mechanism (**Scheme 34**) that describes the oxidation of $[\mathbf{8-H}]^-$ at Pt electrodes. Instead a new, *quasi*-reversible redox wave is observed at a mid-peak potential of +0.98 V vs $\text{Cp}_2\text{Fe}^{0/+}$. When considering the radical anions of the parent boranes, the relative stabilities of $\mathbf{8}^{\bullet-}$ and $\mathbf{24}^{\bullet-}$ contrast greatly. Whilst $\mathbf{8}^{\bullet-}$ rapidly undergoes decomposition in solution to form solvent-specific reaction products (see Chapter 2), chemically-generated $\mathbf{24}^{\bullet-}$ (obtained from the reduction of $\mathbf{24}$ by Na in THF, $E^0 = -3.04$ V vs $\text{Cp}_2\text{Fe}^{0/+}$)^[247] persists in solution with a measured half-life of 115 minutes at 298 K.^[244] The enhanced stability of $\mathbf{24}$ follows from its boron centre being sufficiently sterically shielded by the C_6Cl_5 groups to avoid any reaction with the solvent. Based on this, it can be tentatively proposed that the additional *quasi*-reversible oxidation wave at +0.98 V vs $\text{Cp}_2\text{Fe}^{0/+}$ corresponds to the single-electron oxidation of $[\mathbf{24-H}]^{\bullet}$ radicals, which are likely to be relatively long-lived in comparison to $[\mathbf{8-H}]^{\bullet}$, and which occurs alongside competing dissociation pathways. Note that this hypothesis is also supported by the height of the first (*EC*-like) oxidation wave, which corresponds to a single-electron process for $[\textit{n}\text{Bu}_4\text{N}][\mathbf{24-H}]$, but corresponds to an effective number of electrons transferred that is greater than 1 in the case of $[\textit{n}\text{Bu}_4\text{N}][\mathbf{8-H}]$. Further studies into a series of perchlorinated boranes are ongoing, within the research group, at the time of writing this thesis.

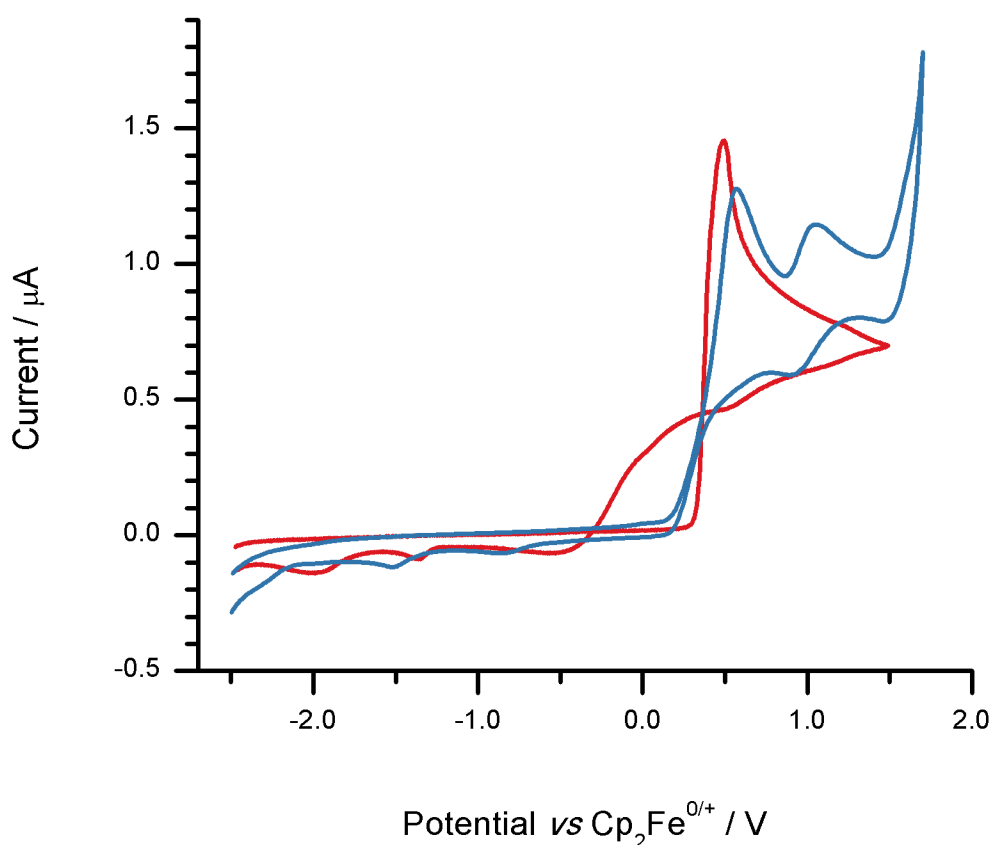


Figure 47 Overlaid CVs comparing the oxidation of 5 mM solutions of [ⁿBu₄N][**8**-H] (red line) and [ⁿBu₄N][**24**-H] (blue line) in CH₂Cl₂ at a Pt macrodisk electrode ($\nu = 100 \text{ mV s}^{-1}$).

4.5 Proof of concept

Finally, for completeness, the *in situ* combined electrochemical-FLP activation of H₂ was studied at Pt (in much the same fashion as the previous efforts at a GCE in Chapter 3). The resulting cyclic voltammetry is shown in **Figure 48**. When a CV of an equimolar solution of the **8**/TMP FLP^[124] in CH₂Cl₂ was recorded at the Pt electrode (in the absence of H₂), the corresponding waves for the reduction of **8** and the oxidation of TMP were clearly observed (blue line, **Figure 48**). The electrolyte solution was sparged with H₂ for 1 hour before a second cyclic voltammogram was recorded (red line, **Figure 48**). Although the kinetics of H₂ cleavage by this FLP system are relatively slow (refer to Chapter 3 for details), within only 1 hour of admitting the sample to H₂, clear voltammetric evidence for the formation of [**8**-H]⁻ is observed as a new, albeit small peak at +0.43 V vs Ag^{0/+}. This oxidation wave lies between the oxidation of TMP and the reduction of **8**. Although this new peak is broad and small compared with the authentic [**8**-H]⁻ owing to its low concentration, its position is characteristic of the voltammetry of [**8**-H]⁻.

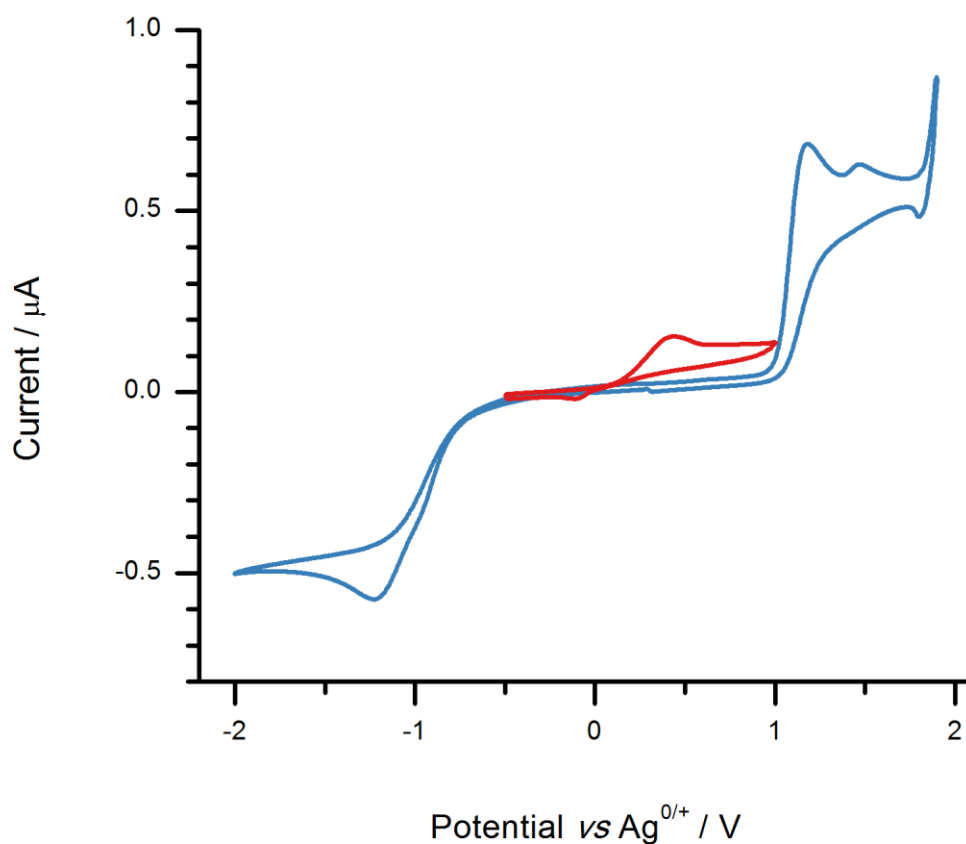


Figure 48 Overlaid CVs demonstrating the **8**/TMP FLP system (5 mM solution in CH_2Cl_2) before (blue line) and after (red line) a 1 h sparge with H_2 ($\nu = 100 \text{ mV s}^{-1}$).

The results of this chapter are less applicable to energy applications than those of Chapter 2. This is because one can oxidize H_2 directly and relatively easily at Pt when an aqueous electrolyte is used, since the electrode potential of the standard hydrogen electrode (SHE) is is $-0.64 \text{ V vs Cp}_2\text{Fe}^{0/+}$.^[14] However, in light of the findings above, it does open up the tantalizing prospect of using combined electrochemical-FLPs to activate H_2 for HAT reactions with potential applications in novel electrosynthesis.

4.6 Summary

In this chapter, the electrochemistry of $[\mathbf{8}\text{-H}]^-$ has been explored at a Pt macrodisk electrode in extension to the study in Chapter 3, which focused on carbon electrodes. Pt electrodes have been found to exhibit strong electrocatalytic surface effects for the oxidation of $[\mathbf{8}\text{-H}]^-$. Evidence for this phenomenon arises from the observation of significant current-crossover (due to a surface change) in the cyclic voltammetry of authentic $[\mathbf{8}\text{-H}]^-$ and, more

importantly, a 390 mV reduction in the oxidation peak potential compared to that obtained at a GCE.

It was postulated that the electrochemical mechanism of [8-H]⁻ oxidation involved HAT between electrogenerated [8-H][•] and the Pt electrode, forming H[•] adatoms on the surface (Pt-H). It was found that this pathway could be competitively blocked in the presence of a competing radical scavenger. Also, when cyclic voltammetry of the bulkier perchlorinated analogue, [24-H]⁻, was explored at Pt, this surface electrocatalytic effect was no longer observed. This is likely to result from steric preclusion of the H atom within the C₆Cl₅ aryl rings. Instead of this, an additional *quasi*-reversible oxidation wave was observed and tentatively assigned to the single-electron oxidation of [24-H][•].

The use of Pt electrodes in conjunction with combined electrochemical-FLP systems permits a significant energy saving for the effective conversion of chemical energy, stored in the H-H bond, to electrical energy that is available for work. The elucidated electrochemical mechanism suggests the prospect of using combined electrochemical-FLP chemistry to activate H₂ for HAT reactions *i.e.* electrosynthesis. Thus, the results of this chapter allude to the prospect of a completely new area of exploration for the combined electrochemical-FLP concept. Since this concept deviates somewhat from main the scope of the project (and the thesis), it was not explored any further.

Chapter 5

Results and discussion

Borenium cations

5.1 Overview

In Chapter 3, a combined electrochemical-FLP approach to H₂ oxidation was explored for the first time using the **8/12** FLP system. Electrochemical oxidation of the resultant borohydride, [**8-H**]⁻, was found to decrease the required potential for non-aqueous H₂ oxidation by 610 mV (117.7 kJ mol⁻¹) at carbon electrodes. However, the presence of unwanted side-reactions (namely the decomposition of **8** in the presence of H⁺), unfortunately prevented the system from turning over.

Borenium cations, [LBR₂]⁺, are an alternative family of boron-based Lewis acids that are relatively unexplored, when compared to their borane counterparts. Unlike boranes, which require strong electron withdrawing groups, the electrophilic nature of borenium cations is imparted by virtue of the positive charge at the boron centre. The electrophilicity and steric hinderance of the boron centre can be easily varied through modification of the ligand and R groups.

Despite numerous attempts to incorporate borenium cations into FLPs for H₂ activation, only a single definitive example exists in the literature – the 9-BBN-derived NHC-stabilised borenium cation (**19**⁺) reported by Stephan's group (discussed in 1.6).^[150,272] The relatively strong hydride donor ability of the neutral NHC-borane adduct, **19-H**, compared to anionic borohydrides, such as [**8-H**]⁻,^[150,156] suggests that NHC-borane adducts are likely to exhibit desirably low oxidation potentials, whilst being sufficiently electrophilic for FLP H₂ activation. In addition to this, the BDE of the B-H bond is effectively decreased by the coordination of a carbene ligand, and NHC boranes have been reported to be effective H⁺ donors.^[273,274] These properties, when combined with the reportedly improved tolerance of **19**⁺ towards different functional groups (compared to the archetypal Lewis acid, **8**) is likely to be beneficial for my electrochemical-FLP approach to H₂ oxidation.

The first example of a borenium cation that is stabilised by an NHC ligand was reported by Matsumoto and Gabbaï in 2009.^[275,276] The borenium cation, [(ImMe₂)BMe₂]⁺ (**25**⁺; ImMe₂ = C₃H₂(NMe)₂}, was prepared as the triflate salt (**25**[OTf]) by refluxing Me₂BF with Me₃SiOTf and the silver(I) NHC salt, [Ag(ImMe₂)₂][Ag₂I₃], in chlorobenzene. Whilst the electrochemical properties of **19**⁺ and **19-H** are hitherto unknown, the cyclic voltammetry of **25**[OTf] was found to be *quasi*-reversible in the conventional (and potentially non-innocent) electrolyte [ⁿBu₄N][PF₆]. Until now, the ability of **25**⁺ to effect H₂ activation as part of a FLP remains unexplored or, at least, unreported.

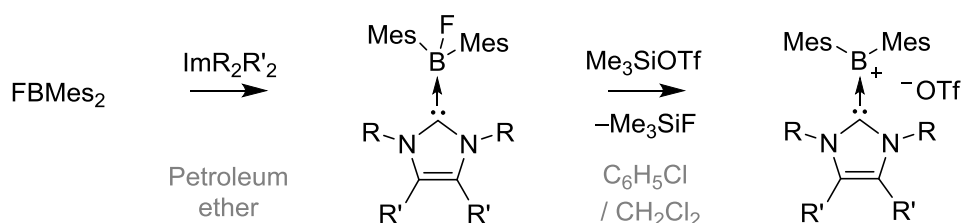
In this chapter, the combined electrochemical-FLP approach is extended from triarylboranes to NHC-stabilised borenium cations. Firstly, the redox chemistry of several (new

and previously reported) NHC-stabilised borenium cations was explored. This allowed an assessment of the H₂-activation abilities of these borenium cations, as part of a FLP system, to be made. Finally, the suitability of the most promising candidate (**19**⁺) for the combined electrochemical-FLP approach was explored using a similar protocol to that of Chapter 3. This involved an electrochemical study of the NHC-borane adduct (**19**-H) and recycling experiments. The results suggest that the substitution of **8** for **19**⁺ gives significant improvements in the recyclability of the Lewis acid, along with a desirable further decrease in the voltage that is required to oxidise the B-H bond. Some of the results contained in this chapter have been published in the journal *Angewandte Chemie International Edition*.^[277]

5.2 Synthesis and characterization of the borenium cations

Firstly, the literature compounds **19**[B(C₆F₅)₄] and **25**[OTf] were prepared. **19**[B(C₆F₅)₄] was prepared according to the literature method of Farrell *et al.*^[150] However, Matsumoto and Gabbaï's original literature procedure^[275,276] for the preparation of **25**[OTf] proved to be difficult in my hands. Additionally, the conditions required (a chlorobenzene reflux at 131°C) seemed rather excessive and the resulting product contained imidazolium triflate salt as an impurity (5%).

I decided to use an alternative method, which gave the required product in relatively good yield and purity at room temperature (**Scheme 36**). Instead of using a NHC silver (I) complex as an NHC transfer agent, I decided to use the free NHC species. Treatment of FBMe₂ with ImR₂R'₂ gave the intermediate NHC-borane adduct (**25**-F). This was then separated from the reaction mixture before F⁻ abstraction was performed with Me₃SiOTf to give the product **25**[OTf]. This step-wise approach gave good results without the need for forcing conditions.



Scheme 36 Preparation of **25**[OTf] (R = Me, R' = H), **26**[OTf] (R = *i*Pr, R' = H) and **27**[OTf] (R, R' = Me).

The NHC, ImMe₂, is an unstable oil when isolated, but persists in THF solution for days at -30°C without substantial decomposition.^[278] I found that it was best to generate and use this directly *in situ*, following deprotonation of the imidazolium chloride salt with NaH. This synthetic method is, of course, limited by the stability of the free carbene. Indeed, this reaction was much

easier and cleaner to perform when the bulkier and more persistent Im^iPr_2 analogue was used. The novel NHC-stabilised borenium salt, $[(\text{Im}^i\text{Pr}_2)\text{BMes}_2][\text{OTf}]$, **26** $[\text{OTf}]$, simply precipitated from the chlorobenzene reaction mixture as a pale yellow solid. Using the same method, the new borenium compound $[(\text{ImMe}_4)\text{BMes}_2][\text{OTf}]$, **27** $[\text{OTf}]$, was also prepared using ImMe_4 .

The steric constraints of the groups around the boron centre in **26** $^+$ are apparent from the ^1H NMR spectrum. Separate singlet resonances are observed for each *ortho*- CH_3 environment of the Mes rings at δ 2.06 and 1.92 ppm. Free rotation of the Mes rings about the B-C bond is impeded by the steric bulk of the Mes groups and NHC ligand. Fluxionality is not exhibited on the NMR timescale, leading to the presence of two signals instead than one signal. This phenomenon was also observed for **25** $^+$.^[275,276] In the case of **26** $^+$, the CH_3 protons from the NHC ^iPr groups are diastereotopic and give rise to the observation of separate doublet resonances at δ 1.46 and 1.15 ppm. This is not the case for **19** $^+$, where the lack of steric encumbrance allows the free rotation of the NHC about the axis of the B-C bond *i.e.* the neighbouring B centre is not chiral.

The molecular structures of the cations **25** $^+$ and **26** $^+$ are shown in **Figure 49**. Crystals of **26** $[\text{OTf}]$ (colourless blocks), suitable for X-ray crystallography, were grown by dissolving the sample in a minimum quantity of CH_2Cl_2 at room temperature, slowly layering with Et_2O and allowing to stand at room temperature. X-ray diffraction data was collected by the EPSRC National Crystallography Service and data solution and refinement was kindly performed by Dr. R. Blagg. Single crystal diffraction data was also collected for **27** $[\text{OTf}]$, but was unfortunately not of a sufficient quality to confirm atomic connectivity without the use of an excessive number of constraints.

In the case of **25** $[\text{OTf}]$ and **26** $[\text{OTf}]$, all structures have a trigonal planar geometry about the boron centre as indicated by the sum of bond angles, which equal 360° .^[150,275,276] For **26** $^+$, the B1-C1 bond connecting the boron centre to the Im^iPr_2 ligand is of a comparable length to that in **25** $^+$ [1.589(2) vs 1.579(7) Å, respectively]. The angle between the two trigonal planes about the boron and the carbon atom of the NHC ligand (C1) is 37.19° and 52.19° for **25** $^+$ and **26** $^+$, respectively. This reflects the increased steric influence of the bulkier Im^iPr_2 ligand compared to ImMe_2 . Indeed, in **26** $^+$, the average torsion angle between the Mes rings and the boron trigonal plane (52.3°) is similar to that between the NHC ligand and the boron plane (46.1°). This is in contrast with **25** $^+$, where the corresponding average torsion angle for the NHC ligand (37.2°) is much more acute than that of the Mes rings (54.32°).

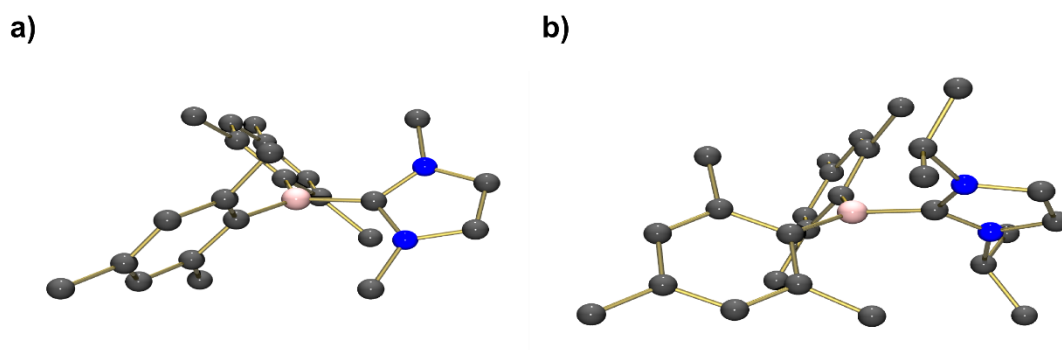


Figure 49 Molecular structures of the dimesitylborenium cations a) 25^+ ,^[275,276] and b) 26^+ .

5.3 Electrochemical study of the borenium cations

Cyclic voltammetric data for $25[\text{OTf}]$, $26[\text{OTf}]$ and $27[\text{OTf}]$ were recorded under my supervision by Ms. K. Resner, whereas data for $19[\text{B}(\text{C}_6\text{F}_5)_4]$ were recorded by myself (**Figure 50**). For consistency, and to allow the cyclic voltammetry of the borenium compounds to be directly compared to that of the original $8/[8\text{-H}]^-$ system (in Chapters 3 and 4), the weakly coordinating supporting electrolyte system $\text{CH}_2\text{Cl}_2/[\text{nBu}_4\text{N}][\text{B}(\text{C}_6\text{F}_5)_4]$ was selected for all electrochemical experiments (which were performed at GCEs).

On sweeping the potential cathodically from the OCP at 100 mV s^{-1} , a reduction wave was observed for all four borenium cations. On the return scan, a large back-peak was observed for 25^+ , 26^+ and 27^+ at mid-peak potentials of -1.62 , -1.72 , and $-1.75 (\pm 0.01) \text{ V vs Cp}_2\text{Fe}^{0/+}$, respectively. The peak-to-peak separation was always in excess of 57 mV , expected for a fully-reversible single-electron system, suggesting that the dimesitylborenium cations exhibit *quasi*-reversible voltammetry. This is in agreement with what was observed by Matsumoto and Gabbaï for the voltammetric reduction of 25^+ using the supporting electrolyte, $[\text{nBu}_4\text{N}][\text{PF}_6]$.

In the case of 19^+ , a reduction wave was observed at $-1.97 \pm 0.01 \text{ V vs Cp}_2\text{Fe}^{0/+}$ (at 100 mV s^{-1}), however there was no back-peak present, even at voltage scan rates as high as 1000 mV s^{-1} . This effect is highly indicative of an underlying *EC* mechanism, and suggests that a rapid chemical follow-up step is in existence. This is likely to be analogous to the chemical follow-up process involved in the corresponding reduction of 8 (discussed in Chapter 2) – which primarily involved the reaction of the radical species with the solvent. However, in the case of 8 , the chemical decomposition kinetics of 8^{*-} were beginning to be outrun at scan rates of 750 mV s^{-1} or greater, as evidenced by the return of a back-peak. This was not the case for the reduction of

19⁺, since the back-peak was absent, even at scan rates as high as 1000 mV s⁻¹. This suggests that the electro-reduced species is very short-lived and rapidly undergoes decomposition before it has time to diffuse away from the electrode surface.

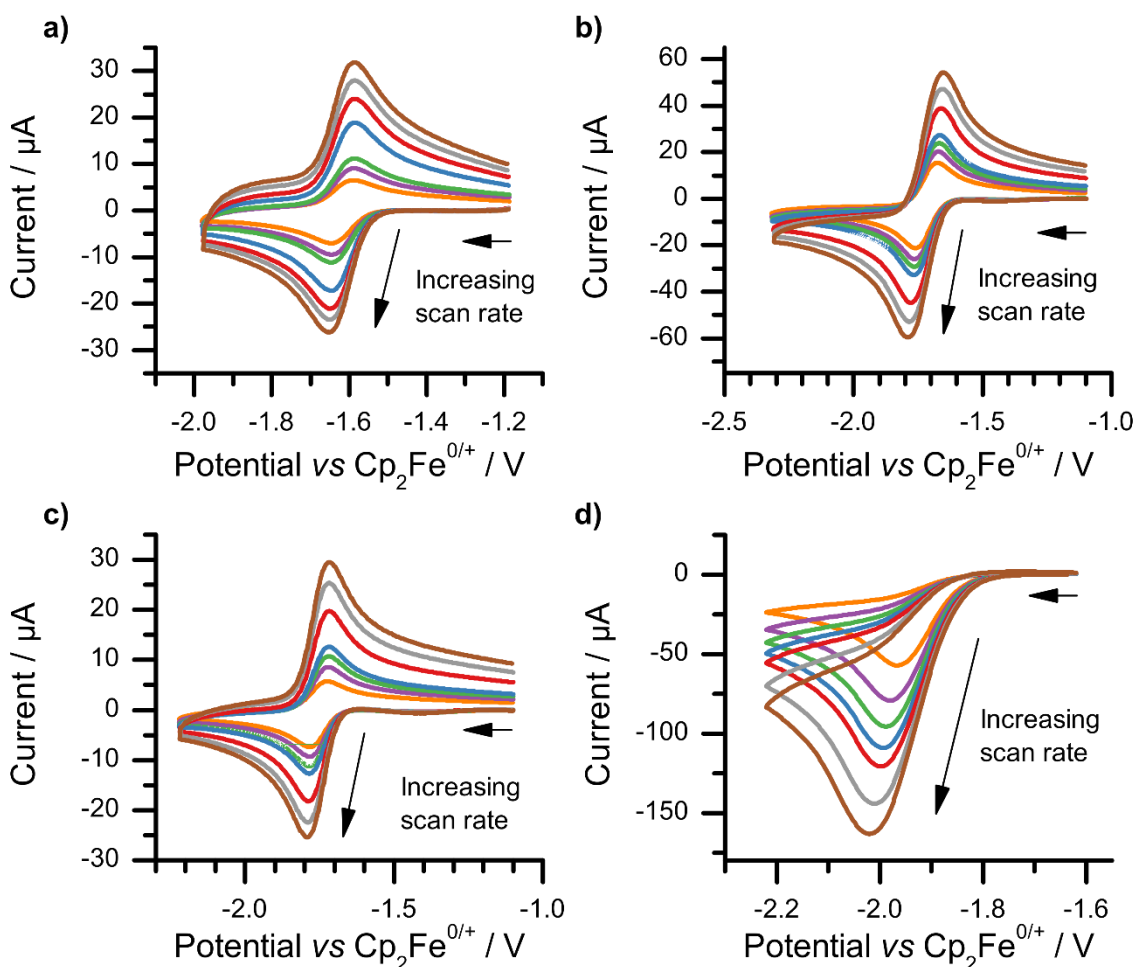
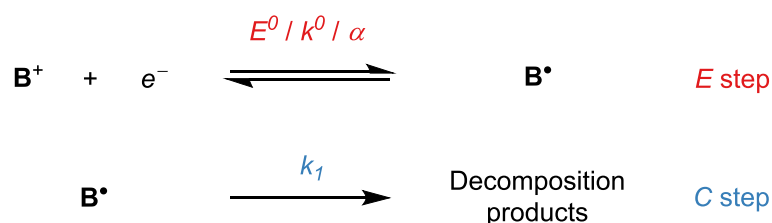


Figure 50 Overlaid CVs for the borenium cations a) **25**[OTf] (1.9 mM), b) **26**[OTf] (1.5 mM), c) **27**[OTf] (1.4 mM), and d) **19**[B(C₆F₅)₄] (4.3 mM) recorded in CH₂Cl₂ at a GCE over the scan rate (ν) range 100-1000 mV s⁻¹.

Digital simulation of the experimental CVs for the reduction of **25**⁺, **26**⁺ and **27**⁺ at a GCE was performed. Initially, the voltammetric reduction of each borenium cation (generically denoted as **B**⁺) was simply modelled as a *quasi*-reversible, single-electron process (*E* mechanism). It was assumed that the electrogenerated neutral NHC-boryl radical species (**B**[•]) was persistent throughout the experimental timescale, becoming re-oxidised (to **B**⁺) on the return scan. However, this assumption resulted in a poor fit for the oxidation wave on the return scan; the simulated current was consistently too large in the case of **25**⁺, **26**⁺ and **27**⁺. Instead, an excellent fit between experimental and simulated CVs (see **Figures 51-54**) was obtained when the

electrochemical reduction of \mathbf{B}^+ was modelled as an *EC* process (shown in **Scheme 37**). This was true for all the borenium cations studied, including $\mathbf{19}^+$.



Scheme 37 The proposed mechanism and associated thermodynamic and kinetic parameters used in digital simulation of the voltammetric reduction of borenium cations (\mathbf{B}^+) $\mathbf{25}[\text{OTf}]$, $\mathbf{26}[\text{OTf}]$, $\mathbf{27}[\text{OTf}]$ and $\mathbf{19}[\text{B}(\text{C}_6\text{F}_5)_4]$ at a GCE.

The simulated CVs do not take contributions from capacitive charging currents into account *i.e.* non-Faradaic current due to electrolyte migration effects (refer to 1.7 for further discussion). Since the experimental data is baseline corrected before simulation, this is not a problem for the forward scan. In the case of the return scan, however, the total current for the oxidation wave includes contributions from both the redox process and capacitive charging. This issue is applicable in the case of the borenium cations $\mathbf{25}^+$, $\mathbf{26}^+$, and $\mathbf{27}^+$. The capacitive charging current contributions were estimated for each scan rate by extrapolating from a region where no Faradaic current was being passed (just before the onset of the back-peak on the return scan) to the observed peak potential for the back-peak (where the current is mainly Faradaic). In **Figures 51b-53b**, open squares denote the simulated peak currents, following an attempt to correct for capacitive charging current contributions. In **Figures 51-53a** the fitted CV is only shown for the 200 mV s^{-1} scan rate. This is because the current offset, arising from capacitive charging currents, makes it difficult to clearly distinguish the separate fits. The goodness of fits can be appreciated by considering the Randles-Sevcik and Laviron plots in **Figures 51b-53b** and **Figures 51c-53c**, respectively.

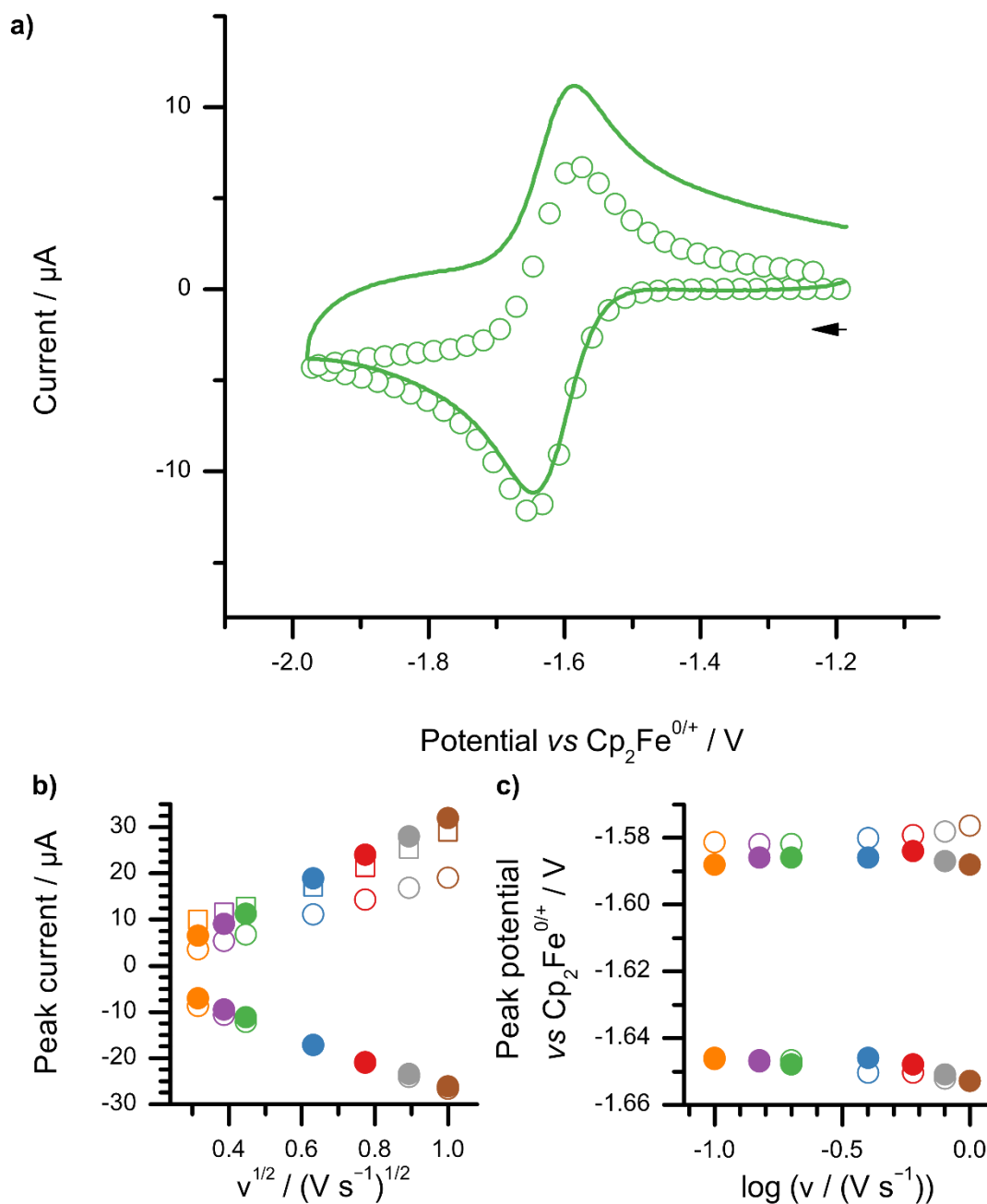


Figure 51 a) Experimental (line) and simulated (open circles) CV for the reduction of **25**[OTf] (1.9 mM) at a GCE in CH_2Cl_2 ($\nu = 200 \text{ mV s}^{-1}$); b) corresponding Randles-Sevcik plot comparing simulated (open circles/squares) and experimental (closed circles) peak currents against the square root of scan rate (ν). Open circles denote non-corrected peak current values whereas open squares attempt to account for current contributions due to capacitive charging (C_{dl}); c) corresponding Laviron plot comparing simulated (open circles) and experimental (closed circles) peak potentials against the logarithm of scan rate (ν). $\nu = 100, 150, 200, 400, 600, 800, 1000 \text{ mV s}^{-1}$.

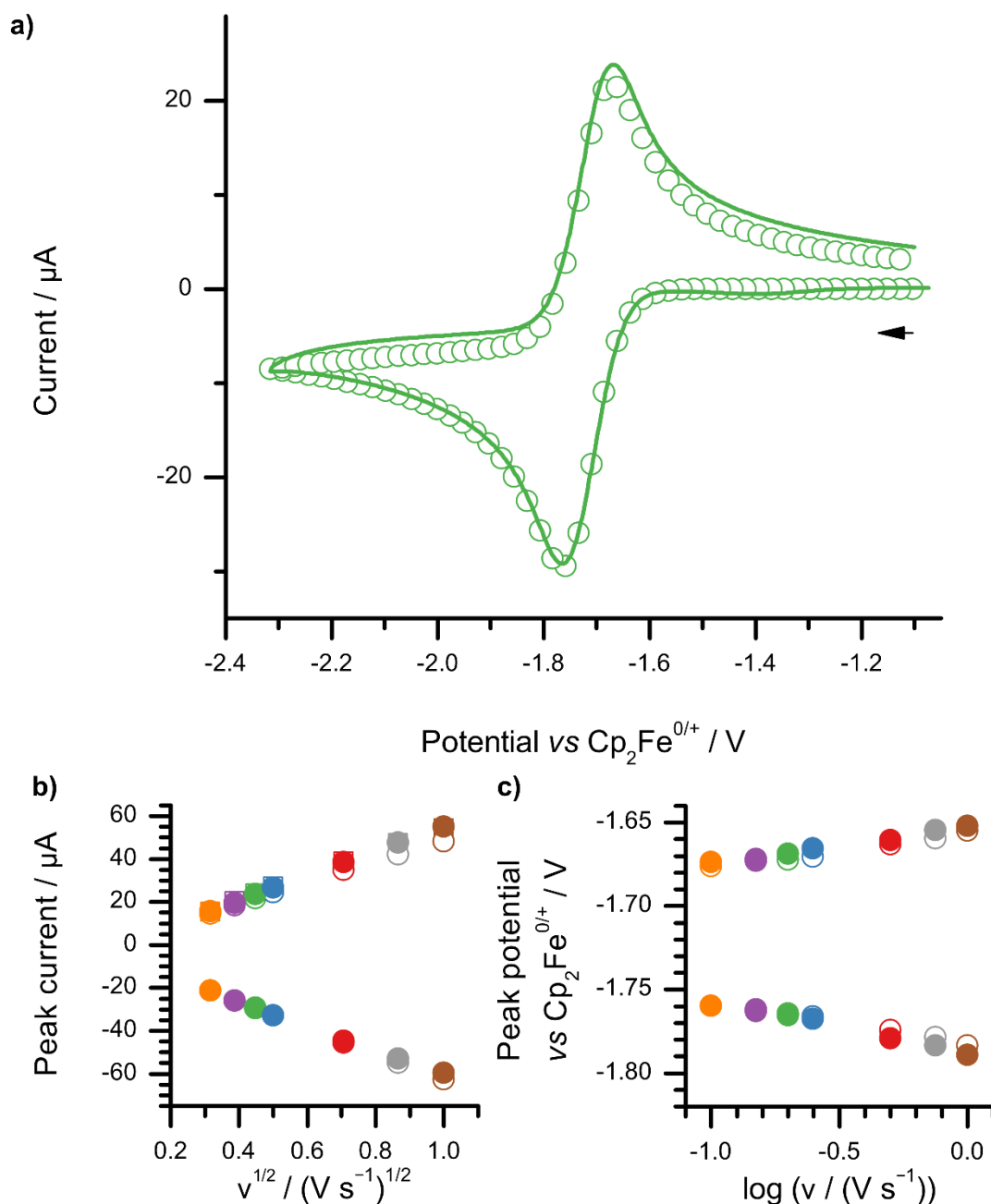


Figure 52 a) Experimental (line) and simulated (open circles) overlaid CVs for the reduction of **26**[OTf] (1.5 mM) at a GCE in CH_2Cl_2 ($v = 200 \text{ mV s}^{-1}$); b) corresponding Randles-Sevcik plot comparing simulated with (open circles) and without (open squares) C_{dl} corrections and experimental (closed circles) peak currents against the square root of scan rate (v); c) corresponding Laviron plot comparing simulated (open circles) and experimental (closed circles) peak potentials against the logarithm of scan rate (v). $v = 100, 150, 200, 250, 500, 750, 1000 \text{ mV s}^{-1}$.

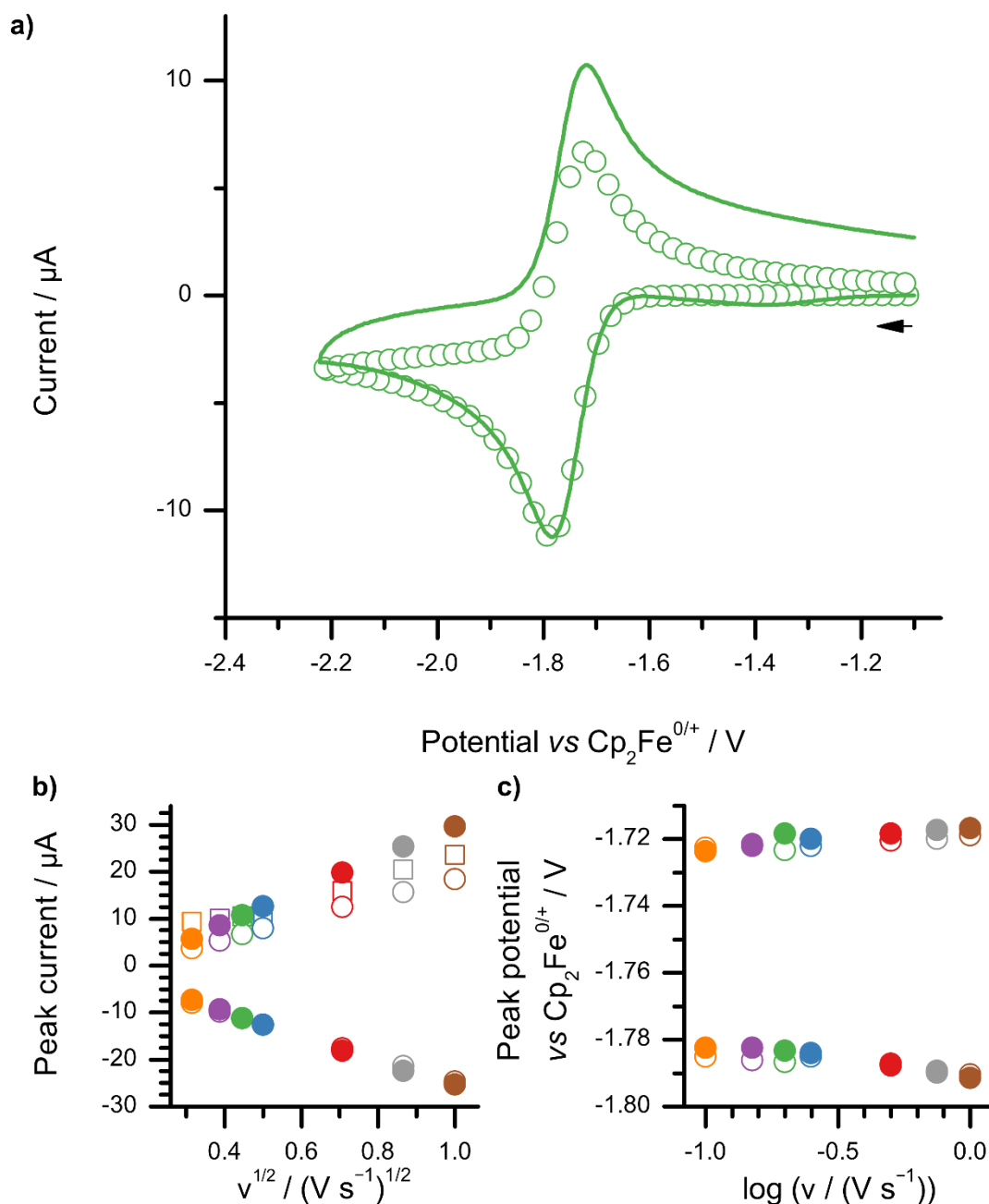


Figure 53 a) Experimental (line) and simulated (open circles) overlaid CVs for the reduction of **27**[OTf] (1.4 mM) at a GCE in CH_2Cl_2 ($\nu = 200 \text{ mV s}^{-1}$); b) corresponding Randles-Sevcik plot comparing simulated with (open circles) and without (open squares) C_{dl} corrections and experimental (closed circles) peak currents against the square root of scan rate (ν); c) corresponding Laviron plot comparing simulated (open circles) and experimental (closed circles) peak potentials against the logarithm of scan rate (ν). $\nu = 100, 150, 200, 250, 500, 750, 1000 \text{ mV s}^{-1}$.

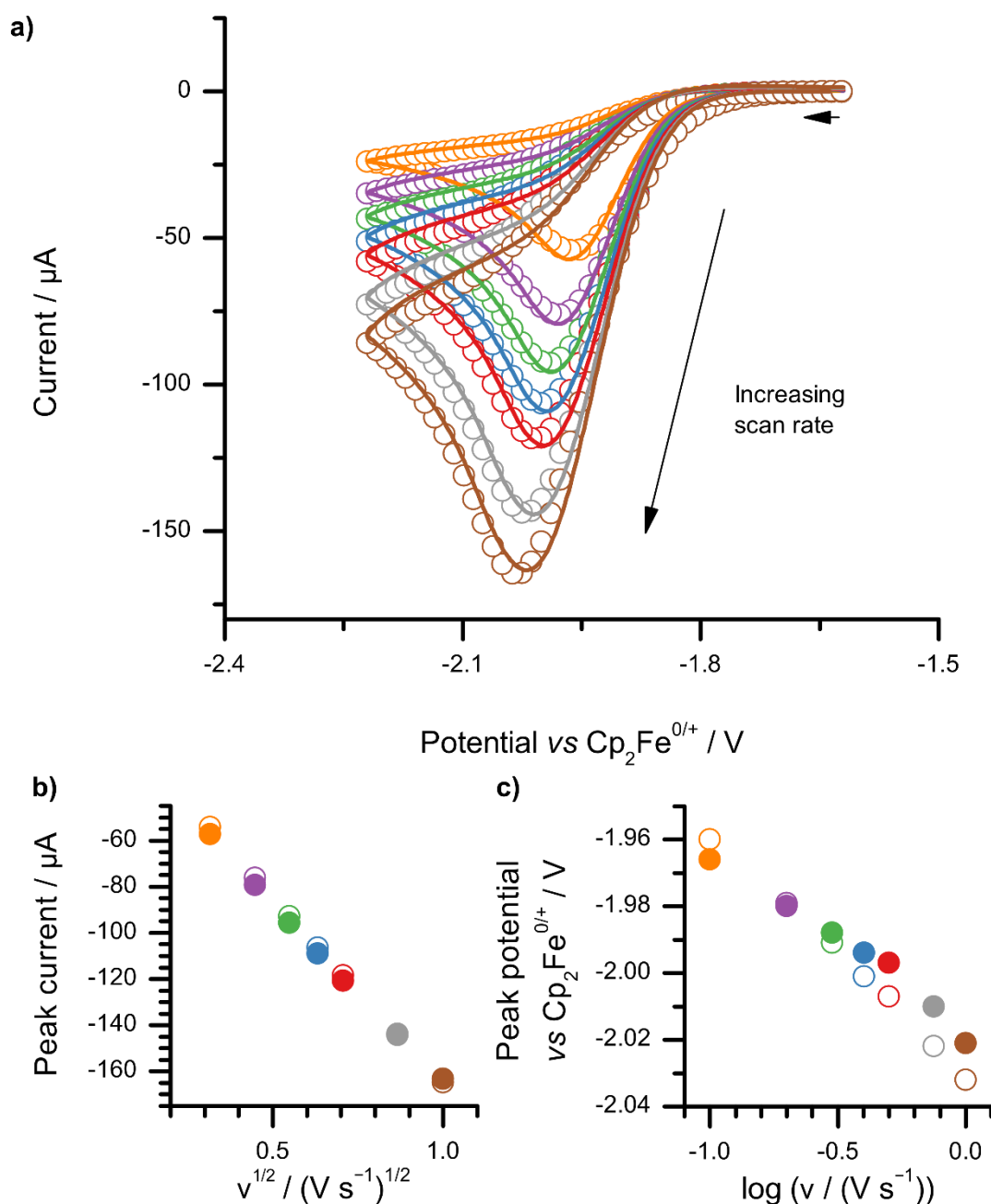


Figure 54 a) Experimental (line) and simulated (open circles) overlaid CVs for the reduction of $19\text{B}(\text{C}_6\text{F}_5)_4$ (4.3 mM) at a GCE in CH_2Cl_2 (multiple scan rates, see below); b) corresponding Randles-Sevcik plot comparing simulated (open circles) and experimental (closed circles) peak currents against the square root of scan rate (v); c) corresponding Laviron plot comparing simulated (open circles) and experimental (closed circles) peak potentials against the logarithm of scan rate (v). $v = 100, 200, 300, 400, 500, 750, 1000 \text{ mV s}^{-1}$.

The proposed *EC* mechanism (**Scheme 37**) is comparable to that proposed in Chapter 2 for the **8/8⁺** redox couple. The electrogenerated species, **B[•]**, is susceptible to decomposition in solution through reaction with the solvent to give a complex product mixture. The presence, or absence, of a back-peak on the reverse scan is dependent on the chemical rate constant, k_1 . Relevant electrochemical and chemical parameters, extracted from digital simulation of the experimental CVs, are summarized in **Table 6**.

Table 6 Globally optimized best-fit thermodynamic and kinetic parameters obtained from digital simulation of the voltammetric data for **25**[OTf], **26**[OTf], **27**[OTf] and **19**[B(C₆F₅)₄] at a GCE, following the mechanism proposed in **Scheme 37**.

Redox parameters	Borenium cation			
	25 ⁺	26 ⁺	27 ⁺	19 ⁺
$E^0 / \text{V vs Cp}_2\text{Fe}^{0/+}$	-1.61 ± 0.05	-1.71 ± 0.05	-1.75 ± 0.05	-1.94 ± 0.05
$k^0 / 10^{-2} \text{ cm s}^{-1}$	6.0 ± 0.1	1.1 ± 0.1	6.4 ± 0.1	0.34 ± 0.1
α	0.5 ± 0.05	0.5 ± 0.05	0.5 ± 0.05	0.6 ± 0.05

Chemical parameters	Borenium cation			
	25 ⁺	26 ⁺	27 ⁺	19 ⁺
k_1 / s^{-1}	0.14 ± 0.05	0.02 ± 0.005	0.10 ± 0.05	$> 2 \times 10^{13}$
$D / 10^{-5} \text{ cm}^2 \text{ s}^{-1}$	1.64 ± 0.1	1.01 ± 0.1	1.01 ± 0.1	0.987 ± 0.1

The formal reduction potentials (E^0), extracted from digital simulation, suggest the electrophilicity series: **25⁺** > **26⁺** \approx **27⁺** > **19⁺**, with **19⁺** being significantly less electrophilic (lower E^0) than the dimesitylborenium cations: **25⁺**, **26⁺** and **27⁺**. The error in the E^0 values for **26⁺** and **27⁺** is greater than the difference between the two values ($\Delta E^0 \approx 0.04 \pm 0.07 \text{ V}$), therefore the electrophilicity order cannot be differentiated for this pair (hence why **26⁺** \approx **27⁺**)

The electronic effects of seventy-six different NHCs have been quantified by Gusev through the measurement of CO ligand infrared (IR) spectroscopic symmetrical stretching frequencies (ν_{CO}) for Ni(CO)₃(NHC).^[279] The lower the ν_{CO} value, the weaker the CO-Ni bond,

suggesting that there is increased electron density on the Ni centre that is available for back-donation to the CO ligand (into the CO π^* orbital). The increased electron density comes from the NHC ligand and therefore ν_{CO} is a good indicator of the relative electron-donating ability of the NHC ligand. The reported ν_{CO} values for the NHC ligands; ImMe₂, ImⁱPr₂ and ImMe₄; are 2054.1, 2051.5 and 2051.7 cm⁻¹, respectively. Based on this, the predicted electrophilicity series for the dimesitylborenium cations is: **25**⁺ > **27**⁺ > **26**⁺, since increasing the electron-donating ability of the NHC ligand is expected to decrease the electrophilicity of the boron centre (and therefore result in a lower reduction potential). This approach also suggests that the electrophilicity strength of **26**⁺ and **27**⁺ are comparable, since the reported ν_{CO} values for the ImⁱPr₂ and ImMe₄ NHC ligands are similar ($\Delta\nu_{CO} = 0.2$ cm⁻¹).

Previous DFT and EPR studies of **25**[•] suggested that the spin density electron is localized in the B-C π -bonding orbital of the ligand, with notable polarization towards the B atom.^[275,276] Considering that there is very little difference in the electronic properties of the NHC ligands used (and they are all poor π acceptors), it is reasonable to assume that the same is true for **26**[•], **27**[•] and **19**[•]. Thus it is likely that any decomposition of the NHC-boryl radicals occurs through reaction with solvent at the boron centre, to form a mixture of various redox-inactive, four-coordinate borates (comparable to the decay of **8**^{•-}, discussed in Chapter 2). The rate of the NHC-boryl radical decomposition step (k_1), and the size of the oxidative back-peak in the cyclic voltammetry, is likely to be a function of the steric preclusion of the boron centre by the surrounding substituents and the NHC ligand R groups. This is illustrated by space-fill models of the borenium cations (shown in **Figure 55**), assuming that no significant structural reorganisation occurs on reduction. The boron atoms are shown in pink. It is clear that the boron atom is most exposed in **19**⁺ (**Figure 55c**), and most sterically encumbered in **26**⁺ (**Figure 55b**). The Mes groups (in **25**⁺ and **26**⁺) are extremely good at sterically protecting the boron centre, whereas the 9-BBN ring system is simply not bulky enough. These steric effects rationalize why the rate constant (k_1) for the decomposition of unencumbered **19**[•] is extremely fast and under diffusion control ($>10^{10}$ s⁻¹), whereas k_1 values for the much bulkier radicals (**25**[•], **26**[•] and **27**[•]) are very small indeed (<0.15 s⁻¹). It is important to note that the electrochemical reduction process is independent of the counteranion, provided that there is no significant ion-pairing between the cation and anion of the borenium salts.

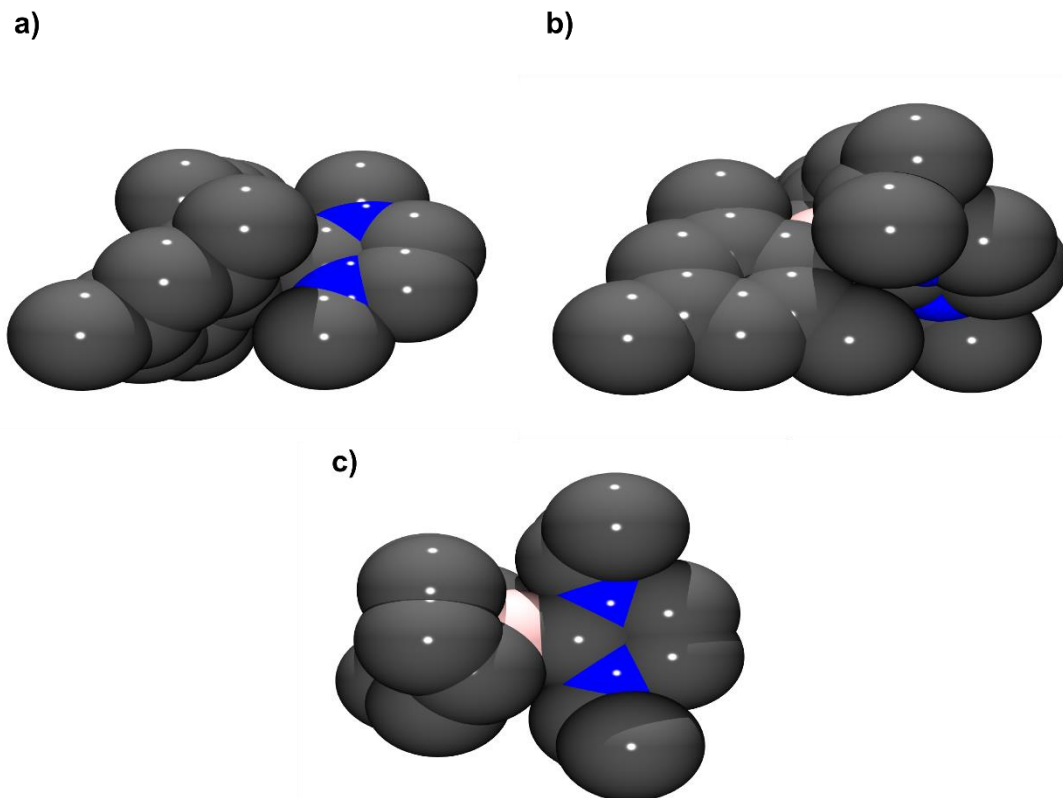


Figure 55 Space-filling view of the borenium cations of a) **25**⁺,^[275,276] b) **26**⁺, c) **27**⁺, and d) **19**⁺^[150] showing the extent of steric shielding of the boron centre by the surrounding groups.

The slow rate constants for the decomposition of **25**[•], **26**[•] and **27**[•] would be advantageous for the electrochemical-FLP system. This is because negligible quantities of Lewis acid would be lost during the borohydride oxidation process through decomposition of the transient NHC-boryl radical, between the first and second successive electron transfer steps. Indeed, a long-lived radical intermediate would make the process truly catalytic. The fact that the stability of such compounds is unaffected by the cheaper and more readily available supporting electrolyte, [ⁿBu₄N][PF₆], would also be highly advantageous.

5.4 Study into FLP H₂ activation

The **19**⁺/**12** system is already proven for H₂ activation, making **19**[B(C₆F₅)₄] an ideal candidate for the exploration of H₂ oxidation using a combined electrochemical-FLP approach. Additional screening was therefore not required. However, the NHC-stabilised dimesitylborenium cations (**25**⁺, **26**⁺ and **27**⁺) exhibited very unusual behaviour when they were screened for H₂ activation as part of a **B**⁺/**12** pair.

Since **26**⁺ is structurally related to **19**⁺ (it has the same NHC ligand), its H₂ activation ability was explored first. When a solution containing equimolar quantities of **26**[OTf] and **12** in CD₂Cl₂ was admitted to H₂ (4 atm), H₂ activation was not immediately observed using NMR spectroscopy. When the sample was left to stand at room temperature overnight, it surprisingly became bright blue in colour (see **Figure 56**). This colour persisted for over 40 days; however, after 49 days at room temperature, it was noted that the sample had become brown in colour. Over this time period, the reaction progress was monitored using NMR spectroscopy, and revealed a number of slowly evolving signals in the ³¹P{¹H} NMR spectra at δ 122.9 (s) and 50.3 (t, *J* = 22 Hz) ppm. These signals appeared at either side of the P^tBu₃ (**12**) singlet signal, which was observed at δ 62.5 ppm. The ¹¹B NMR spectra did not change significantly from that of free **26**⁺ (δ 68 ppm), suggesting that the activation process is not necessarily boron-centered. However, a small additional signal was also observed at δ -11.1 ppm. The NMR spectra that were obtained for the brown solution suggested that the reaction was complete after the 49 day period (the previously observed ³¹P{¹H} NMR signal that corresponded to **12** was no longer apparent). The blue colour possibly indicated the presence of an intermediate radical species, however it is unlikely that there was a large concentration of this species present at any one time, since the NMR spectra did not appear to be paramagnetically shifted.

Curiously, when a molar equivalent of **12** was added to **26**⁺ in CDCl₃, an almost immediate colour change to dark brown was observed (**Figure 56**). This initially suggests that the acidity of the solvent likely plays a role in the observed rate of reaction. The ³¹P{¹H} NMR spectrum showed the presence of two singlet signals (with equal integration values) at δ 122.8 and 46.7 ppm. The former signal is the same as that observed in the reaction with CD₂Cl₂, whereas the latter signal is slightly upfield of that observed for the CD₂Cl₂ activation product. Considering that [^tBu₃P(CH₃)]⁺ gives a ³¹P{¹H} NMR resonance at δ 50 ppm,^[280] the signal at δ 46.7 ppm can be tentatively assigned to the species, [^tBu₃P(CCl₃)]⁺, whereas the 1:1:1 triplet signal resulting from CD₂Cl₂ activation, at δ 50.3 ppm, is tentatively attributed to the formation of [^tBu₃P(CDCl₂)]⁺. Further evidence for the formation of [^tBu₃P(CDCl₂)]⁺ was provided by the observation of a singlet ³¹P{¹H} NMR resonance at δ 50.7 ppm when the reaction was performed in CH₂Cl₂ instead of CD₂Cl₂ – this is indicative of [^tBu₃P(CHCl₂)]⁺. This evidence for phosphine methylation suggests that an electron transfer process may be involved, proceeding *via* the radical cation species, **12**^{•+}.^[281–283] It is uncertain what may be responsible for the chemical oxidation of **12**. In both cases, the signal at δ 122.8 could not be assigned. As before, the ¹¹B NMR spectrum did not deviate significantly from that of free **26**⁺ (δ 67 ppm), although there was a small additional signal at δ -5.4 ppm. The ¹H NMR displayed an upfield shift (Δδ = -0.7 ppm) in the protons that correspond to the unsaturated CHCH backbone of the NHC ligand, with the

relative integral halving from 2 to 1. This observation led me to believe that abnormal carbene adduct formation (**Figure 57**) may be apparent,^[125,147] where the boron centre is now bound to the C-4 NHC ring position and the C-2 position is now bound to a D substituent, originating from the NMR solvent (no additional proton signals were observed for the C-2 position in the ¹H NMR spectrum).



Figure 56 Photograph of samples obtained after 24 hours when **26**[OTf] is treated with a molar equivalent of **12** in either CD₂Cl₂ (top) or CDCl₃ (bottom).

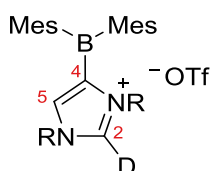


Figure 57 Initially proposed abnormal carbene adduct with C-2, C-4, and C-5 positions labelled in red.

When H₂ activation was attempted in CH₃CN using the **26**⁺/**12** pair, no H₂ cleavage was immediately observed. NMR spectra revealed **26**[OTf] and **12** to be present as separate species (no adduct formation), and no significant reaction had appeared to have occurred with the solvent. However, after leaving the sample under H₂ for 10 days, the appearance of trace amounts of the H₂ cleavage product was suggested by the presence of a very small doublet in the ¹¹B NMR spectrum at δ -19.7 ppm ($J = 84$ Hz). This is likely to be indicative of the formation of **26**-H. Evidence for the presence of trace amounts of [HP^tBu₃]⁺ in the ³¹P{¹H} NMR was given by the appearance of a very small singlet resonance at approximately δ 60 ppm. The H₂ activation reaction did not go any further towards completion, despite leaving the sample for

several weeks and even heating the sample at 60°C for several hours in an attempt to drive the reaction forward. **25**[OTf] was not found to be successful for the H₂ activation either. Perhaps the boron centre of the dimesitylborenium compounds is too sterically precluded to allow the formation an encounter complex with the correct geometry for H₂ activation. One may also speculate that ion-pairing between the borenium cation and the counterion (if present, and to what extent) could influence the propensity of such compounds for H₂ activation.^[284] Indeed, the anion [B(C₆F₅)₄]⁻ is less coordinating than [OTf]⁻.^[285,286] Ingleson and co-workers previously found that the fierce electrophilicity of borenium cations can often lead to deactivation reactions, such as ligand deprotonation, preventing their incorporation into FLPs for H₂ activation.^[272]

To further investigate the possibility of abnormal carbene adduct formation, the tetramethylated-borenium cation **27**⁺ was utilized in order to prevent binding at the C-4 and C-5 NHC ring sites. When a solution of **27**[OTf] in CDCl₃ was treated with a molar equivalent of **12**, ¹H, ³¹P{¹H} and ¹¹B NMR spectra showed no change after 30 minutes. However after leaving the solution for approximately 6 hours at room temperature, the sample had become dark brown in colour. The ³¹P{¹H} NMR spectrum showed the same signals to be present at δ 122.8 and 46.7 ppm, as observed previously for **26**⁺. This observation rebuts the previous comment regarding the formation of abnormal carbene adducts, since the same reaction is observed even when the binding sites (at the C-4 and C-5 positions) are blocked by Me substituents. The chemical shifts of the ³¹P{¹H} NMR resonances also suggest that the P-containing products are not specific to the NHC ligand employed.

Crystals, suitable for X-ray crystallography, were grown from concentrated CH₂Cl₂ and CDCl₃ reaction mixtures of **12** and **26**⁺ *via* the slow evaporation of solvent – a residual brown oil was also apparent. The samples produced multiple crystal morphologies. Both samples resulted in the same unit cell, which corresponded to that of **26**[OTf]. However, for the CH₂Cl₂ sample, another crystal morphology resulted in a different unit cell. When this data was solved and refined by Dr. R. Blagg, it was found to correspond to **26**[Cl]. This suggests that solvent breakdown results in the generation of free Cl⁻, which results in some metathesis of **26**[OTf]. This result generally supports the notion that the borenium cation remains intact (as evidenced by ¹¹B NMR spectroscopy), and suggests that it may catalyse solvent decomposition reactions in the presence of **12**, possibly [CH_(3-n)Cl_n]⁺ (*n* = 1-3) abstraction.^[287] It is highly likely that the tetraalkylphosphonium triflate/chloride salts behave as ionic liquids (the brown oil that was observed), and would be almost impossible to crystallise.^[288]

Since, the solvent activation mechanism and its associated products could not be elucidated, **25**[OTf], **26**[OTf] and **27**[OTf] were not explored any further. All further

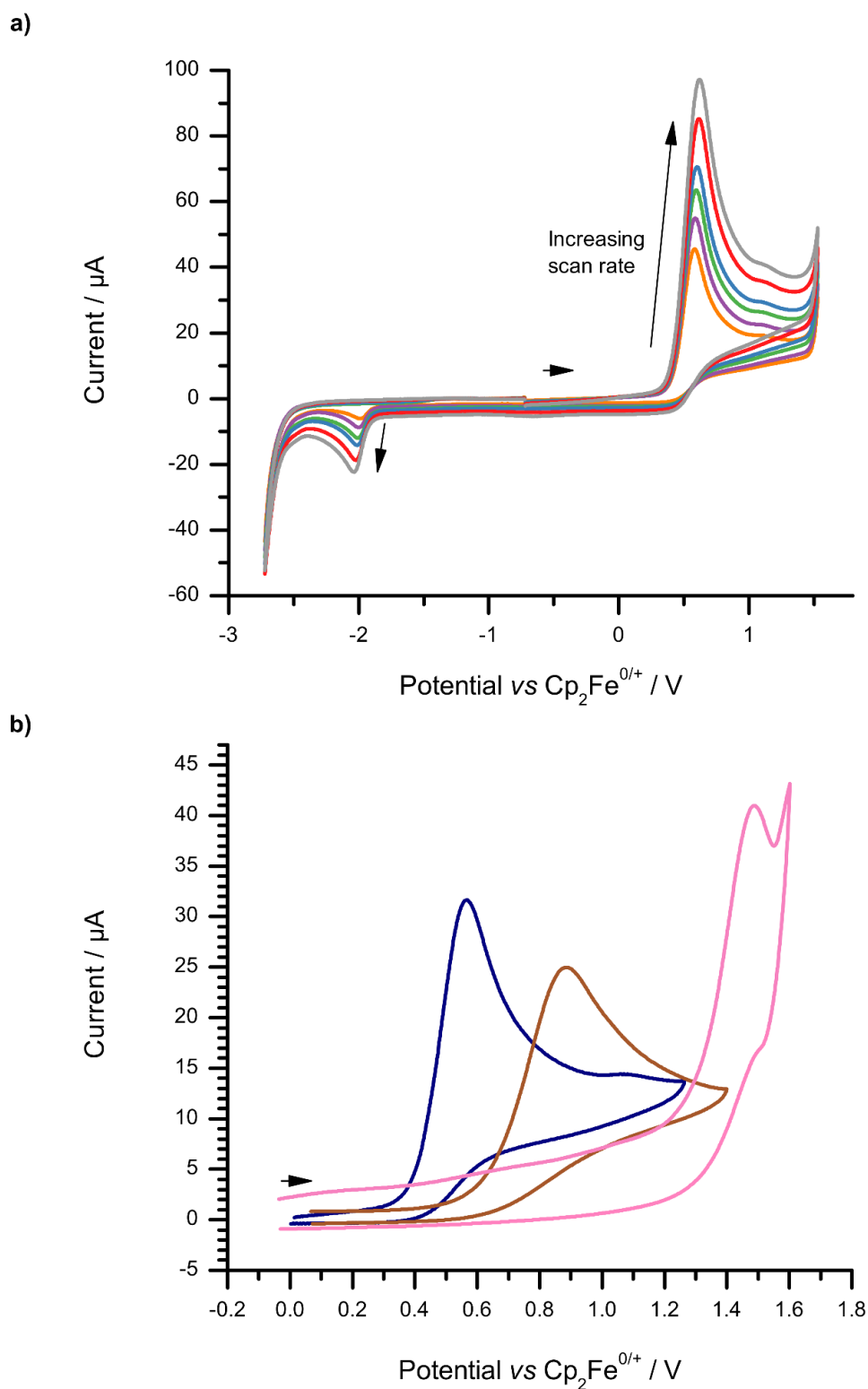


Figure 58 a) Overlaid CVs of **19-H** (2.0 mM) in CH₂Cl₂ recorded at scan rates (ν) of 200, 300, 400, 500 and 750, and 1000 mV s⁻¹ at a GCE; b) CVs at a GCE comparing CH₂Cl₂ solutions of **19-H** (2.0 mM, navy blue), [ⁿBu₄N][**8-H**] (2.0 mM, brown), and H₂ (saturated, pink) at scan rates (ν) of 100 mV s⁻¹.

Upon the application of an oxidising potential, **19**-H undergoes single-electron oxidation to form a transient [**19**-H]^{•+} species. This then undergoes rapid dissociation in solution to give H⁺ and the neutral NHC-boryl radical, **19**[•]. Since the applied potential is very positive of the formal potential for the **19**⁺/**19**[•] couple ($E^0 = -1.94 \pm 0.05$ V vs Cp₂Fe^{0/+}, see 5.3 *vide supra*), this radical undergoes a second one-electron oxidation to generate **19**⁺. This second oxidation occurs in competition with the following side reactions:

- i) The decomposition of **19**[•] through reaction with the solvent.
- ii) The reaction between redox-generated H⁺, and a second incoming molecule of **19**-H to generate **19**⁺ and H₂ (see **Scheme 38**).

On the reverse scan (**Figure 58a**) a smaller, *EC*-like reduction wave was observed at -1.97 ± 0.01 V vs Cp₂Fe^{0/+}. This corresponds to the single-electron reduction of electrogenerated **19**⁺, as discussed above in 5.3. It is worth noting that the reduction of **19**⁺ occurs 150 mV more negative than that of the archetypal Lewis acid **8** (see Chapter 2). The fact that **19**⁺ is less electrophilic than **8**, accounts for the increased hydride donor ability (and lower oxidation potential) of **19**-H compared to [**8**-H]⁻. It is worth noting (in extension to the study in 5.3) that the oxidative back-peak continues to be absent for the reduction of **19**⁺, even at a scan rates up to 5 V s⁻¹. This is due to the rapid decomposition of **19**[•] in solution to form a mixture of various redox-inactive, four-coordinate borates. However, the reduction wave (and hence the concentration) of electrogenerated **19**⁺ arising from the oxidation of **19**-H is much larger than that observed in the **8**/[**8**-H]⁻ system.^[252]

5.6 Proton-mediated generation of the borenium cation

Treatment of **19**-H with one equivalent of Jutzi's strong acid, [H(OEt₂)₂][B(C₆F₅)₄],^[258] was found to result in the quantitative conversion of **19**-H to **19**[B(C₆F₅)₄]. This confirms the protolytic side-reaction between redox-generated H⁺ and **19**-H. This is in stark contrast to the corresponding reaction of [**8**-H]⁻ with H⁺, where neither the free Lewis acid, **8**, nor the etherate adduct, Et₂O·**8**, were found to be present (see Chapter 3). This result, together with the observation of significant amounts of electrogenerated **19**⁺ in the cyclic voltammetry of **19**-H, suggests that Lewis acid **19**⁺ has a markedly improved stability towards H⁺ compared to **8**.

5.7 Digital simulation of the NHC-borane oxidation

Digital simulation of the cyclic voltammetric data for the oxidation of **19**-H was undertaken in order to extract pertinent mechanistic, thermodynamic and kinetic parameters.

The experimental and simulated cyclic voltammograms were found to be in very good agreement (**Figure 59**) when simulated according to the mechanism proposed in **Scheme 38**.

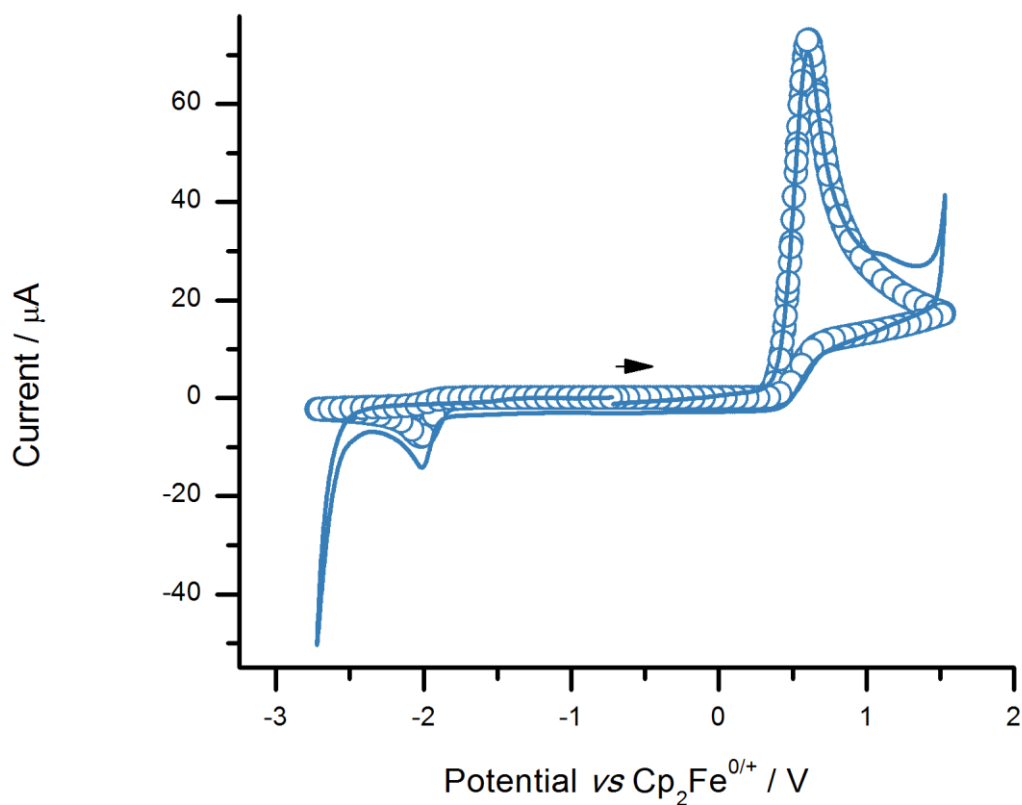


Figure 59 Experimental (line) and simulated (open circles) CVs showing the full potential window following the oxidation of **19**-H (2.0 mM, CH₂Cl₂) at a GCE ($\nu = 500 \text{ mVs}^{-1}$).

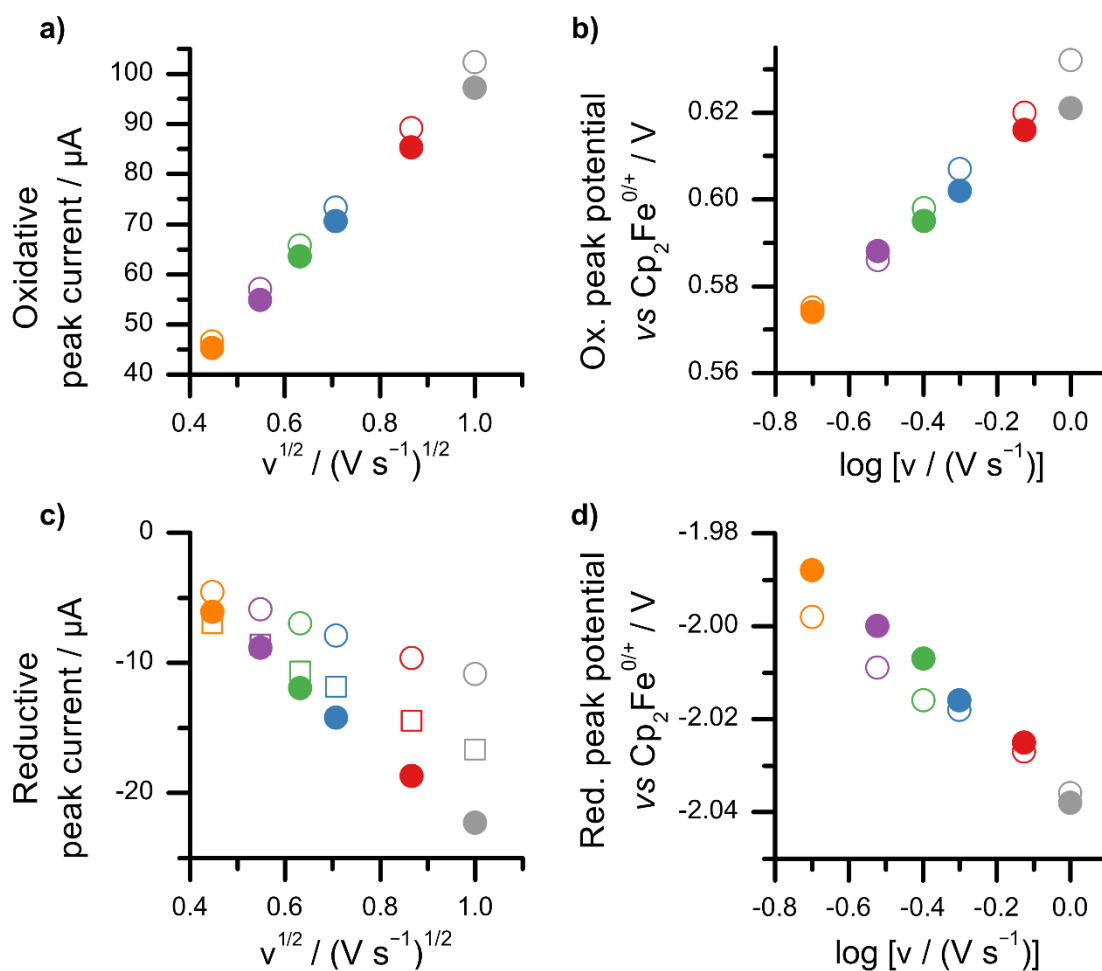


Figure 60 a) Randles-Sevcik plot comparing simulated (open circles) and experimental (closed circles) oxidative peak currents of **19-H** against the square root of scan rate (v); b) Laviron plot comparing simulated (open circles) and experimental (closed circles) oxidative peak potentials of **19-H** against the logarithm of scan rate (v); c) Randles-Sevcik plot comparing simulated (open circles/squares) and experimental (closed circles) reductive peak currents of electrogenerated **19⁺** against the square root of scan rate (v). Open circles denote non-corrected peak current values whereas open squares attempt to account for contributions due to capacitive charging currents; d) Laviron plot comparing simulated (open circles) and experimental (closed circles) reductive peak potentials of electrogenerated **19⁺** against the logarithm of scan rate (v). $v = 200, 300, 400, 500, 750, 1000$ mV s^{-1} .

Table 7 Globally optimized best-fit thermodynamic and kinetic parameters obtained from digital simulation of the voltammetric data for **19-H** at a GCE, following the mechanism proposed in **Scheme 38**.

Redox process	Redox parameters		
	E^0 / V vs $\text{Cp}_2\text{Fe}^{0/+}$	$k^0 / \text{cm s}^{-1}$	α
$[\mathbf{19-H}]^- \rightleftharpoons [\mathbf{19-H}]^{*+} + e^-$	$+0.77 \pm 0.05$	0.89 ± 0.01	0.5 ± 0.05
$\mathbf{19}^* \rightleftharpoons \mathbf{19}^+ + e^-$	$-1.94 \pm 0.05^{[a]}$	$(3.4 \pm 0.1) \times 10^{-3[a]}$	$0.6 \pm 0.05^{[a]}$

Chemical step	k / s^{-1}
$\mathbf{19}^* \rightarrow$ Decomposition products	$k_1 > 2 \times 10^{13} [a]$
$[\mathbf{19-H}]^{*+} \rightarrow \mathbf{19}^* + \text{H}^+$	$k_2 > 3 \times 10^{11} \text{ M}^{-1}$
$\mathbf{19-H} + \text{H}^+ \rightarrow \mathbf{19}^+ + \text{H}_2$	$k_3 = 150 \pm 25$

[a] The parameters for $\mathbf{19}[\text{B}(\text{C}_6\text{F}_5)_4]$ were taken directly from **Table 6**, *vide supra*.

Comparing the results of the digital simulations for the $\mathbf{19-H}/\mathbf{19}^+$ system to the $[\mathbf{8-H}]^-/\mathbf{8}$ system discussed in Chapter 3, four observations are apparent:

- The rate of oxidation of $\mathbf{19-H}$ is approximately seventy times greater than for $[\mathbf{8-H}]^-$, leading to larger oxidative currents (see **Figure 58b**).
- The oxidation potential of $\mathbf{19-H}$ is 300 mV less positive than that of $[\mathbf{8-H}]^-$, corresponding to a significantly large (910 mV) net decrease in the potential required to oxidise H_2 at a GCE (see **Figure 58b**).
- The rate (k_1) of $\mathbf{19}^*$ decomposition is under diffusion control ($> 10^{10} \text{ s}^{-1}$) whereas the corresponding process for $\mathbf{8}^*$ ($> 6.1 \text{ s}^{-1}$) is much slower.
- The rate of unwanted protonation of $\mathbf{19-H}$ by electrogenerated H^+ to generate $\mathbf{19}^+$ and H_2 (k_3) is 10^5 times slower than in the $[\mathbf{8-H}]^-$ system.

Indeed, for point (iv), simulation reveals that only 30-40% of $\mathbf{19}^+$ that is reduced at the electrode surface is generated *via* this undesirable protolytic H_2 regeneration

process, with the majority of **19**⁺ being generated through the two-electron oxidation of **19**-H. This, combined with the greater chemical stability of **19**⁺ towards unsolvated H⁺, demonstrates a significant improvement over the earlier [**8**-H]⁻/**8** system.

5.8 Electrocatalyst recyclability

Encouraged by these findings, the application of **19**⁺ towards *in situ* H₂ oxidation was investigated using a combined electrochemical-FLP approach. Most importantly, an investigation was performed to determine whether this system could then be subsequently recycled. H₂ (1 atm) was admitted to a 1:1 solution of **19**[B(C₆F₅)₄]/**12** in CH₂Cl₂ containing [ⁿBu₄N][B(C₆F₅)₄] electrolyte. The reaction mixture was then left to stir in a sealed flask overnight to allow FLP H₂ cleavage to go to completion. The resulting solution containing **19**-H (as identified from an initial cyclic voltammogram of the solution) and [**12**-H][B(C₆F₅)₄] was then subjected to a bulk electrolysis cycle, holding the electrode at the oxidation potential of **19**-H until complete conversion was achieved. Afterwards, an aliquot of **12** (equimolar to the original quantity of **19**[B(C₆F₅)₄]) was added to the solution, and the reaction mixture was resealed under H₂ overnight. This cycle of bulk electrolysis and subsequent “recharging” under H₂ was repeated a total of three times (see **Figure 61**). The total charge passed (equivalent to the concentration of **19**-H) in the second cycle of electrolysis was 75% that of the first cycle, clearly indicating that the system is capable of turning over more than a single cycle. However, upon the third cycle of electrolysis the current and charge passed had dropped to below 10% of the initial cycle. Closer investigation revealed that the capacitive charging current had diminished considerably and cyclic voltammetry of the solution provided evidence of electrode fouling due to the presence of a broad, ill-defined, surface bound oxidation wave over the range 0.2-0.8 V vs Cp₂Fe^{0/+}. This most likely results from oxidative polymerization of the phosphine Lewis base, which, assuming that 100% of **19**-H could be regenerated in each step, was subsequently present in excess. Although the oxidation potential of **12** occurs at slightly more positive potentials than that of **19**-H, the oxidation of free **12** may still occur to an extent. Whilst it is not yet clear whether improved turnover of the system may have been possible in the absence of fouling, the fact that **19**-H can be recycled even once is an improvement over the previously studied [**8**-H]⁻/**8** system in Chapter 3, where all attempts to recycle the system failed. Note that whilst the system is electrocatalytic in the Lewis acid component, it is stoichiometric in the Lewis base **12**. This is because this study is only concerned with the anodic half-cell reaction *i.e.* H₂ oxidation. If this system as to be utilized as part of a complete electrochemical cell reaction (*e.g.* a fuel cell) then

clearly it would require coupling to a suitable cathodic half-cell reaction, that is capable of consuming the generated protons and closing the catalytic cycle.

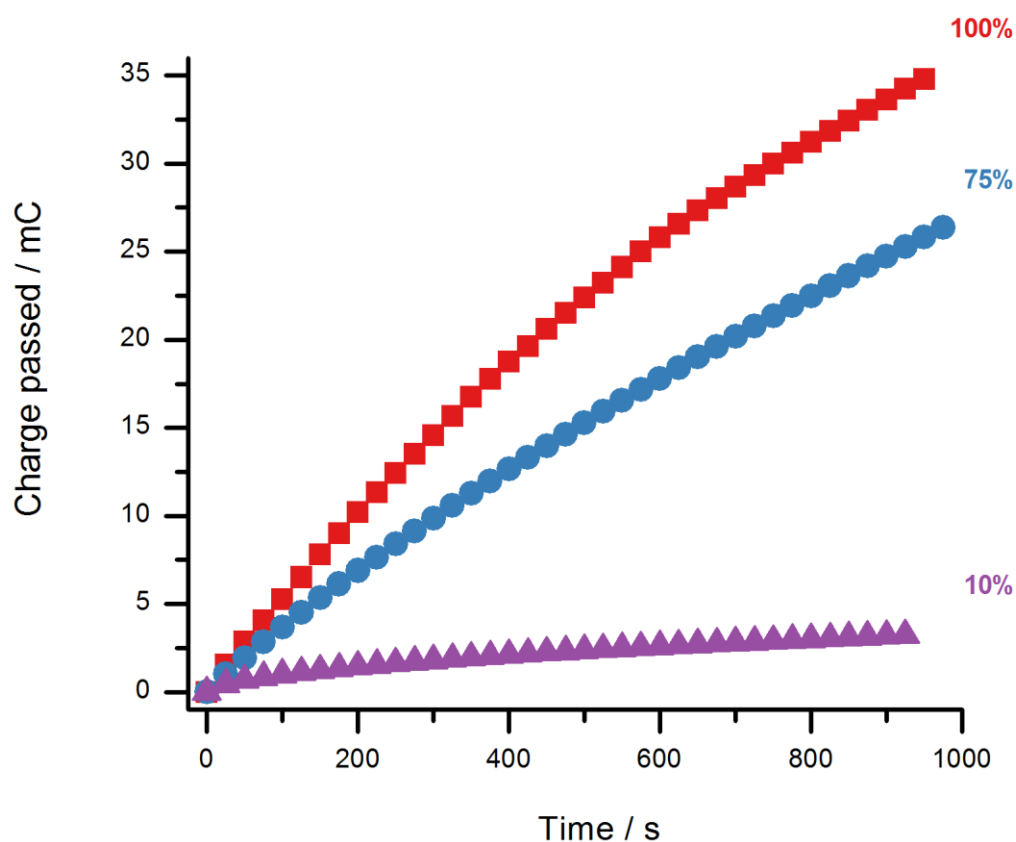


Figure 61 Repeat oxidative bulk electrolysis cycles of **19-H**, generated from the overnight exposure of a 5 mM **19**[B(C₆F₅)₄]/**12** solution (CH₂Cl₂) to H₂ (1 atm), demonstrate that the system can be somewhat recycled (■, cycle 1; ●, cycle 2; ▲, cycle 3).

5.9 Summary

The redox chemistry of several (new and previously reported) NHC-stabilised dimesitylborenium cations, **25**[OTf], **26**[OTf] and **27**[OTf], was explored at a GCE. The borenium cations were found to exhibit *quasi*-reversible voltammetry with a very slow follow-up chemical step resulting in some decomposition of the electrogenerated **B**[•] species. Cyclic voltammetry was also performed on Stephan's borenium compound, **19**[B(C₆F₅)₄]. The boron centre of the electrogenerated **19**[•] species is not sufficiently sterically precluded to prevent significant decomposition of the radical through reaction with the solvent. **19**[B(C₆F₅)₄] therefore exhibits classical *EC*-like voltammetry that is reminiscent of that obtained for **8** in Chapter 2.

The borenium cations, **25**[OTf], **26**[OTf] and **27**[OTf], were found to be very poor candidates for FLP H₂ activation when combined with the Lewis base, **12**. In fact, unusual and colourful behaviour was observed when the **26**⁺/**12** FLP was formed in the chlorinated solvents, CDCl₃ and CD₂Cl₂. I was unable to fully elucidate the reaction mechanisms and products involved. At the time of writing this thesis, the only borenium cation that is known to definitively activate H₂, as part of a FLP, remains to be **19**[B(C₆F₅)₄].

The remainder of this chapter focused on successfully demonstrating the utility of **19**[B(C₆F₅)₄] for H₂ oxidation using a combined electrochemical-FLP approach. Using **19**[B(C₆F₅)₄] as the Lewis acid component of the FLP has several advantages over the initial **8**-based system reported in Chapter 3. Indeed, the oxidative voltage (driving force) required to oxidise H₂ at a carbon electrode is decreased by almost one Volt (910 mV, *ca* 175.6 kJ mol⁻¹), the rate of H₂ oxidation is also faster, producing larger currents, and the NHC-stabilised borenium Lewis acid catalyst is more resistant to unwanted side-reactions with redox-generated H⁺. These factors combine to make the NHC-stabilised borenium system somewhat “rechargeable” – allowing the *in situ* regeneration of **19**-H from **19**⁺ in the presence of **12** and H₂, with 75% efficiency after the first cycle.

Chapter 6

Results and discussion

Tris[bis(trifluoromethyl)phenyl]boranes

6.1 Overview

In Chapter 5, the combined electrochemical-FLP approach was extended from triarylboranes to NHC-stabilised borenium cations. The 9-BBN-derived borenium cation, **19**⁺, was found to proffer significant improvements over **8** (studied in Chapter 3). The electrochemical oxidation of the B-H bond in **19**-H, was found to occur 300 mV lower than in [**8**-H]⁻. In addition to this desirable voltage decrease, it was also possible to recycle the Lewis acid **19**⁺ and regenerate **19**-H after an oxidative bulk electrolysis cycle. This was not possible for the **8**/[**8**-H]⁻ system (Chapter 3).

In this final results and discussion chapter, I return to explore a new class of triarylboranes. Tris[bis(trifluoromethyl)phenyl]boranes, B{C₆H₃(CF₃)₂}₃, (introduced in 1.6) are a lesser studied class of sterically-bulky and strong Lewis acids; their electrochemical properties are hitherto unknown. This chapter addresses this by investigating the reductive redox chemistry of the 3,5- (**20**) and 2,4- (**28**) bistrifluoromethylated isomers using cyclic voltammetry. In addition to this, the electrochemical properties of the bridging, [(μ-H)(**20**)₂]⁻, and the terminal, [**20**-H]⁻, hydrides of **20** are studied for the first time.

As discussed in Chapters 2 and 3, donor solvents such as THF are usually not compatible with FLP systems containing strong Lewis acids such as **8**. This is due to the formation of strong classical Lewis adducts or ring-opening, in the case of THF, to give a gel.^[170] The first reported example of a FLP that functions in donor solvents made use of the borane, HB(fmes)₂ [fmes = 2,4,6-tris(trifluoromethyl)phenyl]. When combined with either 1,4-diazabicyclo[2.2.2]octane (DABCO) or NEt₃, this borane was capable of activating H₂ in the donor solvent, Et₂O. The significant steric bulk of the boron centre in HB(fmes)₂, compared to **8**, precludes the formation of any etherate Lewis adduct; the Lewis acidity of the boron centre therefore remains unquenched.^[149] Ashley and co-workers have since found that the **20**/TMP FLP is capable of heterolytically activating H₂ in Et₂O solvent, presumably the diethyletherate adduct, Et₂O·**20**, dissociates sufficiently at room temperature to allow free **20** to participate in FLP H₂ activation with the Lewis base, TMP.^[146] Since then, Stephan's group have since found that combinations of **8** and near stoichiometric quantities of ethers (including Et₂O) can function as effective hydrogenation catalysts in non-donor solvents such as CD₂Cl₂.^[289] This report prompted our collaborators to investigate the application of ethereal solvents as the frustrated Lewis base for hydrogenation catalysis using a series of perfluorinated/perchlorinated boranes related to **8**; B(C₆F₅)_n(C₆Cl₅)_{3-n} (*n* = 1-3). This approach was successful for hydrogenation catalysis, and (most importantly) eliminated the requirement for the presence of any additional phosphines/amines as the Lewis base.^[290] Stephan very recently extended this approach to provide the first FLP

example of catalytic ketone hydrogenation, affording the corresponding alcohol products.^[137] This was simply achieved using a FLP derived from **8** (5 mol%) and the ethereal solvent, Et₂O.

In this chapter, the use of donor solvents for FLP H₂ activation by **20** is explored for the first time (in the absence of additional P- or N- containing Lewis bases). This provides further mechanistic insight into the various underlying H₂ activation equilibria, involving **20**. The concept of employing a donor solvent as the Lewis base is then also extended to the electrochemical-FLP system.

6.2 Synthesis and characterization of the boranes

In the past, the regioisomers B{C₆H₃(3,5-CF₃)₂}₃ (**20**) and B{C₆H₃(2,4-CF₃)₂}₃ (**28**) were accidentally isolated as either unwanted reaction products or side-products. In both instances, their molecular structures were elucidated using X-ray crystallography (see **Figure 62**).^[291,292]

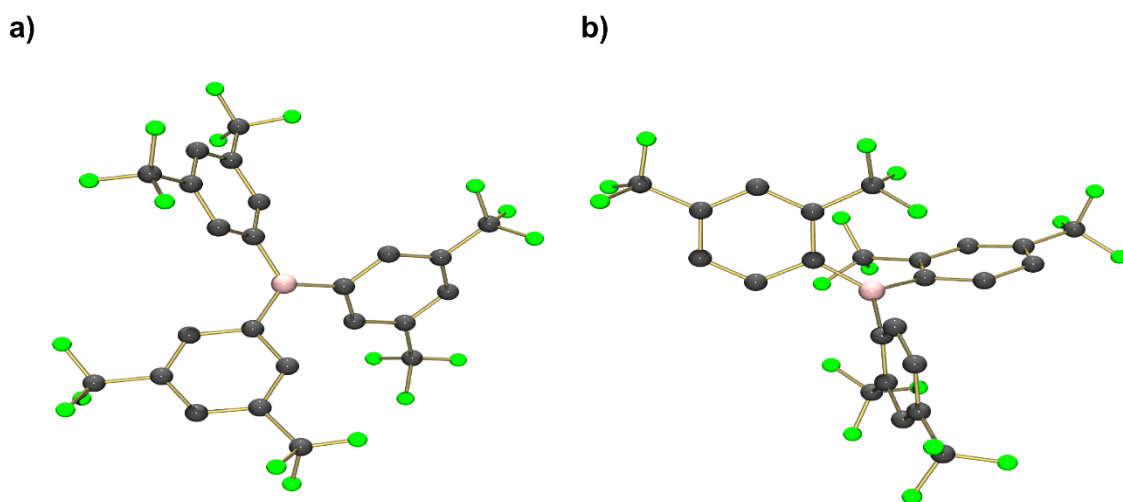


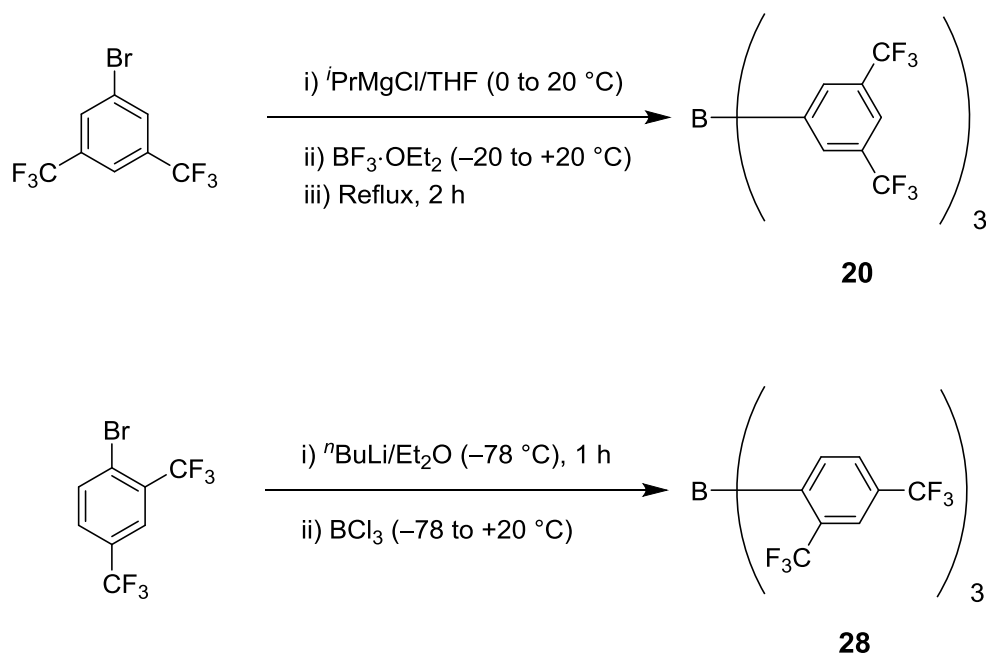
Figure 62 Molecular structures of the B{C₆H₃(CF₃)₂}₃ variants a) **20**,^[291] and b) **28**.^[292]

Remarkably similar methods for the facile preparation of **20** (on a practical scale) were reported independently by the research groups of Ashley and Tamm in 2012.^[146,147] I prepared a sample of **20** by following the method of Tamm and co-workers (according to **Scheme 39a**).^[147] The reason for this was simply that Tamm's protocol for temperature control was easier to implement than that of the alternative method. The separation of **20** from the crude product proved to be more difficult than suggested by the original literature procedures. On removal of the reaction solvent, a sticky solid amber foam resulted. I found that it was best to leave this foam under vacuum (10⁻² mbar) at room temperature overnight, in order to fully remove any residual (unbound) solvent. It was then possible to grind the dry foam into a tan-coloured

powder that could then be sublimed (80°C, 10⁻⁶ mbar) to give pure **20** as a white powder. Unfortunately, the contamination of **20** by the magnesium salts necessitated the need for a second sublimation and recrystallization (hot toluene) step. If the crude product wasn't left under vacuum for prolonged periods of time, the first sublimation step proved to be very difficult due to the continual formation of foam in the sublimation tube apparatus.

Whilst the 2,4-variant (**28**) has also been reported previously, the original preparation method of Cornet *et al.* is far from clean and high yielding. The authors deprotonated C₆H₄(2,4-CF₃)₂ with ⁿBuLi at -78°C to give a mixture of the 1- and 3- organolithiated species, 1/3-LiC₆H₃(2,4-CF₃)₂. Treatment of this reaction mixture with an excess of BCl₃·OEt₂ afforded a product mixture of the mono-, bis-, and tris-substituted boranes: Cl₂B{C₆H₃(2,6-CF₃)₂} (14%), FB{C₆H₃(2,6-CF₃)₂}₂ (5%), and **28** (17%) on warming to room temperature, which were separated by distillation under reduced pressure.

A sample of **28** was prepared by Dr. T. Herrington (of Dr. A. Ashley's research group) using a modified version of the procedure described above (see **Scheme 39b**). Lithium-halogen exchange of BrC₆H₃(2,4-CF₃)₂ with ⁿBuLi at -78°C selectively generated the organolithium species, 1-LiC₆H₃(2,4-CF₃)₂. Treatment of this with a 1/3 of an equivalent of BCl₃, followed by warming to room temperature, subsequent removal of the volatiles and sublimation, allowed **28** to be obtained in excellent yield (90%).



Scheme 39 Preparation of a) **20**,^[146,147] and b) **28**.^[292]

6.3 Electrochemical study of the boranes

Cyclic voltammetric data for **20** and **28** was recorded at a GCE (**Figure 50**), in collaboration with Ms. K. Resner and Dr. R. Blagg. Separate samples of **20** and **28** (2.7 mM) were prepared as solutions in CH₂Cl₂, containing the supporting electrolyte [nBu₄N][B(C₆F₅)₄]. On sweeping the potential cathodically from the OCP at 100 mV s⁻¹, single reduction waves were observed for both of the samples (**20** and **28**) at -1.67 and -1.88 V vs Cp₂Fe^{0/+} respectively. On the reverse scan, however, a back-peak was only observed for **28**, at E_{p,ox} = -1.76 V vs Cp₂Fe^{0/+}. No corresponding oxidation wave was observed for **20**, even when the scan rate was increased to 800 mV s⁻¹. In contrast, the back-peak was always apparent for **28**, independent of the scan rate employed.

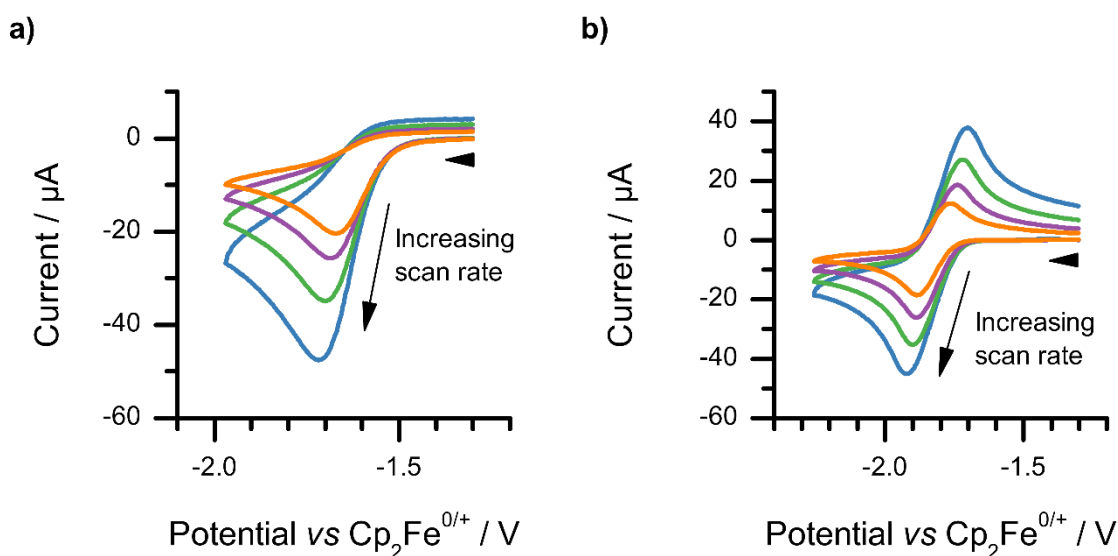


Figure 63 Overlaid CVs for the B{C₆H₃(CF₃)₂}₃ variants a) **20** (2.7 mM), and b) **28** (2.7 mM) recorded at a GCE in CH₂Cl₂ at scan rates (ν) of 100, 200, 400, 800 mV s⁻¹.

Throughout this thesis, the voltammetric reduction of boron-based Lewis acids has been found to be dominated by *EC* electrochemical reactions (refer to Chapters 2 and 5). For the boron-based Lewis acids studied, the electrochemical *quasi*-reversible, single-electron reduction is typically coupled to an irreversible chemical follow-up step, where the reduced boron species undergoes further reaction with the solvent. The B{C₆H₃(CF₃)₂}₃ variants studied here were no exception to this. Indeed, excellent fits (**Figures 64-65**) were obtained when the experimental CVs of **20** and **28** were fitted according to the *EC* process shown in **Scheme 40** (digital simulation was performed in collaboration with Dr. R. Blagg). As was the case for the dimesitylborenium cations (**25⁺**, **26⁺** and **27⁺**) in Chapter 5, the voltammetric reduction of **28** appears to be fully reversible (a simple *E* process) at first glance. However, any attempts to model the experimental

CVs in this way resulted in simulated currents that were consistently too large. This suggests that whilst the electrogenerated radical anion, **28**^{•-}, is significantly more stable than corresponding **20**^{•-}, it is still susceptible to decomposition *via* an *EC*-type mechanism, albeit with a much slower rate constant for the chemical decomposition process.

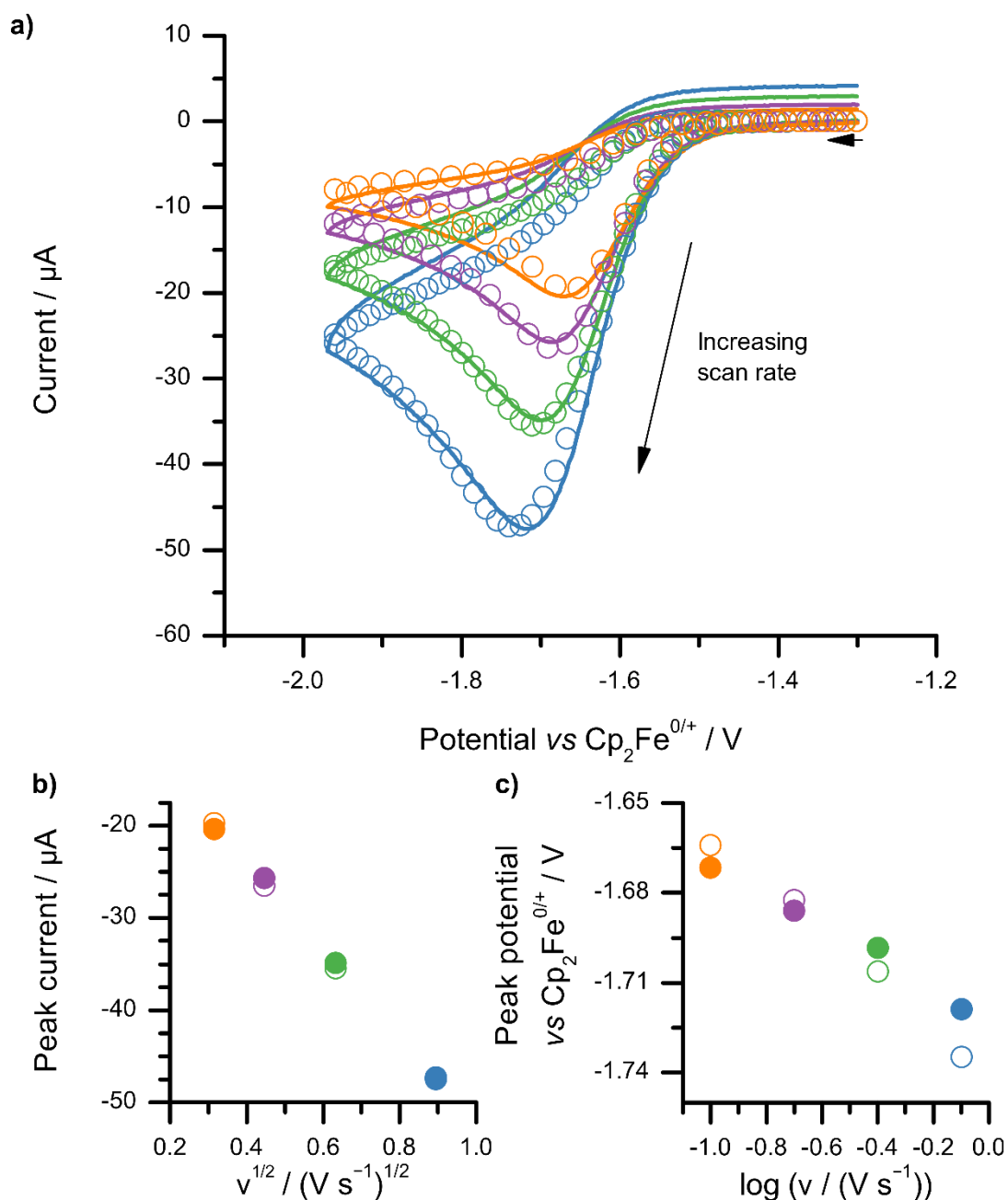


Figure 64 a) Experimental (line) and simulated (open circles) CV for the reduction of authentic **20** (2.7 mM) at a GCE in CH_2Cl_2 (multiple scan rates, see below); b) corresponding Randles-Sevcik plot comparing simulated (open circles/squares) and experimental (closed circles) peak currents against the square root of scan rate (v); and c) corresponding Laviron plot comparing simulated (open circles) and experimental (closed circles) peak potentials against the logarithm of scan rate (v). $v = 100, 200, 400$ and 800 mV s^{-1} .

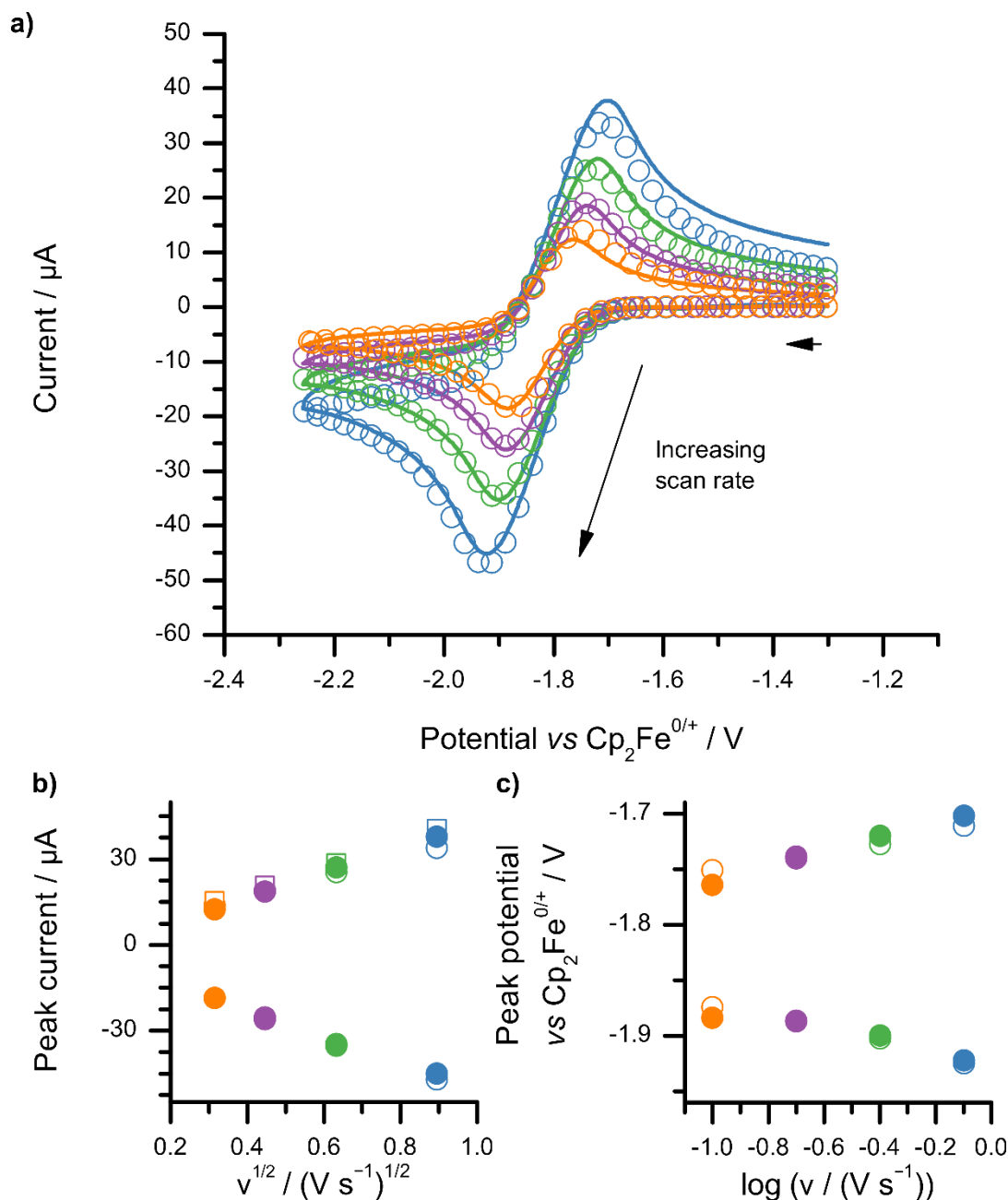
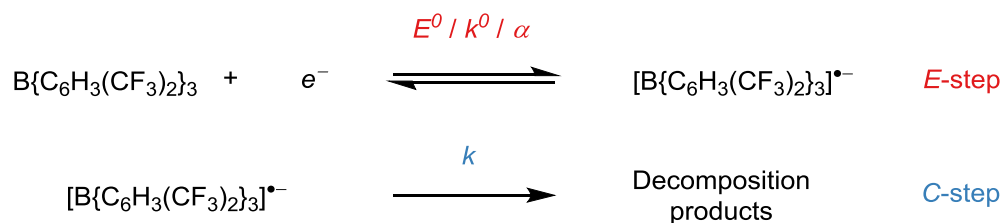


Figure 65 a) Experimental (line) and simulated (open circles) CV for the reduction of authentic **28** (2.7 mM) at a GCE in CH_2Cl_2 (multiple scan rates, see below); b) corresponding Randles-Sevcik plot comparing simulated (open circles/squares) and experimental (closed circles) peak currents against the square root of scan rate (v). Open circles denote non-corrected peak current values whereas open squares attempt to account for current contributions due to capacitive charging (C_{dl}); c) corresponding Laviron plot comparing simulated (open circles) and experimental (closed circles) peak potentials against the logarithm of scan rate (v). $v = 100, 200, 400$ and 800 mV s^{-1} .



Scheme 40 The proposed mechanism and associated thermodynamic and kinetic parameters used in digital simulation of the voltammetric reduction of the $\text{B}\{\text{C}_6\text{H}_3(\text{CF}_3)_2\}_3$ variants (**20** and **28**) at a GCE.

Table 8 Globally optimized best-fit thermodynamic and kinetic parameters obtained from digital simulation of the voltammetric data for **20** and **28** at a GCE, following the mechanism proposed in **Scheme 40**.

Redox parameters	$\text{B}\{\text{C}_6\text{H}_3(\text{CF}_3)_2\}_3$ variant	
	20	28
$E^0 / \text{V vs Cp}_2\text{Fe}^{0/+}$	-1.63 ± 0.05	-1.81 ± 0.05
$k^0 / 10^{-3} \text{ cm s}^{-1}$	24 ± 0.1	9.3 ± 0.1
α	0.34 ± 0.05	0.52 ± 0.05

Chemical parameters	$\text{B}\{\text{C}_6\text{H}_3(\text{CF}_3)_2\}_3$ variant	
	20	28
k_1 / s^{-1}	18 ± 2	$(2.8 \pm 0.05) \times 10^{-3}$
$D / 10^{-5} \text{ cm}^2 \text{ s}^{-1}$	3.7 ± 0.05	1.1 ± 0.05

The formal reduction potential (E^0) for **28** was found to be similar to that of **8**, as determined in Chapter 2 (where $E^0 = -1.79 \pm 0.05 \text{ V}$). However, the E^0 values suggest that **20** is more electrophilic than **28** ($\Delta E^0 = 0.18 \pm 0.07 \text{ V}$). This is surprising, given that a CF_3 substituent at the *para* position of a phenyl group is more electron-withdrawing than that at a *meta* position, as described by the relative Hammett parameter values ($\sigma_{\text{meta}}(\text{CF}_3) = 0.430$ vs $\sigma_{\text{para}}(\text{CF}_3) = 0.540$).^[271] Note that Hammett parameters are not available for substituents in the *ortho*

position, since such parameters attempt to rationalize electronic effects independently of steric effects (and were originally obtained from experimental observations). The Gutmann-Beckett^[293,294] and Childs^[295] methods were not successful for assessing the relative Lewis acidity of **28** relative to **20**, since the significant steric bulk of **28** unfortunately precluded any interaction between the added Lewis bases and the Lewis acidic, boron centre. The apparent contradiction between the expected order of redox potentials using available Hammett parameter values and the experimentally observed formal potentials suggests that additional electronic or steric effects may exist in either **20** or **28**. Considering the electron-withdrawing effects of a CF₃ substituent, one would simply expect **28** to be more electrophilic than **20**. DFT calculations are currently being carried out on the structurally optimised geometries of **20** and **28**. An assessment of the relative partial charge distributions will hopefully allow the rationalization of this phenomenon. At this stage, I suspect that the pendant fluorine atom of the *ortho*-CF₃ substituent on **28** may partially quench the electrophilicity of the boron centre *via* a non-bonding donor-acceptor interaction between the lone pair on the F atom and the central B atom.

Digital voltammetric simulation determined that the rate (*k*) of radical anion decomposition (*via* reaction with the solvent) is approximately 6000 times greater for **20**^{•-} than for **28**^{•-}. This can be accounted for by considering the steric accessibility of the boron centre in the parent Lewis acids. This assumes that negligible structural reorganization occurs on reduction, and also that the unpaired electron of the radical anion is localized on the boron centre (as is the case for **8**^{•-}, see 2.4). This is clearly illustrated by the space-fill models shown in **Figure 55**, where the boron atoms are shown in pink. Whilst the boron centre in **28** appears to be almost completely engulfed by the surrounding aryl rings, the opposite is true for **20** (the boron centre can be easily identified). It is no surprise that solvent molecules can easily approach the SOMO of **20**^{•-} and react with its unpaired electron. It is worth remembering that an *ortho*-CF₃ substituent is extremely effective at sterically protecting the boron centre from interactions with other molecules such as the solvent; this imparts significant stability to the radical anion.

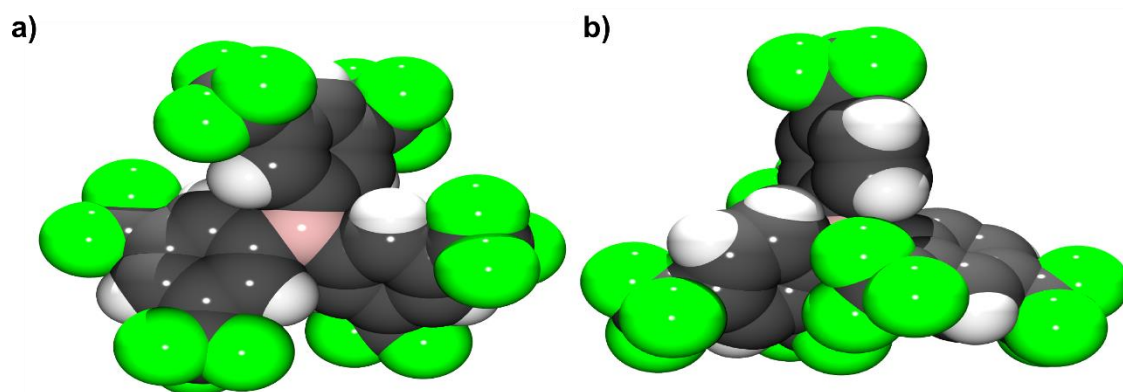


Figure 66 Space-filling view of the $B\{C_6H_3(CF_3)_2\}_3$ variants a) **20**,^[291] and b) **28**^[292] showing the extent of steric shielding of the boron centre by the surrounding $-CF_3$ substituents.

6.4 Exploring FLP H_2 activation using $B\{C_6H_3(2,4-CF_3)_2\}_3$

When the structural isomer **28** was mixed with either **12** or TMP in CH_2Cl_2 , the 1H , $^{19}F\{^1H\}$, $^{31}P\{^1H\}$, and ^{11}B NMR spectra were identical to that of the individual components, suggesting that a classical Lewis adduct had not formed. These mixtures were admitted to H_2 (4 atm) and left for several days, however, the absence of any heterolytic H_2 activation products suggested that **28** is ineffective towards FLP chemistry. Whilst the sterically-protected boron centre of **28** has advantages for limiting the decomposition of 28^{*-} in electrochemical studies (see 6.3), the opposite is true for FLP applications. The added Lewis base and H_2 , simply can't interact with the Lewis acidic boron centre of **28** (refer to the space-fill models above, **Figure 66**). Indeed this effect is likely to be exacerbated by the fact that **28** is also less electrophilic than **20** (as determined from the relative formal potentials in **Table 8**). Since **28** was devoid of any FLP activity, it was not explored any further.

6.5 Ethereal solvents as the Lewis base for FLP H_2 activation

When H_2 is admitted to the **20**/TMP FLP, the bridging hydride, $[TMP-H][(\mu-H)(20)_2]$, is observed to rapidly precipitate from the CH_2Cl_2 reaction mixture.^[146] The equilibrium can be forced towards the terminal hydride, $[TMP-H][20-H]$, by the addition of extra Lewis base (LB), including the donor solvents THF or CH_3CN . The formation of the classical Lewis adduct, $LB \cdot 20$, drives the sequestration of **20** from $[(\mu-H)(20)_2]^-$ to completion.

Interestingly, when an isolated sample of $[TMP-H][(\mu-H)(20)_2]$ (prepared according to the literature method)^[146] was dissolved in THF, the formation of $[TMP-H][20-H]$ and $THF \cdot 20$ was

found to be concomitant with evolution of a small quantity of H₂ gas. Whilst effervescence was not observed, some dissolved H₂ was detected in the product mixture as a singlet resonance at δ 4.53 ppm in the ¹H NMR spectrum.^[296] This suggests that an equilibrium becomes established between [TMP-H][**20**-H] and **20**/TMP/H₂ FLP, although the position of this equilibrium strongly favours the formation of the hydride (see **Scheme 36a**). This can be rationalized in terms of the relative hydride donating abilities of the bridging and terminal hydrides. Compared to [**20**-H]⁻, the hydride donor ability of [(μ -H)(**20**)₂]⁻ is reduced by the presence of an additionally bound **20** unit. This makes the terminal hydride, [**20**-H]⁻, more susceptible to the reverse reaction, where H₂ is regenerated *via* the Brønsted acid/base reaction of [**20**-H]⁻ with [TMP-H]⁺.

Out of curiosity, I subjected the product mixture of [TMP-H][**20**-H] and THF·**20** to a freeze-pump-thaw cycle, and admitted the sample to H₂ (4 atm). NMR spectra were then obtained as soon as possible. To my surprise, a new, broad signal had appeared at δ 4.3 ppm in the ¹¹B NMR spectrum, observed directly between the signals corresponding to [**20**-H]⁻ (δ -9 ppm, broad) and THF·**20** (δ 11 ppm, broad).^[147] This signal was tentatively assigned to the formation of the bridging hydride product [H(THF)_{*n*}][(μ -H)(**20**)₂], where the protons are solvated by THF molecules.^[297,298] Indeed, Ashley and co-workers found that Et₂O·**20**, dissociates sufficiently at room temperature to allow free **20** to participate in FLP H₂ activation with the Lewis base, TMP.^[146] My observations suggest it may be possible to activate H₂ using **20** in ethereal solvents without the need for additional TMP Lewis base.

It is worth noting that Ashley and co-workers had difficulty in obtaining full NMR spectroscopic characterization of [TMP-H][(μ -H)(**20**)₂] due to its poor solubility in most common (deuterated) non-donor solvents. Only when [TMP-H][(μ -H)(**20**)₂] was heated to 80°C in DFB could they obtain a sufficient signal to noise ratio that allowed ¹H NMR assignments be made, and even these are ambiguous. They failed to obtain any ¹¹B NMR spectroscopic information, due to an insufficient sample concentration. Tamm and co-workers have previously assigned [(μ -H)(**20**)₂]⁻ as a broad ¹¹B NMR signal at δ -10 ppm.^[147] However, since they erroneously attempted to characterize their product in the donor solvent THF, and in light of my findings below, I believe Tamm's reported spectral data actually corresponds to the terminal hydride, [**20**-H]⁻, and not the bridging hydride as the authors mistakenly claimed. Tamm and co-workers' error was made despite the authors explicitly discussing the observed formation of [**20**-H]⁻ from [(μ -H)(**20**)₂]⁻ on the addition of the Lewis base, CH₃CN.

Inspired by the previous reports from Stephan's group,^[289] and the work of our collaborators^[290] (which was conducted in parallel to my work, see 6.1), I decided to further investigate whether H₂ activation by **20** was possible using only the donor solvent THF as the Lewis basic component. A sample of **20** was dissolved in d₈-THF to give the classical Lewis adduct,

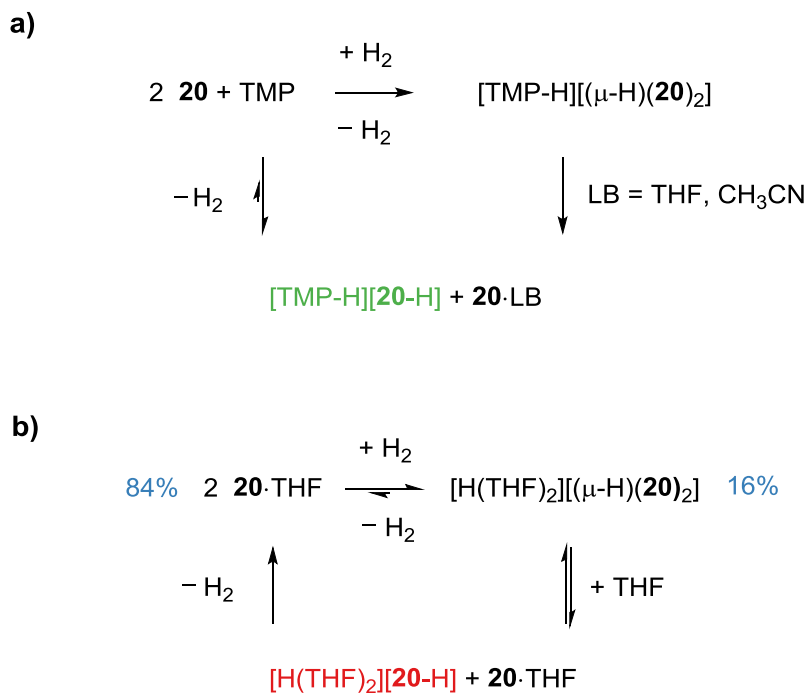
d_8 -THF·**20**, which was observed in the ^{11}B NMR spectrum at δ 10.3 ppm. After admission of the sample to H_2 (4 atm) a broad signal was immediately observed at δ 3.7 ppm; this signal was characteristic of that observed previously when the sample containing [TMP-H][**20**-H] and THF·**20** was admitted to H_2 . A new, broad signal was observed downfield in the ^1H NMR at δ 11.11 ppm. This is assigned to the presence of THF-solvated protons, generated from the heterolytic cleavage of H_2 .^[290,298] New aryl CH multiplets were observed in the ^1H NMR at δ 7.86 and 7.82 ppm with relative integrals of 1 and 2, respectively. Additionally, a new singlet resonance was also observed at δ -63.6 ppm in the $^{19}\text{F}\{^1\text{H}\}$ NMR. Assuming that the new signals correspond to $[\text{H}(\text{THF})_n][(\mu\text{-H})(\mathbf{20})_2]$, integration of the new aryl ^1H and $^{19}\text{F}\{^1\text{H}\}$ NMR signals relative to those of the d_8 -THF·**20** starting material suggests that $[\text{H}(\text{THF})_n][(\mu\text{-H})(\mathbf{20})_2]$ initially forms in 16% conversion on admission to H_2 . When spectra were obtained again after several days, H_2 cleavage had progressed no further, suggesting that the activation of H_2 by **20** in THF is reversible and that equilibrium is rapidly attained within minutes (*i.e.* the time it takes to run the sample on an NMR spectrometer) of H_2 being added to the sample (see **Scheme 36b**).

Attempts were made to isolate the H_2 activation product, $[\text{H}(\text{THF})_n][(\mu\text{-H})(\mathbf{20})_2]$. A sample of **20** in toluene was solubilised by adding several drops of THF, forming THF·**20** in solution. After saturating the solution with H_2 (1 atm), the reaction mixture was stirred overnight at room temperature. The sample was then cooled to -20°C for 5 hours to yield a small crop of colourless crystals. The crystals were washed with light petroleum ether and dried under vacuum. NMR spectra of the product in CD_2Cl_2 strongly suggested that the H_2 activation product, $[\text{H}(\text{THF})_n][(\mu\text{-H})(\mathbf{20})_2]$, previously formed in equilibrium with the THF·**20**, had been successfully isolated. Interestingly, no resonance was observed for the B-H-B unit in the ^1H NMR spectrum, and there was no observable loss of H_2 from prolonged periods under vacuum. Elemental analysis suggested that $[\text{H}(\text{THF})_2][(\mu\text{-H})(\mathbf{20})_2]$ had been obtained and was analytically pure [Calculated analytical C H values for $\text{C}_{56}\text{H}_{36}\text{B}_2\text{F}_{36}\text{O}_2$: C 46.50, H 2.51%. Found: C 46.65, H 2.38%]. Unfortunately, this sample failed to produce crystals of suitable quality for X-ray crystallography. Upon repeated attempts I failed to reproducibly isolate the H_2 -cleavage product from the equilibrium mixture of THF·**20**, and instead isolated only crystals of either free **20** or the Lewis adduct THF·**20**. Further attempts to crystallise the $[\text{H}(\text{THF})_2][(\mu\text{-H})(\mathbf{20})_2]$ product were attempted using both THF/petroleum ether and CH_2Cl_2 /THF/petroleum ether solvent mixtures to no avail. If the co-solvent system is not sufficiently polar then crystallization of the starting material is promoted, whilst if the solvent mixture is too polar then crystallization does not occur at all. It seems that the optimal toluene/THF ratio and the correct concentration of **20** are critical to the selective crystallization of the desired H_2 activation product. For this reason, a crystal structure

could not be obtained for this product despite my best and repeated efforts. Fortunately, there was enough material remaining to record its cyclic voltammetry (see 6.6, below).

One might wonder why the terminal hydride, $[\mathbf{20-H}]^-$, is never observed on exposure of a solution of **20** in THF to H_2 . A logical starting point is to assume that the same underlying chemical equilibria observed for the TMP/**20** FLP system (**Scheme 36a**) also applies to the **20**/THF system (**Scheme 36b**). Since the donor solvent THF is in vast excess in the **20**/THF system, rather than dismissing the existence of $[H(THF)_2][\mathbf{20-H}]$, one can simply assume that it is so unstable to loss of H_2 that it rapidly reverts back to the starting material, THF·**20**. This leads to the onset of the observed chemical equilibrium, which lies towards the starting material. Indeed, evidence for the loss of H_2 was observed spectroscopically for $[TMP-H][\mathbf{20-H}]$ (see above). The relative stabilities of $[H(THF)_2][\mathbf{20-H}]$ and $[TMP-H][\mathbf{20-H}]$ can be rationalized by considering their logarithmic acid dissociation constants (pK_a). pK_a values for the conjugate acids of TMP and THF are 11.1 and -2.1, respectively.^[3,299] Since protonated THF is *ca* 13 orders of magnitude more acidic than $[TMP-H]^+$, it is no surprise that $[H(THF)_2][\mathbf{20-H}]$ is unstable to decomposition (*via* H_2 evolution). Conversely, $[TMP-H]^+$ is not sufficiently protic to react with $[\mathbf{20-H}]^-$ and liberate H_2 .

The behaviour of the **20**/THF FLP, towards H_2 activation, is remarkably similar to that of the previously reported $Al(C_6F_5)_3$ (**22**)/**12** system.^[281] The reaction of the H_2 activation product, $[\mathbf{12-H}][(\mu-H)(\mathbf{22})_2]$, with Lewis bases such as Et_2O or PMe_3 resulted in the rapid evolution of H_2 and the observed formation of the classical Lewis adducts, LB·**22** (where LB = Et_2O , PMe_3). In this case, the added Lewis base sequestered **22** from $[(\mu-H)(\mathbf{22})_2]^-$ and generated the salt $[\mathbf{12-H}][\mathbf{22-H}]$, which is unstable with respect to H_2 loss.



Scheme 41 Postulated H₂ activation equilibria exhibited by **20** when paired with the Lewis bases a) TMP (in CH₂Cl₂), and b) THF (as the reaction solvent).

With an improved mechanistic understanding of the **20**/THF FLP system (**Scheme 36b**), I wondered whether it would be possible to drive the activation of H₂ to completion using stoichiometric quantities of THF in a non-donor solvent. On the admission of a solution of **20**·THF (in CD₂Cl₂) to H₂ overnight, a set of colourless crystals formed. Unfortunately, X-ray crystallography identified that the aqua adduct (THF)₂(H₂O)·**20** had been crystallised, where the associated THF molecules were hydrogen bonded to the aqua adduct. No further attempts have since been made.

Where appropriate Lewis base choices are concerned, TMP and THF contrast greatly. TMP is a significantly stronger Lewis base than THF, as indicated by the relative *pK_a* values of their conjugate acids (TMP = 11.1, THF = -2.1). However, THF is much less sterically encumbered than TMP, hence (with **20**) it forms the classical Lewis adduct, THF·**20**. Out of curiosity, I decided to investigate the combination of **20** with the Lewis base pyrrolidine (**29**), and its ability (or lack of) for FLP H₂ activation. **29** effectively has the Lewis basicity (conjugate acid *pK_a* = 11.3)^[300] of TMP, but has the decreased steric bulk of THF. I postulated that these properties may favour the formation of the terminal hydride, [**29**-H][**20**-H]. When **20** was dissolved in **29**, the formation of **29**·**20** was evidenced by the presence of a sharp singlet resonance in the ¹¹B NMR spectrum at δ -0.4 ppm. On admission to H₂, no change in the NMR spectrum was observed. This

unfortunately suggests that the classical Lewis adduct, **29·20**, is so tightly bound that it is unable to partake in H₂ activation chemistry. An equilibrium involving the partial dissociation of LB·**20** into free LB and **20** is essential for a successful FLP systems – and this must be considered in the development of solvent-based FLP systems that are free from additional Lewis base.

Switching to donor solvents for the combined electrochemical-FLP system is likely to provide the following three advantages:

- i) There is no doubt that the presence of unsolvated protons accelerate the H₂ evolution side-reaction in the previously explored systems (where the non-donor solvent, CH₂Cl₂, is used). Donor solvents such as THF would function as a buffer agent for any redox-generated H⁺, sequestering protons so that unsolvated protons are never present. This effect would reduce the rate of the undesirable side-reaction of H⁺ with the hydridic intermediates formed in the FLP activation of H₂.
- ii) Donor solvents would effectively lock up the Lewis acid as the Lewis adduct. This may reduce the susceptibility for decomposition of the Lewis acid when exposed to trace amounts of air and moisture (in future applications).
- iii) Adopting the solvent as the Lewis base removes the need for additional Lewis bases (such as amines/phosphines *etc.*) in the system. This may eliminate recyclability issues such as those encountered in Chapter 5 for the **19**[B(C₆F₅)₄]/**12** system, where the 87% decrease in total charge passed during the third bulk electrolysis cycle was attributed to electrode fouling by the electro-oxidised Lewis base, **12**.

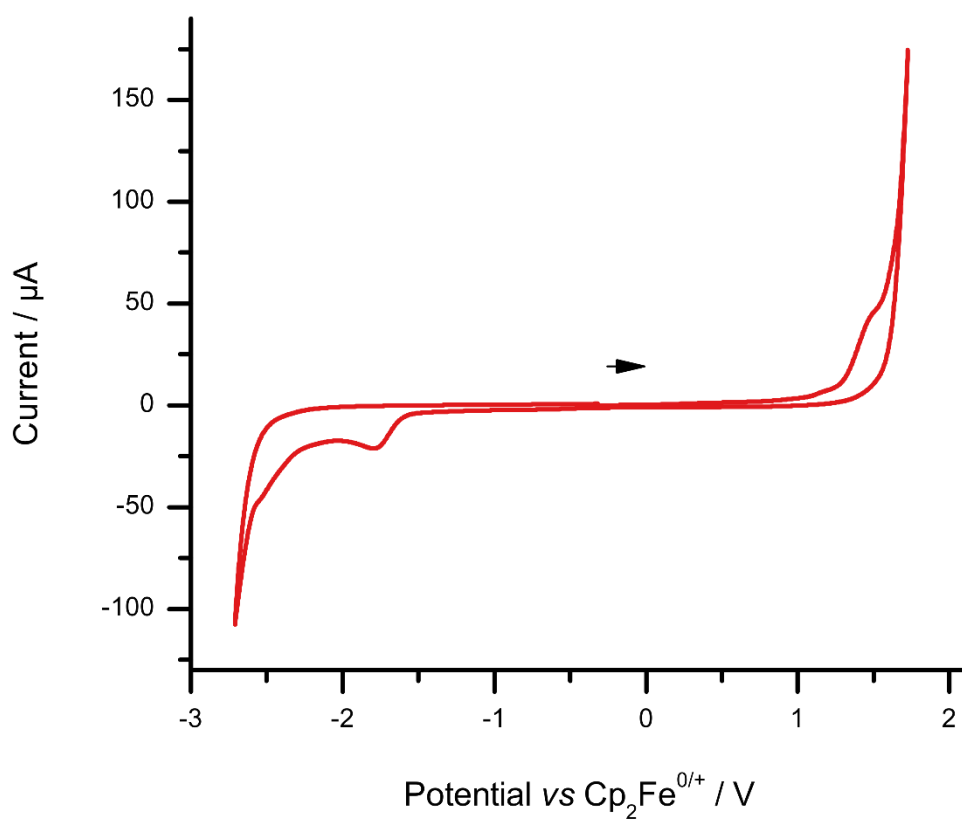
6.6 Electrochemical studies of the H₂ activation products

The redox properties of the bridging hydride products of FLP H₂ activation, [TMP-H][[(μ-H)(**20**)₂] (3.1 mM) and [H(THF)₂][(μ-H)(**20**)₂] (1 mM), were studied at a GCE using cyclic voltammetry (**Figure 67**) in the non-donor supporting electrolyte system, CH₂Cl₂/[ⁿBu₄N][B(C₆F₅)₄]. Note that whilst [TMP-H][[(μ-H)(**20**)₂] is sparingly soluble in C(H/D)₂Cl₂ for NMR studies, it is sufficiently soluble for electrochemical studies. The voltammetric behaviour of both [(μ-H)(**20**)₂]⁻ samples were almost identical. When the potential was scanned anodically from the OCP at 100 mV s⁻¹, an oxidation wave was observed at +1.49 V vs Cp₂Fe^{0/+}. This wave appeared as a shoulder on the edge of the solvent window, where the onset of oxidative solvent/electrolyte breakdown begins to occur. No back-peak was observed when the scan direction was reversed, suggesting that an EC-like mechanism is at play. This oxidation

event is attributed to the two-electron oxidation of $[(\mu\text{-H})(\mathbf{20})_2]^-$ to give H^+ and two molecules of **20**. Unfortunately, the potential required for the oxidation of $[(\mu\text{-H})(\mathbf{20})_2]^-$ is the same as that of molecular H_2 (see Chapter 3). This suggests that whilst FLP H_2 activation by **20**/THF is extremely facile, a decrease in the required oxidation potential is not achieved and hence FLP pre-activation of H_2 by **20**/THF does not provide an electrocatalytic effect. It is likely that the strength of the B-H bond is comparable to that in H_2 (BDE = $435.8 \text{ kJ mol}^{-1}$).^[3] Indeed, the bridging hydride salt can, effectively, be considered as an electrolyte salt within the positive potential window.

On the reverse scan, a reduction wave was observed at *ca* $-1.80 \text{ V vs Cp}_2\text{Fe}^{0/+}$ for both $[\text{TMP-H}][(\mu\text{-H})(\mathbf{20})_2]$ and $[\text{H}(\text{THF})_2][(\mu\text{-H})(\mathbf{20})_2]$. This wave was devoid of a back-peak and reminiscent of that observed for the single electron reduction of the parent borane (**20**) (see 6.3, above). This wave is therefore ascribed to the generation of **20** from the electrooxidation of $[(\mu\text{-H})(\mathbf{20})_2]^-$. The observation of this reduction wave suggests that electrogenerated **20** is less susceptible to protolytic decomposition than previously studied **8**, where an ill-defined corresponding reduction wave is observed (refer to Chapter 3 for details). A second reduction wave was also observed at $-2.39 \text{ V vs Cp}_2\text{Fe}^{0/+}$ for $[\text{H}(\text{THF})_2][(\mu\text{-H})(\mathbf{20})_2]$, and close to the solvent window at $-2.54 \text{ V vs Cp}_2\text{Fe}^{0/+}$ for $[\text{TMP-H}][(\mu\text{-H})(\mathbf{20})_2]$. This second wave likely corresponds to the reduction of H^+ back to H_2 which requires a significantly large overpotential at carbon electrodes in non-aqueous solvents. The varied reduction potential observed likely reflects the relative acidity and hence the ease with which $[\text{H}(\text{THF})_2]^+$ is reduced compared to $[\text{TMP-H}]^+$.^[301] The onset of solvent/electrolyte breakdown close to the observed oxidation wave of $[(\mu\text{-H})(\mathbf{20})_2]^-$ unfortunately prevents digital simulation of the voltammetric data *i.e.* relevant thermodynamic and kinetic parameters cannot be extracted for this system.

a)



b)

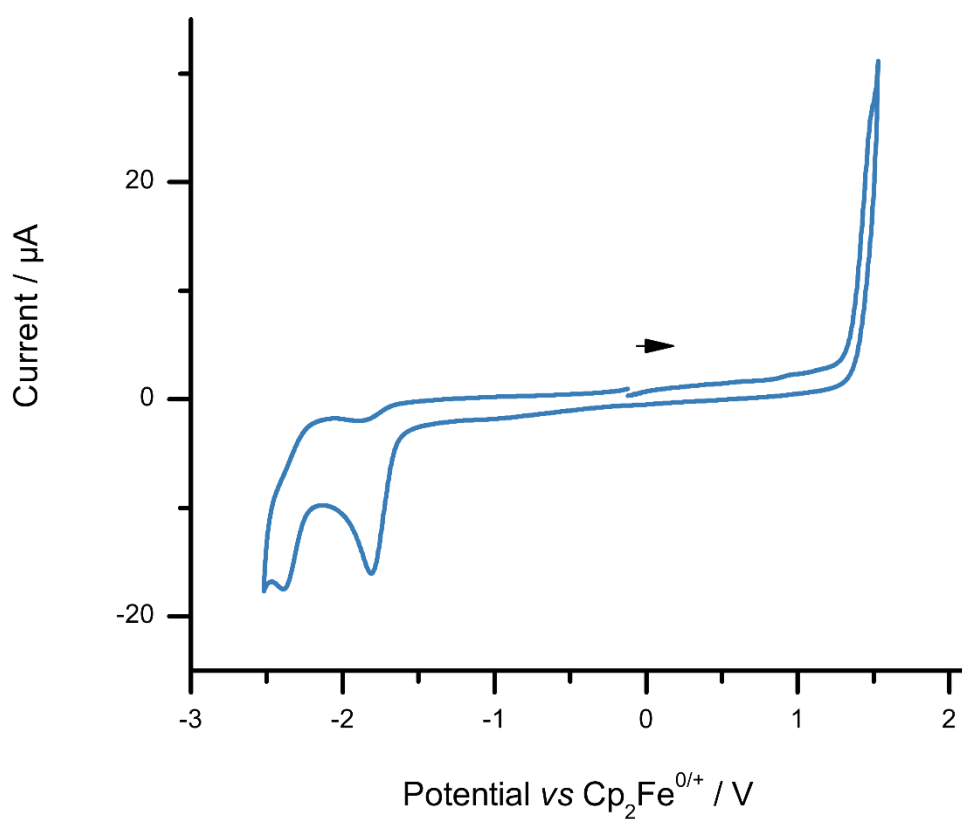


Figure 67 Experimental CVs of the isolated bridging hydrides a) $[\text{TMP-H}][(\mu\text{-H})(\mathbf{20})_2]$ (3.1 mM), and b) $[\text{H}(\text{THF})_2][(\mu\text{-H})(\mathbf{20})_2]$ (1 mM), recorded in CH_2Cl_2 at a GCE ($\nu = 100 \text{ mV s}^{-1}$).

To allow a study into the redox chemistry of the terminal hydride, [20-H]⁻, to be conducted, a sample of authentic Na[20-H] was prepared. Unlike in Chapter 3, metathesis of the Na salt was not necessary, since it is sufficiently soluble in the THF/[ⁿBu₄N][B(C₆F₅)₄] electrolyte system (THF is now the preferred choice of solvent for the electrochemical-FLP approach).

Cyclic voltammetry was performed on a solution of Na[20-H] (3.5 mM) in THF at a GCE (Figure 68). On sweeping the potential anodically from the OCP at 100 mV s⁻¹, an oxidation wave was observed at +0.78 V vs Cp₂Fe^{0/+}. The wave was indicative of an underlying EC mechanism, that is analogous to that of [ⁿBu₄N][8-H] (+0.88 V vs Cp₂Fe^{0/+}, see Chapter 3). However, the required oxidation potential for [20-H]⁻ occurs approximately 100 mV lower than that of [8-H]⁻. This suggests that [20-H]⁻ is significantly more hydridic than [8-H]⁻, albeit not as hydridic as the NHC-borane, 19-H (+0.58 V vs Cp₂Fe^{0/+}, Chapter 5). Note that the voltammetric reduction of the parent Lewis acid, 20, was not observed on the reverse scan. This is because any electrogenerated 20 becomes quenched by the donor solvent, forming the classical Lewis adduct THF·20. Indeed, a solution of 20 in THF/[ⁿBu₄N][B(C₆F₅)₄] electrolyte was found to be electroinactive at all potentials (-2.6 to +1.4 V vs Cp₂Fe^{0/+})^[195] within the electrochemical window. Whilst the coordination of THF to 20 is reversible, its equilibrium position strongly favours the formation of THF·20, hence there is negligible free 20 available at any one time for electro-reduction.

It is not possible to digitally simulate the electrochemical oxidation of Na[20-H] due to the large quantity of unknown thermodynamic and kinetic parameters. The previous hydride systems ([8-H]⁻ and 19-H) were simulated using values obtained from independent fits of the CVs obtained for the reduction of the parent Lewis acids (8 and 19). Since the electroreduction of 20 cannot be measured in donor solvents, these parameters cannot be deduced.

The cyclic voltammetry of [TMP-H][(μ -H)(20)₂] (3.5 mM) was also conducted (at a GCE) in THF solution. Unsurprisingly, an oxidation wave that is characteristic of Na[20-H] was observed, indicating the formation of [TMP-H][20-H] (and electroinactive THF·20). This provides further supporting evidence for the mechanism and equilibria proposed in 6.5 and Scheme 36.

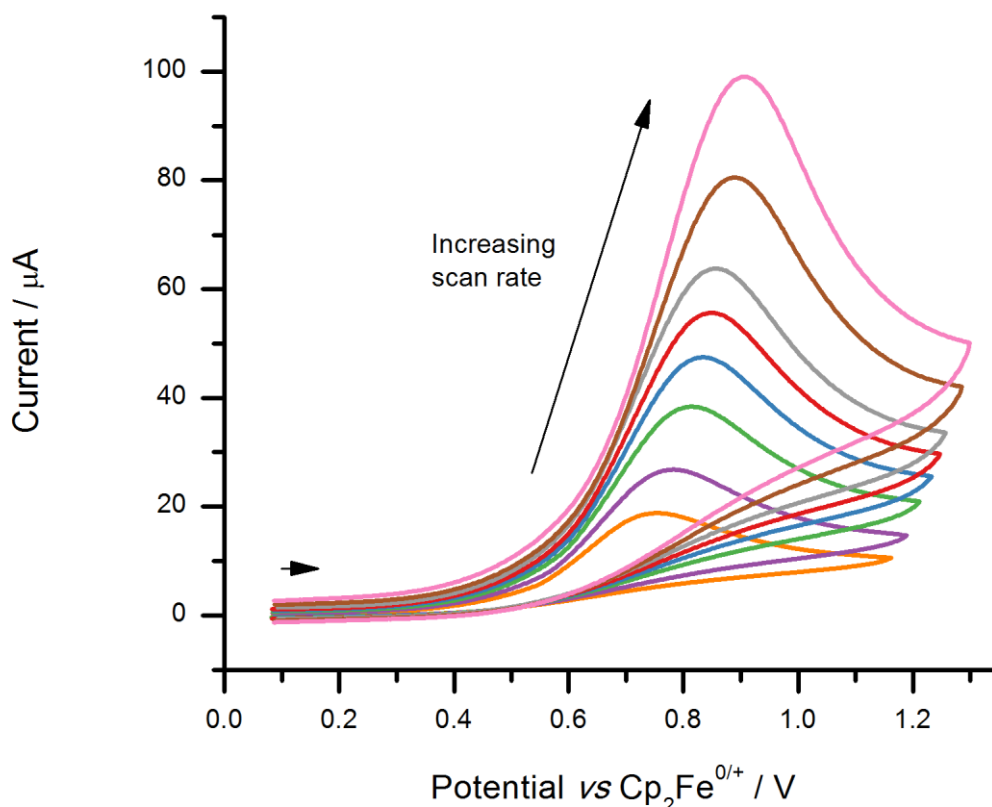


Figure 68 Overlaid CVs for the authentic terminal hydride, Na[**20-H**] (3.5 mM), recorded in THF at a GCE at scan rates (ν) of 50, 100, 200, 300, 400, 500, 750 and 1000 mV s^{-1} .

6.7 Investigating *in situ* H₂ oxidation

In situ electrochemical oxidation of H₂ by **20** using THF as the Lewis base was not attempted for two reasons:

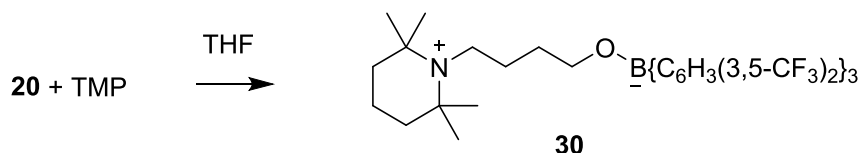
- The pre-activation of H₂ *via* the formation of $[(\mu\text{-H})(\mathbf{20})_2]^-$ does not provide a decrease in the energetic driving force for H₂ oxidation.
- It is not possible to differentiate between molecular H₂ and $[(\mu\text{-H})(\mathbf{20})_2]^-$, since both oxidation waves are observed at +1.49 V vs Cp₂Fe^{0/+}.

Whilst **20**/THF is not an electrocatalyst for H₂ oxidation, and any efforts to utilise this system would be futile, the terminal hydride, [**20-H**]⁻, provides a 710 mV (137.0 kJ mol⁻¹) decrease in the required potential for H₂ oxidation. Considering this benefit, I decided to investigate whether it was possible to activate H₂ *in situ* and oxidise the resulting [**20-H**]⁻. In an

attempt to favour the formation of $[\mathbf{20-H}]^-$, I decided to employ the $\mathbf{20}$ /TMP system in THF solvent.

An equimolar $\mathbf{20}$ /TMP solution (2.5 mM) in THF was sparged with H_2 for 15 minutes before a CV was recorded at a GCE ($\nu = 100 \text{ mV s}^{-1}$). A large EC-like oxidation wave, characteristic of the terminal hydride $[\mathbf{20-H}]^-$, was observed at +1.36 V vs $\text{Cp}_2\text{Fe}^{0/+}$. However, from the previous study on the authentic $\text{Na}[\mathbf{20-H}]$ sample, it was clear that this wave is at too high a potential ($\Delta E_p \approx 550 \text{ mV}$) to correspond to $[\mathbf{20-H}]^-$.

I was concerned that I'd overlooked one of the fundamental reactions exhibited by some FLP systems, their ability to ring-open THF.^[147,170] As a control experiment, the cyclic voltammetry of $\mathbf{20}$ was recorded in THF under N_2 (**Figure 69**); no redox waves observed to be present. When a molar equivalent of TMP was added to generate an active FLP (the system remaining under a N_2 atmosphere) the same wave at +1.36 V vs $\text{Cp}_2\text{Fe}^{0/+}$ was observed, as before. An additional EC-like oxidation wave was also observed at +0.78 V vs $\text{Cp}_2\text{Fe}^{0/+}$; this corresponds to the single-electron oxidation of TMP to its corresponding radical cation^[302] (and was confirmed independently). It is likely that the oxidation wave at +1.36 V vs $\text{Cp}_2\text{Fe}^{0/+}$ corresponds to an oxidation process involving the relatively strong B-O bond of the zwitterionic THF activation product (**30**, **Scheme 42**). Indeed, the ring-opening of THF by $\mathbf{20}$ paired with the bulky NHC carbene, Im^tBu_2 , has been previously reported by Tamm and co-workers.^[147]



Scheme 42 Postulated product (**30**) of THF ring-opening by $\mathbf{20}$ /TMP.

Note that THF is not sufficiently Lewis basic to ring-open itself in the presence of $\mathbf{20}$ during the timescale of electrochemical experiments. Over the course of 1-2 months, solutions of $\mathbf{20}$ in d_8 -THF were observed to become gel-like in appearance, presumably due to the very slow rates of THF activation in the absence of a strong bulky base (such as TMP).

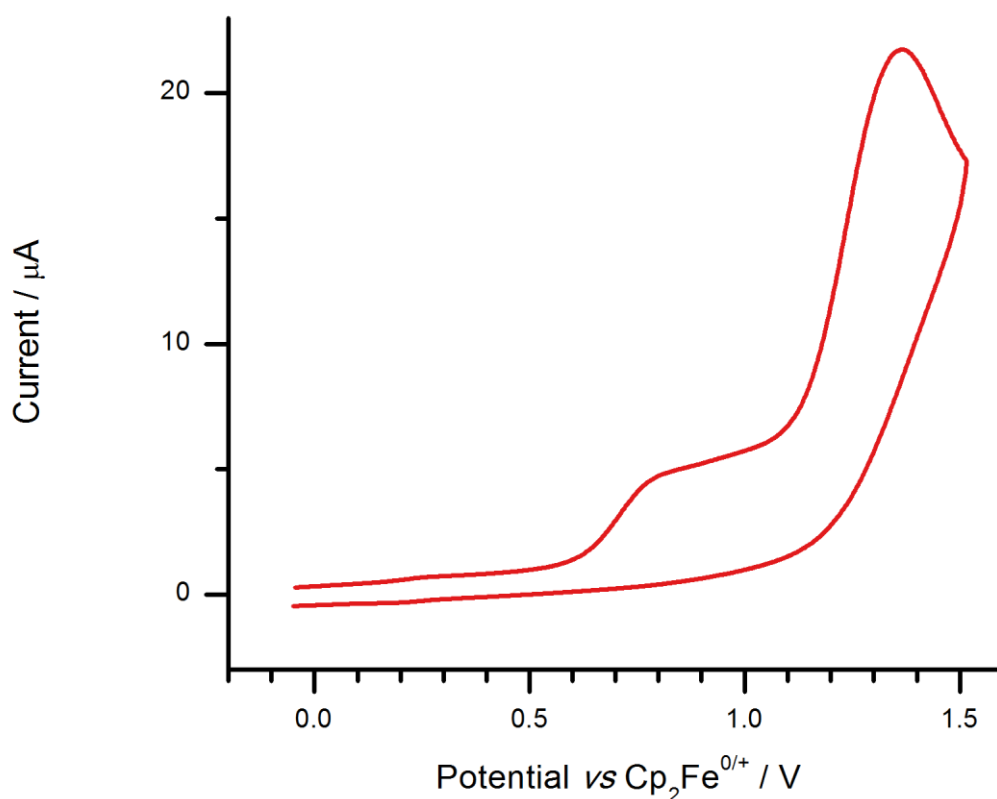
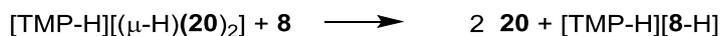


Figure 69 CV of the **20**/TMP FLP (2.5 mM) recorded in THF at a GCE, showing the THF activation product ($\nu = 100 \text{ mV s}^{-1}$).

6.8 Hydride shuttle processes between boranes

Electrochemical studies (6.3) and the Gutmann-Beckett^[293,294] and Childs^[295] methods (by Ashley and co-workers)^[146] suggested that **20** is significantly more electrophilic and Lewis acidic than the more commonly used bulky Lewis acid, **8**. Intuitively, one would normally expect the corresponding hydride of the least Lewis acidic/electrophilic borane to be a stronger hydride donor. Indeed, this has previously been used to assess the relative Lewis acidity of different boron-based Lewis acids.^[272] Since **20** has a tendency to form $[(\mu\text{-H})(\mathbf{20})_2]^-$ in preference to $[\mathbf{20}\text{-H}]^-$ in non-donor media, I was curious as to whether this expectation would still hold true. When a solution of $[\text{TMP-H}][(\mu\text{-H})(\mathbf{20})_2]$ in CD_2Cl_2 was treated with a molar equivalent of **8**, the formation of a clear and colourless solution indicated that the sparingly soluble starting material had undergone reaction. Surprisingly, ^1H , $^{19}\text{F}\{^1\text{H}\}$ and ^{11}B NMR spectra indicated the presence of $[\text{TMP-H}][\mathbf{8}\text{-H}]$ and **20**. The high oxidation potential of $[(\mu\text{-H})(\mathbf{20})_2]^-$ would suggest that it has a low hydride donor ability compared to $[\mathbf{8}\text{-H}]^-$. Given this, the driving force for the observed

hydride transfer reaction (shown in **Scheme 43**) must result from entropic effects *i.e.* the release of two molecules of **20**.



Scheme 43 Hydride shuttle process between $[\text{TMP-H}][\mu\text{-H}(\mathbf{20})_2]$ and **8**.

The rate of $[\mathbf{8-H}]^-$ formation has always been a limiting factor for the electrochemical-FLP systems (refer to Chapter 3). Whilst evidence of H_2 activation is spectroscopically observed after 1 hour in NMR experiments, the observation of a well-defined doublet (corresponding to hydride formation) in the ^{11}B NMR spectrum is not observed until after 12 hours.^[124] While Stephan has described H_2 activation by the **8/12** system as being immediate,^[120] when Rieger and co-workers reported H_2 activation by the **8/TMP** FLP, they found that, unless H_2 activation is driven to completion by either heating or solvent removal, it takes approximately a day for H_2 activation to go to completion. These kinetics are similar to what I observed for the **8/12** system in Chapter 3; Rieger and co-workers postulated that an encounter complex forms between H_2 and the **8/TMP** FLP. There are clearly some discrepancies in the literature with respect to the rate of H_2 cleavage by these FLP systems – this is probably related to the choice of solvent, the presence of additional ionic media (*i.e.* added electrolyte salts), and variation in H_2 pressure/solubility. As demonstrated in Chapter 3, for electrochemical-FLP systems based on **8**, the oxidation potential of $[\mathbf{8-H}]^-$ is much lower than that of H_2 . Conversely, while **20/TMP** exhibits rapid H_2 cleavage kinetics, $[\text{TMP-H}][(\mu\text{-H})(\mathbf{20})_2]$ does not offer an electrocatalytic effect (the potential is the same as that of H_2). The observation of hydride transfer between $[\text{TMP-H}][(\mu\text{-H})(\mathbf{20})_2]$ and **8** led me to consider whether the combined **8/20** Lewis acid pair is capable of facilitating the formation of $[\mathbf{8-H}]^-$ in the presence of TMP and H_2 . Using **20** as a hydride shuttle would provide a system that offers the oxidation potential of $[\mathbf{8-H}]^-$ with the extremely rapid H_2 cleavage kinetics of **20**.

When an equimolar solution of **8**, **20**, and TMP in CD_2Cl_2 were admitted to H_2 (4 atm), the immediate formation of $[\mathbf{8-H}]^-$ was evidenced by the appearance of a doublet resonance in the ^{11}B NMR spectrum at $\delta -24.3$ ppm ($J = 87$ Hz). The presence of an additional broad signal at $\delta 0.0$ ppm was tentatively attributed to the formation of the mixed bridging hydride species, $[\mathbf{20}(\mu\text{-H})\mathbf{8}]^-$. An attempt to accelerate the formation of $[\mathbf{8-H}]^-$ using a catalytic quantity of **20** (10 mol%) did not work. In this case, only after *ca* 12 hours of exposure to H_2 was a fully resolved

doublet observed in the ^{11}B NMR spectrum, characteristic of $[\mathbf{8}\text{-H}]^-$ and similar to the characteristic FLP behaviour of $\mathbf{8}$ alone towards H_2 .

The development of hydride shuttles may allow the optimisation of FLP systems that have a high kinetic barrier to H_2 activation, despite the process being thermodynamically favourable. For example, the acridine-stabilized borenium cation (reported by Clark *et al.*) is an extremely strong carbon-based Lewis acid, however for reasons that are unknown it has a high kinetic barrier to H_2 activation.^[303] If a catalytic hydride shuttle process could be developed then this carbon-based Lewis acid may function effectively as a hydrogenation catalyst. For electrochemical-FLP systems, synergy between two different Lewis acids may combine their best attributes for improved H_2 cleavage kinetics and lower oxidation potentials. In such a case, one would wish for a Lewis acid, that is capable of rapidly cleaving H_2 in THF alone, to act as the FLP hydride shuttle to another Lewis acid that has more favourable electrochemical properties. Whilst this is not possible with Lewis acid combination $\mathbf{20}/\mathbf{8}$ in THF (due to the propensity of THF to undergo ring opening reactions in the presence of $\mathbf{8}$), the $\mathbf{20}/\mathbf{8}/\text{TMP}$ system (in CH_2Cl_2) does at least demonstrate that this tantalising prospect is a strong possibility. Alternative Lewis basic solvent systems, including tetrahydrothiophene (THT) and dioxanes may prove more resistant to ring opening side reactions whilst still enabling added base-free solvent-FLP activation of H_2 to occur. Ideally, however, it would be more desirable to find a solvent-based FLP system that containing only one Lewis acidic component, yet provides an acceptable compromise between fast H_2 cleavage kinetics and a desirably low hydride oxidation potential. Current studies and on-going efforts (within the Wildgoose group) seek to modify the electronic and steric properties of Lewis acids similar to $\mathbf{20}$, to fine tune the electrochemical-FLP approach for the truly electrocatalytic oxidation of H_2 .

6.9 Summary

In this final results and discussion chapter, the electrochemistry of regioisomers of $\text{B}\{\text{C}_6\text{H}_3(\text{CF}_3)_2\}_3$, $\mathbf{20}$ and $\mathbf{28}$, were explored for the first time. The boranes exhibited *quasi*-reversible voltammetry coupled with a follow-up decomposition step in solution. Whilst the decomposition process is very fast for $\mathbf{20}^{\bullet-}$, the boron centre of $\mathbf{28}^{\bullet-}$ is sterically protected by the *ortho*- CF_3 groups, making it more stable towards decomposition. Whilst this was advantageous for electrochemical applications, the steric bulk of $\mathbf{28}$ prevented its utility for H_2 activation when paired with TMP. An optimal balance of steric protection and accessibility to H_2 is clearly required.

Solutions of **20** in THF were highly effective for H₂ activation, with the donor solvent functioning as the Lewis base. On admission of H₂, an equilibrium is immediately established (faster than can be measured using NMR spectroscopy) between the bridging hydride, $[(\mu\text{-H})(\mathbf{20})_2]^-$, and the classical Lewis adduct, THF·**20**. The reaction mechanism was rationalized by comparing the **20**/THF system to the previously studied **20**/TMP system, and considering relative hydride donor abilities and pK_a values. The substitution of additional phosphine or amine Lewis bases by a suitable donor solvent is likely to provide a number of advantages for combined electrochemical-FLP systems. This includes the buffering of redox-generated H⁺ and improvements in recyclability through reduced electrode-fouling in the absence of any added Lewis bases.

The redox properties of the bridging and terminal hydrides were also investigated. The oxidation potential for $[(\mu\text{-H})(\mathbf{20})_2]^-$ was found to be identical to that for H₂. Whilst the **20**/THF system offers extremely fast H₂ cleavage kinetics, the formation of $[(\mu\text{-H})(\mathbf{20})_2]^-$ unfortunately provides no energetic advantages *i.e.* a lower oxidation potential (electrocatalysis), and can be considered as an electrolyte salt. Although $[\mathbf{20}\text{-H}]^-$ decreases the required potential for H₂ oxidation by 710 mV (137.0 kJ mol⁻¹), it is not an easily accessible species under the conditions in which an ideal electrochemical-FLP system would need to operate.

Finally, $[(\mu\text{-H})(\mathbf{20})_2]^-$ was found to participate in hydride transfer reactions to the Lewis acid, **8**. The rate of H₂ activation by the **8**/TMP FLP can be greatly accelerated by using stoichiometric amounts of **20** as a hydride shuttle (full conversion of **8** to $[\mathbf{8}\text{-H}]^-$ in the presence of **20** is observed in the time it takes to run an NMR spectrum, this is compared to several hours in the absence of **20**). The discovery of this shuttle process alludes to the possibility of new electrochemical-FLP systems, where the advantages of two different Lewis acids are combined for improved H₂ cleavage kinetics and lower oxidation potentials.

Chapter 7

Conclusions and future work

7.1 Conclusions

The work contained in this thesis details progress towards the development of electrocatalysts for H₂ oxidation. This new generation of electrocatalysts are unique in that FLPs are utilised for the pre-activation of H₂ for the net conversion of H₂ into 2H⁺ and 2e⁻ at decreased oxidation potentials.

In Chapter 2, an initial study into the fundamental redox chemistry of **8** was conducted in two weakly coordinating solvents, CH₂Cl₂ and DFB. **8** was found to undergo *quasi*-reversible single-electron reduction to give the radical anion, **8**^{•-}. The rapid decomposition of electrogenerated **8**^{•-} in solution results in the formation of redox inactive products. A sample of **8** was chemically reduced using Co^{II}(Cp^{Me5})₂ and some of the decomposition products were identified using multinuclear NMR spectroscopy. The spectra suggested the formation of several four-coordinate borate species, arising from radical reactions with the solvent. This indicated that the reaction of solvent with **8**^{•-} predominantly occurs at the boron centre, and was further supported by spin density and charge distribution calculations on the SOMO of **8**^{•-}.

The fundamental work of Chapter 2 enabled an electrochemical study of the archetypal **8/12** FLP system to be conducted for the first time in Chapter 3 using [ⁿBu₄N][**8-H**]⁻ – an authentic sample of the borohydride. The FLP pre-activation of H₂, when combined with electrochemical oxidation of the resultant borohydride, was found to decrease the required potential for non-aqueous H₂ oxidation by 610 mV (117.7 kJ mol⁻¹) at readily available carbon electrodes. *In situ* oxidation of [**8-H**][**H-12**]⁻, generated by the classical **8/12** FLP system in the presence of H₂, was also explored.

In Chapter 4, the electrochemical study of [**8-H**]⁻ was extended to a Pt electrode, where strong electrocatalytic surface effects were exhibited following its electrooxidation. This was apparent from the significant current-crossover (phase change) observed in the cyclic voltammetry of [**8-H**]⁻ and, more importantly, a 390 mV reduction in the oxidation peak potential compared to that obtained at a GCE. It was postulated that HAT occurs between electrogenerated [**8-H**][•] and the Pt electrode, forming H[•] adatoms on the surface. It was found that this pathway could be competitively inhibited in the presence of a competing radical scavenger. Also, when cyclic voltammetry of the bulkier perchlorinated analogue, [**24-H**]⁻, was explored at Pt, this surface electrocatalytic effect was no longer observed. This is likely to result from steric protection of the H atom within the C₆Cl₅ aryl rings, precluding HAT to the Pt electrode surface.

In Chapter 5, the redox chemistry of several (new and previously reported) NHC-stabilised borenium cations was explored at a GCE. Whilst **25**[OTf], **26**[OTf] and **27**[OTf] were

found to exhibit relatively stable $\mathbf{B}^+/\mathbf{B}^\bullet$ redox couples (with a slow \mathbf{B}^\bullet decomposition step) they were very poor candidates for FLP H_2 activation when combined with the Lewis base, **12**. In fact, these FLPs exhibited unusual behaviour in the chlorinated solvents, CDCl_3 and CD_2Cl_2 , and I was unable to fully elucidate the reaction mechanisms and products involved. In converse, **19**[$\text{B}(\text{C}_6\text{F}_5)_4$] was found to exhibit typical *EC*-like cyclic voltammetry with a rapid rate of **19** $^\bullet$ decomposition, and its ability for hydrogen activation is known. Using **19**[$\text{B}(\text{C}_6\text{F}_5)_4$] as the Lewis acid component of the FLP was found to have several advantages over the initial **8**-based system. Indeed, the voltage required to oxidise H_2 at a carbon electrode was decreased by almost one volt (910 mV, $175.6 \text{ kJ mol}^{-1}$), the rate of H_2 oxidation was also faster, producing larger currents, and **19** $^+$ appeared to be more resistant to undesirable side-reactions with redox-generated H^+ . This electrochemical-FLP system was found to be somewhat “rechargeable” – allowing the *in situ* regeneration of **19**-H from **19** $^+$ in the presence of **12** and H_2 , with 75% efficiency after the first cycle.

In Chapter 6, the electrochemistry of two structural isomers of $\text{B}\{\text{C}_6\text{H}_3(\text{CF}_3)_2\}_3$, **20** and **28**, were explored for the first time. The cyclic voltammetry exhibited by these boranes was analogous to that of the $\mathbf{8}/\mathbf{8}^{\bullet-}$ redox couple explored in Chapter 2. The decomposition of electrogenerated **28** $^{\bullet-}$ is approximately 6000 times slower than that of **20** $^{\bullet-}$, since the boron centre in **28** $^{\bullet-}$ is sterically protected by the *ortho*- CF_3 groups. Whilst this was advantageous for electrochemical applications, the steric bulk of **28** prevents its utility for FLP H_2 . However, solutions of **20** in THF were found to be highly effective for H_2 activation, where the donor solvent functions as the Lewis base. On admission to H_2 , an equilibrium is immediately established between the bridging hydride, $[(\mu\text{-H})(\mathbf{20})_2]^-$, and the classical Lewis adduct, THF-**20**. The redox properties of the bridging and terminal hydrides were also investigated. The oxidation potential for $[(\mu\text{-H})(\mathbf{20})_2]^-$ was found to be identical to that for H_2 . Whilst the **20**/THF system offers extremely fast H_2 cleavage kinetics, the formation of $[(\mu\text{-H})(\mathbf{20})_2]^-$ unfortunately provides no energetic advantages *i.e.* a lower oxidation potential (electrocatalysis). Although $[\mathbf{20}\text{-H}]^-$ decreases the required potential for H_2 oxidation by 710 mV ($137.0 \text{ kJ mol}^{-1}$), it is not easily accessible. Finally, $[(\mu\text{-H})(\mathbf{20})_2]^-$ was found to be highly effective for hydride transfer reactions to the Lewis acid, **8**. The rate of H_2 activation by the **8**/TMP FLP can be greatly accelerated by using stoichiometric amounts of **20** as a hydride shuttle (full conversion of **8** to $[\mathbf{8}\text{-H}]^-$ appears to be immediate, compared to several hours when in the absence of **20**).

The ability of FLPs to activate H_2 provides a significant energy saving (up to one Volt, thus far) for the net conversion of H_2 into 2H^+ and 2e^- without the use of precious metals. This opens up hitherto unexplored routes to the development of economically viable electrocatalysts for H_2 oxidation.

7.2 Future work

This thesis presents the first study of its kind into the development of electrocatalytic FLPs for H₂ oxidation. Whilst there is no doubt that this work has made significant progress since the advent of the initial **8/12** system, it is not surprising that this system is not yet optimal.

The kinetics of H₂ cleavage is usually the rate-limiting step in these systems. This can be improved through the modification of the combined steric and electronic effects of the Lewis acidic and basic FLP components. Indeed, new Lewis acids and improved FLP combinations are constantly being reported within the field. Highly electrophilic Lewis acids (relative to **8**) are likely to exhibit a greater propensity for FLP H₂ activation. For example, FLPs composed of **20** were found to be potent for the facile activation of H₂. However, one must consider the impact imposed on the oxidation potential of the hydride through modifying electronic effects.

The oxidation potential of the hydride is extremely important for these electrochemical-FLP systems. The lower the oxidation potential, the greater the energy saving that is achieved *via* the pre-activation of H₂ by a FLP. The electrophilicity of the Lewis acid is often negatively correlated to the hydride donor ability (and oxidation potential) of the corresponding borohydride. Therefore, it is likely that the optimised electrochemical-FLP system will need to compromise the desired rate of H₂ heterolysis for an appropriate decrease in the oxidation potential compared to that of molecular H₂.

The shortcoming of systems based on **20** was that the bridging hydride failed to provide an adequate electrocatalytic effect. Conversely, the terminal hydride provided a 710 mV decrease in the required potential for H₂ oxidation, but was practically unattainable for an ideal system. Based on this, I propose that short term, future work should focus on incrementally increasing the steric bulk of **20**. Subtle steric changes about the boron centre may favour the formation of terminal hydride whilst retaining its ability for facile H₂ cleavage.

The recent work of Samigullin *et al.* details a systematic approach to the synthesis of boranes containing C₆H₃(3,5-CF₃)₂ groups; essentially, the boranes are assembled in a sequential (ring-by-ring) fashion.^[304] This controlled and selective approach may enable subtle changes in the sterics of **20** to be made through variation of one or two of the surrounding groups. For example, the substitution of one of the C₆H₃(3,5-CF₃)₂ rings for a more encumbering C₆H₃(2,4-CF₃)₂ group. In the medium term, this synthetic protocol could be extended to the synthesis of a huge range of novel Lewis acids containing combinations of C₆F₅, C₆Cl₅, and C₆H₃(CF₃)₂ groups.

The transient radical intermediates that are redox-generated during borohydride oxidation are often highly susceptible to radical decomposition *via* reaction with the electrolyte system. This leads to deactivation of the electrocatalyst, which limits the ability to

turnover/recycle the system and prevents the system from being truly electrocatalytic. Increasing the steric protection of boron centre is likely to improve the stability of any redox-generated intermediates, by limiting the accessibility of the boron-centred unpaired electron to surrounding solvent molecules. However, this effect will negatively impact the rate of FLP H₂ activation, and (as for the oxidation potential) a compromise must be met. Indeed, an electrochemical study of the incredibly bulky borenium cations: **25**⁺, **26**⁺, **27**⁺; and the bulky borane, **28**, suggested that the electrogenerated radicals were relatively stable to decomposition. However, these Lewis acids were completely ineffective for H₂ activation when paired with a Lewis base. The introduction of large, conjugated groups that delocalise spin density from the boron centre may also provide improvements in the stability of radical intermediates and is worth exploring further.

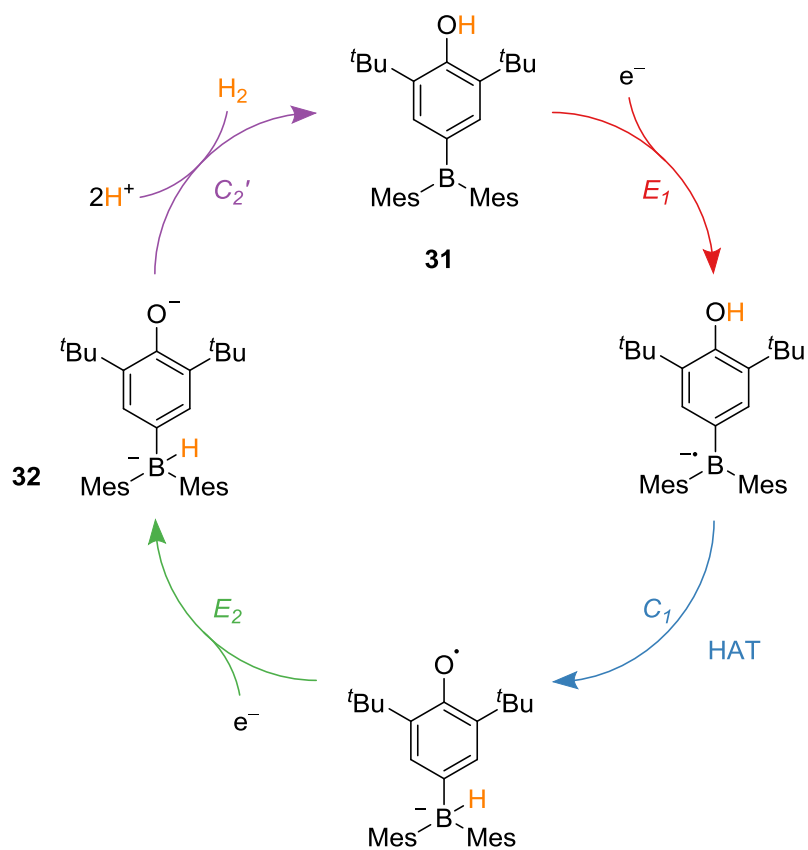
The substitution of additional phosphine or amine Lewis bases for a suitable donor solvent is likely to provide a number of advantages for combined electrochemical-FLP systems. This includes the buffering of redox-generated H⁺ and improvements in recyclability through reduced electrode-fouling. In future, all new Lewis acids must be screened for FLP activity in donor solvents (such as THF, THT, 1,4-dioxane *etc.*) as well as traditional low donor solvents (such as CH₂Cl₂) containing added Lewis base. The electrochemical-FLP may not be limited to ethereal solvents. I envisage that in the future, FLP systems may be stable under aqueous conditions. Indeed, Clark and Ingleson have already reported a new FLP that is active in the presence of trace amounts of water, using carbon-based Lewis acids.^[284]

While our ideal optimized system would be electrocatalytic in the Lewis acid component, it would still be stoichiometric in the Lewis base. Whilst this would generally not be an issue for donor solvent-based systems, where the Lewis base is in large excess, it may cause concern for the systems that rely on the presence of additional Lewis base. So far, all studies into this system have only been concerned with the electrocatalysis of the anodic half-cell reaction *i.e.* H₂ oxidation. However, if the system were to be utilized as part of a complete electrochemical cell reaction (*e.g.* a fuel cell) then clearly it requires coupling to a suitable cathodic half-cell reaction (*e.g.* O₂ reduction) that is capable of closing the catalytic cycle by consuming the redox-generated protons. First, an optimized and economically viable system that is suitable for H₂ oxidation needs to be developed. Future long term goals would then involve the fabrication of this system into prototype fuel cell devices, in an attempt to couple this system to the O₂ reduction half-cell reaction.

Finally, one could digress and question why this type of electrocatalyst should only be restricted to H₂ oxidation processes. Indeed, hydrogenase enzymes mimics have also been developed for the reverse process *i.e.* H₂ evolution/production.^[60] The H₂ evolution side-reaction

that is apparent in the electrochemical-FLP systems alludes to the possibility of using boranes for the electrocatalysis of H₂ production, at least in non-aqueous systems. I previously believed that the formation of a borohydride from H⁺ would present a considerable challenge. The first step would obviously involve single-electron reduction of the borane to give a radical anion. However, the formation of the borohydride from H⁺ is likely to be a challenge. Conventional H₂ production electrocatalysts, based on hydrogenase mimics, make use of pendant amines (which function as H⁺ relays, lowering the barrier for H⁺ transfers to the metal centre) and the versatility of metal centres to occupy different oxidation states (thereby functioning as an electron source). Since our boranes only exhibit single-electron redox chemistry, borohydride formation would need to proceed *via* a HAT or PCET process. Chiu and co-workers recently found that the hydroxylphenyl-substituted borane (**31**) undergoes single-electron reduction followed by intramolecular HAT from the phenol group to the boron centre, resulting in the formation of a phenoxyl radical anion.^[305] This intermediate undergoes a second single-electron reduction to give the borohydride phenoxide dianion (**32**).

While, the authors were concerned with the antioxidant activity of hydroxyphenyl-substituted boranes, from my perspective, such compounds may be better suited as electrocatalysts for H₂ production. I postulate that in the presence of an appropriate Brønsted acid, **32** would become unstable, resulting in concomitant H₂ evolution and re-protonation of the phenoxide to regenerate **31**. It is highly likely that this system would exhibit the $E_1C_1E_2C_2'$ mechanism shown in **Scheme 44**, which would be evidenced by the observation of an electrocatalytic reduction wave in the CV. This is a simple, yet high impact, concept that would open up a whole new area of chemistry to the research group, and I strongly recommend that this idea is explored further.



Scheme 44 New concept for electrocatalytic H₂ production using the hydroxyphenylborane (**31**), $E_1 < E_2$.

Chapter 8

Experimental methods and materials

8.1 General considerations

All synthetic reactions and manipulations were performed under a rigorously dry N₂ atmosphere (BOC Gases) using standard Schlenk-line techniques on a dual manifold vacuum/inert gas line or either a Saffron or MBraun glovebox. All glassware was flame-dried under vacuum before use.

8.2 Materials

8.2.1 Solvents

Anhydrous solvents were dried by reflux over appropriate drying agents and were collected by distillation. THF, Et₂O, hexane, pentane and light petroleum ether were dried by reflux over Na/benzophenone diketyl; toluene was dried by reflux over molten Na; chlorobenzene, bromobenzene, CH₂Cl₂, DFB, pyrrolidine (**29**), and CH₃CN were dried by reflux over CaH₂. All solvents were sparged with N₂ gas to remove any trace of dissolved O₂ and stored in ampoules over activated 4 Å molecular sieves.

Deuterated NMR solvents (CDCl₃, 99.8%; DMSO-d₆, 99.9%; C₆D₆, 99.5%; CD₃CN, 99.8%; [D₈]THF, 99.5%; CD₂Cl₂, 99.9%) were purchased from Cambridge Isotope Laboratories Inc. (MA, USA) and were dried over P₄O₁₀, degassed using a triple freeze-pump-thaw cycle process and stored over activated 4 Å molecular sieves.

8.2.2 Gases

N₂ gas (O₂-free) and H₂ gas (99.995%) were purchased from BOC gases and passed through drying columns containing P₄O₁₀ and 4Å molecular sieves. D₂ gas was generated *in situ* from the reaction of Na with degassed D₂O (99.9%, Cambridge Isotope Laboratories Inc.); and was passed through drying a column containing P₄O₁₀. HCl gas was generated *in situ* from the reaction of H₂SO₄ with NaCl and was passed through drying a column containing CaCl₂.

8.2.3 Reagents

Bromopentafluorobenzene, 3,5-bis(trifluoromethyl)bromobenzene, and 2,4-bis(trifluoromethyl)bromobenzene were purchased from Fluorochem (Hadfield, UK) and used without further purification. Mg turnings were purchased from Alfa Aesar and used as supplied. ⁿBu₄NCl was purchased from Alfa Aesar and recrystallized from anhydrous acetone prior to use. NOPF₆ was purchased from Alfa Aesar and used as supplied. All other reagents were purchased from Sigma-Aldrich and were of the highest grade available and used without further purification.

8,^[306] **24** (prepared and supplied by Dr. T. Herrington of Dr. A. Ashley's group),^[244] FBMe₂,^[307] NHCs (ImⁱPr₂, ImMe₂,^[308] and ImMe₄^[278]), **19-H**,^[150] [**19**][B(C₆F₅)₄],^[150] **20**,^[146,147] [TMP-H][(μ -H)(**20**)₂],^[146] [ⁿBu₄N][B(C₆F₅)₄],^[195,200,309] [H(OEt₂)₂][B(C₆F₅)₄]^[258] and **12**^[310] were prepared according to literature methods. [TMP-D][DB(C₆F₅)₃] was prepared using an adapted literature method, which is detailed below.^[124] **28** was prepared by Dr. T. Herrington of Dr. A. Ashley's group using a modified literature procedure, which is detailed below.^[292]

8.3 Instrumentation

NMR spectra were recorded using either a Bruker Avance DPX-300 MHz or Bruker Avance DPX-500 MHz spectrometer. Chemical shifts are reported in ppm and are referenced relative to appropriate standards: ¹⁹F (CFCl₃); ¹¹B (Et₂O·BF₃); ³¹P (85% H₃PO₄); ¹H (solvent residual signal); ²D (spiked with non-deuterated solvent).^[296] For NMR experiments (other than ²D NMR) performed in non-deuterated solvents a C₆D₆ insert was used.

IR spectra were recorded using a PerkinElmer μ -ATR Spectrum II spectrometer.

Sample headspace analysis was performed using a PerkinElmer Clarus 580 gas chromatograph coupled with a thermal conductivity detector (GC-TCD). Retention time for H₂ gas was calibrated using a standard sample. ESI-MS spectra were recorded using a Shimadzu LCMS 2010EV spectrometer in negative ESI mode.

EPR spectra were recorded using a Bruker ER200D spectrometer fitted with a dual-mode (ER4116M) X-band cavity and interfaced to an EMX control system. A flow-through cryostat used in conjunction with a Eurotherm (B-VT-2000) variable temperature controller provided temperatures ranging from 80-180 K.

Details on electrochemical methods, including the digital simulation of voltammetric data, and density functional theory (DFT) computational modelling are given below.

X-ray crystallographic instrumentation details are given in the appendix of crystallographic data.

8.4 DFT computational modelling

All calculations were performed using the Gaussian 09 computational package.^[311] Geometry optimisation and frequency calculations have been carried out using the three-parameter exchange functional of Becke (B3)^[312] and the correlation functional of Lee, Yang, and Parr (LYP), B3LYP.^[313] In each case an all electron 6-311+G(d,p) basis set has been implemented for all atoms. Structures were geometry optimised in the gas phase with the default convergence criteria and confirmed as minima through frequency calculations. Zero-point energies and

thermodynamic properties were calculated at 298.15 K and 1 atm. All calculations have been performed at spin-unrestricted level of theory. Bond dissociation energies were calculated by taking the difference in the total enthalpies between the original structure and optimized fragments, assuming homolytic cleavage. The enthalpies included both electronic contributions and thermal corrections. The charge distribution shown for $\mathbf{8}^{2-}$ in **Figure 6** is based on Mulliken electron population analysis.

8.5 Electrochemical methods

8.5.1 General methods

All electrochemical experiments were performed using either an Autolab PGSTAT 30 or PGSTAT 302N computer-controlled potentiostat (Utrecht, The Netherlands). Cyclic voltammetry (CV) was performed using a three-electrode configuration consisting of either a Pt macrodisk working electrode (GoodFellow, Cambridge, UK; 99.99%; area $1.4 \pm 0.5 \times 10^{-3} \text{ cm}^2$), glassy carbon macrodisk working electrode (GCE) (diameter of 3 mm; BASi, Indiana, USA), or a Pt microdisk working electrode (GoodFellow, Cambridge, UK; 99.99%; radius $30.5 \pm 0.5 \mu\text{m}$), combined with a Pt wire counter electrode (99.99%; GoodFellow, Cambridge, UK) and a Ag wire *pseudo*-reference electrode (99.99%; GoodFellow, Cambridge, UK). For air- and moisture-sensitive samples, an inert atmosphere three-electrode cell was used (designed and made in-house).

The GCE was polished between experiments using successive grades of diamond paste slurries from 3.0 to 0.1 μm (Kemet, Maidstone, UK), and briefly sonicated and rinsed with ethanol to remove any adhered microparticles. The Pt working electrodes were polished between experiments using successive grades of alumina slurries (from 1.0 to 0.3 μm), rinsed in distilled water and subjected to brief ultrasonication to remove any adhered alumina microparticles. The electrodes (except the GCE) were then dried in an oven at 120°C to remove any residual traces of water.

The GCE and Pt macrodisk working electrode areas were calibrated for each experiment using a 5.0 mM Cp_2Fe solution in either CH_3CN or CH_2Cl_2 solvent containing 0.1 M $[\text{nBu}_4\text{N}][\text{PF}_6]$ as the supporting electrolyte. The macrodisk electroactive areas were accurately determined by construction of a Randles-Sevcik plot from cyclic voltammograms recorded at varying scan rates (50-750 mV s^{-1}).^[187] The Pt microdisk working electrode area was accurately determined from the steady state current, measured using linear sweep voltammetry (scan rate = 5 mV s^{-1}).^[187]

The Ag wire *pseudo*-reference electrodes were calibrated to the $\text{Cp}_2\text{Fe}^{0/+}$ couple in CH_2Cl_2 at the end of each run to allow for any drift in potential, following IUPAC recommendations.^[186]

Controlled potential bulk electrolysis was performed using a three-electrode configuration consisting of a carbon felt (99.0%; Alfa Aesar, Massachusetts, USA) working electrode combined with a Ag wire *pseudo*-reference electrode (99.99%, GoodFellow, Cambridge, UK) and a Pt gauze counter electrode (52 mesh woven from 0.1 mm diameter wire, 99.9%; Alfa Aesar, Massachusetts, USA). The working and *pseudo*-reference electrodes were separated from the counter electrode compartment by a porous glass frit.

All electrochemical measurements were performed at ambient temperatures under an inert N₂ atmosphere in either CH₂Cl₂, THF, CH₃CN or 1,2-difluorobenzene (DFB) containing 0.05-0.1 M [ⁿBu₄N][B(C₆F₅)₄] as the supporting electrolyte (unless stated otherwise).

Prior to performing a cyclic voltammetric experiment at a macrodisk electrode, the uncompensated resistance (*iR* drop) was first determined using a positive feedback technique (a standard Autolab procedure). This technique is based on a trial and error method where a user-defined *iR*-compensated potential pulse was applied to the working electrode, and its current response was measured. The potential of the working electrode was then plotted as a function of time. As the *iR* compensation approaches 100%, the measured potential response shows damped oscillation. The user-defined *iR* compensation value that is required for this damped oscillation effect provides an accurate approximation to the solution resistance. All recorded CV data at macrodisk electrodes was then partially *iR*-compensated to within 85 ± 5% of the determined uncompensated resistance using the positive feedback *iR* compensation circuit that is built into the Autolab PGSTAT series potentiostat.

8.5.2 Digital simulation of voltammetric data

CV simulations were performed on baseline-corrected data using DigiElch – Professional (v 7.030) software.^[215] Any non-Faradaic current, resulting from double-layer capacitance, was not accounted for in the simulations. The postulated electrochemical mechanisms were applied to the baseline-corrected and *iR*-compensated cyclic voltammograms of the system under investigation, taken over various scan rates ranging from 50-2000 mV s⁻¹. The diffusion coefficients for the starting materials were determined using either diffusion-ordered NMR spectra (DOSY) in CD₂Cl₂ or by numerically fitting potential-step chronoamperometric data at a microdisk electrode using the Shoup-Szabo approximation.^[210] The diffusion coefficient values were left fixed for all electrochemical simulations. The other electrochemical and kinetic parameters were initially assigned an approximate starting value before they were allowed to converge to a set of values that provided an optimum fit at all voltage scan rates studied. To provide an approximation of the associated error for each parameter, each of the globally-

optimised electrochemical and kinetic parameters were manually adjusted until the simulation no longer provided a satisfactory fit across the complete scan rate range.

8.6 Synthetic methods

8.6.1 Chemical reduction of **8** for NMR studies

A colourless solution of **8** (49 mg, 0.1 mmol) in dry, degassed CH₂Cl₂ or DFB (4 mL) was added to a saturated brown/yellow solution of Co(Cp^{Me5})₂ (33 mg, 0.1 mmol) in either CH₂Cl₂ or DFB (4 mL) under an inert N₂ atmosphere, shaken and left for 5 minutes during which it rapidly formed a dark yellow/brown solution. An aliquot (0.8 mL) was taken, the solvent was then removed and rigorously dried *in vacuo* to yield a brown residue, which was taken up in CDCl₃ (0.8 mL) for NMR analysis.

8.6.2 Preparation of Na[**8-H**]

To a solution of 1.0 M Na[HBET₃] in toluene (3.7 mL, 3.7 mmol) was added a solution of **8** (1.71 g, 3.3 mmol) in toluene (30 mL). The reaction mixture was left to stir under N₂ at room temperature for 2 h, during which time a white precipitate formed. The precipitate was left to settle before it was filtered and triturated with toluene (2 × 10 mL). The residue was dried *in vacuo* to yield Na[**8-H**] (1.15 g, 2.1 mmol) as a fine white powder in 64% yield.

¹H NMR (300 MHz, DMSO-d₆): δ 3.56 (br. q, *J* = 87 Hz, 1H); ¹⁹F{¹H} NMR (282 MHz, DMSO-d₆): δ -132.9 (m, 6F, *ortho*-F), -162.8 (m, 3F, *para*-F), -166.1 (m, 6F, *meta*-F); ¹¹B NMR (96.3 MHz, DMSO-d₆): δ -25.2 ppm (d, *J* = 87 Hz); ¹³C{¹H} NMR (75.5 MHz, DMSO-d₆): δ 147.5 (dm, *J* = 236 Hz, *ortho*-C), 137.2 (dm, *J* = 243 Hz, *para*-C), 135.8 (dm, *J* = 246 Hz, *meta*-C), 124.9 (s, *ipso*-C).

8.6.3 Preparation of [ⁿBu₄N][**8-H**]

A solution of ⁿBu₄NCl (0.45 g, 1.6 mmol) in CH₂Cl₂ (20 mL) was added to a white suspension of Na[**8-H**] (0.86 g, 1.6 mmol) in CH₂Cl₂ (20 mL) at room temperature, with stirring under N₂. This resulted in the formation of a fine flocculent precipitate with the simultaneous breakup of the suspended material. The reaction mixture was left to stir overnight. The precipitate was then allowed to settle before it was filtered. The filtrate was concentrated *in vacuo* until a minimum quantity of solvent remained. A white precipitate was obtained at room temperature by layering the solution carefully with light petroleum ether (40/60, approximately twice the volume of solution was added). The precipitate was filtered and dried *in vacuo* to afford [ⁿBu₄N][**8-H**] (0.89 g, 1.2 mmol) as a white powder in 74% yield. Crystals suitable for X-ray crystallography (colourless plates) were grown by dissolving [ⁿBu₄N][**8-H**] in a minimum quantity

of CH₂Cl₂, warming to *ca* 35°C, adding an equal quantity of light petroleum ether and slow-cooling to room temperature.

¹H NMR (300 MHz, CDCl₃): δ 3.60 (br. q, *J* = 82 Hz, 1H, BH), 3.07 (m, 8H, CH₂), 1.56 (m, 8H, CH₂), 1.32 (m, 8H, CH₂), 0.92 (t, *J* = 7.2 Hz, 12H, CH₃); ¹⁹F{¹H} NMR (282 MHz, CDCl₃): δ -133.6 (m, 6F, *ortho*-F), -163.4 (m, 3F, *para*-F), -166.7 (m, 6F, *meta*-F); ¹¹B NMR (96.3 MHz, CDCl₃): δ -25.4 (d, *J* = 82 Hz); ¹³C{¹H} NMR (75.5 MHz, CDCl₃): δ 148.3 (dm, *J* = 240 Hz), 138.0 (dm, *J* = 245 Hz), 136.6 (dm, *J* = 248 Hz), 125.0, 58.9, 23.8, 19.6, 13.4. IR (ATR, cm⁻¹): 2424 (*v*_{B-H}, w). Anal. Calcd for C₃₄H₃₇BF₁₅N: C 54.06; H 4.94; N 1.85. Found: C 53.79; H 5.06; N 1.86.

8.6.4 Preparation of [TMP-D][DB(C₆F₅)₃]

A clear yellow solution of TMP (0.28 g, 1.95 mmol) in toluene (10 mL) was added to a clear colourless solution of **8** (1.00 g, 1.95 mmol) in toluene (20 mL) to give a clear, pale yellow solution. The sample was sparged with D₂ gas for 1 h. The pale yellow solution was then concentrated to *ca* 5 mL and pentane (15 mL) was added to give a precipitate. The precipitate was allowed to settle and then filtered to give [TMP-D][DB(C₆F₅)₃] (1.15 g, 1.75 mmol) as a white powder in 90% yield.

¹H NMR (500 MHz, C₆D₆): δ 4.23 (t, *J* = 49 Hz, 1H, NH), 0.76 (m, 2H, CH₂), 0.67 (m, 4H, CH₂), 0.56 (s, 12H, CH₃); ¹⁹F{¹H} NMR (471 MHz, C₆D₆): δ -133.1 (m, 6F, *ortho*-F), -161.7 (m, 3F, *para*-F), -165.5 (m, 6F, *meta*-F); ¹¹B NMR (160 MHz, C₆D₆): δ -23.8 (s); ²D NMR (556 MHz, CH₂Cl₂): δ 5.40 (d, *J* = 1.1 Hz, ND), 3.60 (br. m, BD).

8.6.5 Preparation of [ⁿBu₄N][**8**-D]

A clear colourless solution of [TMPD][DB(C₆F₅)₃] (0.31 g, 0.47 mmol) in toluene (20 mL) was added to NaH (11 mg, 0.47 mmol) to give some effervescence. The reaction mixture was left to stir at room temperature under N₂ overnight. The reaction mixture was then filtered and the filtrate was concentrated *in vacuo*. The residue was dissolved in CH₂Cl₂ (10 mL) to give a clear colourless solution. To this was added a clear colourless solution of ⁿBu₄NCl (0.13 g, 0.47 mmol) in CH₂Cl₂ (10 mL). A very fine precipitate rapidly formed. The reaction mixture was left to stir at room temperature for 1 h before it was filtered. The filtrate was concentrated to *ca* 2 mL to give a white precipitate. This was filtered and the filtrate was concentrated *in vacuo* to yield a colorless viscous oil that solidified overnight to give [ⁿBu₄N][**8**-D] (0.10 g, 0.13 mmol) as an amorphous colorless solid in 28% yield.

¹H NMR (500 MHz, CDCl₃): δ 3.08 (m, 8H, CH₂), 1.57 (m, 8H, CH₂), 1.32 (m, 8H, CH₂), 0.93 (t, *J* = 7.4 Hz, 12H, CH₃); ¹⁹F{¹H} NMR (471 MHz, CDCl₃): δ -133.5 (m, 6F, *ortho*-F), -163.4 (m, 3F, *para*-F), -166.6 (m, 6F, *meta*-F); ¹¹B NMR (160 MHz, CDCl₃): δ -25.3 (d, *J* = 82 Hz). ²D NMR (556 MHz, CH₂Cl₂): δ 3.66 (br. s). IR (ATR, cm⁻¹): 1800 (*v*_{B-D}, w).

8.6.6 Preparation of Na[24-H]

A clear colorless solution of 1.0 M Na[HBET₃] in toluene (0.3 mL, 0.30 mmol) was added to a pale yellow suspension of **24** (0.15 g, 0.20 mmol) in dry toluene (10 mL). The reaction mixture was heated to 80°C and left to stir under N₂ overnight; warming resulted in dissolution of the suspension to give a pale yellow solution and a white precipitate formed as the reaction progressed. The reaction mixture was allowed to cool, and the precipitate was left to settle, before it was filtered and triturated with dry toluene (2 × 3 mL). The residue was dried *in vacuo* to yield Na[**24-H**] (0.14 g, 0.18 mmol) as a white powder in 89% yield.

¹H NMR (300 MHz, DMSO-d₆): δ 4.28 (br. m, 1H); ¹¹B NMR (96.3 MHz, DMSO-d₆): δ -8.42 (br.).

8.6.7 Preparation of [ⁿBu₄N][24-H]

A clear colorless solution of ⁿBu₄NCl (0.041 g, 0.15 mmol) in dry CH₂Cl₂ (3 mL) was added to a white suspension of Na[**24-H**] (0.12 g, 0.16 mmol) in dry CH₂Cl₂ (3 mL) at room temperature, with stirring under N₂. This resulted in the formation of a fine flocculent precipitate with the simultaneous breakup of the suspended material. The reaction mixture was left to stir overnight. The precipitate was then allowed to settle before it was filtered; the residue was triturated with dry CH₂Cl₂ (2 × 1.5 mL). The filtrate and extracts were combined and concentrated *in vacuo* to give [ⁿBu₄N][**24-H**] (0.11 g, 0.11 mmol) as a white powder in 77% yield. Crystals suitable for X-ray crystallography (colorless needles) were grown by dissolving [ⁿBu₄N][**24-H**] in a minimum quantity of dry CH₂Cl₂, warming to approximately 40°C, adding an equal quantity of dry light petroleum ether and slow-cooling to room temperature.

¹H NMR (300 MHz, CDCl₃): δ 4.32 (br. m, 1H, BH), 3.12 (m, 8H, CH₂), 1.57 (m, 8H, CH₂), 1.35 (m, 8H, CH₂), 0.94 (t, *J* = 7.1 Hz, 12H, CH₃); ¹¹B NMR (96.3 MHz, CDCl₃): δ -8.68 (d, *J* = 76 Hz); ¹³C{¹H} NMR (75.5 MHz, CDCl₃): δ 138.2, 138.0, 130.0, 129.7, 127.8, 59.1, 24.1, 19.9, 13.8.

8.6.8 Preparation of [25]OTf

An aliquot of freshly prepared ImMe₂ (0.2 g, 2.1 mmol) in dry light petroleum ether was added to FBMe₂ (0.51 g, 1.90 mmol) with stirring to give a pale orange solution. The precipitation of material was observed within a minute, and the reaction mixture was then left to stir under N₂ for a further 15 minutes. The precipitate was filtered and washed with dry light petroleum ether (3 × 10 mL) to give an orange residue, which was dried *in vacuo*. The residue was dissolved in dry CH₂Cl₂ (5 mL) to give a deep red solution. To this was added Me₃SiOTf (0.42 g, 1.89 mmol) and the reaction mixture was left to stir under N₂ for 1 h. The reaction mixture was then concentrated to approximately half its volume and an equal quantity of Et₂O was added to afford an orange precipitate. The precipitate was filtered and washed with dry toluene

(3 × 5 mL) followed by dry light petroleum ether (3 × 5 mL) before it was dried *in vacuo* to yield [25]OTf (0.57 g, 1.15 mmol) as a pale yellow powder in 61% yield.

^1H NMR (500 MHz, CDCl_3): δ 7.91 (s, 2H, CHCH), 6.90 (s, 4H, Ar CH), 3.51 (s, 6H, NMe), 2.33 (s, 6H, Mes *para*-CH₃), 2.08 (s, 6H, Mes *ortho*-CH₃), 1.87 (s, 6H, Mes *ortho*-CH₃); $^{19}\text{F}\{^1\text{H}\}$ NMR (470.6 MHz, CDCl_3): δ -78.36 (s). ^{11}B NMR (160.5 MHz, CDCl_3): δ 63.3 (br.); $^{13}\text{C}\{^1\text{H}\}$ NMR (125.8 MHz, CDCl_3): δ 144.19, 142.4, 141.0, 138.7, 138.0, 130.0, 129.2, 128.4, 127.6, 125.4, 122.2, 37.3, 22.7, 21.6; Anal. Calcd. for $\text{C}_{24}\text{H}_{30}\text{BF}_3\text{N}_2\text{O}_3\text{S}$: C 58.31, H 6.12, N 5.67%. Found: C 58.41, H 6.25, N 5.53%.

8.6.9 Preparation of [26]OTf

A clear colourless solution of Im^iPr_2 (0.85 g, 5.58 mmol) in dry light petroleum ether (5 mL) was added to a clear colourless solution of FBMe_2 (1.50 g, 5.59 mmol) in dry light petroleum ether (5 mL) to give a pale yellow solution, from which a white precipitate rapidly started to form. The reaction mixture was left to stir at room temperature overnight (under N_2). The white precipitate was filtered and the residue was washed with dry petroleum ether (3 × 5 mL) and dried *in vacuo*. The white residue was dissolved in dry $\text{C}_6\text{H}_5\text{Cl}$ (5 mL) to give a pale yellow solution. To this was added a straw coloured solution of Me_3SiOTf (1.24 g, 5.58 mmol) in dry $\text{C}_6\text{H}_5\text{Cl}$ (1 mL) to give a pale yellow solution. Within minutes, a colourless precipitate had begun to form. The reaction mixture was left to stir at room temperature overnight (under N_2). The precipitate was filtered and washed with dry light petroleum ether (3 × 5 mL). The residue was dried *in vacuo* to give [26]OTf (2.26 g, 4.11 mmol) as a pale yellow powder in 74% yield. Crystals suitable for X-ray crystallography (colourless blocks) were grown by dissolving [26]OTf in dry CH_2Cl_2 , slowly layering with dry Et_2O and leaving to stand at room temperature.

^1H NMR (500 MHz, CDCl_3): δ 8.11 (s, 2H, CHCH), 6.92 (d, J = 3.9 Hz, 4H, Ar CH), 4.20 (m, J = 6.7 Hz, 2H, ^iPr CH), 2.34 (s, 6H, Mes *para*-CH₃), 2.06 (s, 6H, Mes *ortho*-CH₃), 1.92 (s, 6H, Mes *ortho*-CH₃), 1.46 (d, J = 6.8 Hz, 6H, ^iPr CH₃), 1.15 (d, J = 6.6 Hz, 6H, ^iPr CH₃); $^{19}\text{F}\{^1\text{H}\}$ NMR (470.6 MHz, CDCl_3): δ -78.17 (s); ^{11}B NMR (160.5 MHz, CDCl_3): δ 66.0 (br.); $^{13}\text{C}\{^1\text{H}\}$ NMR (75.5 MHz, CDCl_3): δ 144.1, 142.1, 140.7, 130.3, 129.9, 123.7, 52.9, 23.4, 23.0, 22.9, 22.5, 21.6; Anal. Calcd. for $\text{C}_{28}\text{H}_{38}\text{BF}_3\text{N}_2\text{O}_3\text{S}$: C 61.09, H 6.96, N 5.09%. Found: C 60.91, H 6.88, N 5.15%; HRMS (EI, m/z): for $\text{C}_{27}\text{H}_{38}\text{BN}_2^+$ Calcd: 401.3123. Found: 401.3175.

8.6.10 Preparation of [27]OTf

A pale yellow solution of FBMe_2 (1.53 g, 5.71 mmol) in dry light petroleum ether (30 mL) was added to ImMe_4 (0.71 g, 5.72 mmol) to give a yellow reaction mixture. The consumption of ImMe_4 solid was observed with the concomitant formation of an off-white precipitate. The reaction mixture was left to stir under N_2 for 1 h before it was filtered and the resulting residue

washed with dry light petroleum ether (3 × 5 mL). The residue was dried *in vacuo* to afford a pale yellow solid. This was dissolved in dry CH₂Cl₂ (5 mL) and Me₃SiOTf (1.27 g, 5.7 mmol) was added slowly to give a yellow reaction mixture with precipitate. This was left to stir at room temperature under N₂ overnight. The precipitate was allowed to settle before it was filtered to give a pale yellow residue. This was washed with light petroleum ether (3 × 5 mL) and the residue was dried under vacuum to give [27]OTf (1.40 g, 2.68 mmol, 47%) as an off-white powder.

¹H NMR (500 MHz, CDCl₃): δ 6.86 (m, 4H, Ar CH), 3.36 (s, 6H, N-CH₃), 2.37 (s, 6H, Mes *para*-CH₃), 2.30 (s, 6H, C-CH₃), 2.03 (s, 6H, Mes *ortho*-CH₃), 1.89 (s, 6H, Mes *ortho*-CH₃); ¹⁹F{¹H} NMR (470.6 MHz, CDCl₃): δ -78.30 (s); ¹¹B NMR (160.5 MHz, CDCl₃): δ 67.2 (br.); ¹³C{¹H} NMR (75.5 MHz, CDCl₃): δ 143.6, 132.1, 129.9 (Ar CH), 33.9 (N-CH₃), 22.8 (*ortho*-CH₃), 21.6 (C-CH₃), 9.4 (*para*-CH₃); Anal. Calcd. for C₂₆H₃₄BF₃N₂O₃S: C 59.78, H 6.56, N 5.36%. Found: C 59.60, H 6.68, N 5.42%; HRMS (EI, m/z): for C₂₅H₃₄BN₂⁺ Calcd: 373.2810. Found: 373.2822.

8.6.11 Proton-mediated generation of 19[B(C₆F₅)₄]

To a solution of 19-H (0.14 g, 0.53 mmol) in toluene (5 mL) was added a suspension of [H(OEt₂)₂][B(C₆F₅)₄] (0.41 g, 0.53 mmol) in toluene (10 mL). Vigorous effervescence was immediately observed and a gelatinous precipitate was formed. The reaction mixture was left to stir overnight before it was concentrated *in vacuo* to give a white powder. The residue was recrystallized from chlorobenzene (3 mL) overnight at -20°C. The crystals were then filtered and washed with dry petrol (4 × 1 mL). The crystals were dried *in vacuo* to yield 19[B(C₆F₅)₄] (0.42 g, 0.41 mmol, 77%) as a white powder.

¹H NMR (300 MHz, CDCl₃): δ 7.61 (s, 2H), 4.77 (m, *J* = 6.8 Hz, 2H, CH), 2.44-2.24 (br. m, 6H), 2.20-2.12 (br. m, 2H) 2.10-1.94 (br. m, 4H), 1.88-1.59 (br. m, 2H), 1.68 (d, *J* = 6.7 Hz, 12H, CH₃); ¹⁹F{¹H} NMR (471 MHz, CDCl₃): δ -137.7 (m, 8F, *ortho*-F), -168.2 (m, 4F, *para*-F), -172.1 (m, 8F, *meta*-F); ¹¹B NMR (160 MHz, CDCl₃): δ 83.8 (br), -16.7 (s).

8.6.12 Preparation of 28

To a schlenk tube was added C₆(2,4-CF₃)₂H₃Br (2.00 g, 1.16 ml, 6.83 mmol) and Et₂O (100 ml). The solution was cooled to -78°C and, with the aid of rapid stirring, ⁿBuLi (2.87 ml, 7.17 mmol, 2.5 M in hexanes), was added slowly by means of a syringe. Following one hour of stirring, BCl₃ (2.28 ml, 2.28 mmol, 1 M in hexanes) was syringed into the amber solution and the mixture permitted to warm to room temperature. Under vacuum, the volatiles were removed and the off white residue extracted with CH₂Cl₂ (3 × 25 ml) and filtered through Celite®. CH₂Cl₂ was removed under vacuum and, following a high vacuum sublimation step (1 × 10⁻⁶ mbar) at 85 °C, a pure white solid was obtained. Yield 1.33 g (2.04 mmol, 90%).

^1H NMR (400.4 MHz, CD_2Cl_2): δ 8.06 (s, 3H, *meta*-CH), 7.87 (d, 3H, $J = 8$ Hz, *meta*-CH), 7.46 (d, 3H, $J = 8$ Hz, *ortho*-CH); $^{19}\text{F}\{^1\text{H}\}$ NMR (376.8 MHz, CD_2Cl_2) δ -56.6 (s, *ortho*-C(CF₃)), -63.8 (s, *para*-C(CF₃)); ^{11}B NMR (128.4 MHz, CD_2Cl_2) δ 74.0 (s, br); $^{13}\text{C}\{^1\text{H}\}$ NMR (100.6 MHz, CD_2Cl_2) δ 144.2 (br, B-C), 135.9 (s, *ortho*-CH), 134.2 (q, $J = 34$ Hz, C(CF₃)), 133.7 (q, $J = 34$ Hz, C(CF₃)), 127.9 (q, $J = 3$ Hz, *meta*-CH), 123.9 (q, $J = 273$ Hz, CF₃), 123.6 (m, $J = 3$ Hz, *meta*-CH), 123.6 (q, $J = 273$ Hz, CF₃); Anal. Calcd. for $\text{C}_{24}\text{H}_9\text{BF}_{18}$: C 44.34; H 1.40%. Found: C 44.48; H 1.47%. HRMS (EI, m/z): for $\text{BC}_{24}\text{F}_{18}\text{H}_9$ Calcd: 650.0510. Found: 650.0491.

8.6.13 Preparation of Na[20-H]

To a white suspension of **20** (0.40 g, 0.62 mmol) in toluene (10 mL) was added, with stirring under N_2 at room temperature, a 1.0 M solution of $\text{Na}[\text{HBEt}_3]$ (0.6 mL, 0.6 mmol) in toluene. A fine precipitate began to form. The reaction mixture was left to stir for 6 h to give a colourless solution, which was filtered. All volatiles were removed under vacuum to give a white residue, which was washed with light petroleum ether (2×5 mL) and dried under vacuum to give $\text{Na}[\text{HB}\{\text{C}_6(3,5\text{-CF}_3)_2\text{H}_3\}_3]$ (0.40 g, 0.59 mmol) as a white powder in 95% yield.

^1H NMR (500 MHz, CD_3CN): δ 7.70 (s, 6H, *ortho*-CH), 7.58 (s, 3H, *para*-CH), 3.66 (q, 1H, $J = 84$ Hz, BH); $^{19}\text{F}\{^1\text{H}\}$ NMR (470.6 MHz, CD_3CN): δ -63.02 (s); ^{11}B NMR (160.5 MHz, CD_3CN): δ -9.1 (d, $J = 88$ Hz); $^{13}\text{C}\{^1\text{H}\}$ NMR (125.8 MHz, CDCl_3): δ 165.0 (q, $J = 49$ Hz, *ipso*-C), 135.7 (s, *ortho*-C), 130.1 (q, $J = 32$ Hz, *meta*-C), 126.0 (q, $J = 272$ Hz, CF₃), 118.5 (s, *para*-C). Anal. Calcd for $\text{C}_{24}\text{H}_{10}\text{BF}_{18}\text{Na}$: C 42.76, H 1.50%. Found: C 42.95, H 1.61%.

8.6.14 *In situ* formation of $[\text{H}(\text{THF})_n][(\mu\text{-H})(\mathbf{20})_2]$

20 (47.3 mg, 0.073 mmol) was dissolved in THF- d_8 (0.8 mL) and H_2 (4 atm) was admitted to the sample using a freeze-pump-thaw process. $[\text{H}(\text{THF})_2][(\mu\text{-H})(\mathbf{20})_2]$ was formed in 16% conversion.

^1H NMR (300 MHz, THF- d_8): δ 11.11 (s, 4H, $\{\text{THF}\}_2\text{H}$), 7.86 (m, 6H, *para*-CH), 7.82 (s, 12H, *ortho*-CH); $^{19}\text{F}\{^1\text{H}\}$ NMR (282.4 MHz, THF- d_8): δ -63.6 (s); ^{11}B NMR (96.3 MHz, THF- d_8): δ 3.9 (br.).

8.6.15 Isolated $[\text{H}(\text{THF})_2][(\mu\text{-H})(\mathbf{20})_2]$

Trace amounts of $[\text{H}(\text{THF})_2][(\mu\text{-H})(\mathbf{20})_2]$ were isolated by suspending **20** (0.30 g, 0.46 mmol) in dry toluene (10 mL), adding several drops of dry THF to effect the dissolution of solid – through the formation of THF·**20**. After admission of the sample to H_2 , through sparging, the sample was left to stir overnight at room temperature. It was then placed in the freezer for 5 h to give a small quantity of colourless crystals. These were filtered and washed with dry petroleum ether (2×10 mL) and then dried shortly under vacuum.

^1H NMR (500 MHz, CD_2Cl_2): δ 10.24 (br. s, 3H, $\{\text{THF}\}_2\text{H}$), 7.78 (m, 6H, *para*-CH), 7.73 (s, 12H, *ortho*-CH), 3.52 (m, 16H, OCH₂), 1.78 (m, 16H, CH₂CH₂); $^{19}\text{F}\{^1\text{H}\}$ NMR (471 MHz, CD_2Cl_2): δ -63.1 (s); ^{11}B NMR (160.5 MHz, CD_2Cl_2): δ 4.4 (s); $^{13}\text{C}\{^1\text{H}\}$ NMR (100 MHz, CD_2Cl_2): δ 133.1 (s, *ortho*-C), 130.7 (q, $J = 32$ Hz, *meta*-C), 124.5 (q, $J = 272$ Hz, CF₃), 120.8 (m, *para*-C), 68.8 (s, THF), 25.6 (s, THF); Anal. Calcd. for $\text{C}_{56}\text{H}_{36}\text{B}_2\text{F}_{36}\text{O}_2$: C 46.50, H 2.51%. Found: C 46.65, H 2.38%.

8.6.16 Hydride transfer between [TMP-H][[(μ -H)(**20**)₂] and **8**

A solution of **8** (18.2 mg, 0.036 mmol) in CD_2Cl_2 (0.8 mL) was added to [TMP-H][(μ -H)(**20**)₂] (49.0 mg, 0.034 mmol) to give a colourless solution. The formation of free **20** and [TMP-H][**8**-H] was indicated by the NMR spectra.

^1H NMR (500 MHz, CD_2Cl_2): δ 8.24 (br., m, 6H, *para*-CH), 8.03 (br., m, 12H, *ortho*-CH), 5.16 (t, $J = 52$ Hz, 2H, NH₂), 3.48 (br., q, 1H), 1.84 (m, 2H, CH₂), 1.76 (m, 4H, CH₂), 1.49 (br., 12H, CH₃); $^{19}\text{F}\{^1\text{H}\}$ NMR (471 MHz, CD_2Cl_2): δ -63.4 (s, 36F, CF₃), -134.0 (br., 6F, *ortho*-F), -162.9 (m, 3F, *para*-F), -166.4 (br., 6F, *meta*-F); ^{11}B NMR (160.5 MHz, CD_2Cl_2): δ 58.74 (br.), -24.1 (br.).

References

References

- [1] P. A. Gale, S. Coles, *Chem. Sci.* **2012**, 683.
- [2] N. N. Greenwood, A. Earnshaw, *Chemistry of the Elements*, Elsevier, Oxford, **1997**.
- [3] D. R. Lide, *CRC Handbook of Chemistry and Physics, 89th Edition*, CRC Press, Boca Raton, **2008**.
- [4] P. Hoffmann, *Tomorrow's Energy: Hydrogen, Fuel Cells, and the Prospects for a Cleaner Planet*, MIT Press, Cambridge, MA, **2012**.
- [5] H. Cavendish, *Philos. Trans.* **1766**, 56, 141–184.
- [6] B. Sørensen, *Hydrogen and Fuel Cells: Emerging Technologies and Applications*, Academic Press Inc, Oxford, **2005**.
- [7] C. Masters, *Adv. Organomet. Chem.* **1979**, 17, 61–103.
- [8] J. Turner, G. Sverdrup, M. K. Mann, P.-C. Maness, B. Kroposki, M. Ghirardi, R. J. Evans, D. Blake, *Int. J. Energ. Res.* **2008**, 32, 379–407.
- [9] S. Dunn, *Int. J. Hydrogen Energ.* **2002**, 27, 235–264.
- [10] M. Carmo, D. L. Fritz, J. Mergel, D. Stolten, *Int. J. Hydrogen Energ.* **2013**, 38, 4901–4934.
- [11] F. E. Osterloh, *Chem. Mater.* **2008**, 20, 35–54.
- [12] A. Kudo, Y. Miseki, *Chem. Soc. Rev.* **2009**, 38, 253.
- [13] A. Steinfeld, *Sol. Energy* **2005**, 78, 603–615.
- [14] R. G. Compton, G. H. W. Sanders, *Electrode Potentials*, Oxford University Press, Oxford, **1996**.
- [15] M. Ni, D. Y. C. Leung, M. K. H. Leung, K. Sumathy, *Fuel Process. Technol.* **2006**, 87, 461–472.
- [16] A. Melis, T. Happe, *Plant Physiol.* **2001**, 127, 740–748.
- [17] N. S. Lewis, D. G. Nocera, *Proc. Natl Acad. Sci. USA* **2006**, 103, 15729–15735.
- [18] M. Winter, R. J. Brodd, *Chem. Rev.* **2004**, 104, 4245–4270.
- [19] F. Barbir, *PEM Fuel Cells: Theory and Practice*, Academic Press, Waltham, MA, **2013**.
- [20] D. M. F. Santos, C. A. C. Sequeira, *Renew. Sust. Energ. Rev.* **2011**, 15, 3980–4001.

- [21] I. Merino-Jiménez, C. Ponce de León, A. A. Shah, F. C. Walsh, *J. Power Sources* **2012**, *219*, 339–357.
- [22] J. Ma, N. A. Choudhury, Y. Sahai, *Renew. Sust. Energ. Rev.* **2010**, *14*, 183–199.
- [23] W. R. Grove, *Phil. Mag. (III)* **1842**, 417.
- [24] G. Hoogers, *Fuel Cell Technology Handbook*, CRC Press, Boca Raton, **2002**.
- [25] C. P. de Leon, F. C. Walsh, D. Pletcher, D. J. Browning, J. B. Lakeman, *J. Power Sources* **2006**, *155*, 172–181.
- [26] M. J. Croissant, T. Napporn, J.-M. Léger, C. Lamy, *Electrochim. Acta* **1998**, *43*, 2447–2457.
- [27] T. Zhang, A. B. Anderson, *J. Phys. Chem. C* **2007**, *111*, 8644–8648.
- [28] B. E. Conway, B. V. Tilak, *Electrochim. Acta* **2002**, *47*, 3571–3594.
- [29] “Price charts - PMM,” can be found under <http://www.platinum.matthey.com/prices/price-charts>, **2014**.
- [30] R. M. Bullock, Ed. , *Catalysis Without Precious Metals*, Wiley, Weinheim, **2010**.
- [31] A. J. Bard, G. R. Inzelt, F. Scholz, Eds. , *Electrochemical Dictionary*, Springer, Heidelberg, **2012**.
- [32] P. M. Gundry, F. C. Tompkins, *Q. Rev. Chem. Soc.* **1960**, *14*, 257–291.
- [33] A. J. Bard, L. Faulkner, *Electrochemical Methods: Fundamentals and Applications*, John Wiley & Sons, **2001**.
- [34] A. Malinauskas, *Synth. Met.* **1999**, *107*, 75–83.
- [35] T. Fujigaya, N. Nakashima, *Adv. Mater.* **2013**, *25*, 1666–1681.
- [36] X. Yuan, X.-L. Ding, C.-Y. Wang, Z.-F. Ma, *Energy Environ. Sci.* **2013**, *6*, 1105–1124.
- [37] S.-Y. Huang, P. Ganesan, B. N. Popov, *Appl. Catal. B-Environ.* **2009**, *93*, 75–81.
- [38] Y. Si, E. T. Samulski, *Chem. Mater.* **2008**, *20*, 6792–6797.
- [39] E. Yoo, T. Okata, T. Akita, M. Kohyama, J. Nakamura, I. Honma, *Nano Lett.* **2009**, *9*, 2255–2259.
- [40] B. D. James, A. B. Spisak, *Mass Production Cost Estimation of Direct Hydrogen PEM Fuel Cell Systems for Transportation Applications: 2012 Update*, Strategic Analysis Inc., **2012**.
- [41] M. Cao, D. Wu, R. Cao, *ChemCatChem* **2014**, *6*, 26–45.
- [42] E. Antolini, *Energy Environ. Sci.* **2009**, *2*, 915–931.
- [43] N. Hodnik, M. Zorko, B. Jozinović, M. Bele, G. Dražič, S. Hočevar, M. Gaberšček, *Electrochem. Commun.* **2013**, *30*, 75–78.

- [44] X. Zhao, M. Yin, L. Ma, L. Liang, C. Liu, J. Liao, T. Lu, W. Xing, *Energy Environ. Sci.* **2011**, *4*, 2736–2753.
- [45] M. K. Debe, *Nature* **2012**, *486*, 43–51.
- [46] B. Broyde, *J. Catal.* **1968**, *10*, 13–18.
- [47] R. D. Armstrong, A. F. Douglas, D. E. Williams, *Energy Convers.* **1971**, *11*, 7–10.
- [48] H. Chhina, S. Campbell, O. Kesler, *J. Power Sources* **2007**, *164*, 431–440.
- [49] H. Böhm, F. A. Pohl, Troisièmes Journées Internationales D'étude Des Piles À Combustible, Bruxelles, **1969**, p. 183.
- [50] H. Böhm, F. A. Pohl, *Wiss. Ber. AEG-Telefunken* **1968**, *41*, 46–50.
- [51] R. B. Levy, M. Boudart, *Science* **1973**, *181*, 547–549.
- [52] V. S. Palanker, D. V. Sokolsky, E. A. Mazulevsky, E. N. Baybatyrov, *J. Power Sources* **1976**, *1*, 169–176.
- [53] I. Nikolov, T. Vitanov, *J. Power Sources* **1980**, *5*, 273–281.
- [54] X. G. Yang, C. Y. Wang, *Appl. Phys. Lett.* **2005**, *86*, 224104.
- [55] S. Izhar, M. Yoshida, M. Nagai, *Electrochim. Acta* **2009**, *54*, 1255–1262.
- [56] E. J. Rees, K. Essaki, C. D. A. Brady, G. T. Burstein, *J. Power Sources* **2009**, *188*, 75–81.
- [57] P. N. Ross Jr., P. Stonehart, *J. Catal.* **1977**, *48*, 42–59.
- [58] P. M. Vignais, B. Billoud, *Chem. Rev.* **2007**, *107*, 4206–4272.
- [59] C. Tard, C. J. Pickett, *Chem. Rev.* **2009**, *109*, 2245–2274.
- [60] D. L. DuBois, R. M. Bullock, *Eur. J. Inorg. Chem.* **2011**, 1017–1027.
- [61] F. A. Armstrong, N. A. Belsey, J. A. Cracknell, G. Goldet, A. Parkin, E. Reisner, K. A. Vincent, A. F. Wait, *Chem. Soc. Rev.* **2008**, *38*, 36–51.
- [62] S. Ogo, *Chem. Commun.* **2009**, 3317–3325.
- [63] D. J. Evans, C. J. Pickett, *Chem. Soc. Rev.* **2003**, *32*, 268–275.
- [64] J. C. Fontecilla-Camps, A. Volbeda, C. Cavazza, Y. Nicolet, *Chem. Rev.* **2007**, *107*, 4273–4303.
- [65] W. Lubitz, H. Ogata, O. Rüdiger, E. Reijerse, *Chem. Rev.* **2014**, *114*, 4081–4148.
- [66] J. Esselborn, C. Lambertz, A. Adamska-Venkatesh, T. Simmons, G. Berggren, J. Noth, J. Siebel, A. Hemschemeier, V. Artero, E. Reijerse, et al., *Nat. Chem. Biol.* **2013**, *9*, 607–609.
- [67] U. Ryde, C. Greco, L. De Gioia, *J. Am. Chem. Soc.* **2010**, *132*, 4512–4513.

- [68] A. Silakov, B. Wenk, E. Reijerse, W. Lubitz, *Phys. Chem. Chem. Phys.* **2009**, *11*, 6592–6599.
- [69] Y. Nicolet, A. L. de Lacey, X. Vernède, V. M. Fernandez, E. C. Hatchikian, J. C. Fontecilla-Camps, *J. Am. Chem. Soc.* **2001**, *123*, 1596–1601.
- [70] A. Volbeda, M.-H. Charon, C. Piras, E. C. Hatchikian, M. Frey, J. C. Fontecilla-Camps, *Nature* **1995**, 580–587.
- [71] J. W. Peters, W. N. Lanzilotta, B. J. Lemon, L. C. Seefeldt, *Science* **1998**, *282*, 1853–1858.
- [72] J.-F. Capon, F. Gloaguen, F. Y. Pétillon, P. Schollhammer, J. Talarmin, *Eur. J. Inorg. Chem.* **2008**, *2008*, 4671–4681.
- [73] F. Gloaguen, T. B. Rauchfuss, *Chem. Soc. Rev.* **2008**, *38*, 100–108.
- [74] C. Tard, X. Liu, S. K. Ibrahim, M. Bruschi, L. D. Gioia, S. C. Davies, X. Yang, L.-S. Wang, G. Sawers, C. J. Pickett, *Nature* **2005**, *433*, 610–613.
- [75] M. Wang, L. Chen, L. Sun, *Energy Environ. Sci.* **2012**, *5*, 6763–6778.
- [76] C. J. Curtis, A. Miedaner, W. W. Ellis, D. L. DuBois, *J. Am. Chem. Soc.* **2002**, *124*, 1918–1925.
- [77] D. D. Wayner, V. D. Parker, *Acc. Chem. Res.* **1993**, *26*, 287–294.
- [78] C. Bolm, *Nat. Chem.* **2009**, *1*, 420–420.
- [79] A. L. Goff, V. Artero, B. Jousset, P. D. Tran, N. Guillet, R. Métayé, A. Fihri, S. Palacin, M. Fontecave, *Science* **2009**, *326*, 1384–1387.
- [80] M. L. Helm, M. P. Stewart, R. M. Bullock, M. Rakowski-DuBois, D. L. DuBois, *Science* **2011**, *333*, 863–866.
- [81] D. H. Pool, M. P. Stewart, M. O’Hagan, W. J. Shaw, J. A. S. Roberts, R. M. Bullock, D. L. DuBois, *Proc. Natl Acad. Sci. USA* **2012**, *109*, 15634–15639.
- [82] S. Wiese, U. J. Kilgore, D. L. DuBois, R. M. Bullock, *ACS Catal.* **2012**, *2*, 720–727.
- [83] U. J. Kilgore, J. A. S. Roberts, D. H. Pool, A. M. Appel, M. P. Stewart, M. Rakowski-DuBois, W. G. Dougherty, W. S. Kassel, R. M. Bullock, D. L. DuBois, *J. Am. Chem. Soc.* **2011**, *133*, 5861–5872.
- [84] U. J. Kilgore, M. P. Stewart, M. L. Helm, W. G. Dougherty, W. S. Kassel, M. Rakowski-DuBois, D. L. DuBois, R. M. Bullock, *Inorg. Chem.* **2011**, *50*, 10908–10918.
- [85] J. M. Camara, T. B. Rauchfuss, *Nat. Chem.* **2012**, *4*, 26–30.

- [86] D. Chong, I. P. Georgakaki, R. Mejia-Rodriguez, J. Sanabria-Chinchilla, M. P. Soriaga, M. Y. Darensbourg, *Dalton Trans.* **2003**, 4158–4163.
- [87] R. Mejia-Rodriguez, D. Chong, J. H. Reibenspies, M. P. Soriaga, M. Y. Darensbourg, *J. Am. Chem. Soc.* **2004**, *126*, 12004–12014.
- [88] M. E. Carroll, B. E. Barton, T. B. Rauchfuss, P. J. Carroll, *J. Am. Chem. Soc.* **2012**, *134*, 18843–18852.
- [89] M. J. Rose, H. B. Gray, J. R. Winkler, *J. Am. Chem. Soc.* **2012**, *134*, 8310–8313.
- [90] X. Hu, B. S. Brunschwig, J. C. Peters, *J. Am. Chem. Soc.* **2007**, *129*, 8988–8998.
- [91] V. Artero, M. Chavarot-Kerlidou, M. Fontecave, *Angew. Chem. Int. Ed.* **2011**, *50*, 7238–7266.
- [92] J. L. Dempsey, B. S. Brunschwig, J. R. Winkler, H. B. Gray, *Acc. Chem. Res.* **2009**, *42*, 1995–2004.
- [93] Y. Sun, J. P. Bigi, N. A. Piro, M. L. Tang, J. R. Long, C. J. Chang, *J. Am. Chem. Soc.* **2011**, *133*, 9212–9215.
- [94] A. M. Appel, D. L. DuBois, M. Rakowski-DuBois, *J. Am. Chem. Soc.* **2005**, *127*, 12717–12726.
- [95] H. I. Karunadasa, C. J. Chang, J. R. Long, *Nature* **2010**, *464*, 1329–1333.
- [96] H. I. Karunadasa, E. Montalvo, Y. Sun, M. Majda, J. R. Long, C. J. Chang, *Science* **2012**, *335*, 698–702.
- [97] J. Y. Yang, R. M. Bullock, W. J. Shaw, B. Twamley, K. Frazee, M. Rakowski-DuBois, D. L. DuBois, *J. Am. Chem. Soc.* **2009**, *131*, 5935–5945.
- [98] J. Y. Yang, S. Chen, W. G. Dougherty, W. S. Kassel, R. M. Bullock, D. L. DuBois, S. Raugei, R. Rousseau, M. Dupuis, M. Rakowski-DuBois, *Chem. Commun.* **2010**, *46*, 8618–8620.
- [99] J. M. Camara, T. B. Rauchfuss, *J. Am. Chem. Soc.* **2011**, *133*, 8098–8101.
- [100] T. Liu, D. L. DuBois, R. M. Bullock, *Nat. Chem.* **2013**, *5*, 228–233.
- [101] S. Eguchi, K.-S. Yoon, S. Ogo, *J. Biosci. Bioeng.* **2012**, *114*, 479–484.
- [102] T. Matsumoto, S. Eguchi, H. Nakai, T. Hibino, K.-S. Yoon, S. Ogo, *Angew. Chem. Int. Ed.* **2014**, *53*, 8895–8898.
- [103] M. R. Ringenberg, S. L. Kokatam, Z. M. Heiden, T. B. Rauchfuss, *J. Am. Chem. Soc.* **2008**, *130*, 788–789.
- [104] M. R. Ringenberg, M. J. Nilges, T. B. Rauchfuss, S. R. Wilson, *Organometallics* **2010**, *29*, 1956–1965.
- [105] V. Lyaskovskyy, B. de Bruin, *ACS Catal.* **2012**, *2*, 270–279.

- [106] G. N. Lewis, *J. Chem. Technol. Biotechnol.* **1924**, *43*, 17–17.
- [107] J. N. Brønsted, *Recl. Trav. Chim. Pays-Bas* **1923**, *42*, 718–728.
- [108] T. M. Lowry, *Chem. Ind. (London)* **1923**, *42*, 43–47.
- [109] T. M. Lowry, *Chem. Ind. (London)* **1923**, *42*, 1048–1052.
- [110] H. I. Schlesinger, N. W. Flodin, A. B. Burg, *J. Am. Chem. Soc.* **1939**, *61*, 1078–1083.
- [111] H. C. Brown, H. I. Schlesinger, S. Z. Cardon, *J. Am. Chem. Soc.* **1942**, *64*, 325–329.
- [112] G. C. Welch, R. R. S. Juan, J. D. Masuda, D. W. Stephan, *Science* **2006**, *314*, 1124–1126.
- [113] F. Focante, P. Mercandelli, A. Sironi, L. Resconi, *Coord. Chem. Rev.* **2006**, *250*, 170–188.
- [114] W. E. Piers, in *Advances in Organometallic Chemistry*, Academic Press, **2004**, pp. 1–76.
- [115] C. A. Jaska, I. Manners, *J. Am. Chem. Soc.* **2004**, *126*, 9776–9785.
- [116] T. J. Clark, J. M. Rodezno, S. B. Clendenning, S. Aouba, P. M. Brodersen, A. J. Lough, H. E. Ruda, I. Manners, *Chem. Eur. J.* **2005**, *11*, 4526–4534.
- [117] G. C. Welch, D. W. Stephan, *J. Am. Chem. Soc.* **2007**, *129*, 1880–1881.
- [118] T. A. Rokob, A. Hamza, I. Pápai, *J. Am. Chem. Soc.* **2009**, *131*, 10701–10710.
- [119] J. S. J. McCahill, G. C. Welch, D. W. Stephan, *Angew. Chem. Int. Ed.* **2007**, *46*, 4968–4971.
- [120] D. W. Stephan, in *Comprehensive Inorganic Chemistry II (Second Edition)* (Ed.: J.R. Poeppelmeier), Elsevier, Amsterdam, **2013**, pp. 1069–1103.
- [121] D. W. Stephan, G. Erker, *Angew. Chem. Int. Ed.* **2010**, *49*, 46–76.
- [122] D. W. Stephan, *Dalton Trans.* **2009**, 3129.
- [123] “Web of Science [v.5.15] - All Databases Home,” can be found under <http://apps.webofknowledge.com/>, **2014**.
- [124] V. Sumerin, F. Schulz, M. Nieger, M. Leskelä, T. Repo, B. Rieger, *Angew. Chem. Int. Ed.* **2008**, *47*, 6001–6003.
- [125] D. Holschumacher, T. Bannenberg, C. G. Hrib, P. G. Jones, M. Tamm, *Angew. Chem. Int. Ed.* **2008**, *47*, 7428–7432.
- [126] P. A. Chase, D. W. Stephan, *Angew. Chem. Int. Ed.* **2008**, *47*, 7433–7437.
- [127] T. A. Rokob, A. Hamza, A. Stirling, T. Soós, I. Pápai, *Angew. Chem. Int. Ed.* **2008**, *47*, 2435–2438.

- [128] T. Privalov, *Dalton Trans.* **2009**, 1321–1327.
- [129] Y. Guo, S. Li, *Eur. J. Inorg. Chem.* **2008**, 2008, 2501–2505.
- [130] S. Grimme, *J. Comput. Chem.* **2006**, 27, 1787–1799.
- [131] S. Grimme, H. Kruse, L. Goerigk, G. Erker, *Angew. Chem. Int. Ed.* **2010**, 49, 1402–1405.
- [132] T. A. Rokob, I. Bakó, A. Stirling, A. Hamza, I. Pápai, *J. Am. Chem. Soc.* **2013**, 135, 4425–4437.
- [133] P. A. Chase, T. Jurca, D. W. Stephan, *Chem. Commun.* **2008**, 1701.
- [134] D. W. Stephan, *Org. Biomol. Chem.* **2012**, 10, 5740–5746.
- [135] D. W. Stephan, S. Greenberg, T. W. Graham, P. Chase, J. J. Hastie, S. J. Geier, J. M. Farrell, C. C. Brown, Z. M. Heiden, G. C. Welch, et al., *Inorg. Chem.* **2011**, 50, 12338–12348.
- [136] P. Spies, S. Schwendemann, S. Lange, G. Kehr, R. Fröhlich, G. Erker, *Angew. Chem. Int. Ed.* **2008**, 47, 7543–7546.
- [137] T. Mahdi, D. W. Stephan, *J. Am. Chem. Soc.* **2014**, 136, 15809–15812.
- [138] D. Chen, J. Klankermayer, *Chem. Commun.* **2008**, 2130–2131.
- [139] D. Chen, Y. Wang, J. Klankermayer, *Angew. Chem. Int. Ed.* **2010**, 49, 9475–9478.
- [140] Z. M. Heiden, D. W. Stephan, *Chem. Commun.* **2011**, 47, 5729–5731.
- [141] S. J. Geier, D. W. Stephan, *J. Am. Chem. Soc.* **2009**, 131, 3476–3477.
- [142] S. J. Geier, A. L. Gille, T. M. Gilbert, D. W. Stephan, *Inorg. Chem.* **2009**, 48, 10466–10474.
- [143] P. Spies, G. Erker, G. Kehr, K. Bergander, R. Fröhlich, S. Grimme, D. W. Stephan, *Chem. Commun.* **2007**, 5072–5074.
- [144] A. Di Saverio, F. Focante, I. Camurati, L. Resconi, T. Beringhelli, G. D'Alfonso, D. Donghi, D. Maggioni, P. Mercandelli, A. Sironi, *Inorg. Chem.* **2005**, 44, 5030–5041.
- [145] P. Spies, G. Erker, G. Kehr, K. Bergander, R. Fröhlich, S. Grimme, D. W. Stephan, *Chem. Commun.* **2007**, 5072.
- [146] T. J. Herrington, A. J. W. Thom, A. J. P. White, A. E. Ashley, *Dalton Trans.* **2012**, 41, 9019.
- [147] E. L. Kolychev, T. Bannenberg, M. Freytag, C. G. Daniliuc, P. G. Jones, M. Tamm, *Chem. Eur. J.* **2012**, 18, 16938–16946.
- [148] S. C. Binding, H. Zaher, F. M. Chadwick, D. O'Hare, *Dalton Trans.* **2012**, 41, 9061–9066.

- [149] Z. Lu, Z. Cheng, Z. Chen, L. Weng, Z. H. Li, H. Wang, *Angew. Chem. Int. Ed.* **2011**, *50*, 12227–12231.
- [150] J. M. Farrell, J. A. Hatnean, D. W. Stephan, *J. Am. Chem. Soc.* **2012**, *134*, 15728–15731.
- [151] A. L. Travis, S. C. Binding, H. Zaher, T. A. Q. Arnold, J.-C. Buffet, D. O’Hare, *Dalton Trans.* **2013**, *42*, 2431.
- [152] T. S. De Vries, A. Prokofjevs, E. Vedejs, *Chem. Rev.* **2012**, *112*, 4246–4282.
- [153] W. E. Piers, S. C. Bourke, K. D. Conroy, *Angew. Chem. Int. Ed.* **2005**, *44*, 5016–5036.
- [154] P. Koelle, H. Noeth, *Chem. Rev.* **1985**, *85*, 399–418.
- [155] S. A. Solomon, A. Del Grosso, E. R. Clark, V. Bagutski, J. J. W. McDouall, M. J. Ingleson, *Organometallics* **2012**, *31*, 1908–1916.
- [156] P. Eisenberger, A. M. Bailey, C. M. Crudden, *J. Am. Chem. Soc.* **2012**, *134*, 17384–17387.
- [157] M. Horn, H. Mayr, E. Lacôte, E. Merling, J. Deaner, S. Wells, T. McFadden, D. P. Curran, *Org. Lett.* **2011**, *14*, 82–85.
- [158] D. M. Lindsay, D. McArthur, *Chem. Commun.* **2010**, *46*, 2474–2476.
- [159] C. Jiang, O. Blacque, H. Berke, *Chem. Commun.* **2009**, 5518–5520.
- [160] B. Cordero, V. Gómez, A. E. Platero-Prats, M. Revés, J. Echeverría, E. Cremades, F. Barragán, S. Alvarez, *Dalton Trans.* **2008**, 2832–2838.
- [161] C. H. Lee, S. J. Lee, J. W. Park, K. H. Kim, B. Y. Lee, J. S. Oh, *J. Mol. Catal. A: Chem.* **1998**, *132*, 231–239.
- [162] G. Ménard, D. W. Stephan, *Angew. Chem. Int. Ed.* **2012**, *51*, 8272–8275.
- [163] C. B. Caputo, D. W. Stephan, *Organometallics* **2011**, *31*, 27–30.
- [164] C. M. Mömning, S. Frömel, G. Kehr, R. Fröhlich, S. Grimme, G. Erker, *J. Am. Chem. Soc.* **2009**, *131*, 12280–12289.
- [165] M. Ullrich, K. S.-H. Seto, A. J. Lough, D. W. Stephan, *Chem. Commun.* **2009**, 2335.
- [166] M. A. Dureen, D. W. Stephan, *J. Am. Chem. Soc.* **2009**, *131*, 8396–8397.
- [167] C. Jiang, O. Blacque, H. Berke, *Organometallics* **2010**, *29*, 125–133.
- [168] M. A. Dureen, C. C. Brown, D. W. Stephan, *Organometallics* **2010**, *29*, 6594–6607.
- [169] J. G. M. Morton, M. A. Dureen, D. W. Stephan, *Chem. Commun.* **2010**, *46*, 8947–8949.

- [170] G. C. Welch, J. D. Masuda, D. W. Stephan, *Inorg. Chem.* **2005**, *45*, 478–480.
- [171] S. J. Geier, D. W. Stephan, *J. Am. Chem. Soc.* **2009**, *131*, 3476–3477.
- [172] B. Birkmann, T. Voss, S. J. Geier, M. Ullrich, G. Kehr, G. Erker, D. W. Stephan, *Organometallics* **2010**, *29*, 5310–5319.
- [173] S. Moebs-Sanchez, G. Bouhadir, N. Saffon, L. Maron, D. Bourissou, *Chem. Commun.* **2008**, 3435–3437.
- [174] R. C. Neu, E. Otten, A. Lough, D. W. Stephan, *Chem. Sci.* **2010**, *2*, 170–176.
- [175] E. Otten, R. C. Neu, D. W. Stephan, *J. Am. Chem. Soc.* **2009**, *131*, 9918–9919.
- [176] S. D. Tran, T. A. Tronic, W. Kaminsky, D. Michael Heinekey, J. M. Mayer, *Inorg. Chim. Acta* **2011**, *369*, 126–132.
- [177] A. E. Ashley, A. L. Thompson, D. O'Hare, *Angew. Chem. Int. Ed.* **2009**, *48*, 9839–9843.
- [178] C. M. Mömning, E. Otten, G. Kehr, R. Fröhlich, S. Grimme, D. W. Stephan, G. Erker, *Angew. Chem. Int. Ed.* **2009**, *48*, 6643–6646.
- [179] S. Porcel, G. Bouhadir, N. Saffon, L. Maron, D. Bourissou, *Angew. Chem. Int. Ed.* **2010**, *49*, 6186–6189.
- [180] G. Erker, *Dalton Trans.* **2011**, *40*, 7475–7483.
- [181] A. M. Chapman, M. F. Haddow, D. F. Wass, *J. Am. Chem. Soc.* **2011**, *133*, 18463–18478.
- [182] M. T. Whited, *Beilstein J. Org. Chem.* **2012**, *8*, 1554–1563.
- [183] A. Ramos, A. J. Lough, D. W. Stephan, *Chem. Commun.* **2009**, 1118–1120.
- [184] M. J. Kelly, J. Gilbert, R. Tirfoin, S. Aldridge, *Angew. Chem. Int. Ed.* **2013**, *52*, 14094–14097.
- [185] Y. Kojima, T. Haga, *Int. J. Hydrogen Energ.* **2003**, *28*, 989–993.
- [186] G. Gritzner, J. Kůta, *Electrochim. Acta* **1984**, *29*, 869–873.
- [187] R. G. Compton, C. E. Banks, *Understanding Voltammetry*, Imperial College Press, London, **2011**.
- [188] A. Fick, *Lond. Edinb. Dubl. Phil. Mag.* **1855**, *10*, 30–39.
- [189] A. Fick, *Ann. Phys. (Berlin)* **1855**, *94*, 59–86.
- [190] A. Einstein, *Ann. Phys.* **1905**, *322*, 549–560.
- [191] M. von Smoluchowski, *Ann. Phys.* **1906**, *326*, 756–780.
- [192] P. Atkins, J. de Paula, *Atkins' Physical Chemistry*, OUP Oxford, **2006**.
- [193] C. Amatore, C. Pebay, L. Thouin, A. Wang, J.-S. Warkocz, *Anal. Chem.* **2010**, *82*, 6933–6939.

- [194] C. M. A. Brett, A. M. O. Brett, *Electrochemistry: Principles, Methods, and Applications*, OUP Oxford, **1993**.
- [195] R. J. LeSuer, C. Buttolph, W. E. Geiger, *Anal. Chem.* **2004**, *76*, 6395–6401.
- [196] M. R. Rosenthal, *J. Chem. Educ.* **1973**, *50*, 331.
- [197] T. J. Marks, A. M. Seyam, *Inorg. Chem.* **1974**, *13*, 1624–1627.
- [198] E. Y.-X. Chen, S. J. Lancaster, in *Comprehensive Inorganic Chemistry II: From Elements to Applications*, Elsevier, Oxford, **2013**, pp. 707–754.
- [199] H. Nishida, N. Takada, M. Yoshimura, T. Sonoda, H. Kobayashi, *Bull. Chem. Soc. Jpn.* **1984**, *57*, 2600–2604.
- [200] E. Martin, D. L. Hughes, S. J. Lancaster, *Inorg. Chim. Acta* **2010**, *363*, 275–278.
- [201] M. G. Hill, W. M. Lamanna, K. R. Mann, *Inorg. Chem.* **1991**, *30*, 4687–4690.
- [202] R. J. LeSuer, W. E. Geiger, *Angew. Chem. Int. Ed.* **2000**, *39*, 248–250.
- [203] W. E. Geiger, F. Barrière, *Acc. Chem. Res.* **2010**, *43*, 1030–1039.
- [204] T. R. O’Toole, J. N. Younathan, B. P. Sullivan, T. J. Meyer, *Inorg. Chem.* **1989**, *28*, 3923–3926.
- [205] E. Fitzer, K.-H. Kochling, H. P. Boehm, H. Marsh, *Pure Appl. Chem.* **2009**, *67*, 473–506.
- [206] R. L. McCreery, in *Electroanalytical Chemistry* (Ed.: A.J. Bard), **1991**.
- [207] G. M. Jenkins, K. Kawamura, *Nature* **1971**, *231*, 175–176.
- [208] K. Ngamchuea, S. Eloul, K. Tschulik, R. G. Compton, *J. Solid State Electrochem.* **2014**, 1–7.
- [209] F. G. Cottrell, *Physik. Chem.* **1902**, *44*, 385.
- [210] D. Shoup, A. Szabo, *J. Electroanal. Chem.* **1982**, *140*, 237–245.
- [211] R. G. Bates, J. F. Coetzee, E. Bishop, T. Fujinaga, Z. Galus, L. Meites, H. W. Nürnberg, P. Zuman, M. Branica, G. Charlot, et al., *Pure Appl. Chem.* **1976**, *45*, 131–134.
- [212] F. Scholz, in *Electroanalytical Methods* (Ed.: F. Scholz), Springer Berlin Heidelberg, **2010**, pp. 11–31.
- [213] A. C. Testa, W. H. Reinmuth, *Anal. Chem.* **1961**, *33*, 1320–1324.
- [214] R. G. Compton, E. Laborda, K. R. Ward, *Understanding Voltammetry: Simulation of Electrode Processes*, Imperial College Press, London, **2014**.
- [215] *DigiElch - Professional Version 7.FD*, Elchsoft, Kleinromstedt, Germany, **2006**.
- [216] A. G. Massey, Park, A. J., Stone, F. G. A., *Proc. Chem. Soc.* **1963**, 212.
- [217] A. G. Massey, A. J. Park, *J. Organomet. Chem.* **1964**, *2*, 245–250.

- [218] A. G. Massey, A. J. Park, *J. Organomet. Chem.* **1966**, *5*, 218–225.
- [219] M. A. Beckett, D. S. Brassington, S. J. Coles, M. B. Hursthouse, *Inorg. Chem. Commun.* **2000**, *3*, 530–533.
- [220] H. Jacobsen, H. Berke, S. Döring, G. Kehr, G. Erker, R. Fröhlich, O. Meyer, *Organometallics* **1999**, *18*, 1724–1735.
- [221] G. Erker, *Dalton Trans.* **2005**, 1883.
- [222] W. E. Piers, T. Chivers, *Chem. Soc. Rev.* **1997**, *26*, 345.
- [223] D. J. Parks, W. E. Piers, *J. Am. Chem. Soc.* **1996**, *118*, 9440–9441.
- [224] V. Gevorgyan, M. Rubin, S. Benson, J.-X. Liu, Y. Yamamoto, *J. Org. Chem.* **2000**, *65*, 6179–6186.
- [225] J. M. Blackwell, K. L. Foster, V. H. Beck, W. E. Piers, *J. Org. Chem.* **1999**, *64*, 4887–4892.
- [226] J. M. Blackwell, E. R. Sonmor, T. Scoccitti, W. E. Piers, *Org. Lett.* **2000**, *2*, 3921–3923.
- [227] K. Ishihara, H. Yamamoto, *Eur. J. Org. Chem.* **1999**, *1999*, 527–538.
- [228] R. E. LaPointe, G. R. Roof, K. A. Abboud, J. Klosin, *J. Am. Chem. Soc.* **2000**, *122*, 9560–9561.
- [229] I. Krossing, I. Raabe, *Angew. Chem. Int. Ed.* **2004**, *43*, 2066–2090.
- [230] A. Bernsdorf, H. Brand, R. Hellmann, M. Köckerling, A. Schulz, A. Villinger, K. Voss, *J. Am. Chem. Soc.* **2009**, *131*, 8958–8970.
- [231] X. Yang, C. L. Stern, T. J. Marks, *J. Am. Chem. Soc.* **1994**, *116*, 10015–10031.
- [232] E. Y. X. Chen, T. J. Marks, *Chemical Reviews-Columbus* **2000**, *100*, 1391–1434.
- [233] S. J. Lancaster, A. Rodriguez, A. Lara-Sanchez, M. D. Hannant, D. A. Walker, D. H. Hughes, M. Bochmann, *Organometallics* **2002**, *21*, 451–453.
- [234] M. Bochmann, S. J. Lancaster, M. D. Hannant, A. Rodriguez, M. Schormann, D. A. Walker, T. J. Woodman, *Pure Appl. Chem.* **2003**, *75*, 1183–1196.
- [235] M. Bochmann, *Organometallics* **2010**, *29*, 4711–4740.
- [236] C. J. Harlan, T. Hascall, E. Fujita, J. R. Norton, *J. Am. Chem. Soc.* **1999**, *121*, 7274–7275.
- [237] J. Karl, G. Erker, R. Fröhlich, *J. Am. Chem. Soc.* **1997**, *119*, 11165–11173.
- [238] C. J. Beddows, A. D. Burrows, N. G. Connelly, M. Green, J. M. Lynam, T. J. Paget, *Organometallics* **2000**, *20*, 231–233.
- [239] R. J. Kwaan, C. J. Harlan, J. R. Norton, *Organometallics* **2001**, *20*, 3818–3820.

- [240] L. H. Doerrer, A. J. Graham, D. Haussinger, M. L. H. Green, *J. Chem. Soc., Dalton Trans.* **2000**, 813–820.
- [241] C. Lorber, R. Choukroun, L. Vendier, *Organometallics* **2008**, *27*, 5017–5024.
- [242] M. Becker, A. Schulz, A. Villinger, K. Voss, *RSC Adv.* **2011**, *1*, 128–134.
- [243] S. A. Cummings, M. Imura, C. J. Harlan, R. J. Kwaan, I. V. Trieu, J. R. Norton, B. M. Bridgewater, F. Jäkle, A. Sundararaman, M. Tilset, *Organometallics* **2006**, *25*, 1565–1568.
- [244] A. E. Ashley, T. J. Herrington, G. G. Wildgoose, H. Zaher, A. L. Thompson, N. H. Rees, T. Krämer, D. O’Hare, *J. Am. Chem. Soc.* **2011**, *133*, 14727–14740.
- [245] E. J. Lawrence, V. S. Oganessian, G. G. Wildgoose, A. E. Ashley, *Dalton Trans.* **2013**, *42*, 782–789.
- [246] *OriginPro 8*, OriginLab Corporation, Northampton, MA, **2007**.
- [247] N. G. Connelly, W. E. Geiger, *Chem. Rev.* **1996**, *96*, 877.
- [248] C. Jiang, O. Blacque, H. Berke, *Organometallics* **2009**, *28*, 5233–5239.
- [249] C. Bibal, C. C. Santini, Y. Chauvin, C. Vallée, H. Olivier-Bourbigou, *Dalton Trans.* **2008**, 2866.
- [250] A. L. Kenward, W. E. Piers, *Angew. Chem. Int. Ed.* **2008**, *47*, 38–41.
- [251] T. Voss, T. Mahdi, E. Otten, R. Fröhlich, G. Kehr, D. W. Stephan, G. Erker, *Organometallics* **2012**, *31*, 2367–2378.
- [252] E. J. Lawrence, V. S. Oganessian, D. L. Hughes, A. E. Ashley, G. G. Wildgoose, *J. Am. Chem. Soc.* **2014**, *136*, 6031–6036.
- [253] D. D. Tanner, G. J. Xie, J. Hooz, C. M. Yang, *J. Org. Chem.* **1993**, *58*, 7138–7142.
- [254] I. Ryu, S. Uehara, H. Hirao, T. Fukuyama, *Org. Lett.* **2008**, *10*, 1005–1008.
- [255] S. Kobayashi, T. Kawamoto, S. Uehara, T. Fukuyama, I. Ryu, *Org. Lett.* **2010**, *12*, 1548–1551.
- [256] A. Ekomié, G. Lefèvre, L. Fensterbank, E. Lacôte, M. Malacria, C. Ollivier, A. Jutand, *Angew. Chem. Int. Ed.* **2012**, *51*, 6942–6946.
- [257] T. J. Barker, D. L. Boger, *J. Am. Chem. Soc.* **2012**, *134*, 13588–13591.
- [258] P. Jutzi, C. Müller, A. Stammler, H.-G. Stammler, *Organometallics* **2000**, *19*, 1442–1444.
- [259] H. Schmidbaur, G. Blaschke, *Z. Naturforsch., Teil B* **1978**, *33*, 1556–1558.
- [260] L. Greb, P. Oña-Burgos, B. Schirmer, S. Grimme, D. W. Stephan, J. Paradies, *Angew. Chem. Int. Ed.* **2012**, *51*, 10164–10168.

- [261] T. Steiner, *Angew. Chem. Int. Ed.* **2002**, *41*, 48–76.
- [262] E. J. Lawrence, R. J. Blagg, D. L. Hughes, A. E. Ashley, G. G. Wildgoose, *Chem. Eur. J.* **2015**, *21*, 900–906.
- [263] T. Iwasita, *Electrochim. Acta* **2002**, *47*, 3663–3674.
- [264] D. Griller, K. U. Ingold, *Acc. Chem. Res.* **1980**, *13*, 317–323.
- [265] C. Chatgililoglu, K. U. Ingold, J. C. Scaiano, *J. Am. Chem. Soc.* **1981**, *103*, 7739–7742.
- [266] S. U. Pedersen, T. Lund, *Acta. Chem. Scand.* **1991**, *45*, 397–402.
- [267] P. Cauliez, M. Benaskar, A. Ghanimi, J. Simonet, *New J. Chem.* **1998**, *22*, 253–261.
- [268] E. Duñach, A. P. Esteves, A. M. Freitas, M. J. Medeiros, S. Olivero, *Tetrahedron Lett.* **1999**, *40*, 8693–8696.
- [269] D. M. Fang, D. G. Peters, M. S. Mubarak, *J. Electrochem. Soc.* **2001**, *148*, E464–E467.
- [270] A. P. Esteves, A. M. Freitas, M. J. Medeiros, D. Pletcher, *J. Electroanal. Chem.* **2001**, *499*, 95–102.
- [271] D. H. McDaniel, H. C. Brown, *J. Org. Chem.* **1958**, *23*, 420–427.
- [272] E. R. Clark, A. Del Grosso, M. J. Ingleson, *Chem. Eur. J.* **2013**, *19*, 2462–2466.
- [273] P. R. Rablen, *J. Am. Chem. Soc.* **1997**, *119*, 8350–8360.
- [274] S.-H. Ueng, M. Makhlof Brahmi, E. Derat, L. Fensterbank, E. Lacôte, M. Malacria, D. P. Curran, *J. Am. Chem. Soc.* **2008**, *130*, 10082–10083.
- [275] T. Matsumoto, F. P. Gabbaï, *Organometallics* **2009**, *28*, 4252–4253.
- [276] T. Matsumoto, F. P. Gabbaï, *Organometallics* **2009**, *28*, 4898–4898.
- [277] E. J. Lawrence, T. J. Herrington, A. E. Ashley, G. G. Wildgoose, *Angew. Chem. Int. Ed.* **2014**, *53*, 9922–9925.
- [278] A. J. Arduengo, H. V. R. Dias, R. L. Harlow, M. Kline, *J. Am. Chem. Soc.* **1992**, *114*, 5530–5534.
- [279] D. G. Gusev, *Organometallics* **2009**, *28*, 6458–6461.
- [280] *ACD/Labs NMR Database*, Advanced Chemistry Development, Inc., Ontario, Canada, **n.d.**
- [281] G. Ménard, J. A. Hatnean, H. J. Cowley, A. J. Lough, J. M. Rawson, D. W. Stephan, *J. Am. Chem. Soc.* **2013**, *135*, 6446–6449.
- [282] X. Pan, X. Chen, T. Li, Y. Li, X. Wang, *J. Am. Chem. Soc.* **2013**, *135*, 3414–3417.

- [283] R. T. Boéré, A. M. Bond, S. Cronin, N. W. Duffy, P. Hazendonk, J. D. Masuda, K. Pollard, T. L. Roemmele, P. Tran, Y. Zhang, *New J. Chem.* **2008**, *32*, 214–231.
- [284] E. R. Clark, M. J. Ingleson, *Angew. Chem. Int. Ed.* **2014**, *53*, 11306–11309.
- [285] A. Macchioni, *Chem. Rev.* **2005**, *105*, 2039–2074.
- [286] E. Y.-X. Chen, S. J. Lancaster, in *Comprehensive Inorganic Chemistry II (Second Edition)* (Ed.: J.R. Poeppelemeier), Elsevier, Amsterdam, **2013**, pp. 707–754.
- [287] C. Lindner, B. Maryasin, F. Richter, H. Zipse, *J. Phys. Org. Chem.* **2010**, *23*, 1036–1042.
- [288] V. Ermolaev, V. Miluykov, I. Rizvanov, D. Krivolapov, E. Zvereva, S. Katsyuba, O. Sinyashin, R. Schmutzler, *Dalton Trans.* **2010**, *39*, 5564–5571.
- [289] L. J. Hounjet, C. Bannwarth, C. N. Garon, C. B. Caputo, S. Grimme, D. W. Stephan, *Angew. Chem. Int. Ed.* **2013**, *52*, 7492–7495.
- [290] D. J. Scott, M. J. Fuchter, A. E. Ashley, *Angew. Chem. Int. Ed.* **2014**, *53*, 10218–10222.
- [291] W. V. Konze, B. L. Scott, G. J. Kubas, *Chem. Commun.* **1999**, 1807–1808.
- [292] S. M. Cornet, K. B. Dillon, C. D. Entwistle, M. A. Fox, A. E. Goeta, H. P. Goodwin, T. B. Marder, A. L. Thompson, *Dalton Trans.* **2003**, 4395–4405.
- [293] V. Gutmann, *Coord. Chem. Rev.* **1976**, *18*, 225–255.
- [294] M. A. Beckett, G. C. Strickland, J. R. Holland, K. Sukumar Varma, *Polymer* **1996**, *37*, 4629–4631.
- [295] R. F. Childs, D. L. Mulholland, A. Nixon, *Can. J. Chem.* **1982**, *60*, 801–808.
- [296] G. R. Fulmer, A. J. M. Miller, N. H. Sherden, H. E. Gottlieb, A. Nudelman, B. M. Stoltz, J. E. Bercaw, K. I. Goldberg, *Organometallics* **2010**, *29*, 2176–2179.
- [297] C. A. Reed, *Acc. Chem. Res.* **2013**, *46*, 2567–2575.
- [298] D. Stasko, S. P. Hoffmann, K.-C. Kim, N. L. P. Fackler, A. S. Larsen, T. Drovetskaya, F. S. Tham, C. A. Reed, C. E. F. Rickard, P. D. W. Boyd, et al., *J. Am. Chem. Soc.* **2002**, *124*, 13869–13876.
- [299] E. M. Arnett, C. Y. Wu, *J. Am. Chem. Soc.* **1962**, *84*, 1684–1688.
- [300] H. K. Hall, *J. Am. Chem. Soc.* **1957**, *79*, 5441–5444.
- [301] B. D. McCarthy, D. J. Martin, E. S. Rountree, A. C. Ullman, J. L. Dempsey, *Inorg. Chem.* **2014**, *53*, 8350–8361.
- [302] X. Chen, X. Wang, Y. Sui, Y. Li, J. Ma, J. Zuo, X. Wang, *Angew. Chem. Int. Ed.* **2012**, *51*, 11878–11881.
- [303] E. R. Clark, M. J. Ingleson, *Organometallics* **2013**, *32*, 6712–6717.

- [304] K. Samigullin, M. Bolte, H.-W. Lerner, M. Wagner, *Organometallics* **2014**, *33*, 3564–3569.
- [305] P.-Y. Feng, Y.-H. Liu, T.-S. Lin, S.-M. Peng, C.-W. Chiu, *Angew. Chem. Int. Ed.* **2014**, *53*, 6237–6240.
- [306] S. J. Lancaster, “Alkylation of boron trifluoride with pentafluorophenyl Grignard reagent; Tris(pentafluorophenyl)boron; borane,” can be found under <http://cssp.chemspider.com/215>, DOI: 10.1039/SP215, **2003**.
- [307] H. C. Brown, V. H. Dodson, *J. Am. Chem. Soc.* **1957**, *79*, 2302–2306.
- [308] T. Schaub, M. Backes, U. Radius, *Organometallics* **2006**, *25*, 4196–4206.
- [309] T. E. Krafft, *Method for the Synthesis and Use of Pentafluorophenyl Lithium to Produce Tetrakis Pentafluorophenyl Borate*, **2004**, EP1186608 B1.
- [310] R. C. Srivastava, *J. Chem. Res. (S)* **1985**, 330–331.
- [311] M. J. Frisch, G. W. Trucks, H. B. Schlegel, G. E. Scuseria, M. A. Robb, J. R. Cheeseman, J. A. Montgomery Jr, T. Vreven, K. N. Kudin, J. C. Burant, et al., *Gaussian, Inc., Wallingford, CT* **2004**.
- [312] A. D. Becke, *J. Chem. Phys.* **1993**, *98*, 5648.
- [313] C. Lee, W. Yang, R. G. Parr, *Phys. Rev. B: Condens. Matter* **1988**, *37*, 785–789.
- [314] L. J. Farrugia, *J. Appl. Cryst.* **1999**, *32*, 837–838.
- [315] L. J. Farrugia, *J. Appl. Cryst.* **2012**, *45*, 849–854.
- [316] G. M. Sheldrick, *Acta Cryst.* **2008**, *A64*, 112–122.
- [317] O. V. Dolomanov, L. J. Bourhis, R. J. Gildea, J. A. Howard, H. Puschmann, *J. Appl. Cryst.* **2009**, *42*, 339–341.
- [318] L. Palatinus, G. Chapuis, *J. Appl. Cryst.* **2007**, *40*, 786–790.
- [319] L. Palatinus, S. J. Prathapa, S. van Smaalen, *J. Appl. Cryst.* **2012**, *45*, 575–580.

Appendix of crystallographic data

Appendix of crystallographic data

Diffraction intensities were recorded, an absorption correction applied, and the data reduced by the EPSRC UK National Crystallography Service at the University of Southampton.^[1] Data solution and refinement was kindly performed by either Dr. D. Hughes, or Dr. R. Blagg

The structures of [ⁿBu₄N][**8**-H] and [ⁿBu₄N][**24**-H] were solved (by Dr. D. Hughes) using WinGX,^[314,315] and space groups assigned with ShelXS-97^[316] using direct methods, and then refined with the ShelXL-97^[316] refinement programme using least squares minimisation.

The structure of **26**[OTf] was solved (by Dr. R. Blagg) using Olex2,^[317] and space group assigned with SuperFlip/EDMA^[318,319] using charge flipping, and then refined with the ShelXL-2013/4^[316] refinement programme using least squares minimisation.

Table 9 Crystallographic data

Parameter	[ⁿ Bu ₄ N][8-H]	[ⁿ Bu ₄ N][24-H]	26[OTf]
Elemental formula	C ₁₆ H ₃₆ N, C ₁₈ H B F ₁₅	C ₁₆ H ₃₆ N, C ₁₈ H B Cl ₁₅	C ₂₈ H ₃₈ B F ₃ N ₂ O ₃ S
Formula weight	755.46	1002.21	550.47
Temperature / K	100	140 (1)	100(2)
Crystal system	Monoclinic	Orthorhombic	Monoclinic
Space group	<i>P</i> 2 ₁ / <i>n</i>	<i>Pbca</i>	<i>P</i> 2 ₁ / <i>c</i>
<i>a</i> / Å	10.141(4)	19.8043(10)	9.2387(14)
<i>b</i> / Å	18.471(7)	20.3022(9)	12.2592(17)
<i>c</i> / Å	18.792(7)	21.5428(8)	25.386(4)
<i>α</i> / °	90	90	90
<i>β</i> / °	100.504 (7)	90	98.023(3)
<i>γ</i> / °	90	90	90
Volume / Å ³	3461 (2)	8661.7(7)	2847.0(7)
<i>Z</i>	4	8	4
ρ_{calc} / mg mm ⁻³	1.450	1.537	1.284
μ / mm ⁻¹	0.140	0.980	0.165
<i>F</i> (000)	1552	4064	1168
Crystal size / mm ³	0.21 × 0.11 × 0.04	0.03 × 0.05 × 0.18	0.14 × 0.07 × 0.03
Reflections collected	25957	92236	25007
Independent reflections	6049 [<i>R</i> (int) = 0.030]	5652 [<i>R</i> (int) = 0.141]	6505 [<i>R</i> (int) = 0.1464]
'Observed' data [<i>I</i> ≥ 2σ(<i>I</i>)]	5559	4734	6505
Data / restraints / parameters	6049 / 0 / 548	5652 / 0 / 605	6505 / 0 / 495
Goodness-of-fit on <i>F</i> ²	1.128	1.307	1.055
Final <i>R</i> indexes [<i>I</i> ≥ 2σ(<i>I</i>)]	<i>R</i> ₁ = 0.054 <i>wR</i> ₂ = 0.117	<i>R</i> ₁ = 0.077 <i>wR</i> ₂ = 0.101	<i>R</i> ₁ = 0.0506 <i>wR</i> ₂ = 0.1307
Final <i>R</i> indexes [all data]	<i>R</i> ₁ = 0.061 <i>wR</i> ₂ = 0.121	<i>R</i> ₁ = 0.097 <i>wR</i> ₂ = 0.106	<i>R</i> ₁ = 0.0541 <i>wR</i> ₂ = 0.1357
Largest difference peak / hole / e.Å ⁻³	0.41 / -0.30	0.34 / -0.27	0.407 / -0.673